Systems Integration of Concentrator Photovoltaics and Thermoelectrics for Enhanced Energy Harvesting

A thesis submitted to Cardiff University in the candidature for the degree of **Doctor of Philosophy**

By

Matthew Henry Rolley

School of Engineering

Cardiff University

March 2018

Declaration and statements

DECLARATION

This work has not been submitted in substance for any other degree or award at this or any other university or place of learning, nor is being submitted concurrently in candidature for any degree or other award.

Signed ……....Date ……

STATEMENT 1

This thesis is being submitted in partial fulfilment of the requirements for the degree of PhD.

Signed ……..Date ……

STATEMENT 2

This thesis is the result of my own independent work/investigation, except where otherwise stated, and the thesis has not been edited by a third party beyond what is permitted by Cardiff University's Policy on the Use of Third Party Editors by Research Degree Students. Other sources are acknowledged by explicit references. The views expressed are my own.

Signed ……..Date ……

STATEMENT 3

I hereby give consent for my thesis, if accepted, to be available online in the University's Open Access repository and for inter-library loan, and for the title and summary to be made available to outside organisations.

Signed ……..Date ……..

STATEMENT 4: PREVIOUSLY APPROVED BAR ON ACCESS

I hereby give consent for my thesis, if accepted, to be available online in the University's Open Access repository and for inter-library loans after expiry of a bar on access previously approved by the Academic Standards & Quality Committee.

Signed ……..Date ……

Acknowledgements

And so, a thesis is written, and this landmark stage of my life appears to be coming to an end. Throughout this process, I have been faced with many times of elation and success, matched by equally equivalent times of struggle and self-discovery. Throughout this time, there are those few people, who through their integrity, inherent value and honest purity have helped me substantially. It almost feels as if this small page of writing is not nearly enough to express my gratitude, but I hope it should suffice as recognition to their efforts and contributions to my life. It's something which I don't believe I could have achieved this without them. Firstly, I am thankful and grateful for The Lord, my God who through Jesus Christ has perpetually given me encouragement, strength and wonder in the beauty and fantastic nature of His creation - in addition to placing me here to do this PhD in the first place. I lift up this work for His use, and hope it may be used in some small way for His plan and the good of mankind. I am forever grateful to my brilliant parents and family who have listened, supported and encouraged me through everything. I will never forget what they have done for me. Next, to my beautiful and amazing Ngân, who consistently makes my life happier in every way and has been so patient and loving with me - sometimes more than I deserved. I am lucky to have these people who which every second I spend with them, brings me great happiness.

Then, along the way through this journey, there were those exceptional people whose friendship and encouragement have made things all the more worthwhile and brightened up my life. To Dr. Mateusz Augustyniak with whom I shared many, many happy evenings arguing, discussing, debating and laughing with during our nights at the pub and days in the office! To my brother in arms: James Ho whose companionship throughout the entirety of my undergraduate degree and this PhD was invaluable. To *"the guys*" in the office, Tibin, Lahiru, and Marios; who daily made things so much more enjoyable with their consistent jokes, witty banter and intellectual discussions. My respect and friendship will be there always for you all – you need only ask.

I am grateful to those who have helped me achieve this professionally. To my supervisor Tracy Sweet, who's consistent guidance, direction and has taught so much academically and professionally. But someone more than a supervisor, someone it has been a privilege of which to work with, and a brilliant friend. I hope the future brings you Chris, Alex and Becky many years of success and health – as is only deserving of someone who has helped someone so much, in so many ways. To Nick Jenkins, Gao Min and Wenlong Ming for their ever-watchful and ever-constructive guidance, support, opinions and caring advice of which has proved to be invaluable many times over. To Wenguang Li and Manosh Paul, with whom it was a pleasure to work with and strive alongside, a brilliant experience with similarly brilliant people. To Eduardo F. Fernández, Florencia Almonacid and all the team at the University of Jaén who are as fantastic people as they are brilliantly competent. The visit working with you all was fantastic there was something I will always remember! To my friends and colleagues of the SUNTRAP project (Hasan Baig, Andrew Knox, Andrea Montecucco and Jonathan Siviter), the DEPICT Project, and the CIREGS group - for even as my work does not focus on power electronics, they adopted me as a second family nonetheless.

Finally, I hope you, the reader will find the work in this thesis useful and interesting. It has asked so much from me, even more than I thought at the start - but in return has taught and grown me more than I could've anticipated. I am a different person since when I started, but hopefully a stronger, wiser, or perhaps at the very least - a more knowledgeable one.

Some of the hardest fights

are with the hidden darkness inside.

Doubt, loneliness and failure delights

when the ability to dream dies.

With dark is always light.

A sweet ending, regardless of plight.

The mind can be shifted, changed and twisted,

it's the heart that must be trusted.

So protect and fight,

for what you believe is right.

When closing our eyes,

and through seeking the whys;

it allows us to loose connection

with depressing distractions;

And lets our psyche address

Life's sordid mess.

So, as the sun goes away

bringing back with it a new day,

so can our hope be replenished

from every worldly blemish;

And explode powerful delights

taking existence to new heights.

-

To overcome our self limitations

takes courage, grace and patience.

But every battle won strengthens

Our lessons to teach future generations.

Good luck to both you, reader, and to all those who dare to dream.

Abstract

Alongside other photovoltaic technologies, Concentrator photovoltaics (CPV) capitalise on the recent progress for high-efficiency III:V based multi-junction photovoltaic cells, combining them with low cost optics for increased power production. Thermoelectrics are semiconductor devices that can act as solid-state heat pumps (Peltier mode) or to generate electrical power from temperature differentials (Seebeck effect). In this work, new designs for the integration of a thermoelectric module within a CPV cell receiver were proposed and substantiated as a reliable and accurate temperature control platform. The thermoelectric was used for accurate and repeatable cooling, exhibiting high temporal-thermal sensitivity. Testing was done under varying irradiance and temperature conditions. A novel Closed Loop Integrated Cooler (CLIC) technique was tested, demonstrated and validated as a useful experimental metrology tool for measuring sub-degree cell temperature within hybrid devices using the material properties of the thermoelectric module. Proof-of-concept circuitry and a LabVIEW based deployment of the technique were designed built and characterised. The technique was able to detect thermal anomalies and fluctuations present when undertaking an I-V curve, something otherwise infeasible with a standard k or t-type thermocouple. A full CPV-TE hybrid module with primary and secondary optical elements (POE-SOE-CPV-TE) was built using a further optimised receiver design and tested on-sun for evaluation under outdoor operation conditions in southern Spain. A unique TE-based “self-soldering” process was investigated to improve manufacture repeatability, reproducibility and minimise thermal resistance. A manually-tracked gyroscopic test rig was designed, built and used to gain valuable outdoor baseline comparison data for a commercially available CPV module and a Heterojunction Intrinsic Thinlayer (HIT) flat plate panel with the POE-SOE-CPV-TE hybrid device. An energetic break-even between the power consumed by the TE and the power gain of the CPV cell from induced temperature change was experimentally measured. This work demonstrated the unique functionalities a thermoelectric device can improve CPV power generation. The potential of a TEM to improve CPV power generation through active cooling was highlighted and quantified.

Contents

List of Figures

List of Tables

List of Abbreviations

3J (PV cell) – Triple Junction cell. A photovoltaic cell which comprises of having three internal junctions, usually Ge, Ga(In)As and Ga(In)P as used in this work.

ADC – Analogue to Digital Converter. Converts an analogue signal to a digital value through using binary staircases within an integrated chip.

ALT – Accelerated Life Testing

AM1.5G – Air Mass 1.5 Global. The standard solar irradiance for standard testing conditions (See Section 2.1.2).

AR (coating) – Anti reflection (coating)

a-Si – Amorphous Silicon

BOC – Balance of Cost. Similar to above, this parameter shows a financial breakdown for a photovoltaic panel and their contributions to a system LCOE.

BPD – Bi-pass Diode. A one-way diode included on CPV receivers to allow a secondary current path and eliminate series limiting for devices.

CAPEX – Capital Expenditure. The amount of financial assets (capital) outlay on a particular item or choice.

CCPC – Cross-Compound Parabolic Concentrator. A reflective type of SOE which combined two or more parabolic profiles in a 3D shape.

CIGS – Copper Indium Gallium (Di) Selenide

CLIC – Closed Loop Integrated Cooler (See Chapter 4).

CNC – Computer Numerically Controlled. A type of digital machining that used 3D co-ordinate space (typically Euclidian or Polar) to articulate and define the manufacturing profile the machine tool follows.

COP – Co-efficient of Performance. A value given for heat-pumps to describe the amount of heat moved, over the amount of power consumed (an effective opposite to thermal efficiency)).

CP – Compound Pyramid. A type of SOE which combines a pyramidal shape with another geometrical profile (typically a parabola).

CPV – Concentrator Photovoltaic

CR – Concentration Ratio

CREST – Centre for Renewable Energy Systems Testing. An independent test centre at Loughborough University.

CSOC – Concentrator photovoltaic Standard Operating Conditions, defined as 900 Wm^{-2}, 20 °C ambient temperature, 2 ms^{-1} wind velocity, and direct normal AM1.5 spectral Irradiance distribution as listed in IEC 60904-3.

CSTC – Concentrator photovoltaic Standard Test Conditions, defined as 1000 Wm^{-2}, 25^{o}C Cell temperature and direct normal AM1.5 spectral

DB – Direct Bonding (See Section 3.1.2).

DC – Direct Current in Amps (A).

DFMA – Design For Manufacture Assembly. An industry standard technique for minimising or improving the simplicity of manufacture for a component or device.

DNI – Direct Normal Irradiance in Wm^{-2}.

DSSC – Dye Sensitized Solar Cell

DUT – Device Under Test

DWB – Direct Wafer Bonded

EDM – Electrical Discharge Machining. An advanced technique which uses large induced currents to erode an accurate or complex pattern into the workpiece through using a sacrificial copper electrode.

Eff, PCE or η – Photon Conversion Efficiency. The measured photon-to-electrical power conversion efficiency. Units: %.

EQE – External Quantum Efficiency. A parameter that determines the photon-to-voltage conversion within a solar cell material or junction.

FF – Fill Factor. A parameter dependant on the series and shunt resistances within a solar cell. Denotes the fraction of power produced at the maximum power point (I_{mpp} x V_{mpp}), over the total potential power available (I_{sc} x V_{oc}). Units: %.

FOM – Figure-of-Merit. A value used to summarise a thermoelectric material's performance.

GEN x – "Generation x", where x is a number in roman numerals from I to VIII. This denotes the specific design of the quoted hybrid receiver – relating to the iterative design cycle used (see Chapter 3 and Chapter 5).

GHI – Global Horizontal Irradiance Wm^{-2}.

Gyro – short for "gyroscope". An affectionate name given to the outdoor manual tracker built in this work for on-sun testing (See Section 3.1.9).

HiT – Heterojunction with Intrinsic Thin-layer. A tandem solar cell which consists usually of a mono-crystalline solar cell coated with a thin layer of amorphous.

I^2C – "I squared C" or Inter-Integrated Circuit. An industry standard communication protocol for serial data transfer, developed by Phillips in 1982.

IC – Integrated Circuit

III:V –A compound semiconductor III:V material, comprising elements that reside in groups three and five of the period table (e.g. GaAs).

I_{mpp} – Measured Current value in Amps (A) at the Maximum Power Point.

IPP – In-Plane Pyranometer. Measures the in-plane global irradiance in Wm^{-2}.

IR – Infrared

Irradiance distribution as listed in IEC 60904-3.

I_{sc} – Short-circuit Current. The Current measured in Amps (A) when the voltage applied through the device is 0.

I-V – Current-Voltage (graph). Denotes a plot of measured current values verse an applied bias voltage.

LCOE – Levelized Cost of Energy. The cost per Watt-hour of electrical energy produced from a photovoltaic system. Includes system costs divided typically by the predicted or scheduled energy production of a device during its lifetime.

LPE – Liquid Phase Epitaxy

MBE – Molecular Beam Epitaxy

MOCVD – Metal Organic Chemical Vapour Deposition

MOSFET – Metal Oxide Semiconductor Field Effect Transistor.

MOVPE – Metal Organic Vapour Phase Epitaxy

MPPT – Maximum Power Point Tracker. Electronics which measures the I-V characteristics of a solar device and modifies an electrical load to operate the device at a voltage which corresponds to extracting the maximum power.

m-Si – Monocrystalline Silicon

MTTF – Mean Time to Failure in Hours (h).

Mx (where x is a number) – A standard sizing range, for metric screw and bolt diameters, where the number corresponds to an external thread diameter in mm.

NOCT – Nominal Operating Cell Temperature. An expected operating temperature in ^{o}C or K of the photovoltaic cell within a module or device, due to thermal design or other factors such as optical concentration.

NPN – Negative Positive Negative. Refers to the pin/leg output polarities on a bipolar transistor.

On-Sun – Outdoor testing of solar device under natural solar irradiation.

OPV – Organic Photovoltaic

PCB - Printed Circuit Board

PCM – Phase Change Material

PH- Pyrheliometer. A thermopile measures direct beam normal irradiance in Wm^{-2}.

PID - Proportional Integral Derivative. A control algorithm giving an output error value based on proportional (constant gain/scaler on the input), Integral (cumulative error of output verses input) Derivative (rate of change input feedback signal).

PMMA – Poly(methyl methacrylate). Also known as acrylic, acrylic glass, Perspex or Plexiglass.

P_{mpp} – Measured Power value in Watts (W) at the Maximum Power Point.

p-n or p-i-n – Refers to the internal structure of a semiconductor junction: either "Positive-Negative" layering (p-n) or "Positive-Intrinsic-Negative" (P-i-N).

POA – Plane Of Array

POE – Primary Optical Element

PSU – Power Supply Unit

PV – Photovoltaic

P-V – Power-Voltage (graph). Denotes a plot of measured power values verse an applied bias voltage.

PWM – Pulse Width Modulation. A technique of varying the current output from a fixed source, by changing the time period of a series of constant time pulses.

"Receiver" – Defined within this work, as a device with an electrically-connected solar cell, that can subsequently be tested. This is consistent to CPV-TE Hybrid receivers, where until the CPV cell is bonded, and electrically contacted, is named a "device".

SF – Safety Factor. A multiplier that is used within engineering design best-practise which helps define an operational specification for a component that gives a failure limit or tolerance above normal operation conditions.

SiLO – Single Lens Optic. A type of SOE typically found for both solar cell receiver and light emitting diodes.

SOE – Secondary Optical Element

SOG – Silicon-on-glass

SOTA – State-of-the-art

SSA – Selective Solar Absorber

STC – Standard Testing Conditions. Experimental standard where testing should be done at 25^{o}C, 1atm (ambient) pressure, 1000 Wm^{-2} Irradiance and an AM1.5G spectrum.

STEG – Solar Thermoelectric Generator

T_c – The "Cold-side" temperature of a thermoelectric module (the heat absorption side). Units: ^{o}C or K.

TE – Thermoelectric

TEG – Thermoelectric Generator

TEM – Thermoelectric Module

Temp – Temperature

T_h – The "Hot-side" temperature of a thermoelectric module (the heat rejection side).

UHCPV – Ultra High Concentrator Photovoltaics. Typically includes CPV systems with designed Concentration Ratios of >500x.

UI – User Interface

UKAS – United Kingdom Accreditation Service. An independent, government run institution for accreditation.

V_{mpp} – Measured Voltage value in Volts (V) at the Maximum Power Point.

V_{oc} – Open Circuit Voltage. The voltage measured in Volts (V) when the current through the device is 0.

ΔT – "Delta T". A temperature differential, generally calculated from subtracting a temperature from a secondary "datum" temperature. Units: ^{o}C or K.

Δt – A change in time, or a time period in Seconds (s).

1. Introduction

Our planet needs solutions to satiate our ever increasing demand for energy. Increasing the sustainability in its production would help address the issues of climate change in today's world and preserve it for future generations to come. With the increased adoption of renewable power for large scale power generation, renewable power contributed to 60% of the new power generation installation worldwide in 2014 [1]. These "clean" energy sources are being used as alternatives to fossil fuel powered options, which contribute to some of the major driving factors of climate change. Current attitudes of both policy makers and the general public in the UK are also changing towards this focus, endeavouring to protect and preserve the environment and nature through our choice of power generation technology [2].

Photovoltaics are a scalable and cost effective way of generating renewable power using the solar resource. Recent technological advances for photovoltaics increase their light-to-electricity conversion efficiency, and improve their economic feasibility for wide-spread deployment in large "solar farms". Recent achievements of the UK in this area has resulted in landmark photovoltaic power generation records being set last year [3]. The change in the governmental focus for early adoption of photovoltaic technology was shown and incentivised through the introduction of the "Feed-in-tariff" which enabled consumers and the general public to sell their electricity back to the national grid at a favourable market price. Recent legislative changes have made this tariff less attractive with relation to payback-times, but PV remains a viable option for large-scale production – evident with multiple "subsidy-free" farms being built [4, 5].

Concentrator Photovoltaics (CPV) is a PV technology which uses high-efficiency multi-junction cells combined with low cost concentrating optics to increase power yield. CPV has been shown to be a more economically viable option than conventional PV for large scale plants, with competitive "cost-per-Watt" values being quoted in countries with a Direct Normal Irradiance (DNI) [6]. Following the emergence of III:V based solar cells in 1970 [7, 8], multi-junction PV

cells have been created with these compound semiconductors, and have the highest photon conversion efficiency (PCE) for PV technology for any type of technology reaching a world record 46% at the cell level [9, 10]. Of the many different types of multi-junction configurations that exist, triple-junction lattice matched cells [11] are one of the most practical for commercial production. All types of multi-junction cells incur a high cost-of-manufacture compared to other technologies. This is due to their complicated structure, high temperature manufacturing methods and low production volume.

The low-cost concentrating optics which are used to increase the incident photon flux upon the solar cell, reduces the cost-per-Watt and increases the energy yield per active area of PV cell. For CPV, these optics are typically silicon-on-glass (SOG) or PMMA-based Fresnel lenses to achieve designed concentration ratios (CR) of approximately 500x. The use of these refractive optical designs dictates that solar trackers have to be used due to the smaller light acceptance angle of the optical train. CPV systems are used for larger-scale power generation. Additionally, this increased incident photon flux can marginally increase the PCE at the cell level [11]. Commercial PV cells are optimised for specific concentration ratios. Fabrication of wafers capitalises on this effect and modifying the aspect ratio of their contacting bars on the cell surface and optimising with respect to designed CR.

There are many challenges that currently face the CPV industry. One such challenge is the reduction in power generation exhibited by the III:V semiconductor devices at temperatures higher than Standard Testing Conditions (STC). As the devices heat up under incident sunlight, the amount of energy produced decreases [12, 13]. This effect, quantified through a “temperature co-efficient” in multi-junction cells however, is less than other types of solar technologies (V_{oc} temperature co-efficients: -0.4 to -0.6 mV/K for triple junction cells compared to -0.6 V/K for Silicon-based cells). The elevated operating temperature [14] that can occur due to the concentrating optics placed upon the PV cells can also negatively affect lifetimes of devices [15, 16].

Thermoelectrics (TE) have long since been known as reliable solid-state cooling devices, with a diverse range of applications [17-19]. The combination of

CPV and TE has the potential to address these issues and increase solar energy harvesting. Existing work in the field of CPV-TE has predominantly focused on using a Thermoelectric Module (TEM) for Seebeck-based power generation. The integration of these devices have been done in a few ways, most notably that of a direct-bonded approach (where the CPV cell is in contact with the TEM) or within a spectrum-splitting design. Likewise, there exist main theoretical simulations and calculated optimisation studies for the integration of thermoelectric within several PV technologies. Of this, the previously published literature that experimentally investigate the use of thermoelectric with multi-junction cells is limited. The work in this thesis therefore is to investigate this niche of integrating thermoelectric device with CPV cells in novel CPV-TE hybrid receiver designs.

1.1 Research Objectives

The main objectives of this work were to:

1. Design, develop and manufacture a robust integration of a thermoelectric module with a multi-junction cell.
2. Test the developed CPV-TE receiver for performance evaluation.
3. Investigate the temperature-control capability of a thermoelectric module to set the CPV cell within a hybrid receiver at various temperature and irradiance conditions.
4. Test the hybrid devices under low concentration ratios using Secondary Optical Elements (SOE) to evaluate sub-module performance in-depth.
5. Transition the testing of the hybrid receiver to under Primary Optical Elements (POEs) and higher concentration ratios. This was to further evaluate the performance of the hybrids under realistic CPV operating conditions.
6. Use the experimental outcomes of objectives 1-4 to further innovate, develop and investigate other avenues of novel research or opportunities through integrating the multi-functional thermoelectric within a solar cell receiver.

7. Investigate and optimise areas of power generation losses when transitioning a single hybrid device into a full module with both SOEs and POEs. This included the series resistances of the wiring, the thermal design the related temperature-induced PCE losses for the cells, and to quantify the performance of the TEM under higher CRs.
8. Conduct preliminary Accelerated Life Testing (ALT) of the CPV cells with a hybrid device, to investigate modes of failure that would be present in CPV-TE hybrid devices.
9. Evaluate the role a thermoelectric device could play during ALT in reducing the mean times to failure or otherwise improve the system efficiency lifetimes.

1.2 Thesis Outline

This thesis is split up into five sections. It starts with the literature review, continuing with the three main content contributions, then followed by the overall conclusions and future work sections. The novel contributing work within this thesis is presented in three chapters (3-5). These are organised into the hybrid receiver design and temperature-control substantiation for chapter three, an overview of the "Closed loop Integrated cooler" (CLIC) technique with calibration and validation upon an active hybrid device for chapter four. Finally chapter five is about integrating the hybrid devices into a full module including Primary Optical Elements (POEs), with on-sun experimental evaluation of CPV cell and thermoelectric performance with quantified performance changes.

For the first chapter, a brief overview of the major principles of multi-junction solar cells and thermoelectric device operation is given for context and reference. Following this, an in-depth literature survey of the field of Concentrator Photovoltaics was undertaken and the major challenges to the industry as a whole highlighted and summarised to give a broader context for the subsequent work. These "challenges of CPV" are further split into three subsections: that of work done at the device level (which focuses on the receiver and cell design), work at module level (which includes work relating to optical trains, and higher-level

considerations such as current matching and system cost). Finally that of the system level research is given (inclusive of trackers, the solar resource prediction). The field of CPV-TE hybrid devices directly addresses both the device and the module level challenges for CPV. In section two of the literature review, the current literature for the field of PV-TE hybrid devices is organised into two further sub-sections, experimental and simulation based work. Any publication with an experimentally validated model is presented in the experimental section, to differentiate that of tangible device creation, with that of theoretical evaluation or optimisation. The area of experimental, multi-junction hybrid devices using a direct-bonded approach was chosen as the focus of this research.

Chapter three describes the preliminary investigation for the temperature control ability of the thermoelectric device, and demonstrates the feasibility of this unique functionality of hybrid architectures for CPV. A brief overview of the iterative receiver designs (generations I to IV) is given, and the changes undertaken to develop a robust and accurate testing platform, are discussed. The experimental apparatus, equipment and methodology used for the subsequent experiments are summarised in chapter 4. The experimental equipment as described in the methods section was extensively characterised, the results analysed and summarised for clarity and to ensure confidence in results. The experimental accuracy, and repeatability of the methodology and of the hybrid devices manufacture was evaluated as a foundation for the work within the chapters 4 and 5. The temperature control using the TE was experimentally verified and investigated. Preliminary reliability data and ALT data for the hybrid receivers was obtained, documented and discussed. Outdoor datasets for a commercial CPV and flat-plate PV module are shown as a benchmark and for comparison and context for the later outdoor testing work done in Chapter five with the improved hybrid designs.

Chapter four describes in detail the “Closed Loop integrated Cooler” (CLIC) technique, developed for the measurement of CPV cell temperature within CPV-TE hybrid devices. Firstly, an overview of the technique, its novelty, and a detailed breakdown of its operation within a hybrid system is given. The methodology and systematic calibration methods used to evaluate and validate the technique are

then described. Using these described experimental apparatus, the technique was investigated in detail. The thermocouple datums, the TEM performance, the efficacy of an Arduino-based “proof-of-concept” circuit, a more sensitive data logger based circuit, and the resultant LabVIEW-controlled setup are evaluated. The electrical and system designs of each deployment method is documented and critically reviewed. The limitations of the designed calibration rig are evaluated and explained for further clarity. An absolute deviation from the calibration datum is calculated and stated as a reference accuracy for the following measurements in Chapter five. The functionality of the technique is further demonstrated through combining the technique with the previously designed receivers developed in Chapter two.

Chapter 5 describes the work done to transition the Concentrator Photovoltaic-Thermoelectric with Secondary Optical Element (SOE-CPV-TE) hybrid receiver designs to module level testing under POEs. To facilitate the larger-scale manufacture for producing batches of hybrid receivers, a novel “self-soldering” technique was described and experimentally investigated. This self-soldering technique was experimentally investigated with the exact conditions required for adequate bonding and technique limitations being discussed. Further design changes of the receiver are documented and described (up to generation VII). The experimental setups and hybrid device testing at both Cardiff University and the University of Jaén are explained as part of an experimental collaboration visit to obtain on-sun datasets. In-depth characterisation of the built batches of Gen VII receivers was completed and analysed, pre and post travel to Jaén University for detailed analysis of the devices and for dataset comparability. The data obtained from testing these devices under higher optical concentration ratios is discussed and the process of the full module manufacture (including alignment and acceptance angle characterisation) is described. This full module characterisation is obtained prior to on sun testing, and likewise the resulting efficacy of using a TEM for on-sun cooling within a hybrid device is examined. An energetic break-even condition was found between the power consumption of a thermoelectric module cooling within a CPV-TE hybrid receiver with a power production increase of the

CPV cell. These performance increases achieved from specific TEM excitation current and the discovered areas for performance improvement for POE-SOE-CPV-TE hybrid architectures is investigated and the potential of such designs discussed.

1.3 Summary of Thesis Contributions

In summary, the main contributions of work presented in this thesis can be further condensed into the three statements below:

1. *That the TEM within CPV-TE hybrid devices can be used for rapid, sensitive (sub-degree adjustment) and independent "per-device" temperature control during experimental testing, for a range of temperature under STC and varied irradiance conditions (Chapter 3).*

2. *That the TEM can be used as a "dual-use" functionality for cell temperature measurement and as an active cooling mechanism simultaneously to a degree of accuracy adequate for experimental testing and research for CPV systems (±1^{o}C) (Chapter 4).*

3. *Using the two conclusions from above, using TEM active cooling is beneficial for power generation within a POE-SOE-CPV-TE module as compared to not applying any current to the TEM in a POE-SOE-CPV-TE module (Chapter 5).*

1.4 List of Thesis Publications

From the conclusions above, multiple works have been published throughout the duration of this PhD. These are listed below (in reverse-chronological order), and also cross-referenced (in brackets, underlined and blue at the end of each reference) where relevant to the discovered thesis chapter conclusions as above.

1.4.1 Journal Papers

1. Sweet, T.K.N., M.H. Rolley, W. Li, M.C. Paul, A. Johnson, J.I. Davies, R. Tuely, K. Simpson, Design and Characterization of Hybrid III-V Concentrator Photovoltaic–Thermoelectric Receiver Designs under Primary and Secondary Optical Elements. Applied Energy **[Submitted Dec 2017, recommended paper from ICAE17].** (Chapter 5).

2. Hasan Baig, J.S., W. Li, M.C. Paul, A. Montecucco, **M.H. Rolley**, T.K. N. Sweet, M. Gao, P.A. Mullen, E.F. Fernandez, G. Han, D.H. Gregory, A.R. Knox, Tapas Mallick, Conceptual design and performance evaluation of a hybrid concentrating photovoltaic system In preparation for Energy. Energy, 2017.

3. **Rolley, M.H.**, T.K. Sweet, and G. Min, Photovoltaic–thermoelectric temperature control using a closed-loop integrated cooler. IET Optoelectronics, 2017. (Chapter 4).

4. Li, W., M. Paul, **M. Rolley**, et al., A scaling law for monocrystalline PV/T modules with CCPC and comparison with triple junction PV cells. Applied Energy, 2017. 202: p. 755-771. (Chapter 3).

5. Li, W., M. Paul, **M. Rolley**, et al., A coupled optical-thermal-electrical model to predict the performance of hybrid PV/T-CCPC roof-top systems. Renewable Energy, 2017. 112: p. 166-186. (Chapter 3).

1.4.2 Conference Papers

1. **Rolley, M.H.**, T.K. Sweet, L. Eerens, J.P Ferrer- Rodríguez, E.F. Fernández. Experimental Comparison of a III:V Triple-Junction Concentrator Photovoltaic-Thermoelectric (CPV-TE) Hybrid Module with Commercial CPV and Flat Plate Silicon Modules. **[Accepted Abstract for CPV-14, for future publication in AIP Conference Proceedings 2018, AIP Publishing].** (Chapter 5).

2. **Rolley, M.H.**, T.K. Sweet. Addressing Secondary Optical Element Misalignment of Concentrator Photovoltaic-Thermoelectric Hybrid Receivers, via Multispectral Computer Vision, Artificial Neural Networks, Deep Learning and a Thermoelectric-

Enhanced Spectral Emissivity Map Correction Technique. **[Accepted Abstract for CPV-14, for future publication in AIP Conference Proceedings 2018, AIP Publishing].**

3. Sweet, T., **M. Rolley**, W. Lib, et al., Experimental Characterization and Multiphysics Simulation of a Triple-Junction Cell in a Novel Hybrid III: V Concentrator Photovoltaic–Thermoelectric Receiver Design with Secondary Optical Element. Energy Procedia, 2017. (Chapter 5).

4. Sweet, T.K.N., **M.H. Rolley**, M.J. Prest, et al., Novel hybrid III:V concentrator photovoltaic-thermoelectric receiver designs. AIP Conference Proceedings, 2017. 1881(1): p. 080009. (Chapter 5).

5. **Rolley, M.H.**, T.K. Sweet, and G. Min. In-situ thermoelectric temperature monitoring and "Closed-loop integrated control" system for concentrator photovoltaic-thermoelectric hybrid receivers. in AIP Conference Proceedings. 2017. AIP Publishing. (Chapter 4).

6. **Rolley, M.**, T. Sweet, V. Stoichkov, et al. Triple-junction concentrator photovoltaic-thermoelectric hybrid receivers: robustness, validation and preliminary reliability studies in 13th Photovoltaic Science, Application and Technology Conference (PVSAT-13); Bangor, Wales, UK, 5- 7 April 2017. 2017. http://orca.cf.ac.uk/id/eprint/100662. (Chapter 3).

7. **Rolley, M.**, T. Sweet, and G. Min. Device Integration of Concentrator Photovoltaics and Thermoelectrics in 16th Semiconductor and Integrated Optoelectronics Confernce (SIOE '16), Cardiff, Wales, UK. 2016. (Chapter 3).

8. Sweet, T.K., **M. Rolley**, G. Min, et al. Scalable solar thermoelectrics and photovoltaics (SUNTRAP) in AIP Conference Proceedings. 2016. AIP Publishing. (Chapter 3).

1.5 References

1. [Online] Greenpeace, *Energy [R]evolution 2015*. (Report) 2015. [Accessed:01/05/18]. Available at: https://www.greenpeace.org/archive-international/Global/international/publications/climate/2015/Energy-Revolution-2015-Full.pdf
2. Demski, C., A. Spence, and N. Pidgeon, *Transforming the UK energy system: public values, attitudes and acceptability: summary findings from a survey conducted August 2012.* 2013. [Accessed: 01/05/18]. Available at: http://eprints.nottingham.ac.uk/2242/1/SURVEY_FINAL.pdf
3. [Online] BBC News, *UK achieves solar power record as temperatures soar*, in *BBC*. 2017. [Accessed: 01/05/18]. Available at: http://www.bbc.co.uk/news/business-40058074?intlink_from_url=http://www.bbc.co.uk/news/topics/c302m85q132t/solar-power&link_location=live-reporting-story.
4. [Online] Lamb, H., *UK's first subsidy-free solar farm opens in Bedfordshire*, in *IET Engineering and Technology*. 2017, IET. [Accessed: 01/05/18]. Available at: https://eandt.theiet.org/content/articles/2017/09/uk-s-first-subsidy-free-solar-farm-opens-in-bedfordshire_.
5. [Online] Staff, R., *Britain opens first subsidy-free solar power farm*, in *Reuters UK*. 2017, Reuters. [Accessed: 05/01/17]. Available at: https://uk.reuters.com/article/us-britain-solar-subsidies/britain-opens-first-subsidy-free-solar-power-farm-idUKKCN1C10L5
6. Talavera, D.L., et al., *A worldwide assessment of levelised cost of electricity of HCPV systems.* Energy Conversion and Management, 2016. **127**: p. 679-692. [Accessed: 01/05/18]. Available at: https://www.sciencedirect.com/science/article/pii/S0196890416308536
7. Alferov, Z.I., 1970. Electroluminescence of heavily-doped heterojunctions pAlxGa1-xAs-nGaAs. *Journal of Luminescence*, *1*, pp.869-884. [Accessed on: 01/05/18]. Available at: https://www.sciencedirect.com/science/article/pii/0022231370900992
8. Alferov, Zh I., V. M. Andreyev, V. I. Korol'Kov, and E. L. Portnoi. "Preparation and Investigation of Epitaxial Layers of AlxGa1-xAs solid Solutions and of

Heterojunctions in the AlAs-GaAs system." *Crystal Research and Technology* 4, no. 4 (1969): 495-503. [Accessed: 01/05/18]. Available at: https://onlinelibrary.wiley.com/doi/abs/10.1002/crat.19690040406

9. Dimroth, F., et al., *Four-Junction Wafer-Bonded Concentrator Solar Cells.* IEEE Journal of Photovoltaics, 2016. **6**(1): p. 343-349. [Accessed: 01/05/18]. Available at: http://ieeexplore.ieee.org/abstract/document/7342876/
10. Lackner, D., et al., *Status of Four-Junction Cell Development at Fraunhofer ISE.* E3S Web Conf., 2017. **16**: p. 03009. [Accessed: 01/05/18]. Available at: https://search.proquest.com/openview/58ac5e2e6110db0bd4974c6c900c826a/1?pq-origsite=gscholar&cbl=2040555
11. Cotal, H., et al., *III–V multijunction solar cells for concentrating photovoltaics.* Energy & Environmental Science, 2009. **2**(2): p. 174-192. [Accessed: 01/05/18]. Available at: http://pubs.rsc.org/-/content/articlehtml/2009/ee/b809257e
12. Fernández, E.F., et al., *Temperature coefficients of monolithic III-V triple-junction solar cells under different spectra and irradiance levels.* AIP Conference Proceedings, 2012. **1477**(1): p. 189-193. [Accessed: 01/05/18]. Available at: http://aip.scitation.org/doi/abs/10.1063/1.4753865
13. Siefer, G. and A.W. Bett, *Analysis of temperature coefficients for III–V multi-junction concentrator cells.* Progress in Photovoltaics: Research and Applications, 2014. **22**(5): p. 515-524. [Accessed: 01/05/18]. Available at: https://onlinelibrary.wiley.com/doi/full/10.1002/pip.2285
14. Micheli, L., et al., *Performance, limits and economic perspectives for passive cooling of High Concentrator Photovoltaics.* Solar Energy Materials and Solar Cells, 2016. **153**: p. 164-178. [Accessed: 01/05/18]. Available at: https://www.sciencedirect.com/science/article/pii/S0927024816300307
15. Espinet-Gonzalez, P., et al. *Preliminary temperature accelerated life test (ALT) on III-V commercial concentrator triple-junction solar cells*. in *Photovoltaic Specialists Conference (PVSC), Volume 2, 2012 IEEE 38th*. 2012. [Accessed: 01/05/18]. Available at: http://ieeexplore.ieee.org/abstract/document/6750496/

16. Espinet-González, P., et al., *Temperature accelerated life test on commercial concentrator III–V triple-junction solar cells and reliability analysis as a function of the operating temperature.* Progress in Photovoltaics: Research and Applications, 2015. **23**(5): p. 559-569. [Accessed: 01/05/18]. Available at: https://onlinelibrary.wiley.com/doi/full/10.1002/pip.2461

17. Li, J., et al., *Study on a cooling system based on thermoelectric cooler for thermal management of high-power LEDs.* Microelectronics Reliability, 2011. **51**(12): p. 2210-2215. [Accessed: 01/05/18]. Available at: https://www.sciencedirect.com/science/article/pii/S0026271411001703

18. Min, G. and D. Rowe, *Experimental evaluation of prototype thermoelectric domestic-refrigerators.* Applied Energy, 2006. **83**(2): p. 133-152. [Accessed: 01/05/18]. Available at: https://www.sciencedirect.com/science/article/pii/S0306261905000085

19. Min, G., D. Rowe, and F. Volklein, *Integrated thin film thermoelectric cooler.* Electronics letters, 1998. **34**(2): p. 222-223. [Accessed: 01/05/18]. Available at: http://digital-library.theiet.org/content/journals/10.1049/el_19980148

Chapter 2 : Literature Review

This literature review is split up into three sections. Firstly, a background overview is given describing the operation of a photovoltaic cell and the reason for multi-junction cell architectures combined with a contextual look at the solar resource. Concentrator photovoltaics (CPV) systems are described and an overview of thermoelectric devices and their operating principles is also listed. In the second section, the field of CPV is explored in greater detail, further split into research scopes focusing at the device level, the module level and then finally the system level. The third section reviews the current status of work with regards to CPV-thermoelectric (CPV-TE) hybrid devices is summarised and assessed. This section is split up into the theoretical advances and numerical simulations and the experimental deployments and devices that have been researched. An overall conclusion is then given to position the work within this thesis both within the context of CPV and then more specifically within the field of CPV-TE hybrid research. Included in Figure 2-1, is a graphical representation of the literature review as an "at-a-glance" reference guide.

2.1 Background

In our ever-increasing need for power, solar energy provides a form of renewable energy production that could satisfy our planet's needs, both today and for the future. Capitalising on this ever-present and replenishing resource with the exponential increase in deployed photovoltaics in recent years [1, 2] and with the increasing research interest in this area, photovoltaics remains a viable components to solve or improve the pertinent global challenge of climate change resulting from fossil fuels- alongside providing a sustainable form of power.

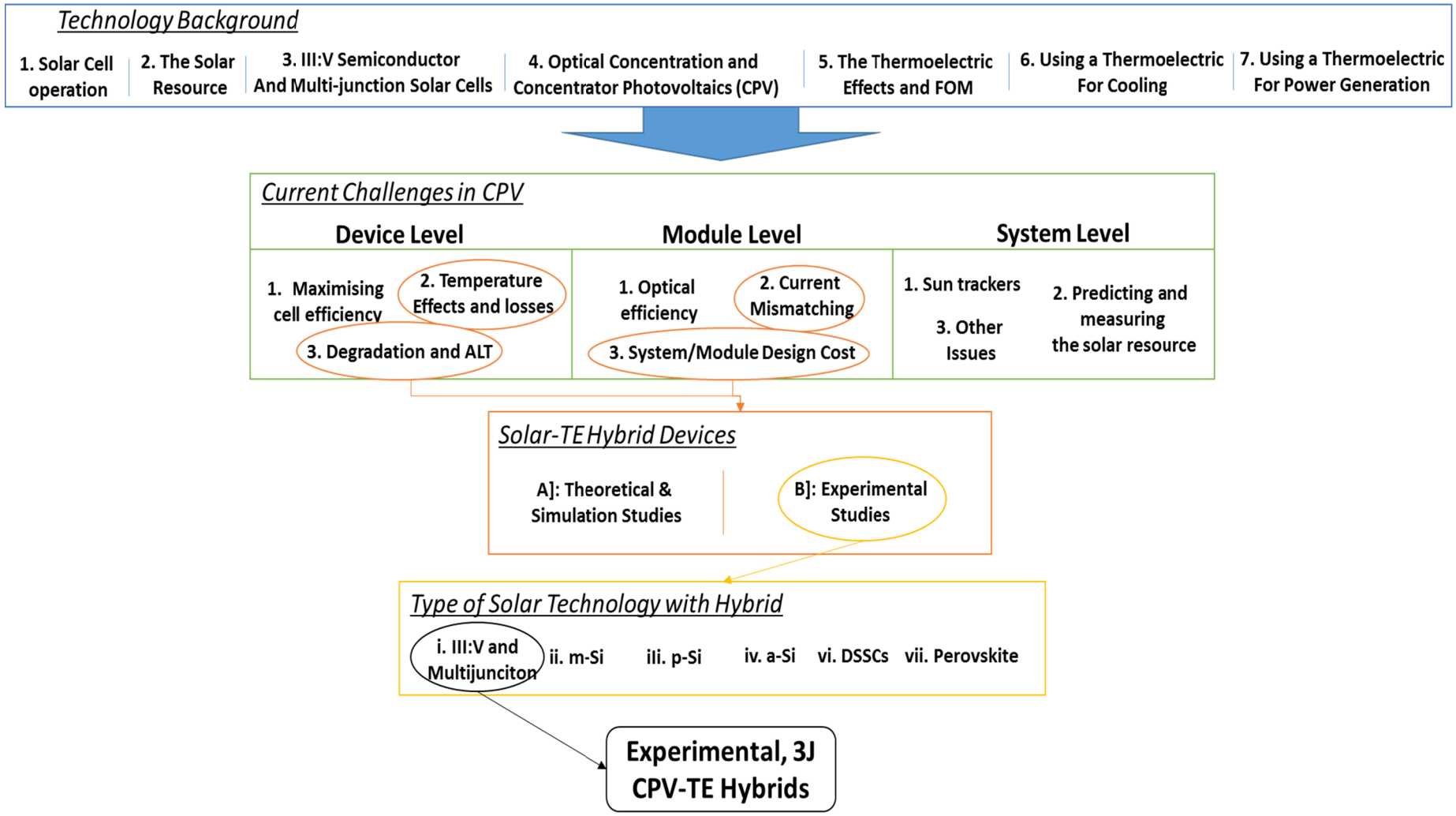

Figure 2-1. Overview Diagram of the Literature Review

2.1.1 Photovoltaic Cell Operation

Photovoltaic cells are semiconductors that are designed for the conversion of light into electrical power. Internally a two- energy band structure arises from having closely-packed atomic lattices, where the electron energy levels for excitation overlap [3]. These two bands are called the conduction and valence band, for the high and low energy excitations respectively [4]. Between these two bands exists a forbidden energy level, called the bandgap. The energy in light photons is defined by Planck's equation, and is directly related to the frequency of the light [5]. When light is absorbed with an energy level of equal or higher to that of the bandgap, an electron (electric charge of 1 electron = 160.217 zeptocoulombs (zC)) is promoted to the conduction band, and a hole created in the valence band establishing an electro-potential [6, 7]. This electron-hole pair is called an exciton. When a load is connected, the created electrical potential is allowed to establish a current flow and hence usable electrical power from sunlight is achieved. Within the semiconductor, the achieved potential can be enhanced through using a positive-negative (p-n) junction. Doping improves the carrier concentration by adding elements with low electron affinity through their atomic structure which supply a larger amount of easily-excitable outer shell electrons. The p-n junction promotes voltage by preventing recombination through improving charge carrier separation from internal material atoms. Recombination is the diffusion of the electrons and holes through the material via the electro-static gradient and re-joining, hence degrading the exciton [6, 8]. The p-n junction establishes an equilibrium near the surface between the two polarities called a depletion region and an electric field (called dark voltage) resisting recombination. This dark voltage and p-n junction structure allows a photovoltaic cell to be electrically considered analogous to a diode.

2.1.2 The Solar Resource

The solar resource is a plentiful and accessible form of clean energy for today and future generations. Solar irradiation is the energy component of the sun created from the internal Helium fusion reactions that occur within its core. Irradiation as measured from outside the earth's atmosphere, has been well

documented through using computer simulation [9] and metrology data from satellites [10-12]. The satellites used predominantly for this data were the ATLAS 1 and 2 missions [13-17], and the EURECA mission [18]. The combined spectra for solar irradiation outside the Earth's atmosphere is defined as a standard; the "Air mass" (AM) 0 spectrum [19] and was first consolidated into a complete spectrum via the "Simple Model of Atmospheric Transmission of Sunshine of Gueymard" (SMARTS2) model [20-23]. Air mass is a term defining the amount (mass) of air that the light travels through before its receiver by an active device. It effectively adjusts the AM0 solar energy resource as per the spectrum changes that occur through transmission and absorption losses through the atmosphere [6, 24]. The standard Air Mass for evaluating solar device performance at sea level is taken as AM1.5, with this being assumed to be the average yearly irradiance per m^2 of land and corresponding to a solar zenith angle of 48.19^o. Air Mass spectra can also have "global" (combined direct and diffuse radiation, AM1.5G) and "Direct" (direct only AM1.5D) components [25], as shown in Figure 2-2. This complex spectral nature of the solar resource, gives rise to challenges for single-junction solar cells, due to their semiconductor architecture only having one energetic bandgap (e.g. 1.12eV for Silicon based cells) for conversion, giving rise to a theoretical conversion efficacy limit of 30% [26, 27].

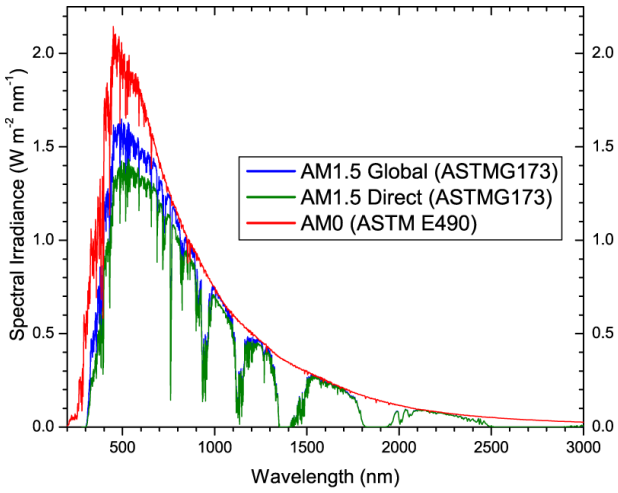

Figure 2-2. The Solar Spectrum as defined by ASTMG173 for AM1.5 [25], and ASTM E490 for AM0 [19] (Image Source: [28]).

2.1.3 Emergence of III:V PV Cells, and Multi-Junction cells

An alternative approach to creating PV cells, is to use III:V compound semiconductors instead of silicon. This was first demonstrated to be feasible with a single junction structure GaAs cell [29, 30]. III:V semiconductors exhibit a unique advantage as the bandgap of the junction can be engineered depending on the elemental composition. Additionally, multiple layers of different material compositions with similar lattice constants can be grown sequentially, creating more advanced crystal structures and hence p-n junction configurations. A Lattice constant or "coordination number" is a value that describes the physical shape of atoms in a material lattice [4], and can be directly related to the crystal formation through the semiconductor growth process and hence the overall cell material quality (and subsequant performance) achieved. Multiple individual cell junctions with different bandgaps can be grown sequentially. This provides a feasible alternative workaround for the Shockley-Quiesser limit, through allowing a larger amount of the incident spectrum to be converted. A multi-junction cell consists of multiple p-i-n sub-cells (positive-intrinsic-negative regions, where the intrinsic represents the space-charge region) which selectively absorb photons from different wavelength regions of the solar spectrum according to the junction bandgaps. Between these sub-cells are heavily doped "tunnel" layers to prevent recombination and promote series coupling inside the cell between the individual junctions. "Tunnel layers" have the effect of creating further potential barriers, resisting inter-cell recombination, and positively facilitating current flow through the cell [31]. These tunnel layers are most effective when they have a large bandgap, and are heavily doped [32].

Multi-junction III:V structures can be grown monolithically onto semiconductor substrates, typically with the middle and upper layers grown on to a bottom wafer (usually Germanium) although an "inverted" technique is also used [p108][33]. The crystal growth of the junctions is challenging, as the materials must have similar lattice constants to give a high yield of cells that won't fracture during production [p90][33]. There exist multiple tolerance limits for material growth aprameters, such as the doping level, composition and thicknesses. Additionally the

used pre-fabricated substrate wafers need to have good surface morphology and no “grown-in” defects which facilitate the resulting crystal growth, and prevent recombination sites respectively. include Germanium is used as it has a narrow bandgap energy, and can convert the lowest frequencies and hence energy of the spectrum (Infrared, IR) which penetrate the furthest into the cell due to not being absorbed in the other layers. The layers can be grown onto each other using Metal-Organic, Vapour Phase Epitaxy (MOVPE), Metal-Organic Chemical vapour Deposition (MOCVD), Liquid Phase Epitaxy (LPE), Direct wafer bonding (DWB) or Molecular Beam Epitaxy (MBE) [34]. An example of the cell structure is shown in Figure 2-3.

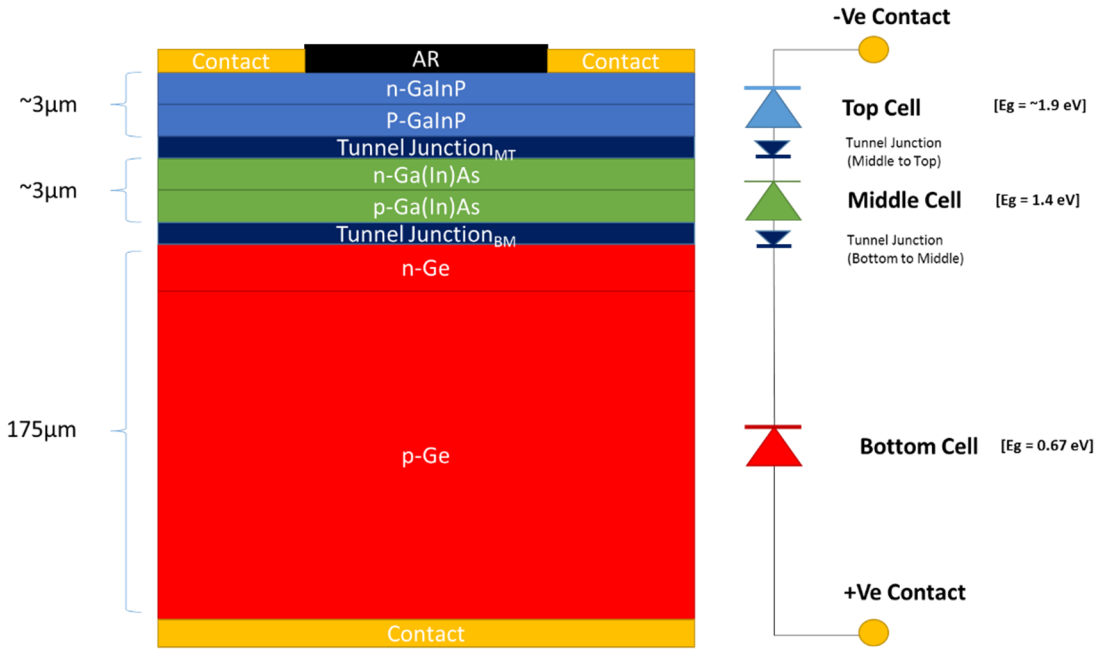

Figure 2-3. Representative Overview of a Lattice-matched Triple Junction Solar Cell (adapted from [34]) [Not to Scale]

As an additional complexity for multi-junction cell design, the junction bandgaps must be designed so the current output by each cell is matched to ensure a maximum power output [35]. The mechanical material properties also need to be considered alongside the chemical, as the subtle differences in Co-efficient of Thermal Expansion (CTE) for each material has been highlighted to create cracking and hence premature failures within the cell during temperature cycling [36].

Through their internal architecture, III-V cells are able to achieve much higher efficiencies than other technologies of around 40% [33, 37, 38], with the current world record for any type of photovoltaic cell being held at 46% with a wafer bonded four junction design [39]. One disadvantage with this technology is the high cost of manufacture due to the energy intensive, accurate chemical composition and morphology of the epitaxial growth. Commercial market availability for these cells is still challenging in low volumes. Additionally, the base cost of the Ge substrate wafers alone is roughly 100 times that of comparable solar-grade silicon [33]. One system level solution for this, due to the higher efficiency and lower thermal co-efficient of multi-junction cells over silicon, is use of optical concentrators (see Section 2.1.4). This makes multi-junction cells more viable due to establishing a lower "levelized cost of energy" (LCOE), giving favourable system-wide "balances of cost" (BOC). CPV technology had the second lowest energy payback time (the time needed to generate the same amount of energy consumed during the device's production and lifetime) from the technologies analysied (mSi, Multi-Si, a-Si, µm-Si, CdTe, CIGS and CPV – see Figure 2-4), according to the Fraunhofer institute [p33][40]. Additionally, CPV exhibits a greater efficacy for large

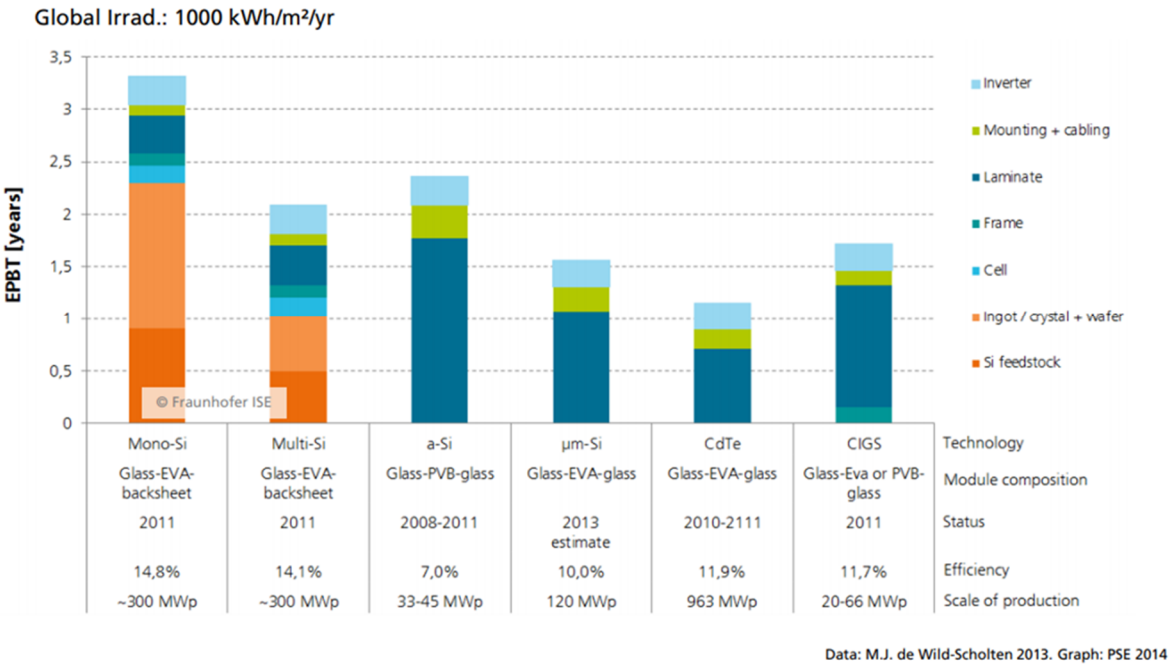

Figure 2-4. Energy Payback Times for multiple PV technologies as Reported by Fraunhofer ISE in 2018 [40]

scale power generation than silicon technologies in sunbelt countries with annual final yield of greater than 1800 kWh/(kWp year) [41].

2.1.4. Optical Concentration and Concentrator Photovoltaics (CPV)

Concentrators have great potential to increase the overall system efficiency of a solar farm [6][p121], [33][p88]. These systems "bundle" and concentrate the incident solar irradiation, which drastically improves the energy output of a module. As has been previously mentioned they can also increase the cost/benefit ratio of the allied photovoltaic cell technology. Non-imaging concentrator optics have the ability to be made from relatively cheap materials, and hence are widely used in the CPV generation industry to maximise financial returns and further lower $/Wh. There are multiple inherent phenomenon that happen when concentrators are used. Optical concentration increases cell short-circuit current through irradiating the cell with an increased photon flux. Additionally the increase incident flux affects the cell's Fill Factor, and produces a slight change in the PV cell efficiency depending on other optimisation parameters. The collector bus bar aspect ratios, cell-area dependant sheet resistance and temperature co-efficients all play a factor to the overall device reaction and performance under concentration [6][p122]. The concentration ratio can be defined as described in Equation 2-1[42, 43].

$$CR = \frac{A_a}{A_r} \qquad \textit{- (Equation 2-1)}$$

Where:

CR = The concentration ratio

A_a = The area of the aperture

A_r = The area of the receiver

Two predominant research fields of non-imaging optical design exist for solar concentration, being that of reflective and refractive type optics. The simplest concentrators are typically of a reflective type, and use the geometry of a hollowed structure to reflect the light onto a focal point. Lower concentration ratios are more common (<10x) due to the amount of material and mechanical structure needed to

achieve the concentration and to minimise the form factor of the final devices improving power yield per m^2 of land. However, better acceptance angles are exhibited over refractive optics as the rays can be reflected multiple time on the different walls of the concentrator [44]. This high acceptance angle capability gives rise to feasible un-tracked, or single axis tracked concentrator designs at the cost of lower achievable concentration ratios. One such family of reflective Secondary Optical Elements (SOEs) is that of the compound parabolic concentrator (CPV). Shown in Figure 2-5 is a selection of these potential design selections, with the Crossed CPC being used within this work (See section 3.3.5). Refractive lenses work using the principles of Snell's law. They re-direct a large area of incident parallel rays (DNI) of the sun onto a fixed focal point thereby concentrating it. Refractive-based concentrator systems require trackers to follow the sun's movement across the sky due to the small (1-2%) acceptance angle of the optics as a trade-off for achieving high concentration ratios. The Fresnel lens structure is commonly used for higher refractive concentration ratios, due to the short focal distances (and hence small CPV module form factor) and lower manufacture costs that can be achieved as compared to achromatic lenses [45]. Another challenge with refractive lenses is the manufacturing imperfections that can occur on the back of the lens. Here light can be scattered by a non-smooth surface, and an optical inefficiency is introduced [42]. This is usually in the region of a few percent however, and can be improved through appropriate material and structural design. Internal parasitic light absorption also occurs within the lens material, further decreasing the maximum optical efficiency possible. Issues also arise from the inherent spectral sensitivity of these multi-junction cells and the required alignment of the optics to the cell active area. The CPV community has recently brought into effect new standards to regulate the performance of the concentrator systems that are released, and maintain industry engagement with the technology. In 2007 the IEC62108 was released and has since become widely accepted as the minimum operational requirement for CPV assemblies [1, 46, 47]. Other standards are currently under development to provide a more substantial legislative framework for CPV technology assessment. These include the IEC 62688, 2011; the UL 8703, 2011; and the IEC 62925, 2014.

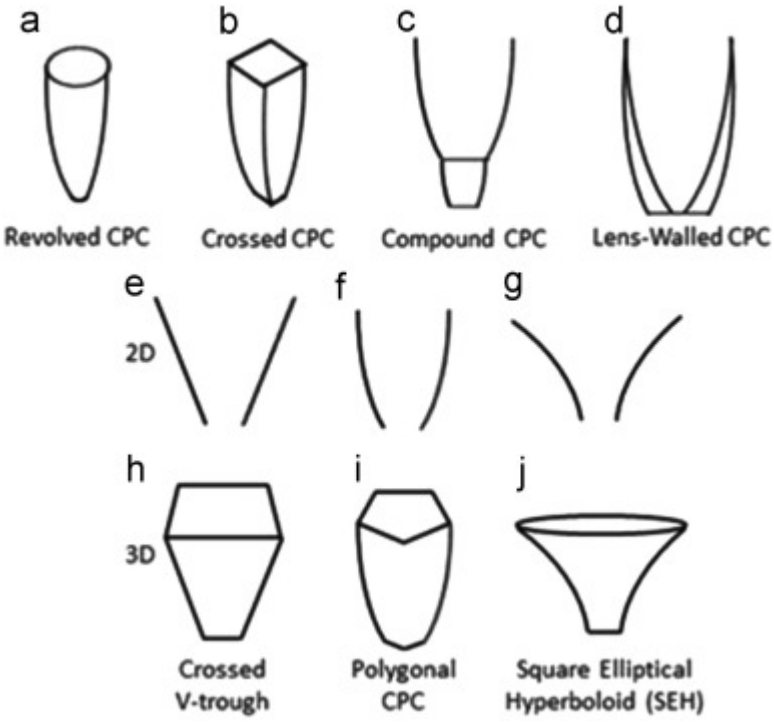

Figure 2-5. A Selection of CPC SOEs, Highlighting the Wide Range of Design Options for CPV Systems. Within this Family is Included the CCPC, as Used within the Subsequent Work in this Thesis. [44]

2.1.5 The Thermoelectric Effects and Figure-Of-Merit (FOM)

2.1.5.a The Seebeck Effect

Among other phenomena inside, two predominant thermoelectric effects exist – that of the Seebeck effect and the Peltier effect. The Seebeck effect is where an electrical potential (voltage) that is generated within any isolated conducting material subjected to a temperature gradient [48]. This generated voltage can be described by the Equation 2-2 below:

$$\Delta V = \alpha(\Delta T) \qquad \text{– (Equation 2-2)}$$

Where:

V = The voltage generated in Volts (V)

ΔT = The difference in temperature in degrees Celsius of Kelvin (^{o}C or K)

α = The Seebeck co-efficient (with the units volts per degree: V/^{o}C)

2.1.5.b The Peltier Effect

The Peltier effect allows the thermoelectric device to act as a heat pump or "Peltier Cooler". Here the current is driven through the thermoelectric device, and heat is moved from one side of the junction to the other. This can be expressed using Equation 2-3:

$$Q = \Pi_{ab} I \qquad \textit{– (Equation 2-3)}$$

Where:

Q = The heat transferred in Wm^{-2}

Π_{ab} = The Peltier co-efficient between a,b (in W/m^2A)

I = The applied current in Amps (A)

These two respective effects occur when a p-n semiconductor junction is placed electrically in series, but thermally in parallel [49]. A common way that is used to establish this configuration for the junction is to arrange the components into thermocouples. Figure 2-6 below shows a representation of this.

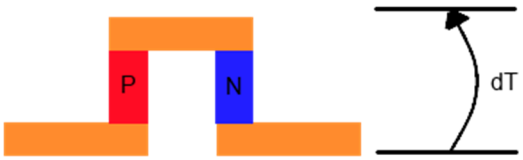

Figure 2-6. A Basic Representation of a Thermocouple

The two effects occur at the semiconductor-metal interfaces that make up the thermocouple structure. The heat energy is absorbed by the charge carriers on one side of the junction, and this energy is used to promote the charge carriers into the condition band – similar to how light is absorbed in PV cells. This generates an exciton pair which, when connected to a load allows an electric current to flow. Likewise, at the opposite side of the junction, the heat is rejected and the carriers fall back into the valence band, completing the circuit [50]. These occur simultaneously within a thermoelectric device in an equilibrium. This equilibrium is then shifted or biased through applying an electrical current in one direction.

Depending on this current bias configuration (input/output), determines whether the device acts as a heat pump (Peltier mode) or as an electricity generator (Seebeck mode).

A thermoelectric module is then built up of multiple thermocouples, in a way that allows access to their combined power production or heat pumping capabilities. This is achieved by connecting the alternating polarities; creating a series electrical circuit [51]. The effectiveness of this thermoelectric circuit is a two factor trade-off between electrical and thermal material properties. Electrically, this can be related a variety of factors such as the charge carrier density, their related Hall mobility, the electrical resistance, and electric contact resistance within the junctions themselves [52]. Thermally, this can be related to the thermal conductivity, the thermal residence time, and the heat flow rate or drift rate of the phonons (heat energy quantas represented as acoustic vibrations within a material lattice, similar to photons in light). Due to the internal electrical resistance of the TEM, an additional parasitic effect occurs, called Joule heating. Joule heating can be

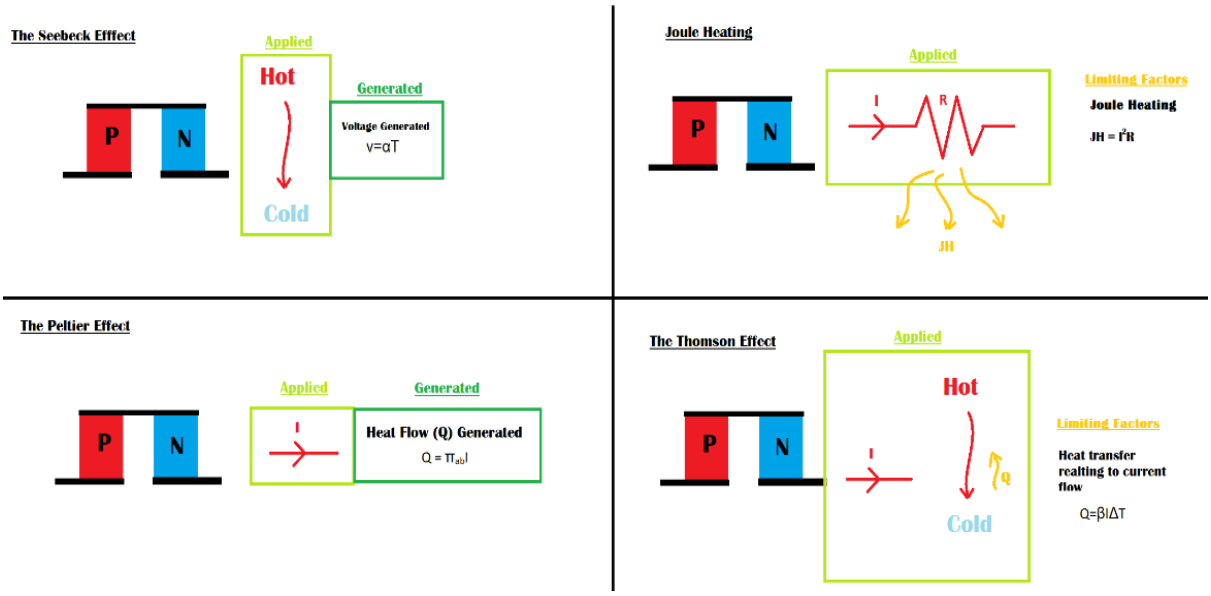

Figure 2-7. A diagrammatic representation of the Seebeck, Peltier Thomson and Joule heating effects - demonstrating the references as shown above.

considered a “self-heating” effect, produced by thermal dissipation of the current passing through the device’s own internal resistance and opposes the established temperature differential. Likewise, the Thomson effect describes another simultaneous performance limitation within thermoelectric modules (TEMs). Here,

the amount of heat absorbed by a conductor with certain sections held at different temperatures, is proportional to the rate of current flow through that conductor [53]. This has obvious implications in thermocouple and module design, as perfect thermal homogeneity in realistic conditions is difficult to achieve [54, 55] and as such this would limit the amount of heat absorption and hence heat flow throughput. A summary of these four combined thermoelectric effects is shown in Figure 2-7.

2.1.5.c The Figure of Merit (FOM)

To appropriately compare the performance of different thermoelectric materials and modules, there exists a parameter called the Figure Of Merit (FOM) represented by the letters 'ZT' and expressed as in Equation 2-4:

$$ZT = \frac{\alpha^2 \sigma}{\lambda} = \frac{\alpha^2}{\lambda \rho} \qquad \textit{– (Equation 2-4)}$$

Where:

Z = The Figure Of Merit

α = The Seebeck Co-efficient in V/^{o}C

λ = The Thermal Conductivity in W/mK

σ = The Electrical Conductivity = $\frac{1}{Electrical\ Resistance\ (\rho)}$ in Ω^{-1}

The FOM can also be expressed graphically as a function of the operating temperature, giving an effective dataset to evaluate the most appropriate material choice for TEM junction design at different temperatures of operation. The most effective (and common) material for "room temperature" (<100^{o}C) applications in the current work is that of Bismuth Telluride (Bi_2Te_3) [56, 57] which exhibits typical COPs of approximately 1 [58]. Additionally, recent progress in nanostructured materials has shown potential improvements of this with a ZT up to 1.4 at 100^{o}C [59].

2.1.6 Using a Thermoelectric Module for Cooling

2.1.6.a Calculating the Induced Heat Flow

Using the equations in Section 1.22 and 1.23, we can calculate the amount of heat pumped by a thermoelectric device (from the cold side and rejected at the hot side) operating in Peltier mode through Equation 2-5 [48, 49, 53]. This equation can be explained in three sections: The thermoelectric cooling power, the loss through thermal transfer and the losses due to the Joule heating effect.

$$Q_c = (\alpha_p - \alpha_n) I T_c - K\Delta T - \frac{I^2 R}{2} \qquad \text{– (Equation 2-5)}$$

Where

Q_c = The heat removed/pumped from the cold side in W

K = The total thermal conductance in W/mK

I = The current in A

R = The internal device resistance which contributes to Joule Heating in Ω

T_c = The cold side temperature in K

$\Delta T = T_h - T_c$ = hot side temperature - cold side temperature in ^oC or K

$\alpha_{n,p}$ = The Seebeck co-efficient of n,p respectively in V/K

2.1.7.b The Co-efficient of Performance (COP)

A useful performance evaluation parameter for TEMs acting in Peltier (cooling) mode and heat pumps in general is the “Co-efficient Of Performance” (COP). This value quantifies a device’s ability to heat or cool with relation to the electrical energy supplied to the device. (Note, this value Using a thermoelectric for cooling can actually be larger than 1 (100%) due to it being a measure of the heat that is pumped in a certain direction – and hence is a different but related concept to efficiency). Disregarding the Thomson effect, the COP (Ø) can be defined through Equation 2-6:

$$\emptyset = \frac{Q_c}{W} = \frac{equation\ (34)}{equation\ (35)} = \frac{(\alpha_p - \alpha_n) I T_c - K\Delta T - \frac{I^2 R}{2}}{I[(\alpha_p - \alpha_n)\Delta T + IR]} \qquad \textit{- (Equation 2-6)}$$

2.1.7 Using a Thermoelectric Module for Power Generation

For use in power generation, a different viewpoint must be taken for describing both the heat flow, and evaluating the losses involved in the system. We can express the heat flow through the module from the source to sink using Equation 2-7 in terms of the Peltier effect contribution, the thermal conduction losses and the Joule heating. Q_H is used here as the heat energy input into the system is applied to the hot side.

$$Q_H = K\Delta T + (\alpha_p - \alpha_n) I T_H - 0.5 I^2 R \qquad \text{- (Equation 2-7)}$$

The electrical generation efficiency on the module can then be expressed using Equation 2-8:

$$\eta = \frac{W}{Q_H} = \frac{(\alpha_p - \alpha_n) I \Delta T - I^2 R}{(\alpha_p - \alpha_n) I T_H + K\Delta T - \frac{I^2 R}{2}} \qquad \text{– (Equation 2-8)}$$

Where W is the electrical work done (W)

2.2 Current Research Trends in CPV Technology

2.2.1 Device Level: Cell Efficiency

Cell efficiency is one of the most fundamental challenge to the CPV industry. Predominantly, a higher efficiency at the cell level in turn guarantees higher module efficiency regardless of further design and manufacture steps. Module efficiency increases themselves are just as favourable, and with every extra Watt of power gained, making the technology more economically feasible and profitable. Market speculation offers that 50% efficient multi-junction CPV cells would mark a turning point of the industry as a whole with current world-record cell efficiencies closely approaching this goal. The reason for 50% is that this would entail an overall system efficiency of >40%, and hence a LCOE of around $80 per MWh - making CPV a competitive electricity source for utility scale production [60-62] in countries with high DNI - specifically the UAE, Chile, Egypt, Israel, Jordan, Namibia, Oman, Saudi

Arabia, or South Africa. Soitec led this drive until it unfortunately closed its solar department in 2015 [63] after accumulating huge losses. Wafer bonding is a well-established industrial technique used to bond together semiconductors, and has shown great success with silicon [64]. Fraunhofer have been working closely on a direct wafer bonding technique for quad junction CPV cells, with the first wafer-bonded quad-junction cells being produced with a conversion efficiency of 44.7% at 297 suns [65]. Fraunhofer has since improved their work and created a similar architecture cell with an efficiency of 46% at 508 suns [39, 66], the current world record. The institute then integrated this cell into a proof-of-concept "mini module" using a full glass achromatic lens. This was then tested at Fraunhofer ISE [67], giving a mini-module efficiency of 43%. The mini-module as used by Fraunhofer ISE is shown in Figure 2-8.

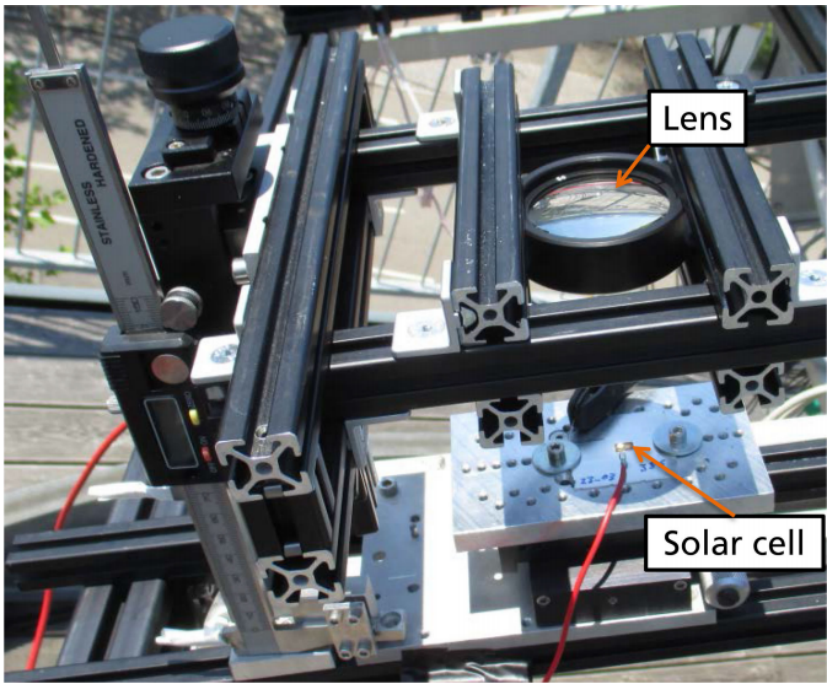

Figure 2-8. The 43% "Mini-module" Designed, Built Tested and Reported by Fraunhofer, Highlighting the World-leading Efficiency of a Wafer-bonded 4J Solar Cell. [67]

Alternative manufacture techniques for quad-junction cells are inverted metamorphic growth processes resulting in [68] a 43.8% efficiency at 327x, or quantum-well based structures that allow the optimum four-junction bandgaps to be met with the material compositions [69]. Quantum-well cells currently show low overall PCEs due to the technology's infancy. Alongside the regular publications

summarising cell PCEs for photovoltaics, NREL maintains an overview chart for these PCEs as shown in Figure 2-9 [70]. The technology leaders for triple-junction (3J) cells are inverted metamorphic triple junctions and Lattice matched triple junctions. The world record 3J cells for this architecture have achieved 43.5% efficiency at 400-600x by Solar Junction for a lattice matched structure, using "dilute nitride" sub cell to achieve the required junction bandgaps [73]. Alternatively, the world record for a triple-junction CPV cell grown with an inverted metamorphic structure is 43.5% also, at a concentration of 306.5 suns, obtained by Sharp [74] and built on work previously done by NREL on IMM structures and cell processing techniques [75, 76]. However, market availability for these prototype cells is a different issue. For commercially and industry available triple-junction cells, the lattice matched record is held by Spectrolab, with an efficiency of 41.6% at 364x concentration [77]. Alternatively, the metamorphic (upright) record is held by Fraunhofer with an efficiency of 41.1% at 454x concentration [78].

Anti-Reflection (AR) coatings are typically added to the cell active areas to minimise any losses through reflecting light back and are crucial area of cell performance optimisation. An AR coating's effectiveness depends on the underlying design and composition. AR coatings with different numbers of layers, changing the refraction and absorption properties [71, 72] are of huge consequence to cell performance through changing the optical transmission into the cell. The number of cell junctions and the optical collection and specific control of the transmission of light into the cell and are major components to consider for the AR coating at the cell level.

The end cost of each CPV cell is related to the manufacture technique, manufacture volume and market pricing (with new products inevitably being sold at a higher price). Lattice matched structures are easier to grow than inverted metamorphic due to less expensive substrates. Additionally, lattice matched 3J CPV cells have demonstrated integration to existing MOVPE manufacture of semiconductor wafer supply chains.

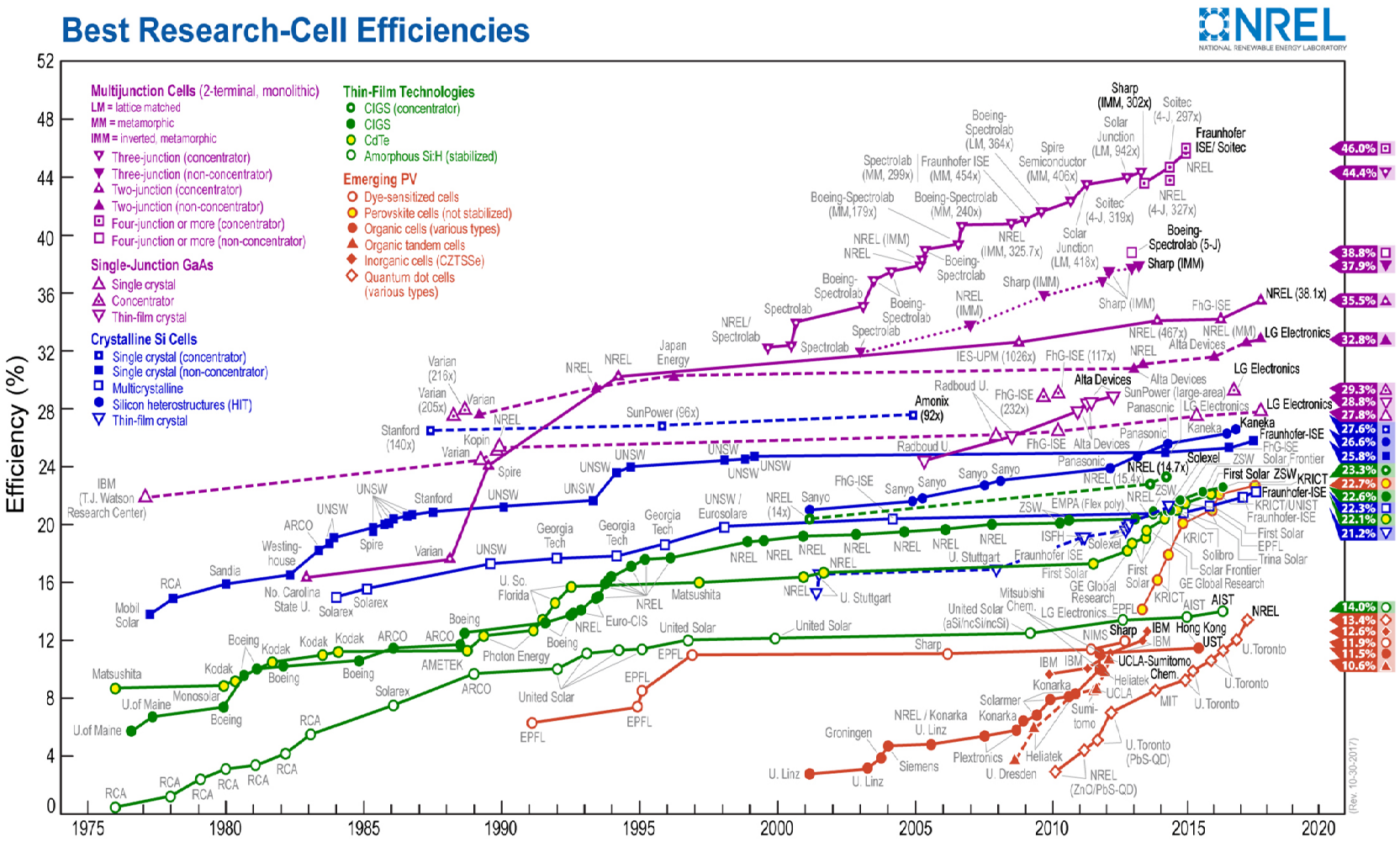

Figure 2-9. An Overview and Cross-comparison Chart Showing the PCEs of Photovoltaic Technologies [70]

Further advances have been made by increasing the number of sub cells. Five and six junction cells have now been shown to be possible to manufacture. The experimental viability and their preliminary performance have been examined, alongside demonstrating an effect of diminishing returns with a larger number of sub cell junctions (see Figure 2-10)[61]. Current work shows a wafer-bonded five junction cell is possible of achieving a 41% conversion efficiency at only a 10x concentration. Concerns have been expressed regarding high resistances created through the wafer bonding process [79]. An experimental six junction CPV cell has been fabricated with an efficiency of 33.7% at 1 sun conditions [80] with no current matching and three graded buffer layers to overcome the high lattice mismatch incurred by the material combinations needed for the sub cell bandgaps. Optimum bandgap values have since been calculated for use in these cell designs up to 10 sub-cells, to give the maximum efficiency for AM1.5 spectral conditions through computational models [81]. No reliability studies at cell or module levels have yet been done on these new cell structures.

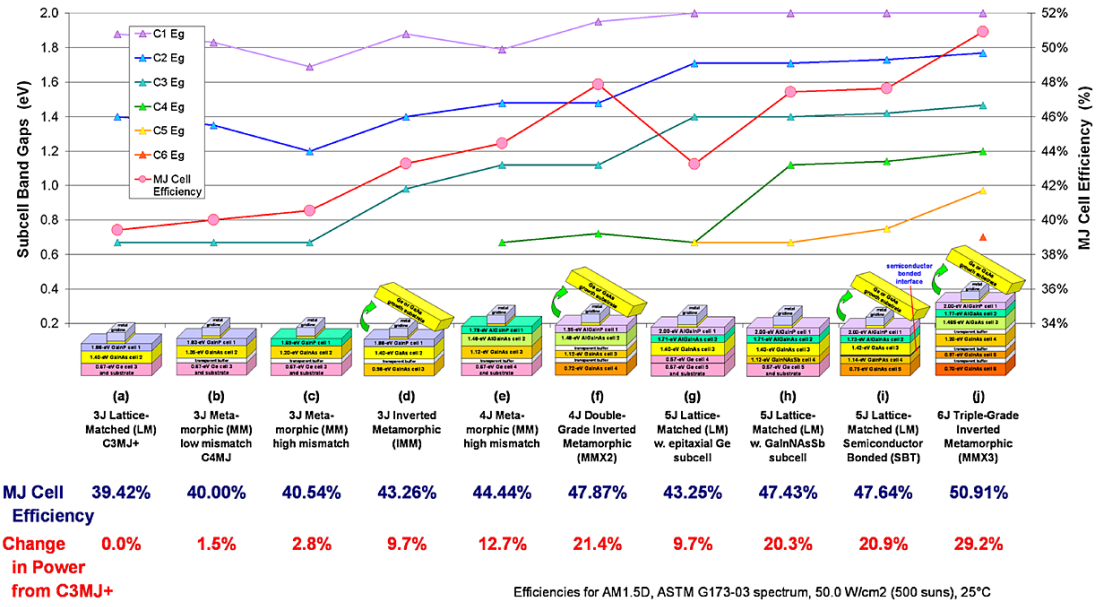

Figure 2-10. Theoretical Evaluation of Higher Number Multiple Junction Cells [61]

Changes in the irradiance spectrum can have a huge impact on the output from a CPV MJ cell. Bandgap optimisations are done at the cell level design stages, to optimise the energies corresponding to sections of the solar spectrum to achieve close to ideal external quantum efficiencies (EQEs). Likewise, a need for a “testing

correction factor" was highlighted by Fraunhofer early in the developments of multi-junction III:V cells to ensure accurate performance representation [82] and then further adapted for use with solar simulators [83]. This was then described into multiple standards such as the IEC62670 [84], and standardised CTSC (concentrator standard test conditions), CSOC (concentrator standard operating conditions) and NOCT (nominal operating cell temperature) test conditions for CPV [85]. The necessary steps to transition data obtained outdoors to be comparable to that measured in controlled simulators [86] were also developed.

Natural irradiance is complex, with spectral variations occurring due to a variety of natural atmospheric and meteorological effects. The three areas of environmental spectral effects can be quantified as the Air Mass due to the sun angle (see Section 2.1.2), the Aerosol Optical Depth (AOD) (with the limiting sub cell junction being related to the Ångstrom law and the size of the suspended particles in the air and hence the effects to the light wavelength diffractions) and the light absorption by precipitable water – with a universal "spectrum factor" being defined [24]. An incremental model has since been studied which evaluated the difference in spectrum for central and circumsolar (DNI not from the "sun disk") irradiance areas, finding that a "spatially distributed spectra" (spectral inhomogeneity across a defined plane) is another crucial cell design factor [87]. Taking these ideas further, a study has shown that the inhomogeneity of concentrated light has the potential to negatively affect a solar module's yearly generation capability by up to 5% [88]. Figure 2-11 shows a graphical representation of these atmospheric effects on the incident spectrum [88].

Preliminary research has been done on the benefit of designing CPV cells for "real-world" changes in spectrum, finding that spectral changes were more significant for cells with four or more junctions and drastic with eight or more [81]. A general trend was experimentally shown that shifting the spectral distributions into the infrared range created generation losses [89]. This is an under-developed area of cell design and as such, location-specific bandgap combination cells could be realised for bespoke manufacture, with subtle efficiency gains being achieved through appropriate design [90].

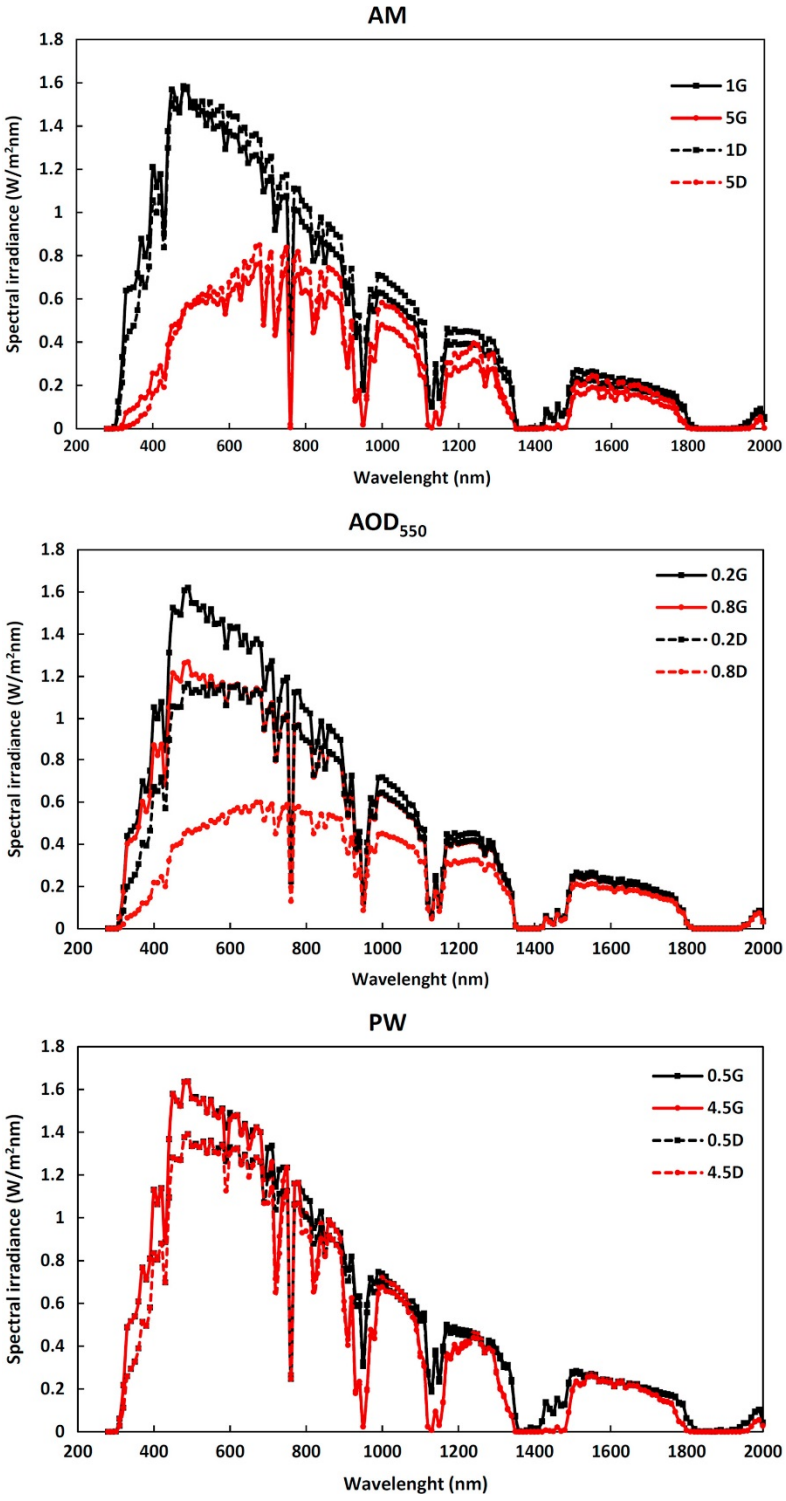

Figure 2-11. A Figure Showing the Effective Changes in Different Incident Spectra, Arising from Various Phenomenon. Shown in the Graph are the Plots for Direct (D) and Global (G) Spectral, with Co-efficient Multiples Denoting the Spectrum Factor Scalar. Given Above are the Graphs for the Changes in Air Mass (AM), Aerosol Optical Depth (AOD) and Precipitable Water. As can be seen, the Effect of each Atmospheric Parameter has a Noticeable Effect on the Incident Spectra. [88]

A study was done to compare commercially available triple junction cells, and found that due to the different metal contact grid footprints, the cells were optimised for different concentration ratios. Commercial Fresnel lenses have also been shown to induce spectral inhomogeneity through inherent chromatic aberration. This creates a scenario where different cells placed in a string within a module can receive significantly different spectra [91].

Following the trends of increasing the number of sub cells to capitalise on a larger band of light frequencies of the incident solar spectrum, works have been done to evaluate the future of such a trend and the potential for PCE improvements. A publication by Sharp [31] summarised the material science challenges that faced current multi-junction cells, including lattice matching using Indium, use of highly doped tunnel layer to promote current and voltage generation, having a thinner secondary buffer layer to improve the bottom Germanium external quantum efficiency, and having a large top bandgap for sub cell current matching. A later detailed theoretical study by Spectrolab, found an architecture defined "law of diminishing returns" with cells that had more than four junctions. The returns were shown to be being especially low with respect to reducing the $/Watt for energy generation. It was re-iterated here that 50% CPV cell was theoretically achievable showing great promise for CPV technology in the future [61].

Combined efforts are continually undertaken by collaborations between NREL and Fraunhofer ISE to track, document and facilitate the growth trends of CPV technology. The general viability of solar in the real world, and the independent verification and testing facilities they both offer, and their annual reports on the current CPV status and efficiencies [37, 92, 93]. These efforts are an invaluable point of benchmarking, information and trust for researchers and industry alike, with reports also providing a contextual basis for progress [1, 40, 94].

2.2.2 Device Level: Temperature effects

Temperature and thermalisation losses in PV cells have been well documented within literature. Photovoltaic cells in general exhibit negative "temperature co-

efficients", with the exception of organic photovoltaics (OPV), Perovskite and dye-sensitised solar cells (DSSCs). This effect means that the cells generate less power at higher temperatures - leading to significant annual energy losses without control of the inherent thermal conditions. The drop in efficiency is caused primarily by a reduction in the bandgap at a higher temperature, where with increasing temperature the I_{sc} increases slightly, but the V_{oc} decreases dramatically. The Voc decreases because the reduced bandgap establishes a smaller electro potential. A larger number, of lower-energy carriers [95, 96] are therefore created. This effect also leads to non-optimised cell junction bandgap combinations, and hence current limiting scenarios if the operating temperature isn't taken into account through the cell design or through appropriate thermal management of the CPV system [97, 98]. A summary of the main fundamental loss mechanisms in a single p-n junction is given in Figure 2-12. In this figure, E_c and E_v are the energies of the conduction and valence band respectively, and E_{fn} and E_{fp} are the Fermi levels of the electrons and holes.

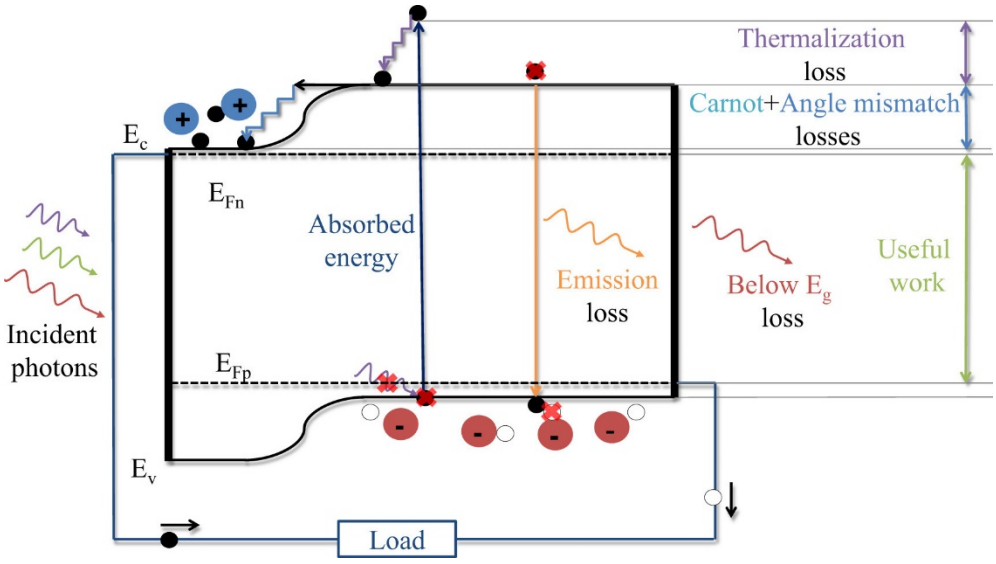

Figure 2-12. An Overview of the Major Fundamental Loss Mechanisms within a Single p-n Junction [98]

The spectral absorption properties of multi-junction cells also change with temperature. Multi-junction cell designs are less susceptible to efficiency drops than other photovoltaic technologies as the combination of multiple bandgaps still cover a larger amount of the incident solar spectrum for conversion. Multiple models, experimental classification and documentation on this complex internal

phenomenon within multi-junction cell structures provide a useful reference tool for CPV research [99, 100].

When under concentration, cooling systems are commonly used to protect the cells from overheating and from thermal damage. The knock-on thermal effects of CPV concentrators have been evaluated through simulation models. One such work describes that cells of area $1cm^2$ can be passively cooled for concentrations up to 500x, with the condition that the attached heat sink resistance of <1.63 K/W at ambient conditions of 25^oC. The work also showed that to prevent operating cell conditions of $>90^oC$ (at ambient temperatures of 40^oC) the heat sink resistance must be less than 1.4K/W for the same concentration [101]. The non-homogeneity of the thermal distributions under concentration and within modules is an under-explored area with relation to cell lifetime, as the only studies of multi-junction cells have been done under "cell-only" conditions. Interestingly, a study on a-Si has shown a PV cell semiconductor junction temperature could drastically differ from its outer packaging temperature (113^oC as opposed to 43^oC) [102]. This suggests a detailed system-level thermal design could be applicable for CPV technologies and not purely cell level studies.

A full CPV module model was made based on a concentrator triple-junction photovoltaic cell combined with a reflective compound parabolic secondary optical elements (SOE) and a silicon-on-glass (SOG) primary optical element (POE). It was found that due to the thermal deformation of the POEs, the lens underwent random deflections and hence gave poor homogeneity of spatial light distribution. This work further emphasised the complex nature of CPV systems, and the necessity for module-level thermal design resulting [103].

More recently, miniaturisation has recently been suggested as a feasible solution to module temperatures [104]. Additionally, aluminium heat exchangers have been noted as being more economical option to copper without critically sacrificing cooling performance. It's suggested that the cost of a heat sink to cool a 3mm x 3mm cell at 1000x could be only double that at 500x, but a law of diminishing returns with relation to power generation applies to cooling over 500x. Other areas of interesting research exist, including novel ways to cool a cell with one such fledgling technology being that of "direct liquid immersion" in silicon oil. Poor optical performance has been exhibited by this approach, and conventional cooling methods maintain a strong list of advantages [105, 106]. An overview diagram of this technique is given in Figure 2-13.

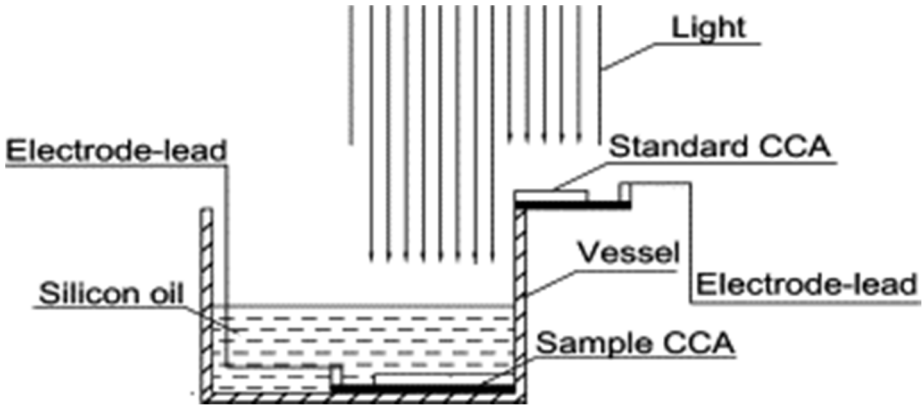

Figure 2-13. The Experimental Setup and Overview of the Proposed "Direct Liquid Immersion" Technique [105]

2.2.3 Device Level: Degradation and ALT

The financial outlay for a CPV system is considerable which brings with it a high investment risk. One industry standard technique to mitigate this risk is to look at a technology's historical performance throughout a given financial pay-back period – typically 25 years. This provides only limited datasets and trends for potential investors and would-be adopters, by keeping the risk high. To approach this issue and gain industry trust for CPV, efforts have been undertaken to provide a standardised design, manufacture and testing framework though international standards and accreditation routes. World leaders have been spearheading this

effort, with Fraunhofer ISE, and NREL releasing regular reports and suggesting standards for approval by the international CPV community.

An alternative way to help mitigate this financial risk is to generate historical data regarding module and system reliability, through accelerated life testing (ALT). Reliability studies for III:V semiconductor PV cells were initially investigated with research on GaAs/Ge tandem (two-junction) cells. The cells in these tests were subjected to high-temperatures, and it was found that contact diffusion into the sub-cell junctions seemed to be a common failure mode. GaAs/Ge cells were shown to operate at temperature up to 180^{o}C for periods of up to eight years – highlighting potential for III:V cell longevity early within its research lifecycle [107]. Fraunhofer undertook a study on single junction AlGaAs/GaAs III:V cells in an accelerated aging test. It was suggested that exposure to steam at 95^{o}C was the best ageing procedure, with "control" modules kept outside of the ovens for comparison and benchmarking against a nominal degradation rate [108]. A study on the degradation mechanisms was released later, and evaluated the effects of oxidation through the change in measured current densities [109].

Crucial developments for reliability studies include an in-depth comparison of LED manufacture processes and their related reliabilities. This was then compared to that of multi-junction cells with a claimed theoretical potential of a cell with a 34 year lifetime at 1000x concentration [110], if analogous process production improvements were made. Likewise, another crucial advancement for CPV cell reliability studies was described where the PV cell was forward biased as the mechanism inside an environmental chamber. This emulated the cells operating under high concentration, as dark currents were injected to exhibit the same cell working conditions found at this concentration [111]. A cell's efficiency degradation was shown to be closely related to the series resistance through cell shorts that would typically occur over its lifetime.

A theoretical study was done of the location and weather effects on a CPV module. It was found that the deployment location of the modules alone dictates the thermal cycling – hence the physical fatigue and damage that a module would receive over its lifetime. A critical cell temperature was stated, and cells that were

operated at less than 77^{o}C under concentration would accumulate less damage and exhibit a longer lifetime [112].

A large body of work has been done over multiple years by the Universidad Politécnica de Madrid (Carlos Algora's group) and ISFOC (Instituto de Sistemas Fotovoltaicos de Concentración, Institute for Concentration Photovoltaics Systems) on the topic of III:V cell reliability. One of the earlier studies was based around a single junction GaAs cell, with the conclusions that GaAs was a reliable device and at 1100x simulated concentration (active cell temp cooled to 30^{o}C), exhibited 1% degradation in efficiency over a 20 year life [113]. It was also mentioned that as multi-junction III:V cells have a high perimeter-area ratio, perimeter recombination effects are detrimental - an effect recorded previously by [114]. Temperature step-stress testing at 90^{o}C to 150^{o}C were then done, giving a mean time to failure (MTTF) of 69.2 years for single junction GaAs cells [115], with any catastrophic failures being attributed to manufacturing errors. A lifetime goal for CPV was mentioned to be 25 years – to be competitive with silicon module warrantees.

A new testing methodology was proposed and tested using single junction GaAs cells, which used dark current injection into the cells to forward bias them and simulate working conditions [116]. The cells were then subjected to an accelerated life test under a higher temperature. A "dark I-V curve" was obtained and compared to an ideal diode model to evaluate the cell performance. The nominal working temperature for a CPV cell was set to be 65^{o}C, and temperatures of 130^{o}C and 150^{o}C were used giving an acceleration factor (AF) difference of 3.8 times higher for these two temperatures during the accelerated test. It was mentioned that cell perimeters coated with an encapsulant could greatly enhance cell reliability. This effect was investigated in further detail by the same team, finding that a MTTF of a magnitude larger was achieved through a cell perimeter protected with a silicone elastomer for GaAs single junction cells [117]. General improvements and suggestions were reviewed, and a 32 cell module was tested outdoors for 7 months. The I_{sc} degraded over time due to strong degradation of the concentration optics, giving a module MTTF of only 7080h (~2.5 years) with manual assembly being a suggested cause [118].

A detailed description of the used instrumentation for module reliability testing was then documented. Similar to before, cell working conditions were mimicked by forward-biasing the cell in the environmental chambers, and dark I-V curves were gathered to evaluate the cell parameters. A PCB design was described, with individual current generators for each cell on an array controlled and monitored by an external computer [119]. Further reliability testing was undertaken on GaAs cells with a working temperature being suggested for 65^{o}C. Progressive power degradation was shown of 3.5% at 3.29x10^{6}h (1127 years) under a CR of 700x, and 2.5% over 8.05x10^{5}h (276 years) at 1050x with an operating temperature of 65^{o}C [120].

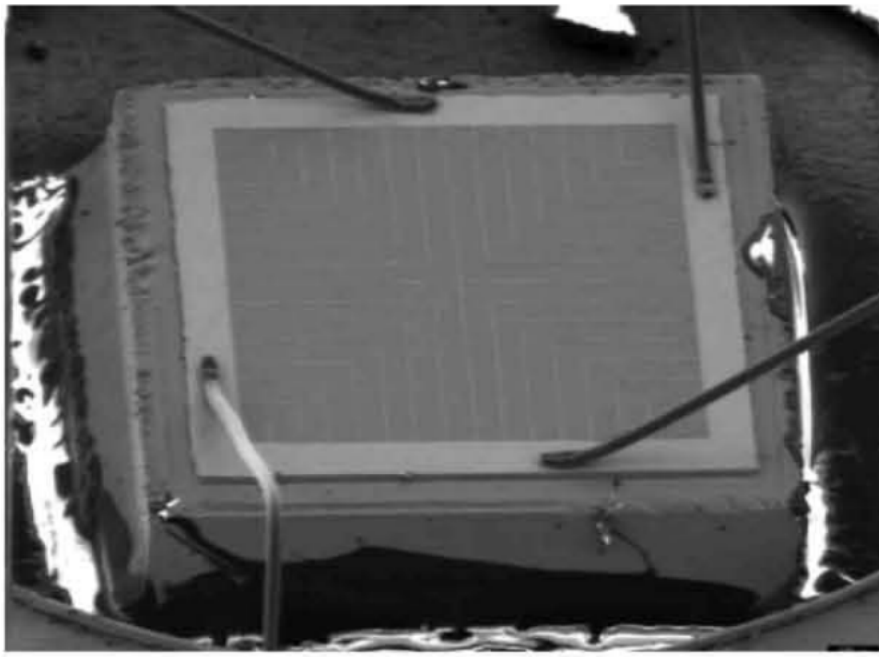

Figure 2-14. A SEM Image of a GaAs Single-Junction CPV cell with Wire-bonding to Busbars. [119]

Building on previous expertise gained from GaAs III:V cells, preliminary investigative work has since been undertaken on III:V triple junction cells. The nominal working conditions were defined as 820x and 80^{o}C, with an ambient temperature of 25^{o}C. All cells at 164^{o}C failed within the scope of the test, and a characteristic life (the time for 63.2% of devices to fail) of only 32.04 hours was calculated [121]. Failure mechanisms of burned and shorted contacts were found. Three temperatures were then used (119^{o}C, 126^{o}C, and 164^{o}C) for further accelerated ageing, and similar lifetime parameters extracted from the data

gathered. At an operating temperature of 80°C and 820x, the MTTF was 302 years for 5h/day operation (equivalent to 189 years for 8h/day), and 100°C and 820x the MTTF was 18 years at 5h/day (11.25 years at 8h/day) [122]. Clearly at 100°C, the triple junction cell itself would not achieve a typical 25 year warrantee lifetime, let alone the modules that they would then be built into. Reliability improvements for the cell would be greatly beneficial with the drastic difference in lifetime between 80°C and 100°C cell lifetimes highlighting a niche for a CPV thermal temperature protection system.

A "thermal runaway" effect in Ge sub cells was studied. It was described that small carbon particles between a Ge and a GaAs layer could cause a temperature cascade resulting in cell failure. As the cell was heated, the resistance dropped, the current increased, the Joule heating likewise increased the temperature, further driving the effect. These carbon particles are inherent to the growth process of III:V cells, but the effect could be mitigated in future for triple junction cells if the sub cells were connected in parallel [123].

A recent work described a new approach to accelerated life testing for multi-junction cells, with the cell receiver being placed on a heat exchanger, and encapsulated with silicone elastomer [124]. A shutter on a concentrator lens was then opened and closed repeatedly to thermally cycle the cell with safety limits being set to ensure degradation, not catastrophic failure, shown in Figure 2-15. Temperatures between 105°C and 50-55°C were cycled, and a significant efficiency drop of 12.65% relative (25.30% absolute pre-degradation efficiency) was shown over 1000 cycles. Perimeter degradations of the solder layer in the form of shunts were also exhibited. A long term, on-sun outdoor study was done by NREL with a 30 cell multi-junction CPV module. A 10% degradation in power produced was shown over a year, under average environmental conditions of 925Wm^{-2}, and 24.5°C [125]. Package charring from off-sun events were recorded too, with one fully shunted cell and shunts found on other cells - once more at the perimeter, at the edge of the

bus bar. Humidity and water ingress was additionally an issue, with cell exfoliation occurring.

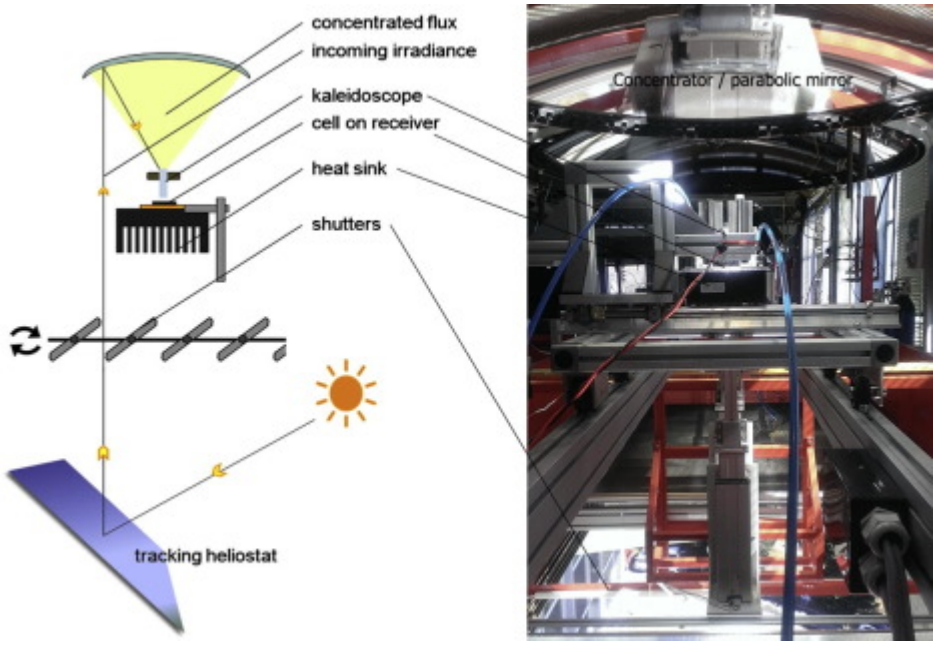

Figure 2-15. An Alternative Experimental Setup Using a tracking On-Sun Heliostat to achieve High Concentration Ratios for Testing [124]

The high operating temperatures seen by CPV cells, has a high likelihood of contributing to mechanical fatigue, and therefore degrading cell life longevity. Multi-junction cells are at risk more so than other technologies due to the different co-efficients of thermal expansion between the sub cell layers – although these layers are extremely thin and include strain balancing and compressive/tensile stresses achieved within the material growth to address this. Lattice matching of the growth layers also helps to minimise this risk, but with other technologies like inverted metamorphic structures, and wafer-bonded quad junction cells - thermal degradation issues may become a huge issue. This is an under-explored, but of high commercial interest area of CPV evaluation and research. A critical cross-comparison of all the different growth architectures with a focus on reliability and failure modes or mechanisms would be invaluable both to the material science of the cells and industry manufacture as a whole.

2.2.4 Module Level: Optical Efficiencies and concentrations

Huge potential gains are achievable through well-considered module designs. One early example of the CPV module format and form factor mostly used today, is

the FLATCON module designed by Fraunhofer in 2003. This module achieved an efficiency of >22% in outdoor measurements [126-129], which was a landmark result at the time. An image of the designed FLATCON module is given in Figure 2-16. Fresnel lenses are the subject of major research, due to as previously mentioned being low-cost, but still being capable of achieving high optical concentration ratios and hence high power yield from CPV farms.

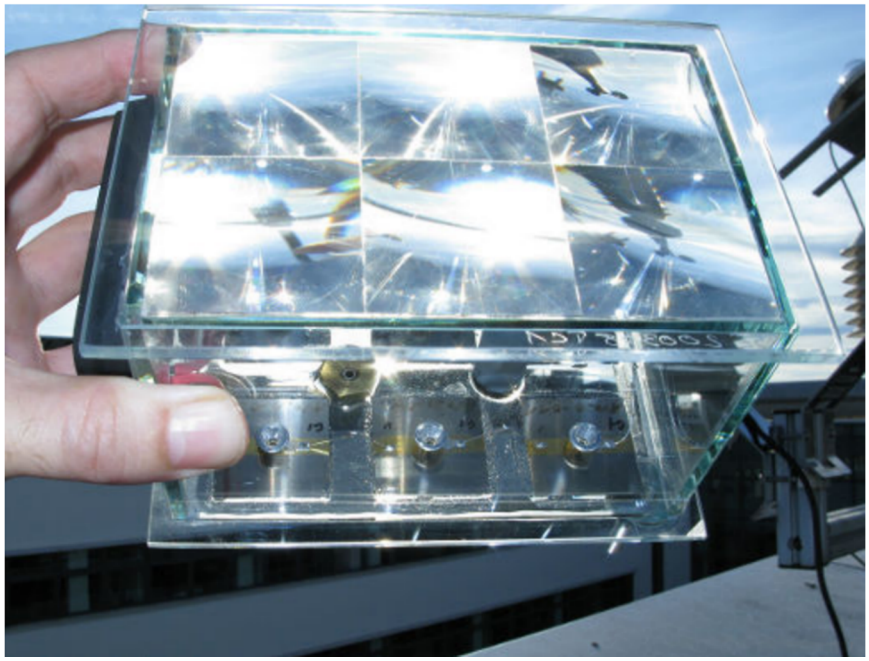

Figure 2-16. An Example Sub-module of a FLATCON CPV Module [128]

There are many complex issues that are related to Fresnel lens based CPV. Typical market concentration values for CPV modules are around 500x, but there are plans to expand the field into “ultra-high concentration (UHCPV)” to extrapolate the increase in power output (and similarly the return on investment and reduction of $/Wh) trend to its maximum. Effective CPV system design is limited by the cell efficiency drop off at higher concentrations, giving a trade-off of power generation to financial outlay and returns. Additionally, cell contact design are optimised in conjunction with the concentration ratio. Thinner bus bar contacts and better aspect rations give less shading, but a higher series resistance and hence limit the maximum current, and likewise CR and power output for the resulting module. Additionally at higher concentrations the temperature increases (see Section 2.2.3).

There are two predominant technologies that are used for optical concentration with refractive non-imaging optics. These are the Achromatic lens and the much cheaper Fresnel lens. Fresnel lenses are typically made from one of two materials –silicon on Glass (SOG) or the polymer Poly(methyl methacrylate) (PMMA). Chromatic aberration is another separate challenge for Fresnel-based concentrating optics. The Fresnel lens is comparatively cheap to manufacture but exhibits strong chromatic aberration (CA) at higher suns. The facets on the lens split the wavelength differently giving a lower optical efficiency, and a non-homogenous irradiance on the CPV cell [130]. This leads to hotspots, spectral mismatches and current limiting issues for the cell itself. Additionally, Fresnel lenses are susceptible to thermal expansion, hence deformation and temperature-induced misalignment losses within the module itself. Likewise a change in their refraction and the aberration worsens at high temperatures, further lowering the optical efficiency of the concentrator. Achromatic lenses do not exhibit chromatic aberration, but are expensive to manufacture and can be fragile due to being made of glass. Work has shown that hybrid Fresnel-Achromatic shaped devices are capable of achieving concentration ratios of up to 8500x [131].

As previously mentioned, an alternative to using refractive optics is to use reflective based optics. These have the advantage of acceptance angle and lower parasitic light absorption within the lens itself, but the disadvantage of mainly lower effective concentration ratios being cost-effective or practical. A crossed compound parabolic shape [133], which has been used in this work for testing with triple junction PV-TE devices. It has been stated that although there is a positive correlation of concentration to in-homogeneity of the irradiance on a cell, Fresnel lenses in general exhibit better irradiance uniformity than reflective technologies. Direct comparisons exist, such as work done by [134] for a cylindrical trough.

Some recent novel innovations relating to the optics of CPV include that of attaching cells directly to lens arrays [135], polymer “compound eye” structures for encapsulation [136], novel contacting methods for cells involving etched silicon “nano-pillars” [137], and sub-wavelength lithography with wet etching for rapid cell contacting [138]. As an alternative to both Fresnel lens designs and Achromatic lens

designs, preliminary investigation work has been done on the use of even lower cost optical fibres. Results show low optical efficiencies in the region of 26-50% [139, 140] and small acceptance angles <0.5^{o} [141].

Soiling is a big issue affecting the power output of a CPV module, and the cumulative power losses can be substantial over a year's generation cycle. Optics being researched include different super hydrophilic and super-hydrophobic surfaces and coatings through modifying the wettability angles. The idea is to either maintain a water film of the surface that prevents the dirt particles to stick; or to have the water repelled and the water droplets carry dirt particles away with them but likewise, this is still at the inception to proof-of-concept level research.

Within this work, two types of SOE were used; that of a CCPC and a SiLO SOE. Likewise, to achieve the require POE train a standard "off-the-shelf" Fresnel POE was used. These are shown in Figure 2-17 for context and cross-reference for the reader with the above literature review.

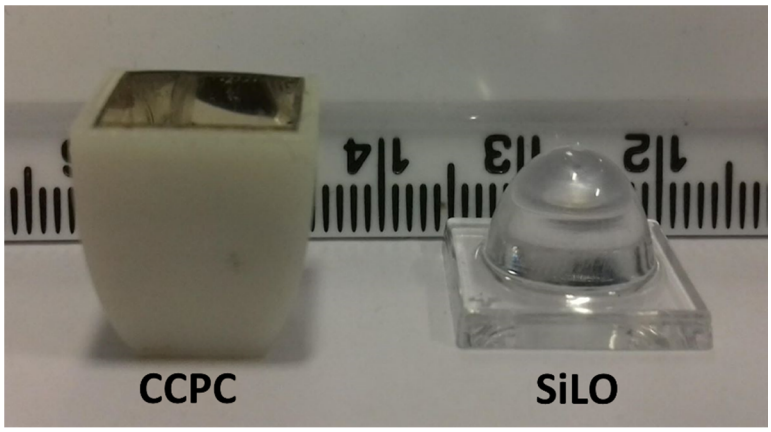

Figure 2-17. An Image of the SOE Designs used in this Work for Context within the Literature Review

2.2.5 Module Level: Current Mis-match

Realistic deployment of CPV technology inevitably leads to scenarios where the irradiance that falls on a module in a string will be non-uniform. Cloud patterns, module self-shading, and thermal deformation of the lenses are some of the natural phenomena that affect solar generation. Within a string of solar cells in a CPV module, these varied conditions across it result in mismatched current

generation by the individual cells. Non-matched current conditions on a string of cells create losses at the inverter, even when using bi-pass diodes in the receivers. This power loss is a system-level consideration and heavily influences the LCOE and plant profitability, but little work has been done on this issue. The simulations above have briefly focused on it only as part of a larger system study for the trackers themselves [142]. Module shading has been also been individually studied, and shown to have a substantial negative effect on I-V curves of PV cells in strings [143, 144]. The effects of shading in PV arrays have also been mentioned as an issue regarding elevating cell operating temperatures. It has been shown that in "solar farms" where arrays are wired together in a series string, shading on one or more of the panels can lead to those panels being forced into forward bias. This has the effect of producing hotspots and cell damage through temperature [144-146]. Additionally, work has shown that the reverse biasing condition that occurs due to the power dissipation through the cells can cause hotspots and hence thermal fatigue throughout a cell leading to premature failure [145, 146]. Bi-pass diodes are the industry standard solution for these un-matched situations and allow the current to flow through a secondary path as opposed to through the cell, preventing fatigue.

2.2.6 System Level: Sun Tracker Accuracy

The effectiveness of a sun tracker can greatly influence the amount of power that is generated from a CPV module. Due to the sun's trajectory and small acceptance angles of high CR optics, the cost, accuracy of tracking and reliability of solar trackers remain substantial issues for CPV systems. The high initial capital cost of the CPV modules compared to other PV technologies, and the lack of CPV reliability data (See Section 2.2.3) restricts the lifetime profit potential of the system through initial financial outlay and maintenance. Tracker accuracy also limits the maximum feasible CR and hence effective plant power generation [147]. Non-uniform tracking errors between modules connected to the same inverter can further introduce losses due to current mismatch unless multiple inverters are used [142]. One suggested solution for this is to use "micro-inverters" mounted one per tracker, as opposed to string inverters. The antonymous solution can also give a

direct cost saving for a “solar farm” through using one large central inverter, depending on the system design. Mechanical deformation can also occur on a tracker due to the module’s own weight, giving miss-alignment issues and subsequent create solar generation losses [148], with the experimental setup used given in Figure 2-18.

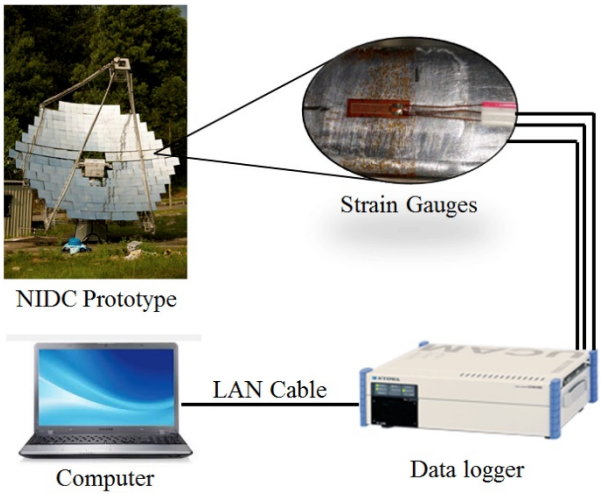

Figure 2-18. The Setup Used to Experimentally Determine the "Self-weight" Deflection Characteristic of a Non-Imaging Dish concentrator (NIDC).

In general, through positional-based optimisation of received irradiance, trackers levelize the power generation of a CPV module throughout the day. This improves plant power profitability by increasing power generation in the morning and evening hours where the electricity can be sold at a premium rate to the market as it better matches the typical daily consumer demand cycle. They are a crucial and necessary component of CPV farms and as such, improvements here remain a viable area of system improvement.

2.2.7 System Level: Weather and solar resource prediction

The power output generated from a CPV plant is directly related to the amount of irradiance. In order to correctly forecast the energy generation potential, it is important to be able to predict the yearly cycles of irradiance and weather [104, 149] for a given location on the globe. There are certain parameters that have substantial contributions to this area. Firstly, the Aerosol Optical Depth (AOD) determines the amount of particle refraction and absorption by contaminants within the atmosphere and its effect on the incident spectrum. Secondly, is the relative humidity of the atmosphere throughout the day, as the water droplets

themselves have two effects: light absorption and additional light scattering. Finally are the inherent spectral changes that occur throughout the seasons of the year and through other atmospheric phenomenon. These spectral changes also depend on geographic location as well as the sun's position in the sky. As multi-junction cells have sub-cells connected in a series configuration, the current they produce respectively needs to be matched to prevent a limiting condition. As previously mentioned, BPDs are an effective solution in deployment (see Section 2.2.5).

As previously suggested (See Section 2.2.1), multi-junction cells are typically designed for "optimal" conditions with the bandgaps of the constituent sub cells matched to that of a "perfect" solar spectrum: AM1.5G (see Section 2.1.3). The optimised combination of bandgap energies for the constituent sub-cell junctions are determined by the wavelength using Planck's constant (see Equation 2-9). These bandgap energies are then achieved within the cells by varying the percentage material composition of the ternary compounds within the multijunciton architecture (e.g. Ga(In)P, Ga(In)As where Indium here has been used to finely adjust the sub cell bandgap energies). These ideal bandgaps are anylysed and simulated through a numerical calculation of the cell external quantum efficiencies (EQEs). Figure x.x below gives a representative EQE graph from a lattice matched triple Junction CPV cell at two different temperatures [98]. Changes in spectral irradiance conditions will therefore introduce losses resulting from a III:V multi-junction cell design that has not had its bandgaps engineered in such a way so geographically spectrum-shifted issues are addressed. Thereby modifying the cell to have a location-specific maximum efficiency - rather than design around a perfect spectral distribution which is unrealistic.

$$E_b = hf \qquad \textit{– (Equation 2-9)}$$

Where

E_b is the bandgap absorption energy for the semiconductor in eV

h is Planck's constant (6.63 x10^{-34} Js or in this case, 4.14 x10^{-15} eVs)

f is the frequency of the light or electromagnetic radiation in Hz.

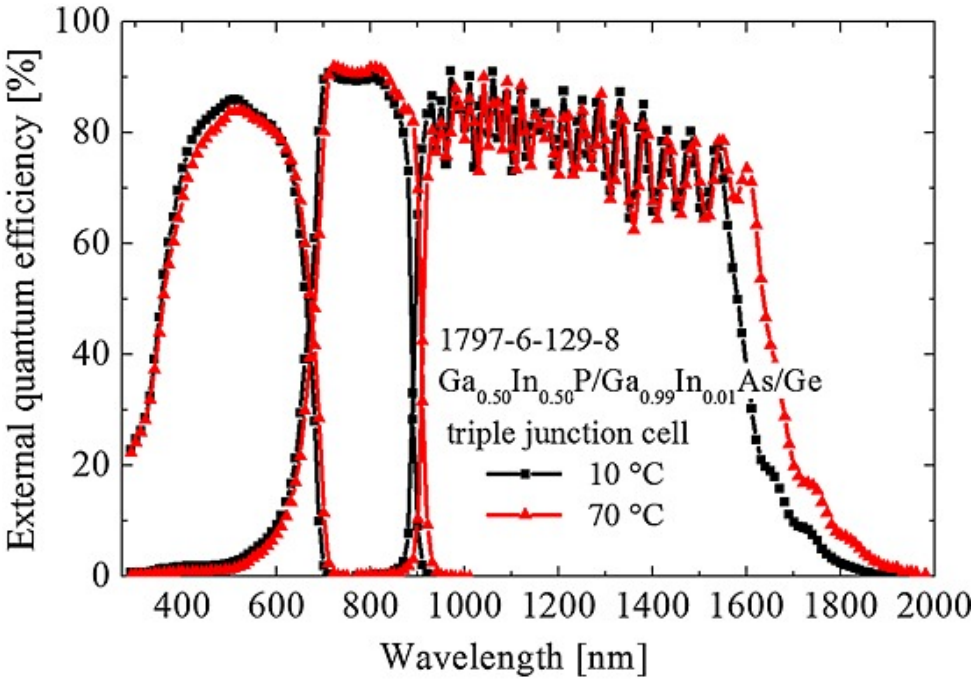

Figure 2-19. An EQE Graph for a Lattice-matched Triple-junction CPV Cell at Two Temperatures; 10°C and 70°C [98]

2.2.8 System Level: Other issues

As CPV systems are designed around large-scale power generation, there are multiple necessary components that add complexity. Inverter choice, system design (e.g. structural and sizing factors) and deployment strategies are essential to correctly produce grid-compatible electricity that conforms to the frequency, voltage and power requirements (G83 and G59 regulations) - throughout the variable solar cycle [150, 151]. Additionally, module configuration and wiring designs have significant effects on the power produced by a plant, and likewise can be a substantial limitation with improper electrical design. Shading is a huge issue for CPV, but at a system level this issue becomes complicated. For example, trackers at certain orientation will shade parts of some modules, and others not, and site location or disparity can create additional issues such as environmental shading from trees, buildings or other structures. Natural events can change the power generation distribution of arrays, including bird flights shading cells and proximity to wind turbines, to cloud-lensing effect creating current surges and temperature spikes. Therefore, due to the reality's unpredictable variations,

tolerances and safety margins need to be included in module design. Unfortunately this can be detrimental to maximum power generation.

Current CPV systems' economic viability is limited to large-scale power generation, so the large set-up costs can be evaluated over a long time-scale (e.g. 25 years). This large cost comes therefore at a higher financial risk to investors, but CPV is still the most effective solution long term for high-capacity level system, or for situations where land costs are high and area is at a premium. NREL reports that CPV's total capital expenditure (CAPEX) requirement could potentially be less than that of flat-plate technologies through design and manufacture processes [1]. In this report, it was estimated that a HCPV system, with Fresnel POE and refractive SOE would be approximately $0.55/Wp (DC) [1, p8], when the optics were manufactured by an external third party. CPV excels in areas with high direct normal irradiance (DNI). With the global demand of coal and oil falling dramatically, the reality that grid parity has been achieved in 30 countries, and Navigant Research predicts that the crucial module efficiency of 50% will be reached by 2020 - making CPV increasingly competitive in the global energy generation market [152]. Additionally in Greenpeace's Energy [R]evolution predictive scenarios, it was stated that renewable technologies will become "economically favourable by 2030" [153].

Controlling the energy generation cycle to match grid demand is another wider-context issue. The PV generation cycle closely follows the sun's motion and as such the generation peaks at midday, and has minimums during sunrise and sunset. Solar trackers can help normalise this effect, as the sun is in comparable angles to the module throughout the day, giving a flatter and broader generation curve (See Section 2.2.6). Unfortunately, the demand cycle for electricity, and hence the grid price is opposite to that of PV generation, with peak electricity demand during the evenings (i.e. when the sun isn't shining). This gives a need for an energy storage, or a time offset technology [152, 154], which needs further development to keep up with the increased adoption of intermittent renewable generation sources [153]. Feasible solutions to this are firstly combining PV power at a country level with that of a Hydro-Electric Power (HEP) plant. Secondly, there are companies that manufacture large battery systems in the magnitude of up to 15 megawatt. These

require a large shelter building (complete with planning permission requirements), degrade electrically over their lifetime, are of considerable cost and include a non-perfect recuperation of the stored energy (<100% storage efficiency). Thirdly are PV applications which concentrate sunlight to then use it as a heat source such as in Solar Thermoelectric Generators (STEG) and Photovoltaic-thermal (PV-T) generation plants. These systems have the advantage that storing the energy as latent heat can elongate the power generation cycle and match demand better, and the expense of not directly generating electricity (A further conversion loss) and vastly larger system complexity.

The main market share (~90%) for PV power generation globally is currently dominated by cheap poly-crystalline technology being exported from China. The low cost is achieved through the abundance of cheap Chinese labour [154] and particularly in rural areas. Low electricity costs [155] differentiate polycrystalline production in China from the markets in the US, alongside plentiful governmental funding most Chinese production chains are based on. China's stock market is very volatile and the energy prices in China are heavily dependent on current and future carbon emission legislations.

Widening the focus still, there are real-world problems for the technology. The supply of the rare-earth materials (e.g. Indium and Germanium) that are needed for multi-junction cells is a huge engineering challenge and hypothetical scale-up scenarios have been forecasted to evaluate any potential future problems. In 2015, NREL published a comprehensive study on the future industry-related challenges related to III-V cells [2]. Firstly, the production for commercial modules needed to be scaled-up in order to compete with silicon in the photovoltaics market. Secondly, the material availability could become a challenge – especially the Germanium needed for the bottom sub-cell. The report states that this "is not a limiting factor in expanding production".

2.2.9 CPV Trends : Section Conclusion

Clearly through this review of CPV literature, it has been shown that there exist many major topics of beneficial, interesting and novel research directions for the advancement of CPV, and PV in general. After reviewing the major challenges

that were feasible to address within the scope of this project, it was decided that PV-TE hybrid devices could make the most impact in addressing some of the temperature effects relating to CPV systems, as given in Section 2.2.2 and 2.2.3. Additional foci of appropriate optical module design and current mismatching within receiver strings (Sections 2.2.4, and 2.2.5 respectively) are included to guide prototype design and throughout the resulting manufacture of experimental devices needed to substantiate and achieve the above objectives. In order to further determine avenues of novel research within these temperature challenges to CPV, and to discovered what prior art exists already – a further more detailed review of the field of PV-TE hybrid devices is discussed and given below.

2.3 PV-TE Hybrid Devices: *State Of The Art (SOTA) Literature Review*

Following the larger context of the work within CPV, as set out above – this next section will look at summarising the key literature with regards to PV-TE hybrid devices. This section is split up into firstly the theoretical models and simulations that currently exist, and followed by a summary of any work that included an experimental section. Finally an "at-a-glance" overview is given at the end of the chapter, in the form of a referenced table organised by the PV technology used for context and as a guide for the reader.

2.3.1 Theoretical models and simulations

As PV-TE hybrid systems are a new topic for scientific study, the most effective way of evaluating the idea credibility with respect to time and cost is through the use of computer simulation. This avoids expensive experimental testing apparatus and the substantial time required for experimental devices– in addition to providing idea performance validation.

A spectrum splitting method was suggested with an optimised cut-off light wavelength [156]. This was done to equally distribute the solar energy most appropriately between the PV cell and the TEG. All three cases studied of a m-Si, an a-Si and a polymer Organic Photovoltaic (OPV) cell showed a power generation increase from a hybrid system, with the low efficiency polymer thin-films exhibiting the largest increase, but with sub-optimal conversion of the incident solar

spectrum, and hence overall conversion efficiency. It is unclear in this work if the negative temperature co-efficients of the Silicon-based cell technologies were included within the electrical model, or compared against the OPV's positive temperature co-efficient.

A high temperature alternative (TE maximum temperature = 800K, PV maximum temperature = 500K) to the hybrid system, again using a spectrum-splitting architecture, was evaluated [157]. A GaAs cell was combined with a cobalt antimony skutteride ($CoSb_3$) based thermoelectric generator. The relative thermoelectric contribution fraction to the overall device (defined in the paper as $\frac{P_{TE}}{P_{Pv-TE}}$) increased with the concentration ratio up to an optimum condition. When the incident irradiance wavelength was varied, it was found that the TE power decreased whereas the PV power increased with increasing wavelength. Hence, an optimum cut-off wavelength condition was described for integrated devices. No series limited interconnection was evaluated, as the two devices were assumed to have two independently connected loads.

A third spectrum splitting design was theoretically simulated consisting of a multi-layer thin film SiO_2 and Si_3Ni_4 filter and evaluated with bismuth telluride modules and m-Si and a-Si cells. It was shown that with an optimised number of deposition layers for the filter, hybrid device performance could be improved. However, the thermoelectric module and PV cell efficiencies were assumed as

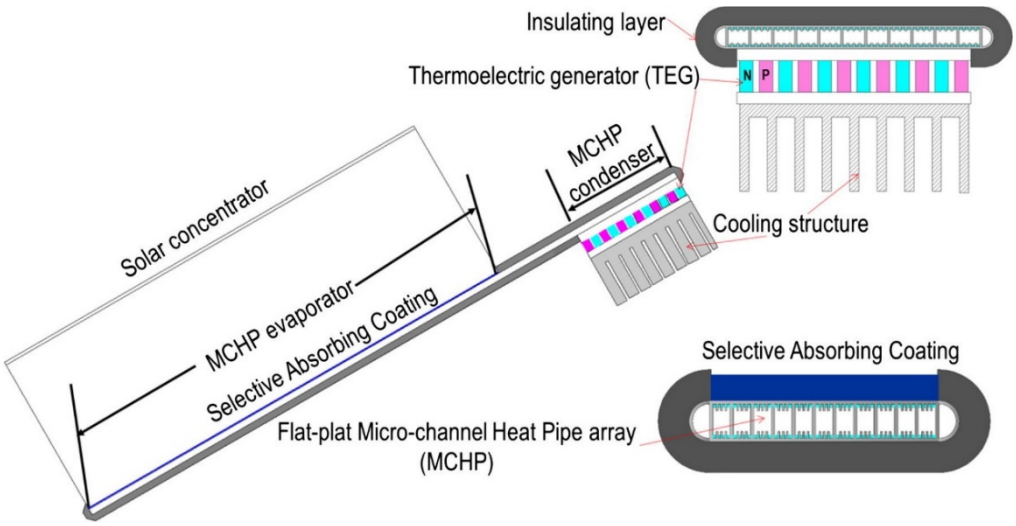

Figure 2-20. The Proposed Design of an STEG-based Solar Collector, combined with Heat-pipes for Enhanced Lateral Heat Flow [160]

constant values and only one irradiance/simulation condition was done (STC), and AM1.5G. The performance contribution of the thermoelectric verses the lone PV was not discussed and out of the scope for this paper [158].

An interesting thermal study was done with an integrated PV-TE cogeneration system with the use of heat pipes. Heat pipes are a well-established alternative for heat transfer and uses a very small area and working fluid flow rate, therefore can better utilise on the latent heat of evaporation and through different condenser - evaporator area ratios to obtain large heat flow [159]. Micro-channel heat-pipe designs are the currently cutting-edge and as such the new integrated system by greatly improving the contact surface area to the working fluid, giving a retro-fitted payback time of only 5 years through minimising the number of TEGs needed. Additionally, large ΔTs across the thermoelectric were decoupled the PV cell, as would be the case with a direct-bonded approach. This work built on previous work with heat-pipes for use with concentrated STEG technologies [160], and an overview of the design is given in Figure 2-20. The studies were corroborated by [161] on a model built for Silicon cells, showing system-level efficiency improvements through both utilising a hybrid system architecture, and exploring designs with heat pipes. Heat pipes have also been shown in previous literature to improve the temperature distribution homogeneity of a PV cell with temperature extremes not surpassing 2.5^{o}C throughout a cell [162].

A preliminary study was done on a power converter of a PV-TEC building-integrated system. The conclusions state that cooling a PV panel could lead to lifetime and efficiency increases. It is unclear in the work the relative consumption of power for the TEC, the experimental setup used and no description was given of any experimental validation. Likewise the simulated panel temperatures were different to that used further in the model. The chosen PV technology unclear and the geometries used were not discussed [163].

A model based on bismuth telluride and 14.03% mono-crystalline PV module efficiency was investigated [164]. The model evaluated the temperature components of the irradiance, with a co-efficient multiplier (“c”) to describe the module’s installation method. Hence its effect on the received solar irradiance was

quantified. The contribution of the thermoelectric was shown to increase the annual electricity yield of the lone PV module by 11-14.7% at 25^{o}C. Heat losses were not taken into account throughout the model, and this result was only as a perfect case scenario for heat transfer and flow through the device.

A low concentrated polycrystalline hybrid system with bismuth telluride thermoelectric modules was modelled and the load resistance to the system was varied, resulting in optimal load conditions being found [165]. This work emphasised the importance of both the thermal conductance between the PV and the TEG, and the concentration ratio. These are crucial design factors when designing hybrid systems. It was shown that increasing the optical concentration increased the power produced by the hybrid system, and the load resistance showing an optimum peak depending on the concentration ratio. It was stated that: "the power output and efficiency [was] always larger than that of the CPV or the TEG" (p163) and the "performance of the hybrid device than that of the CPV device [was] improved significantly".

Silicon thin-film (amorphous), crystalline Silicon, Copper Indium Gallium Selenide (CIGS), and polymer PV cell materials were evaluated as part of a hybrid system [166]. The designs incorporated a fan-cooled heat exchanger, and considered differing levels of optical concentration. The results showed that there was a break-even point for the thermal contact resistance of the system (at a value of 600mm^{2}K/W) which would make a hybrid device feasible. Additionally, this work showed that for all four technologies considered, the power generation efficiency of the hybrid was always higher than the lone PV cell. This increased to an optimum concentration ratio, after which the efficiency decreased. The power consumption of the fan itself was not included within the power production calculations, which could lead to over-positive estimation.

Another integrated device with 300 GaAs/Ge tandem cells connected in series, and 300 bismuth telluride couples in a laminated architecture was investigated [167]. It was found that the PV-TE system had a comparable thermal efficiency to an equivalent PV-T system; in addition to providing a further 8% electrical efficiency relative to the lone PV technology. It was shown in this work

that as the length of the thermoelectric legs increased, as did the electrical efficiency. This increase being larger than the decrease in efficiency seen caused by the increased temperature of the cell (with a 20°C water heat exchanger, leg lengths between 0.6-2.2mm and with a maximum ΔT of 70°C (T_{max} of 90°C). This was also consistent with early work in thermoelectric literature with a focus on module design [51]. The simulated design is shown in Figure 2-21.

In another study, four different PV technologies (crystalline silicon, amorphous silicon, copper indium gallium di-selenide, and cadmium telluride) were analysed, again in a hybrid system with bismuth telluride [168]. As part of the literature review, previous work in this area was evaluated. Criticisms were made on some of the accuracy of the results that have been previously stated, stating that unfeasible results infringing the system Carnot efficiencies were being reported. This included the work of [169], the work of [170] additionally

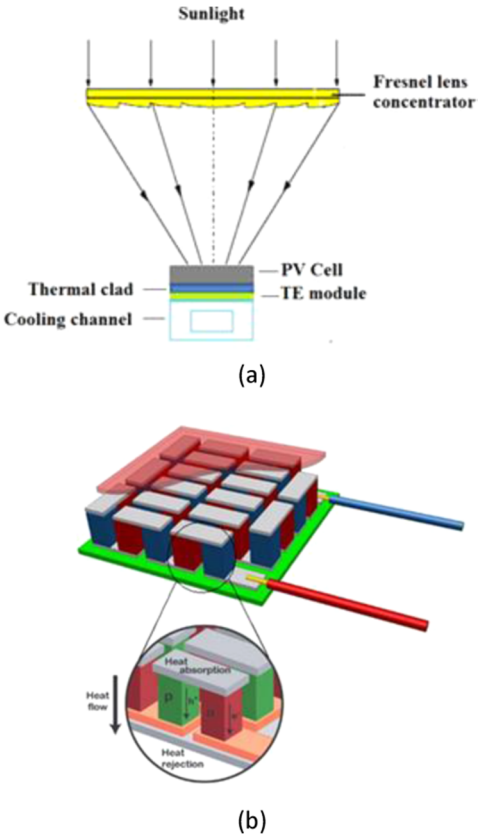

Figure 2-21. The Hybrid Architecture, as Simulated in [167]. The system Comprised of a CPV-based System with a Cooling channel (a), bonded to a TEM (b)

investigated by [171], and work by Micropelt [172], additionally investigated by [173]. This results for this work found that amorphous silicon was the only technology of the four that showed an overall performance increase with a TEG - giving a relative performance increase in total output power of 30%.

An interesting study relating to the geographic location effects on a hybrid PV-TE system were evaluated at multiple European sites [174]. It was found that the high irradiance and low ambient temperature in Southern European countries would be beneficial to the deployment and design of an integrated device, and that the performance of the hybrid device was always greater than that of the PV alone. This work suggested that hybrid devices should be designed with the end location in mind and as such operation location is another factor of design optimisation that can be considered. A further study was undertaken for a hybrid panel system in different locations in Europe. It was stated that a larger temperature difference was available and hence better hybrid performance was exhibited during the spring in Northern Europe, and due to the higher irradiances achieved in summer for maximum power in Southern Europe [175]. This corroborates the results as shown by Van Sark et al [164].

The effects of load matching were studied on a hybrid device [176]. It was again shown that the integrated system had the capability of producing more power than the PV alone. The work also suggested there was an optimal operating current for the system and hence an optimal load resistance for a hybrid system that was different to a lone PV system. The resistance contributions to this value from the individual sub-components, the thermoelectric and the cell, were not listed making it difficult to extrapolate this conclusion to other designs.

Perovskite cells have gained increasing attention within the photovoltaic community due to the rapid increase in their generation efficiency. As part of this trend, a theoretical study on a hybrid Perovskite-TE device was investigated [177] and it was found that the addition of a thermoelectric added 0.8% to the overall generation efficiency. The use of a thermal concentrator was also an effective way to reduce the system cost, due to an increased T_h and hence a smaller, cheaper TEG being required.

MATLAB was used in a thermodynamic model [178] that simulated a concentrated hybrid system using a crystalline-silicon Siemens SP75 module. It was once more shown that the design of an integrated systems relied on an optimal concentration ratio, with the integrated PV-TE device giving marginally greater power output than the PV or the TE alone (111W compared with 97.97W and 12.99W respectively). However, only low concentration ratios were evaluated (< 5x) limiting these conclusions solely to this experimental region.

A model by [179] described the benefits of changing the internal geometry of the thermoelectric itself within a hybrid system. It was shown through using MATLAB and COMSOL that the maximum power output of the TEG corresponded to an optimum thermoelement length. A trend was found that the greater area a module had, the longer the optimal thermoelement length for TE power generation was optimised. The trade-off being that the longer the legs, the higher the thermal resistance, the higher the temperature and hence a performance drop was noted in the PV – as was shown previously [180]. Therefore there existed an optimum balance between hybrid system performance, and the design of the included thermoelectric.

The performance of three solar-TE hybrid devices were compared [181], one of which was a PV-TE. It was shown that the PV-TE system had no negative effects of adding a thermoelectric. The addition of a selective solar absorber (SSA) (which converted low frequency light into heat) increased the hybrid device's power generation efficiency over the lone PV. However, it was noted that this slight power increase was only exhibited when using wide-bandgap cells, due to the temperatures that were modelled here.

A tandem DSSC-TE hybrid device was investigated with two wire series (named "HTC2" in the paper) and four wire parallel (named "HTC1") connections for the sub-cells [182]. The series connected prototypes were then optimised through current-matching of the two component devices. It was shown that a 10% additional conversion efficiency was achieved by the device that included the thermoelectric. This maximum was shown at the maximum tested irradiance of AM1.5G, 1000Wm^{-2}.

A further optimisation study for DSSC-TE hybrid devices was conducted and a parametric analysis done to find the optimum temperature co-efficient of the DSSC for maximum hybrid efficiency [183]. Maximum hybrid conversion efficiency was reported to be over 4.50% with simulated cell efficiency temperature co-efficients of magnitude smaller than -0.00501 %/^{o}C for their design and model.

A MATLAB study was done to evaluate MPPTs and their effect of co-generation hybrids. The results that showed that it was beneficial to design the MPPT algorithm whilst considering both simultaneous thermally dependant contributions of the PV and the TEM [184]. However in this model, the PV panel was modelled with temperatures ranging from 328K-358K (55^{o}C-85^{o}C). The maximum power point condition for the TEM was simulated at a ΔT of 50K. Thereby, the simulated panel temperature was uncharacteristic of those in reality, as thermoelectric cold side temperature down to 5^{o}C with solar operation at 55^{o}C would be difficult to achieve without a secondary cooling system.

Again, four more types of PV technology (compound silicon, CIGS, GaAs and a triple junction GaInP/InGaAs/Ge) were theoretically modelled by [185] as part of a hybrid system. This time with the addition of a phase-change thermal storage component. The PCM in this design (shown in Figure 2-22) was enclosed within Copper and placed in between the Bismuth Telluride thermoelectric module and the PV. It was shown that for the triple junction architecture under both 1-sun and higher concentrations, the hybrid device showed a larger system efficiency. GaAs cells showed the largest benefit from a hybrid system due to the system inherently having higher temperature operation from the thermoelectric's large thermal resistance. It was suggested that the additional of the PCM layer was an additional benefit and thermal concentration was also noted to have a positive effect on overall system performance.

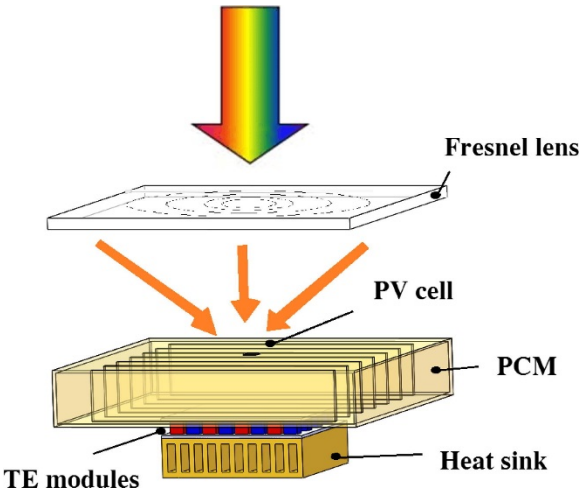

Figure 2-22. A Schematic of a proposed CPV-PCM-TEM Hybrid device [185]

What is clear from the theoretical studies done for thermoelectric hybrid devices, is that the majority of works focus on using the thermoelectric module in Seebeck mode for additional power generation. Model validation is sparse, and where included, the used experimental methodology is not well documented. However, multiple areas of hybrid optimisation and thermal coupling were highlighted. The following three avenues as suggested by the literature review are included and further explored through the work in this thesis:

1. *Hybrid devices have an optimum operating concentration ratio* [165, 178].
2. *TEM geometry (leg length and surface area) in hybrids is a crucial contributing factor to TEM performance* [166, 167].
3. *Thermal conductance of the included interfaces between the PV are a key design parameter for optimal heat flow* [165, 166].

2.3.3 Experimental Assemblies and Results

Experimental work offers an alternative method of research and discovery to that of simulation. Although a less number of factors can be easily controlled and investigated, experimental work offers a platform with which to combine with that of simulation work to synergistically approach progress. This next section summarises any literature found throughout this literature review that included any experimentally substantiated conclusions or design optimisations.

A PV-TE system design utilizing concentration was suggested and evaluated [186]. Both polycrystalline (η = 16%) and amorphous (η = 10%) silicon PV modules were considered alongside the experimentally characterised bismuth telluride TEGs. It was stated that with a 50x optical concentration, a temperature above 200^{o}C could be reached with there being an overall optimal concentration for the hybrid system. It was found that the total energy generated by this hybrid system was higher than that for a stationary PV module alone, when scaled down from a representative tracking system. It was also stated that the inclusion of a TEG minimised the detrimental temperature effects on the generation efficiency therefore increasing the temperature stability of the power generation. This study experimentally measured the performance of the TEM with different thermal interfaces, but the PV module was only simulated for the evaluation of hybrid devices. Additionally the experimental setup used a hot air gun for temperature below 100^{o}C. In this region, this technique is unlikely to exhibit stable steady-state conditions for accurate or repeatable thermoelectric evaluation. When evaluating the hybrid system performance throughout the day, this hybrid model concluded that it would perform worse than that of a lone PV.

Electrical circuit studies were done using a crystalline silicon and bismuth telluride hybrid device [171]. Here, the attempt was to match the current output of the cell to the thermoelectric and minimise current limiting losses through the deployment circuit configuration alone. It was shown that the thermal interdependencies of the internal resistances (and their temperature sensitivities) the thermoelectric and the photovoltaics made such a combined circuit ineffective. However, with a 15^{o}C temperature gradient, it was reported that a hybrid system increased the generation efficiency when compared to a sole PV device by 30% (12.5% to 16.3% absolute η). No studies on the thermal interfaces were done. The two devices within the hybrid were connected in series creating a substantial current limiting scenario, as that produced by the PV would be drastically larger in all cases than that of the thermoelectric module, giving rise to a dramatic current liming scenario. It's unclear whether the work in this paper could be easily

circumvented simply by independent electrical connection circuits, as shown by [165].

A preliminary description of interconnecting PV and TE technologies was done by [187]. A simply joined device consisting of a 50Wp polycrystalline PV panel and TEGs on the rear was made and tested. It was shown that this system had a slight increase in generated power over the bare PV, but few datasets were given, the design not listed, and the experimental methodology not present – so hence the scientific confidence in this specific case is limited.

A thin-film thermoelectric was used in a spectrum splitting design to experimentally evaluate the performance increase of decoupling the thermoelectric section of the hybrid system from the PV [188]. A thin film of $Bi_2Te_{2.7}Se_{0.3}$ of 1µm thickness was used in conjunction with an amorphous silicon PV module. Small power densities of the order of $6x10^{-3}$ % of the PV module were achieved by the thermoelectric, with a ΔT of 20°C with an overall 1.3% power output increase for the hybrid device over the PV alone being reported from Seebeck conversion. However this increase could also be within experimental measurement error (~1%), especially as none were stated for the used apparatus.

Another experimental realisation of a spectrum-splitting hybrid design was demonstrated as in Figure 2-23 with an 800nm cut-off wavelength [189]. A novel "honeycomb" structure was applied to the top surface to prevent convection losses from the panel. Interestingly, the spectrum splitting design showed better performance than a full spectrum PV panel during the early and late extremities of a simulated daily irradiance cycle. This is due to the spectral shifts in the solar spectrum that occur. A performance enhancement up to 20% was shown, with higher full-spectrum temperature being shown throughout the day without spectrum splitting. The power consumption of the cooling system was not included in the energy balance calculations.

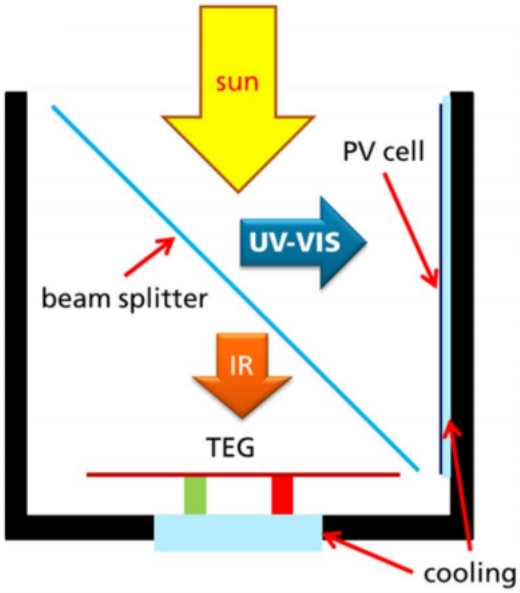

Figure 2-23. The CPV-TE Hybrid Experimental Setup, utilizing a Hot Mirror Spectrum-Splitting Design [189]

A poly-crystalline silicon based hybrid system was experimentally investigated by [190] with bismuth telluride modules and a fan-cooled heat exchanger. It was again stated that the hybrid system's power production was greater when the PV module was connected to a separate circuit to the TEG. The work argued a hybrid device was unbeneficial due to the TE power being negligible in comparison to the PV power. The device used in this paper was tested at 1x concentration, using TEGs of area 30mmx30mm of a 60mmx60mm cell and no thermal concentration or conduction mass, and operated a cell temperature of <42^{o}C, sub-optimal design conditions for the TEM.

The use of a thermal concentrator was further explored with a hybrid design that used a TEG of much smaller area than that of the PV cell [191]. A monocrystalline Silicon PV cell was then combined with four TEGs in series which were water cooled, and a 25% performance increase was shown compared to the PV contribution within the hybrid structure. Through use of a copper block thermal concentrator, a temperature difference of 52^{o}C was created through the TEM under illumination of 650Wm^{-2} and a representative cold side temperature of 20^{o}C. Although the relative contribution as increased, this improvement was not evaluated alongside a PV-only system that wouldn't have the additional thermal

resistances to the water cooler. Hence the overall cell temperature was lower and the power produced larger than the hybrid. Even at the time=0 condition as evaluated as the “PV lone” conversion efficiency, would be different without the TEM additional thermal resistance and hence this condition is not enough to assume as a lone PV case.

A phase-change material (PCM) hybrid system was developed and experimentally investigated [192] using GaAs cells and a 40mmx40mm TEM. Two concentration ratios were investigated (529x and 1156x). Water-cooled, under both concentrations, the electrical output from the lone-PV system was shown to outperform that of the integrated hybrid not including the exergy gain of the PCM. However for the air-cooled scenario the hybrid was showed potential improvement to the system. This highlights a possible direction for future experimental hybrid research for passive cooling approaches, with well-documented temperature metrology and device design being documented. However the on-sun irradiance data is quoted as a constant value of 750Wm^{-2} which is unusual for on-sun experimental testing due to atmospheric changes being likely (See Section 2.2.7) throughout sustained testing.

Another study was done on the design of the applied heat exchanger to a Bismuth-telluride thermoelectric module combined with a monocrystalline PV panel [193]. “Fin” and “Pin” type heat exchangers were evaluated, with pin type being shown to cool a lone PV module more effectively. A thermal resistance temperature increase contribution from the thermoelectric module was observed, as can be expected by the increased thermal resistance to the heat exchanger. This highlights an inherent challenge of integrating the TEMs into hybrid devices, although no discussion was made as to the overall impact on PV module conversion efficiency, or the TEM conversion efficiency.

Two types of PV technology were evaluated in a hybrid device: poly-crystalline silicon and DSSCs experimentally with bismuth telluride modules and a water heat exchanger [194]. This work confirmed the results of earlier simulations ([179], [167]) and suggested that further hybrid designs should attempt to use smaller length thermoelement modules to capitalise on the small temperature

differences inherent to the hybrid deployment scenarios. This minimised the temperature increase that occurred on the PV cell, and as the cell generation still dominated overall efficiency, this had a substantial effect. It was also shown that the hybrid designs' generation exceeded that of the sole PV cell in all four investigated cases (2 PV technologies, 2 TE leg lengths). The improvement to the DSSC hybrid system was higher than that of the poly-crystalline Silicon with the DSSCs showing a 30.2% relative improvement, and the polycrystalline 22.5% improvement. However, the power resistors that were used as heaters in the experimental setup, and the LED lamp test equipment wasn't representative of true operating conditions and adds a lack of confidence to the conclusions obtained. The in-homogeneity, stability, controllability or measurability of the heating supply wasn't mentioned or measured. The hugely spectrally limited output from an LED light source being dissimilar to the spectrum was not quantified either.

The properties of changing the composition of the bismuth telluride material within the TEM was investigate using a DSSC cell [195]. Two compositions were investigated (p-type $Bi_{0.5}$ $Sb_{1.5}$ Te_3 with n-type Bi_2 $Se_{0.15}$ $Te_{2.85}$, and p-type $Bi_{0.4}$ $Sb_{1.6}$ Te_3 and n-type $Bi_{2.85}$ $Se_{0.15}$ Te_3). This second TEM composition was shown to greatly improve the performance of the hybrid device over that of the lone DSSC. This was due to creating a specific charge carrier interaction within the cell itself. Only one device was ever made in this work that had this improved power production, so it is unclear if this effect is repeatable, stable or productive as a design criteria or optimisation technique.

Investigation of another series-connected DSSC-TE hybrid device with an included Selective Solar Absorber (SSA) coating on a micropelt TE, with the SSA increasing the overall hybrid device efficiency by limiting reflection and increasing the Voc of the TE [173]. Hybrid device efficiency of 13.8% was reported. However this was using cell and TE areas of 6.25mm^2 –potentially not allowing for the parasitic sheet resistances to be established which are inherent to larger DSSC devices, perhaps more feasible for power generation. Additionally, doubt has already been cast on this work by other literature regarding the reported efficiencies [168].

Studies have been done on the integration of Perovskite in PV-TE systems, with preliminary results showing efficiency improvements of 0.8% absolute over a base of 17.8%. Thermal concentration methods were evaluated to be unbeneficial in such a system [196]. Organic PV cells have been successfully integrated monolithically with a PEDOT:PSS thermoelectric film module, to produce a hybridized fully-organic PV-TE cell [197]. Performance improvements were shown, but due to technology infancy are negligible to the system.

A novel designed system using a thermoelectric module under a Fresnel concentrator was evaluated with monocrystalline Silicon cells being situated in the same plane as the concentrating lens [198]. The results show a system improvement through adding a secondary thermoelectric part. The profitability of such a complicated design is debatable as it may simply be more beneficial to use more silicon at a lower cost per Watt with the same lens. However, this study focused on having a single pre-made PV module that had a PV and thermoelectric components rather than a fully integrated hybrid structure and as such device optimisation was therefore limited in the used design.

Two recent publications have focused on utilising a TEM to be retro-fitted to off-the-shelf commercial silicon-based panels [199,200]. For the first, two heat exchanger designs and the efficacy to a PV-TE system was evaluated. The TEM was shown to produce an increased output power, of 3.9% using a “pin” design as compared to a “fin” design [199]. An arbitrary lamp was used as the light source for testing, with no analysis of spectrum or calibration. A slight decrease was shown in the experimentally obtained data comparing the lone PV with that of the PV-TE device. The experimental comparison of the devices is shown in Figure 2-24 below. Two case designs were assessed for their compatibility to be retro-fitted with commercially available TEMs, made from Bismuth Telluride [200]. One case design was shown to be an improvement of the other with relation to the TEM overall electrical contribution to the hybrid device – further highlighting the importance of assessing the included thermal interfaces within hybrids. However, no electrical analysis was included within the paper regarding the cell performance or

comparison with a lone PV system. Both papers focused on using the TEM in Seebeck operation, as opposed to Peltier.

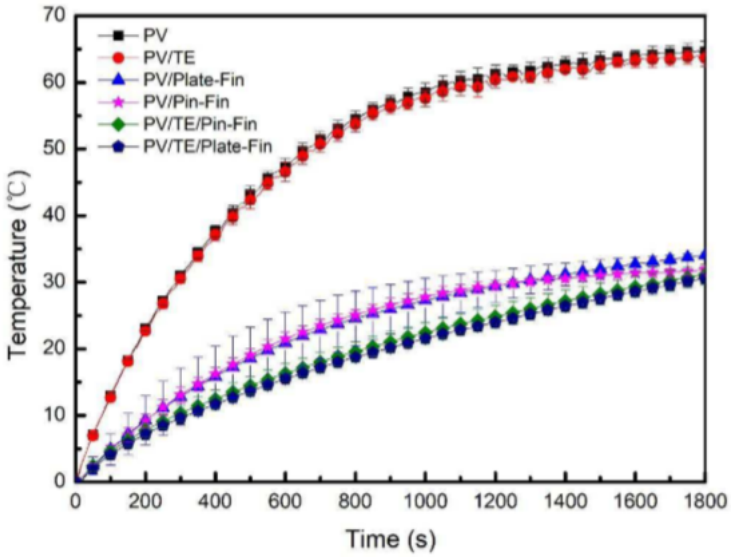

Figure 2-24. The Experimentally Obtained PV-TE hybrid Data Using a Monocrystalline Silicon Panel [199]

A hybrid PV-TE high system and high optical concentration (~200x) was described [201]. This was the only experimental paper found throughout the literature review to use a triple junction cell. The individual PV and TE were connected in separate circuits to minimise current limiting losses. A reflective-type outdoor solar heliostat was used to achieve the require concentration ratios for testing, as shown in Figure 2-25. With increasing optical concentration, in the hybrid system it was shown that the TEG's relative contribution increased. The hybrid gave more power output than the PV alone at concentrations larger than 100x. It was also stated that the inherent Thomson effect in the TEG improved things further by inherently lowering the temperature of the hybrid system during operation. The individual contributions of the PV and the TE were not discussed in great detail, with the performances recorded at each concentration ratio not being given. The temperature co-efficient of the PV cell, and the figure-of-merit contributions to the overall conversion efficiency were not investigated or discussed. Likewise the temperature reached by the cell at any concentration was not evaluated, and the additional thermal resistance (hence heating the cell as compared to a lone PV device) was not highlighted. No one-sun evaluation was done, the performance

comparison with and without optics was not included and the temperature control efficacy of the Peltier mode for the TEM was not investigated.

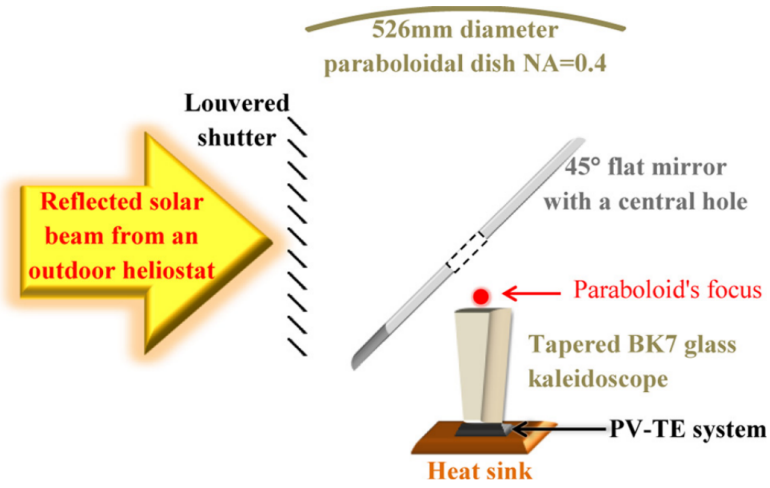

Figure 2-25. The Experimental Apparatus Used to Achieve high concentration Ratios (Simulating Operation Under POE) [201]

Throughout the experimental literature review the following avenues were highlighted to carry through to further hybrid designs:

1. Experimental testing at optimal concentration ratios remains crucial due to the temperature dependency and internal parameters reached. [185, 186, 199].
2. Optimising the internal leg lengths of the TEM [167, 179, 194]. The thermoelectric fill factor and area geometry could also be explored.
3. Reducing the number or thermal resistance of thermal interfaces between the TEM and the cell [173, 186, 193].

2.4 Chapter Conclusion, Summary and Thesis Directions

The work in this thesis will evaluate the performance of integrating multi-junction CPV cells within a CPV-TE hybrid device to address some of the crucial challenges to CPV in general, as defined above. Multiple optimisation areas and consistent suggested improvements have been given by both the theoretical and experimental prior art. These include investigating the relationship between concentration ratio and hybrid device performance, the optimisation of the internal TEM leg geometries, and reducing where possible thermal resistances in the

interface between the cell and the TEM. These avenues will investigated and evaluated in this research where possible.

Key research opportunities exist for PV-TE hybrid devices in general. Predominantly there is limited work on experimentally evaluating the performance increase of PV or CPV cells through Peltier cooling and hence the energy cost or engineering trade-offs thereof of the TEM module. TEM design optimisation with a combined consideration for the larger POE-SOE-CPV-TE hybrid system as a whole is sparse, with leg lengths being highlighted as the predominant optimisation method.

2.4 PV-TE Hybrid References Overview: *Hybrid Review at a glance*

Table 2-1. A Concise Summary of the PV-TE SOTA Literature Review

PV Technology	**Theoretical Work**	**Experimental Work**
Silicon Based Cells		
m-Si	[156], [158], [161], [164], [166], [168], [178]	[186], [171], [187], [191], [193], [198], [199], [200]
p-Si	[165]	[186], [190], [194]
a-Si	[156], [158], [166], [168]	[188]
c-Si	[185]	NONE
III:V Based Cells	-	-
GaAs (1J)	[157], [185]	[192]
GaAs/Ge (2J)	[167]	
LM or IMM (3J)	**[185]**	**[201]**
Organic Based Cells	-	-
Perovskite	[177]	[196]
DSSCs	[182], [183]	[194], [195], [173]
Polymer-based OPV	[156], [166]	NONE
Other	-	-
CIGS	[166], [168], [185]	NONE
CdTe	[168]	NONE

2.5. References

1. NREL and Fraunhofer, Current Status of Conventrator Photovoltaic (CPV) Technology. (Report). 2016. [Accessed 01/05/18]. Available at: https://www.nrel.gov/docs/fy16osti/65130.pdf
2. Philipps, S.P., A.W. Bett, K. Horowitz, et al., *Current status of concentrator photovoltaic (CPV) technology*. 2015, NREL (National Renewable Energy Laboratory (NREL), Golden, CO (United States)). [Accessed: 1/05/18]. Available at: https://www.ise.fraunhofer.de/content/dam/ise/de/documents/publications/studies/cpv-report-ise-nrel.pdf
3. Pope, M. and C.E. Swenberg, *Electronic processes in organic crystals and polymers, 2nd Edition*. 1999: Oxford University Press. ISBN: 9780195129632. Pp 59-61.
4. Ramsden, E., *A-Level chemistry*, *4th Edition*. 2000: Nelson Thornes Publishing. ISBN: 9780748752997.
5. Johnson, K., S. Hewett, S. Holt, et al., *Advanced physics for you, Revised 2nd Edition*. 2015: Nelson Thornes. ISBN: 9780748752966.
6. Mertens, K., *Photovoltaics: fundamentals, technology and practice, 1st Edition*. 2013: John Wiley & Sons. ISBN: 9781118634165. Pp 54-59.
7. Wenham, S.R., *Applied photovoltaics, 3rd Edition*. 2012: Routledge. ISBN: 9781849711425. Pp 29-31.
8. Green, M.A., *Solar cells: operating principles, technology, and system applications.* 1982. [Accessed 01/05/18]. OSTI ID: 6051511. Available at: https://www.osti.gov/biblio/6051511.
9. Kurucz, R. *The solar irradiance by computation*. in *Proceedings of the 17th Annual Conference on atmospheric transmission models*. 1995. Rep. PL-TR. [Accessed 01/05/18]. Available at: http://www.dtic.mil/get-tr-doc/pdf?AD=ADA295597 (pp 333-334).
10. Thekaekara, M.P. and A.J. Drummond, *Standard values for the solar constant and its spectral components.* Nature, 1971. **229**(1): p. 6-9. [accessed 01/05/18]. Available at: https://www.nature.com/articles/physci229006a0

11. Drummond, A. and M. Thekaekara, *Extraterrestrial solar spectrum.* (Experimental dataset). 1973. [Accessed 01/05/18]. Available at: http://rredc.nrel.gov/solar/spectra/am0/text/Thekaekara.txt

12. Tobiska, W. and A. Nusinov, *Status of the draft ISO solar irradiance standard.* Physics and Chemistry of the Earth, Part C: Solar, Terrestrial & Planetary Science, 2000. **25**(5-6): p. 387-388. [Accessed 01/05/18]. Available at: http://spacenvironment.net/pdf/C01_0014_04.pdf

13. Thuillier, G., M. Hersé, P. Simon, et al., *Observation of the solar spectral irradiance from 200 nm to 870 nm during the ATLAS 1 and ATLAS 2 missions by the SOLSPEC spectrometer.* Metrologia, 1998. **35**(4): p. 689. [Accessed: 01/05/18]. Available at: http://iopscience.iop.org/article/10.1088/0026-1394/35/4/79/meta

14. Thuillier, G., M. Hersé, P.C. Simon, et al., *Observation of the UV solar spectral irradiance between 200 and 350 nm during the Atlas I mission by the SOLSPEC spectrometer.* Solar Physics, 1997. **171**(2): p. 283-302. [Accessed: 01/05/18]. Available at: https://link.springer.com/article/10.1023%2FA%3A1004930219506

15. Thuillier, G., M. Hersé, P.C. Simon, et al., *The visible solar spectral irradiance from 350 to 850 nm as measured by the SOLSPEC spectrometer during the ATLAS I mission*, in *Solar Electromagnetic Radiation Study for Solar Cycle 22*. 1998, Springer. p. 41-61. [Accessed: 01/05/18]. Available at: https://link.springer.com/article/10.1023%2FA%3A1004953215589

16. Cebula, R., G. Thuillier, M.E. VanHoosier, et al., *Observations of the solar irradiance in the 200–350 nm interval during the ATLAS-1 Mission: A comparison among three sets of measurements-SSBUV, SOLSPEC, and SUSIM.* Geophysical research letters, 1996. **23**(17): p. 2289-2292. [Accessed: 01/05/18]. Available at: ftp://ftp.nist.gov/pub/physics/lunarproject/References/Solar_Spectrum/1998_SolPh_Thuillier_SOLSPEC_Vis.pdf

17. Woods, T.N., D. Prinz, G. Rottman, et al., *Validation of the UARS solar ultraviolet irradiances: Comparison with the ATLAS 1 and 2 measurements.* Journal of Geophysical Research: Atmospheres, 1996. **101**(D6): p. 9541-

9569. [Accessed: 01/05/18]. Available at: https://agupubs.onlinelibrary.wiley.com/doi/pdf/10.1029/96JD00225

18. Thuillier, G., M. Hersé, T. Foujols, et al., *The solar spectral irradiance from 200 to 2400 nm as measured by the SOLSPEC spectrometer from the ATLAS and EURECA missions.* Solar Physics, 2003. **214**(1): p. 1-22. [Accessed: 01/05/18]. Available at: http://www.ioccg.org/groups/Thuillier.pdf
19. International, A., *ASTM E490-00a Standard Solar Constant and Zero Air Mass Solar Spectral Irradiance Tables*. 2014. [Accessed: 01/05/18]. Available at: ftp://halo.ess.uci.edu/public/prather/code/solar_2014W/E490-RED.1583960-1-errata.pdf
20. Gueymard, C.A., *Parameterized transmittance model for direct beam and circumsolar spectral irradiance.* Solar Energy, 2001. **71**(5): p. 325-346. [Accessed:01/05/18]. Available at: http://www.stratosolar.com/uploads/5/6/7/1/5671050/20_gueymard_parameterized_transmittance_model_for_direct_beam_and_circumsolar_spectral_irradiance.pdf
21. Gueymard, C.A., *Direct solar transmittance and irradiance predictions with broadband models. Part I: detailed theoretical performance assessment.* Solar Energy, 2003. **74**(5): p. 355-379. [Accessed: 01/05/18]. Available at: http://www.physics.arizona.edu/~cronin/Solar/References/Irradiance%20Models%20and%20Data/GUE03.pdf
22. Gueymard, C.A., *Direct solar transmittance and irradiance predictions with broadband models. Part II: validation with high-quality measurements.* Solar Energy, 2003. **74**(5): p. 381-395. [Accessed: 01/05/18]. Available at: https://www.sciencedirect.com/science/article/pii/S0038092X03001968
23. Gueymard, C.A., *The sun's total and spectral irradiance for solar energy applications and solar radiation models.* Solar energy, 2004. **76**(4): p. 423-453. [Accessed: 01/05/18]. Available at: https://www.sciencedirect.com/science/article/pii/S0038092X03003967?via%3Dihub
24. Fernández, E.F., F. Almonacid, J.A. Ruiz-Arias, et al., *Analysis of the spectral variations on the performance of high concentrator photovoltaic modules*

operating under different real climate conditions. Solar Energy Materials and Solar Cells, 2014. **127**: p. 179-187. [Accessed: 01/05/18]. Available at: https://www.sciencedirect.com/science/article/pii/S0927024814002347?via%3Dihub

25. British Standards Institute, *ASTM G173-03 Standard Tables for Reference Solar Spectral Irradiances: Direct Normal and Hemispherical on 37° Tilted Surface*. 2012. Purchasable full copy available at: https://shop.bsigroup.com/ProductDetail/?pid=000000000030288644 . [Accessed: 01/05/18]. Online summary version available from NREL at: http://rredc.nrel.gov/solar/spectra/am1.5/astmg173/astmg173.html
26. Shockley, W. and H.J. Queisser, *Detailed Balance Limit of Efficiency of p-n Junction Solar Cells.* Journal of Applied Physics, 1961. **32**(3): p. 510-519. [Accessed:01/05/18]. Available at: https://aip.scitation.org/doi/abs/10.1063/1.1736034
27. Tiedje, T., E. Yablonovitch, G.D. Cody, et al., *Limiting efficiency of silicon solar cells.* IEEE Transactions on electron devices, 1984. **31**(5): p. 711-716. [Accessed: 01/05/18]. Available at: https://pdfs.semanticscholar.org/9e1f/7899ffabdb3a86451811d47014ab3012ae1b.pdf
28. [Online]. “pveducation.org”, *Standard Solar Spectra*. [Accessed: 01/05/18]. Available at: http://www.pveducation.org/pvcdrom/appendices/standard-solar-spectra
29. Alferov, Z.I., 1970. Electroluminescence of heavily-doped heterojunctions pAlxGa1-xAs-nGaAs. *Journal of Luminescence*, *1*, pp.869-884. [Accessed on: 01/05/18]. Available at: https://www.sciencedirect.com/science/article/pii/0022231370900992
30. Alferov, Zh I., V. M. Andreyev, V. I. Korol'Kov, and E. L. Portnoi. "Preparation and Investigation of Epitaxial Layers of AlxGa1-xAs solid Solutions and of Heterojunctions in the AlAs-GaAs system." *Crystal Research and Technology* 4, no. 4 (1969): 495-503. [Accessed: 01/05/18]. Available at: https://onlinelibrary.wiley.com/doi/abs/10.1002/crat.19690040406

31. Yamaguchi, M., T. Takamoto, K. Araki, et al., *Multi-junction III–V solar cells: current status and future potential.* Solar Energy, 2005. **79**(1): p. 78-85. [Accessed: 01/05/18]. Available at: https://www.sciencedirect.com/science/article/pii/S0038092X04002944

32. Jani, O., I. Ferguson, C. Honsberg, et al., *Design and characterization of GaN/InGaN solar cells.* Applied Physics Letters, 2007. **91**(13): p. 132117. [Accessed: 01/05/18]. Available at: https://aip.scitation.org/doi/abs/10.1063/1.2793180

33. Nozik, A.J., *Advanced concepts for photovoltaic cells*. 2003, National Renewable Energy Laboratory (NREL), Golden, CO. [Accessed: 01/05/18]. Available at: https://www.nrel.gov/docs/fy03osti/33621.pdf

34. Cotal, H., C. Fetzer, J. Boisvert, et al., *III–V multijunction solar cells for concentrating photovoltaics.* Energy & Environmental Science, 2009. **2**(2): p. 174-192. [Accessed: 01/05/18]. Available at: https://pdfs.semanticscholar.org/e528/e2d097e6df1dcfbe5c4ef09c28fd123a12ef.pdf and http://pubs.rsc.org/en/content/articlelanding/2009/ee/b809257e#!divAbstract

35. Olson, J.M. and S.R. Kurtz, *Current-matched high-efficiency, multijunction monolithic solar cells*. 1993, Google Patents. [Accessed: 01/05/18]. Available at: https://patents.google.com/patent/US5223043A/en

36. Tamboli, A.C., M.F. van Hest, M.A. Steiner, et al., *III-V/Si wafer bonding using transparent, conductive oxide interlayers.* Applied Physics Letters, 2015. **106**(26): p. 263904. [Accessed: 01/05/18]. Available at: http://aip.scitation.org/doi/abs/10.1063/1.4923444

37. Green, M.A., K. Emery, Y. Hishikawa, et al., *Solar cell efficiency tables (version 47).* Progress in Photovoltaics: Research and Applications, 2016. **24**(1): p. 3-11. [Accessed on: 01/05/18]. Available at: http://onlinelibrary.wiley.com/doi/10.1002/pip.2728/pdf

38. Green, M.A., Y. Hishikawa, W. Warta, et al., *Solar cell efficiency tables (version 50).* Progress in Photovoltaics: Research and Applications, 2017.

25(7): p. 668-676. [Accessed: 01/05/18]. Available at: https://onlinelibrary.wiley.com/doi/abs/10.1002/pip.2909

39. Dimroth, F., T.N.D. Tibbits, M. Niemeyer, et al., *Four-Junction Wafer-Bonded Concentrator Solar Cells.* IEEE Journal of Photovoltaics, 2016. **6**(1): p. 343-349. [Accessed:01/05/18]. Available at: http://ieeexplore.ieee.org/abstract/document/7342876/
40. Fraunhofer, *Photovoltaics Report*. 2018, Fraunhofer ISE. (Prepared by Fraunhofer Institute for Solar Energy Systems, ISE with support of PSE Conferences & Consulting GmbH). [Accessed: 01/05/18]. Available at: https://www.ise.fraunhofer.de/content/dam/ise/de/documents/publications/studies/Photovoltaics-Report.pdf
41. Talavera, D.L., J.P. Ferrer-Rodríguez, P. Pérez-Higueras, et al., *A worldwide assessment of levelised cost of electricity of HCPV systems.* Energy Conversion and Management, 2016. **127**(Supplement C): p. 679-692. [Accessed: 01/05/18]. Available at: https://www.sciencedirect.com/science/article/pii/S0196890416308536
42. [Online] Geyer, W.B.S.a.M., *Power From The Sun*. 2001. [Accessed: 01/05/18]. Available at: http://www.powerfromthesun.net/book.html .
43. Shanks, K., S. Senthilarasu, and T.K. Mallick, *High-concentration optics for photovoltaic applications.* High concentrator photovoltaics: fundamentals, engineering and power plants'(Springer International Publishing, 2015, 2015: p. 85-113. [AccesseD: 01/05/18]. Available at: https://link.springer.com/chapter/10.1007/978-3-319-15039-0_4
44. Shanks, K., S. Senthilarasu, and T.K. Mallick, *Optics for concentrating photovoltaics: Trends, limits and opportunities for materials and design.* Renewable and Sustainable Energy Reviews, 2016. **60**(Supplement C): p. 394-407. [Accessed: 01/05/18]. Available at: https://www.sciencedirect.com/science/article/pii/S1364032116001192
45. Pérez-Higueras, P. and E.F. Fernández, *High concentrator photovoltaics: fundamentals, engineering and power plants*. 2015: Springer. Pp115 – 152. ISBN: 9783319150390.

46. Huang, M.C., A.Y. Tzeng, C.-W. Hsu, et al. *CPV module Qualification and IEC 62108 experiences at Arima EcoEnergy*. in *Photovoltaic Specialists Conference (PVSC), 2009 34th IEEE*. 2009. IEEE. [Accessed: 01/05/18]. Available at: http://ieeexplore.ieee.org/abstract/document/5411339/

47. Muñoz, E., P. Vidal, G. Nofuentes, et al., *CPV standardization: An overview.* Renewable and sustainable Energy reviews, 2010. **14**(1): p. 518-523. [Accessed: 01/05/18]. Available at: https://www.sciencedirect.com/science/article/pii/S1364032109001701

48. Nolas, G.S., J. Sharp, and J. Goldsmid, *Thermoelectrics: basic principles and new materials developments*. Vol. 45. 2013: Springer Science & Business Media. Pp 4-10. ISBN: 9783662045695

49. Rowe, D.M., *CRC handbook of thermoelectrics*. 1995: CRC press. Pp19-26. ISBN: 9780849301469

50. Rowe, D.M., *Thermoelectrics handbook: macro to nano*. 2005: CRC press. Pp 2-10. ISBN: 9780849322648

51. Rowe, D.M. and G. Min, *Design theory of thermoelectric modules for electrical power generation.* IEE Proceedings - Science, Measurement and Technology, 1996. **143**(6): p. 351-356. [Accessed: 01/05/18]. Available at: http://digital-library.theiet.org/content/journals/10.1049/ip-smt_19960714

52. Rowe, D.M., *Materials, preparation, and characterization in thermoelectrics, 1st edition*. Vol. 1. 2012: CRC press. Pp 20.1 – 20.6. ISBN: 9781439874707.

53. Rowe, D.M., *Modules, systems, and applications in thermoelectrics, 1st edition*. Vol. 2. 2012: CRC press. Pp 1.1-1.6 . ISBN: 9781439874721.

54. Chen, J., Z. Yan, and L. Wu, *The influence of Thomson effect on the maximum power output and maximum efficiency of a thermoelectric generator.* Journal of Applied Physics, 1996. **79**(11): p. 8823-8828. [Accessed: 01/05/18]. Available at: https://aip.scitation.org/doi/abs/10.1063/1.362507

55. Huang, M.-J., R.-H. Yen, and A.-B. Wang, *The influence of the Thomson effect on the performance of a thermoelectric cooler.* International Journal of Heat and Mass Transfer, 2005. **48**(2): p. 413-418. [Accessed: 01/05/18]. Available at: https://www.sciencedirect.com/science/article/pii/S0017931004003783

56. Mishra, S., S. Satpathy, and O. Jepsen, *Electronic structure and thermoelectric properties of bismuth telluride and bismuth selenide.* Journal of Physics: Condensed Matter, 1997. **9**(2): p. 461. [Accessed on: 01/05/18]. Available at: http://iopscience.iop.org/article/10.1088/0953-8984/9/2/014/meta

57. Goldsmid, H. and R. Douglas, *The use of semiconductors in thermoelectric refrigeration.* British Journal of Applied Physics, 1954. **5**(11): p. 386. [Accessed: 01/05/18]. Available at: http://iopscience.iop.org/article/10.1088/0508-3443/5/11/303/meta

58. Goldsmid, H., A. Sheard, and D. Wright, *The performance of bismuth telluride thermojunctions.* British Journal of Applied Physics, 1958. **9**(9): p. 365. [Accessed: 01/05/18]. Available at: http://iopscience.iop.org/article/10.1088/0508-3443/9/9/306/meta

59. Poudel, B., Q. Hao, Y. Ma, et al., *High-Thermoelectric Performance of Nanostructured Bismuth Antimony Telluride Bulk Alloys.* Science, 2008. **320**(5876): p. 634. [Accessed: 01/05/18]. Available at: http://science.sciencemag.org/content/320/5876/634.short

60. [Online] Runyon, J. *CPV Solar Manufacturer Soitec Sets Its Sights on 50% Efficiency*. 2013. [Accessed: 01/05/18]. Available at: https://www.renewableenergyworld.com/articles/2013/07/cpv-solar-manufacturer-soitec-sets-its-sights-on-50-efficiency.html

61. King, R.R., D. Bhusari, D. Larrabee, et al., *Solar cell generations over 40% efficiency.* Progress in Photovoltaics: Research and Applications, 2012. **20**(6): p. 801-815. [Accessed: 01/05/18]. Available at: https://onlinelibrary.wiley.com/doi/full/10.1002/pip.1255

62. Ekins-Daukes, N.J., P. Sandwell, J. Nelson, et al., *What does CPV need to achieve in order to succeed?* AIP Conference Proceedings, 2016. **1766**(1): p. 020004. [Accessed: 01/05/18]. Available at: https://aip.scitation.org/doi/abs/10.1063/1.4962072

63. [Online] Soitec. *Soitec announces the end of negotiations with Concensolar regarding a sale of solar assets and continues its refocus on electronics*. 2015. [Accessed: 01/05/18]. Available at:

http://inpublic.globenewswire.com/2015/08/05/SOITEC+SOITEC+ANNOUNCES+THE+END+OF+NEGOTIATIONS+WITH+CONCENSOLAR+REGARDING+A+SALE+OF+SOLAR+ASSETS+AND+CONTINUES+ITS+REFOCUS+ON+ELECTRONICS+HUG1943916.html

64. Bhat, K., A.D. Gupta, P. Rao, et al., *Wafer bonding-a powerful tool for MEMS.* Indian Journal of Pure and Applied Physics, 2007. **45**(4): p. 311-316. [Accessed: 01/05/18]. Available at: http://nopr.niscair.res.in/handle/123456789/2327

65. Dimroth, F., M. Grave, P. Beutel, et al., *Wafer bonded four-junction GaInP/GaAs//GaInAsP/GaInAs concentrator solar cells with 44.7% efficiency.* Progress in Photovoltaics: Research and Applications, 2014. **22**(3): p. 277-282. [Accessed: 01/05/18]. Available at: https://onlinelibrary.wiley.com/doi/abs/10.1002/pip.2475

66. Lackner, D., O. Höhn, A.W. Walker, et al., *Status of Four-Junction Cell Development at Fraunhofer ISE.* E3S Web Conf., 2017. **16**: p. 03009. [Accessed: 01/05/18]. Available at: https://search.proquest.com/openview/58ac5e2e6110db0bd4974c6c900c826a/1?pq-origsite=gscholar&cbl=2040555

67. Steiner, M., G. Siefer, T. Schmidt, et al., *Sunlight to Electricity Conversion Efficiency Using CPV.* IEEE Journal of Photovoltaics, 2016. **6**(4): p. 1020-1024. [Accessed: 01/05/18]. Available at: http://ieeexplore.ieee.org/abstract/document/7469840/

68. France, R.M., J.F. Geisz, I. Garc, et al., *Quadruple-Junction Inverted Metamorphic Concentrator Devices.* IEEE Journal of Photovoltaics, 2015. **5**(1): p. 432-437. [Accessed: 01/05/18]. Available at: https://ieeexplore.ieee.org/abstract/document/6945794/

69. Toprasertpong, K., H. Fujii, T. Thomas, et al., *Absorption threshold extended to 1.15 eV using InGaAs/GaAsP quantum wells for over-50%-efficient lattice-matched quad-junction solar cells.* Progress in Photovoltaics: Research and Applications, 2016. **24**(4): p. 533-542. [Accessed: 01/05/18]. Available at: https://onlinelibrary.wiley.com/doi/full/10.1002/pip.2585

70. [Online] NREL, *Photovoltaic Cell Efficiency Chart*. 2018. [Accessed: 01/05/18]. Available at: https://www.nrel.gov/pv/assets/images/efficiency-chart.png

71. Aiken, D.J., *High performance anti-reflection coatings for broadband multi-junction solar cells.* Solar Energy Materials and Solar Cells, 2000. **64**(4): p. 393-404. [Accessed: 01/05/18]. Available at: https://www.sciencedirect.com/science/article/pii/S0927024800002531

72. Yeo, C.I., H.J. Choi, Y.M. Song, et al., *A single-material graded refractive index layer for improving the efficiency of III-V triple-junction solar cells.* Journal of Materials Chemistry A, 2015. **3**(14): p. 7235-7240. [Accessed: 01/05/18]. Available at: http://pubs.rsc.org/-/content/articlehtml/2015/ta/c4ta06111j

73. Sabnis, V., H. Yuen, and M. Wiemer, *High-efficiency multijunction solar cells employing dilute nitrides.* AIP Conference Proceedings, 2012. **1477**(1): p. 14-19. [Accessed: 01/05/18]. Available at: http://aip.scitation.org/doi/abs/10.1063/1.4753823

74. Sasaki, K., T. Agui, K. Nakaido, et al., *Development of InGaP/GaAs/InGaAs inverted triple junction concentrator solar cells.* AIP Conference Proceedings, 2013. **1556**(1): p. 22-25. [Accessed: 01/05/18]. Available at: https://aip.scitation.org/doi/abs/10.1063/1.4822190

75. Geisz, J.F., D.J. Friedman, J.S. Ward, et al., *40.8% efficient inverted triple-junction solar cell with two independently metamorphic junctions.* Applied Physics Letters, 2008. **93**(12): p. 123505. [Accessed: 01/05/18]. Available at: https://aip.scitation.org/doi/abs/10.1063/1.2988497

76. Duda, A., S. Ward, and M. Young, *Inverted metamorphic multijunction (IMM) cell processing instructions.* Contract, 2012. **303**: p. 275-3000. [Accessed: 01/05/18]. Available at: https://www.osti.gov/biblio/1036035

77. King, R.R., A. Boca, W. Hong, et al. *Band-gap-engineered architectures for high-efficiency multijunction concentrator solar cells*. in *24th European Photovoltaic Solar Energy Conference and Exhibition, Hamburg, Germany*. 2009. [Accessed:01/05/18]. Available at: http://www.spectrolab.com/pv/support/Band-Gap-

Engineered_Architectures_for_High-Efficiency_Multijunction_Concentrator_Solar_Cells.pdf

78. Guter, W., J. Schöne, S.P. Philipps, et al., *Current-matched triple-junction solar cell reaching 41.1% conversion efficiency under concentrated sunlight.* Applied Physics Letters, 2009. **94**(22): p. 223504. [Accessed: 01/05/18]. Available at: https://aip.scitation.org/doi/abs/10.1063/1.3148341

79. Chiu, P.T., D.C. Law, R.L. Woo, et al., *Direct Semiconductor Bonded 5J Cell for Space and Terrestrial Applications.* IEEE Journal of Photovoltaics, 2014. **4**(1): p. 493-497. [Accessed: 01/05/18]. Available at: https://ieeexplore.ieee.org/abstract/document/6595564/

80. Patel, P., D. Aiken, D. Chumney, et al. *Initial results of the monolithically grown six-junction inverted metamorphic multi-junction solar cell*. in *Photovoltaic Specialists Conference (PVSC), Volume 2, 2012 IEEE 38th*. 2012. [Accessed:01/05/18]. Available at: http://ieeexplore.ieee.org/abstract/document/6656717/

81. Vossier, A., E.A. Alam, A. Dollet, et al., *Assessing the Efficiency of Advanced Multijunction Solar Cells in Real Working Conditions: A Theoretical Analysis.* IEEE Journal of Photovoltaics, 2015. **5**(6): p. 1805-1812. [Accessed: 01/05/18]. Available at: http://ieeexplore.ieee.org/abstract/document/7229250/

82. Meusel, M., R. Adelhelm, F. Dimroth, et al., *Spectral mismatch correction and spectrometric characterization of monolithic III–V multi-junction solar cells.* Progress in Photovoltaics: Research and Applications, 2002. **10**(4): p. 243-255. [Accessed: 01/05/18]. Available at: https://onlinelibrary.wiley.com/doi/full/10.1002/pip.407

83. Siefer, G., C. Baur, M. Meusel, et al. *Influence of the simulator spectrum on the calibration of multi-junction solar cells under concentration*. in *Photovoltaic Specialists Conference, 2002. Conference Record of the Twenty-Ninth IEEE*. 2002. [Accessed: 01/05/18]. Available at: http://ieeexplore.ieee.org/abstract/document/1190709/

84. Muller, M., S. Kurtz, and J. Rodriguez, *Procedural considerations for CPV outdoor power ratings per IEC 62670.* AIP Conference Proceedings, 2013.

1556(1): p. 125-128. [Aceessed: 01/05/18]. Available at: https://aip.scitation.org/doi/abs/10.1063/1.4822214

85. Kurtz, S.R., M. Muller, B. Marion, et al., *Considerations for how to rate CPV.* 2011. [Accessed: 01/05/18]. Available at: https://aip.scitation.org/doi/abs/10.1063/1.3658287

86. Muller, M., S. Kurtz, M. Steiner, et al., *Translating outdoor CPV I–V measurements to a CSTC power rating and the associated uncertainty.* Progress in Photovoltaics: Research and Applications, 2015. **23**(11): p. 1557-1571. [Accessed: 01/05/18]. Available at: https://onlinelibrary.wiley.com/doi/full/10.1002/pip.2590

87. Cole, I.R. and R. Gottschalg, *Improved Model for Circumsolar Irradiance Calculation as an Extended Light Source and Spectral Implications for High-Concentration Photovoltaic Devices.* IEEE Journal of Photovoltaics, 2016. **6**(1): p. 258-265. [Accessed: 01/05/18]. Available at: https://ieeexplore.ieee.org/abstract/document/7327120/

88. Fernández, E.F., A. Soria-Moya, F. Almonacid, et al., *Comparative assessment of the spectral impact on the energy yield of high concentrator and conventional photovoltaic technology.* Solar Energy Materials and Solar Cells, 2016. **147**: p. 185-197. [Accessed: 01/05/18]. Available at: https://www.sciencedirect.com/science/article/pii/S0927024815006510

89. Ghitas, A.E., *Studying the effect of spectral variations intensity of the incident solar radiation on the Si solar cells performance.* NRIAG Journal of Astronomy and Geophysics, 2012. **1**(2): p. 165-171. [Accessed: 01/05/18]. Available at: https://www.sciencedirect.com/science/article/pii/S2090997712000223

90. Norton, M., V. Paraskeva, R. Kenny, et al. *Field investigation of the effect of spectral response upon photovoltaic energy yields*. in *Photovoltaic Specialist Conference (PVSC), 2015 IEEE 42nd*. 2015. [Accessed: 01/05/18]. Available at: http://ieeexplore.ieee.org/abstract/document/7419246/

91. Sweet, T., D. Yuan, W. Brooks, et al. *A comparison of the spectral and electrical performance characteristics of commercially vailable triple-junction concentrator photovoltaic cells.* in *Photovoltaic Science Applications*

and Technology (PVSAT-10). 2014. Loughborough University: Internation Solar Energy Society. [Not Available Online. Paper copy available from corresponding author, Dr. Tracy Sweet: SweetT@Cardiff.ac.uk].

92. Green, M.A., K. Emery, Y. Hishikawa, et al., *Solar cell efficiency tables (Version 45).* Progress in photovoltaics: research and applications, 2015. **23**(1): p. 1-9. [Accessed:01/05/18]. Available at: https://onlinelibrary.wiley.com/doi/pdf/10.1002/pip.2573
93. Green, M.A., K. Emery, Y. Hishikawa, et al., *Solar cell efficiency tables (version 46).* Progress in Photovoltaics: Research and Applications, 2015. **23**(7): p. 805-812. [Accessed: 01/05/18]. Available at: https://onlinelibrary.wiley.com/doi/abs/10.1002/pip.2637
94. [Online] Fraunhofer, *Photovoltaics Report*. 2016, Fraunhofer ISE. (Report). [Accessed: 01/05/18]. Available at: https://ecee.colorado.edu/~ecen5009/Resources/Photovoltaics/Fraunhofer2016.pdf
95. Wysocki, J.J. and P. Rappaport, *Effect of Temperature on Photovoltaic Solar Energy Conversion.* Journal of Applied Physics, 1960. **31**(3): p. 571-578. [Accessed: 01/05/18]. Available at: http://aip.scitation.org/doi/abs/10.1063/1.1735630
96. Dupré, O., R. Vaillon, and M.A. Green, *Physics of the temperature coefficients of solar cells.* Solar Energy Materials and Solar Cells, 2015. **140**: p. 92-100. [Accessed: 01/05/18]. Available at: https://www.sciencedirect.com/science/article/pii/S0927024815001403
97. France, R.M., J.F. Geisz, M.A. Steiner, et al. *Pushing inverted metamorphic multijunction solar cells toward higher efficiency at realistic operating conditions*. in *Photovoltaic Specialists Conference (PVSC), Volume 2, 2012 IEEE 38th*. 2012. [Accessed: 01/05/18]. Available at: https://ieeexplore.ieee.org/abstract/document/6656740/
98. Siefer, G. and A.W. Bett, *Analysis of temperature coefficients for III–V multi-junction concentrator cells.* Progress in Photovoltaics: Research and Applications, 2014. **22**(5): p. 515-524. [Accessed: 01/05/18]. Available at: https://onlinelibrary.wiley.com/doi/full/10.1002/pip.2285

99. Kinsey, G.S., P. Hebert, K.E. Barbour, et al., *Concentrator multijunction solar cell characteristics under variable intensity and temperature.* Progress in Photovoltaics: Research and Applications, 2008. **16**(6): p. 503-508. [Accessed: 01/05/18]. Available at: https://onlinelibrary.wiley.com/doi/abs/10.1002/pip.834

100. Fernández, E.F., G. Siefer, M. Schachtner, et al., *Temperature coefficients of monolithic III-V triple-junction solar cells under different spectra and irradiance levels.* AIP Conference Proceedings, 2012. **1477**(1): p. 189-193. [Accessed: 01/05/18]. Available at: https://aip.scitation.org/doi/abs/10.1063/1.4753865

101. Theristis, M. and T.S. O'Donovan, *Electrical-thermal analysis of III–V triple-junction solar cells under variable spectra and ambient temperatures.* Solar Energy, 2015. **118**: p. 533-546. [Accessed: 01/05/18]. Available at: https://www.sciencedirect.com/science/article/pii/S0038092X15003059

102. Jang, S.H. and M.W. Shin, *Thermal Characterization of Junction in Solar Cell Packages.* IEEE Electron Device Letters, 2010. **31**(7): p. 743-745. [Accessed: 01/05/18]. Available at: http://ieeexplore.ieee.org/abstract/document/5471188/

103. Lv, H., F. Sheng, J. Dai, et al., *Temperature-dependent model of concentrator photovoltaic modules combining optical elements and III–V multi-junction solar cells.* Solar Energy, 2015. **112**: p. 351-360. [Accessed: 01/05/18]. Available at: https://www.sciencedirect.com/science/article/pii/S0038092X14005957

104. Micheli, L., E.F. Fernández, F. Almonacid, et al., *Performance, limits and economic perspectives for passive cooling of High Concentrator Photovoltaics.* Solar Energy Materials and Solar Cells, 2016. **153**: p. 164-178. [Accessed: 01/05/18]. Available at: https://www.sciencedirect.com/science/article/pii/S0927024816300307

105. Xin, G., Y. Wang, Y. Sun, et al., *Experimental study of liquid-immersion III–V multi-junction solar cells with dimethyl silicon oil under high concentrations.* Energy Conversion and Management, 2015. **94**: p. 169-177. [Accessed:

01/05/18]. Available at: https://www.sciencedirect.com/science/article/pii/S019689041500076X

106. Sun, Y., Y. Wang, L. Zhu, et al., *Direct liquid-immersion cooling of concentrator silicon solar cells in a linear concentrating photovoltaic receiver.* Energy, 2014. **65**: p. 264-271. [Accessed: 01/05/18]. Available at: https://www.sciencedirect.com/science/article/pii/S0360544213010335

107. Gasner, S., G. Pack, M. Gates, et al. *Stability of GaAs/Ge solar cells with standard front contacts after long-term, high-temperature exposure*. in *Photovoltaic Specialists Conference, 1990., Conference Record of the Twenty First IEEE*. 1990. [Accessed: 01/05/18]. Available at: https://ieeexplore.ieee.org/abstract/document/111825/

108. Van Riesen, S., A. Bett, and G. Willeke. *Accelerated ageing tests on III-V solar cells*. in *Photovoltaic Energy Conversion, 2003. Proceedings of 3rd World Conference on*. 2003. IEEE. [Accessed: 01/05/18]. Available at: https://ieeexplore.ieee.org/abstract/document/1305413/

109. Van Riesen, S. and A.W. Bett, *Degradation study of III–V solar cells for concentrator applications.* Progress in Photovoltaics: Research and Applications, 2005. **13**(5): p. 369-380. [Accessed: 01/05/18]. Available at: http://onlinelibrary.wiley.com/doi/10.1002/pip.603/full

110. Vázquez, M., C. Algora, I. Rey-Stolle, et al., *III-V concentrator solar cell reliability prediction based on quantitative LED reliability data.* Progress in Photovoltaics: Research and Applications, 2007. **15**(6): p. 477-491. [Accessed: 01/05/18]. Available at: https://onlinelibrary.wiley.com/doi/full/10.1002/pip.753

111. Antón, I., G. Sala, K. Heasman, et al., *Performance prediction of concentrator solar cells and modules from dark I–V characteristics.* Progress in Photovoltaics: Research and Applications, 2003. **11**(3): p. 165-178. [Accessed: 01/05/18]. Available at: https://onlinelibrary.wiley.com/doi/full/10.1002/pip.477

112. Bosco, Nick, and Sarah Kurtz. "Quantifying the thermal fatigue of CPV modules." *AIP Conference Proceedings*. Vol. 1277. No. 1. AIP, 2010.

[Accessed: 01/05/18]. Available at: https://aip.scitation.org/doi/abs/10.1063/1.3509197

113. Rey-Stolle, I. and C. Algora, *High-irradiance degradation tests on concentrator GaAs solar cells.* Progress in Photovoltaics: Research and Applications, 2003. **11**(4): p. 249-254. [Accessed: 01/05/18]. Available at: https://onlinelibrary.wiley.com/doi/full/10.1002/pip.487

114. Stellwag, T., P. Dodd, M. Carpenter, et al. *Effects of perimeter recombination on GaAs-based solar cells*. in *Photovoltaic Specialists Conference, 1990., Conference Record of the Twenty First IEEE*. 1990. IEEE. [Accessed: 01/05/18]. Available at: http://ieeexplore.ieee.org/abstract/document/111663/

115. González, J.R., M. Vázquez, N. Núñez, et al., *Reliability analysis of temperature step-stress tests on III–V high concentrator solar cells.* Microelectronics Reliability, 2009. **49**(7): p. 673-680. [Accessed: 01/05/18]. Available at: https://www.sciencedirect.com/science/article/pii/S0026271409001115

116. Núñez, N., M. Vázquez, J.R. González, et al., *Novel accelerated testing method for III–V concentrator solar cells.* Microelectronics Reliability, 2010. **50**(9–11): p. 1880-1883. [Accessed:01/05/18]. Available at: https://www.sciencedirect.com/science/article/pii/S0026271410003586

117. González, J.R., M. Vázquez, N. Núñez, et al., *Reliability Improvement in III-V Concentrator Solar Cells by Means of Perimeter Protection.* 2010. [Accessed: 01/05/18]. Available at: http://aip.scitation.org/doi/abs/10.1063/1.3509196

118. Algora, C., *Reliability of III–V concentrator solar cells.* Microelectronics Reliability, 2010. **50**(9): p. 1193-1198. [Accessed: 01/05/18]. Available at: https://www.sciencedirect.com/science/article/pii/S0026271410003185

119. Núñez, N., M. Vázquez, J. González, et al., *Instrumentation for accelerated life tests of concentrator solar cells.* Review of Scientific Instruments, 2011. **82**(2): p. 024703. [Accessed: 01/05/18]. Available at: http://aip.scitation.org/doi/abs/10.1063/1.3541800

120. Núñez, N., J.R. González, M. Vázquez, et al., *Evaluation of the reliability of high concentrator GaAs solar cells by means of temperature accelerated*

aging tests. Progress in Photovoltaics: Research and Applications, 2013. **21**(5): p. 1104-1113. [Accessed: 01/05/18]. Available at: https://onlinelibrary.wiley.com/doi/full/10.1002/pip.2212

121. Espinet-Gonzalez, P., C. Algora, V. Orlando, et al. *Preliminary temperature accelerated life test (ALT) on III-V commercial concentrator triple-junction solar cells*. in *Photovoltaic Specialists Conference (PVSC), Volume 2, 2012 IEEE 38th*. 2012. [Accessed: 01/05/18]. Available at: http://ieeexplore.ieee.org/abstract/document/6750496/
122. Espinet-González, P., C. Algora, N. Núñez, et al., *Temperature accelerated life test on commercial concentrator III–V triple-junction solar cells and reliability analysis as a function of the operating temperature.* Progress in Photovoltaics: Research and Applications, 2015. **23**(5): p. 559-569. [Accessed: 01/05/18]. Available at: https://onlinelibrary.wiley.com/doi/full/10.1002/pip.2461
123. Zimmermann, C.G., *Thermal runaway in multijunction solar cells.* Applied Physics Letters, 2013. **102**(23): p. 233506. [Accessed: 01/05/18]. Available at: https://aip.scitation.org/doi/abs/10.1063/1.4809952
124. Tsanakas, J.A., M. Sicre, C. Carriere, et al., *A novel approach of accelerated ageing tests for high concentration III–V multijunction solar cells through rapid irradiation/thermal cycles.* Solar Energy, 2015. **116**: p. 205-214. [Accessed: 01/05/18]. Available at: https://www.sciencedirect.com/science/article/pii/S0038092X15001590
125. Bosco, N. and S. Kurtz. *CPV cell characterization following one-year exposure in Golden Colorado*. in *Proc. AIP Conference*. 2014. [Accessed: 01/05/18]. Available at: http://aip.scitation.org/doi/abs/10.1063/1.4897070
126. Bett, A., C. Baur, F. Dimroth, et al. *FLATCON modules: technology and characterisation*. in *Photovoltaic Energy Conversion, 2003. Proceedings of 3rd World Conference on*. 2003. IEEE. [Accessed: 01/05/18]. Available at: https://ieeexplore.ieee.org/abstract/document/1305361
127. Gerstmaier, T., S. van Riesen, A. Gombert, et al. *Software modeling of FLATCON© CPV systems*. in *AIP conference proceedings*. 2010. [Accessed:

01/05/18]. Available at: https://aip.scitation.org/doi/abs/10.1063/1.3509185

128. Jaus, J., G. Peharz, A. Gombert, et al. *Development of FLATCON® modules using secondary optics*. in *Photovoltaic Specialists Conference (PVSC), 2009 34th IEEE*. 2009. IEEE. [Accessed: 01/05/18]. Available at: https://ieeexplore.ieee.org/abstract/document/5411559

129. Lerchenmüller, H., A. Bett, J. Jaus, et al. *Cost and market perspectives for FLATCON®-systems*. in *Proceedings of the 3rd International Conference on Solar Concentrators (SC3) for the Generation of Electricity or Hydrogen*. 2005. [Accesed: 01/05/18]. Available at: https://www.researchgate.net/profile/Andreas_Bett/publication/238681317_Cost_and_market_perspectives_for_FLATCON-systems/links/00b7d52bed48809f09000000.pdf

130. Cole, I.R. and R. Gottschalg. *Optical modelling for CPV systems: investigating the Fresnel lens*. in *Photovoltaic Science Applications and Technology (PVSAT-10).* 2014. Loughborough: International Solar Energy Society. *[Accessed: 01/05/18]. Available at: https://ieeexplore.ieee.org/abstract/document/7127201/*

131. Languy, F. and S. Habraken, *Nonimaging achromatic shaped Fresnel lenses for ultrahigh solar concentration.* Optics Letters, 2013. **38**(10): p. 1730-1732. [Accessed: 01/05/18]. Available at: https://www.osapublishing.org/abstract.cfm?uri=ol-38-10-1730

132. Ferrer-Rodríguez, J.P., E.F. Fernández, F. Almonacid, et al., *Optical design of a 4-off-axis-unit Cassegrain ultra-high concentrator photovoltaics module with a central receiver.* Optics Letters, 2016. **41**(9): p. 1985-1988. [Accessed: 01/05/18]. Available at: https://www.osapublishing.org/ol/abstract.cfm?uri=ol-41-9-1985

133. Li, W., M.C. Paul, N. Sellami, et al., *Coupled Simulation of Performance of a Crossed Compound Parabolic Concentrator with Solar Cell.* Energy Procedia, 2015. **75**(Clean, Efficient and Affordable Energy for a Sustainable Future: The 7th International Conference on Applied Energy (ICAE2015)): p. 325-330.

[Accessed: 01/05/18]. Available at: https://www.sciencedirect.com/science/article/pii/S187661021501139X

134. Amanlou, Y., T.T. Hashjin, B. Ghobadian, et al., *A comprehensive review of Uniform Solar Illumination at Low Concentration Photovoltaic (LCPV) Systems.* Renewable and Sustainable Energy Reviews, 2016. **60**: p. 1430-1441. [Accessed: 01/05/18]. Available at: https://www.sciencedirect.com/science/article/pii/S1364032116002677

135. Arase, H., A. Matsushita, A. Itou, et al., *A Novel Thin Concentrator Photovoltaic With Microsolar Cells Directly Attached to a Lens Array.* IEEE Journal of Photovoltaics, 2014. **4**(2): p. 709-712. [Accessed: 01/05/18]. Available at: https://ieeexplore.ieee.org/abstract/document/6684322/

136. Leem, J.W. and J.S. Yu, *Artificial inverted compound eye structured polymer films with light-harvesting and self-cleaning functions for encapsulated III–V solar cell applications.* RSC Advances, 2015. **5**(75): p. 60804-60813. [Accessed: 01/05/18]. Available at: http://pubs.rsc.org/-/content/articlehtml/2015/ra/c5ra05991g

137. Narasimhan, V.K., T.M. Hymel, R.A. Lai, et al., *Hybrid Metal–Semiconductor Nanostructure for Ultrahigh Optical Absorption and Low Electrical Resistance at Optoelectronic Interfaces.* ACS Nano, 2015. **9**(11): p. 10590-10597. [Accessed: 01/05/18]. Available at: https://pubs.acs.org/doi/abs/10.1021/acsnano.5b04034

138. Wang, W. and A. Freundlich. *Rapid sub-wavelength texturing for III-V solar cells by laser interference lithography and wet etching*. in *Photovoltaic Specialist Conference (PVSC), 2015 IEEE 42nd*. 2015. [Accessed: 01/05/18]. Available at: http://ieeexplore.ieee.org/abstract/document/7355658/

139. Lee, S.C., H. Park, J. Woo, et al., *Design and construction of high efficiency fiber optic solar concentrator for solar lighting*, in *The Second International Energy 2030 Conference*. 2008, Energy 2030: Abu Dhabi, UAE. [Accessed: 01/05/18]. Available at: http://web.anl.gov/PCS/acsfuel/19_FUEL_S.pdf

140. Feuermann, D., J.M. Gordon, and M. Huleihil, *Solar fiber-optic mini-dish concentrators: first experimental results and field experience.* Solar Energy,

2002. **72**(6): p. 459-472. [Accessed: 01/05/18]. Available at: https://www.sciencedirect.com/science/article/pii/S0038092X02000257

141. Feuermann, D., J.M. Gordon, and M. Huleihil, *Light leakage in optical fibers: experimental results, modeling and the consequences for solar concentrators.* Solar Energy, 2002. **72**(3): p. 195-204. [Accessed: 01/05/18]. https://www.sciencedirect.com/science/article/pii/S0038092X01001001
142. Rodrigo, P., R. Velázquez, E.F. Fernández, et al., *Analysis of electrical mismatches in high-concentrator photovoltaic power plants with distributed inverter configurations.* Energy, 2016. **107**: p. 374-387. [Accessed: 01/05/18]. Available at: https://www.sciencedirect.com/science/article/pii/S0360544216304455
143. Fialho, Luis, et al. "Effect of shading on series solar modules: simulation and experimental results." *Procedia Technology* 17 (2014): 295-302. [Accessed: 01/05/18]. Available at: https://www.sciencedirect.com/science/article/pii/S2212017314004769
144. Quaschning, V. and R. Hanitsch, *Numerical simulation of current-voltage characteristics of photovoltaic systems with shaded solar cells.* Solar Energy, 1996. **56**(6): p. 513-520. [Accessed: 01/05/18]. Available at: https://www.sciencedirect.com/science/article/pii/0038092X96000060
145. Ramabadran, R. and B. Mathur, *Effect of shading on series and parallel connected solar PV modules.* Modern Applied Science, 2009. **3**(10): p. 32. [Accessed: 01/05/18]. Available at: http://www.ccsenet.org/journal/index.php/mas/article/view/3937
146. Ramaprabha, R. and B. Mathur, *Impact of partial shading on solar PV module containing series connected cells.* International Journal of Recent Trends in Engineering, 2009. **2**(7): p. 56-60. [Accessed: 01/05/18]. Available at: http://citeseerx.ist.psu.edu/viewdoc/download?doi=10.1.1.479.6970&rep=rep1&type=pdf
147. Fthenakis, V.M. and H.C. Kim, *Life cycle assessment of high-concentration photovoltaic systems.* Progress in Photovoltaics: Research and Applications,

2013. **21**(3): p. 379-388. [Accessed: 01/05/18]. Available at: https://onlinelibrary.wiley.com/doi/full/10.1002/pip.1186

148. Tan, M.-H. and K.-K. Chong, *Influence of self-weight on electrical power conversion of dense-array concentrator photovoltaic system.* Renewable Energy, 2016. **87, Part 1**: p. 445-457. [Accessed: 01/05/18]. Available at: https://www.sciencedirect.com/science/article/pii/S096014811530375X
149. Almonacid, F., E.F. Fernández, P. Rodrigo, et al., *Estimating the maximum power of a High Concentrator Photovoltaic (HCPV) module using an Artificial Neural Network.* Energy, 2013. **53**: p. 165-172. [Accessed: 01/05/18]. Available at: https://www.sciencedirect.com/science/article/pii/S0360544213001382
150. Energy Networks Association, *Engineering Recommendation G83: The connection of small-scale embedded generators (up to 16A per phase) in parallel with public low voltage distribution networks*. (Standard). 2002, UK. [Accessed: 01/05/18]. Available at: https://www.ofgem.gov.uk/ofgem-publications/52354/er-g83-2-v5-master-09-07-12-inc-ofgem-comments-clean-version-pdf
151. Energy Networks Association, *Generation Connection Guide: A Guide for Connecting Generation to the Distribution Network that Falls Under G59/3 and is 50kW or Less. (3-Phase or 17kW). (Standard).* 2014: p. 51. [Accessed: 01/05/18]. Available at: http://www.energynetworks.org/assets/files/electricity/engineering/distributed%20generation/DG%20Connection%20Guides/June%202017/DGCG%20G59%2050kW%20full%20June%202017.pdf
152. [Online] Friends Of The Earth International (FOEI), "*An energy revolution is possible"*. [Accessed: 01/05/18]. Available at: https://www.foei.org/wp-content/uploads/2016/09/foe-energy-revolution-full-reportNEWdraft2.pdf
153. [Online] Greenpeace, *Energy [R]evolution 2015*. (Report) 2015. [Accessed:01/05/18]. Available at: https://www.greenpeace.org/archive-international/Global/international/publications/climate/2015/Energy-Revolution-2015-Full.pdf

154. International Energy Agency., *Technology Roadmap: Solar Photovoltaic Energy - 2014 edition*. 2014. [Accessed: 01/05/18]. Available at: https://www.iea.org/publications/freepublications/publication/TechnologyRoadmapSolarPhotovoltaicEnergy_2014edition.pdf

155. Fu, R., T.L. James, and M. Woodhouse, *Economic Measurements of Polysilicon for the Photovoltaic Industry: Market Competition and Manufacturing Competitiveness.* IEEE Journal of Photovoltaics, 2015. **5**(2): p. 515-524. [Accessed: 01/05/18]. Available at: http://ieeexplore.ieee.org/abstract/document/7042229/

156. Kraemer, D., L. Hu, A. Muto, et al., *Photovoltaic-thermoelectric hybrid systems: A general optimization methodology.* Applied Physics Letters, 2008. **92**(24): p. 243503. [Accessed: 01/05/18]. Available at: http://aip.scitation.org/doi/abs/10.1063/1.2947591

157. Ju, X., Z. Wang, G. Flamant, et al., *Numerical analysis and optimization of a spectrum splitting concentration photovoltaic–thermoelectric hybrid system.* Solar Energy, 2012. **86**(6): p. 1941-1954. [Accessed: 01/05/18]. Available at: https://www.sciencedirect.com/science/article/pii/S0038092X12000886

158. Skjølstrup, E.J.H. and T. Søndergaard, *Design and optimization of spectral beamsplitter for hybrid thermoelectric-photovoltaic concentrated solar energy devices.* Solar Energy, 2016. **139**: p. 149-156. [Accessed: 01/05/18]. Available at: https://www.sciencedirect.com/science/article/pii/S0038092X1630442X

159. Li, G., X. Zhao, and J. Ji, *Conceptual development of a novel photovoltaic-thermoelectric system and preliminary economic analysis.* Energy Conversion and Management, 2016. **126**: p. 935-943. [Accessed: 01/05/18]. Available at: https://www.sciencedirect.com/science/article/pii/S0196890416307488

160. Li, G., G. Zhang, W. He, et al., *Performance analysis on a solar concentrating thermoelectric generator using the micro-channel heat pipe array.* Energy Conversion and Management, 2016. **112**: p. 191-198. [Accessed: 01/05/18]. Available at: https://www.sciencedirect.com/science/article/pii/S019689041600042X

161. Makki, A., S. Omer, Y. Su, et al., *Numerical investigation of heat pipe-based photovoltaic–thermoelectric generator (HP-PV/TEG) hybrid system.* Energy Conversion and Management, 2016. **112**: p. 274-287. [Accessed: 01/5/18]. Available at: https://www.sciencedirect.com/science/article/pii/S0196890415011784

162. Wu, S.-Y., Q.-L. Zhang, L. Xiao, et al., *A heat pipe photovoltaic/thermal (PV/T) hybrid system and its performance evaluation.* Energy and Buildings, 2011. **43**(12): p. 3558-3567. [Accessed: 01/05/18]. Available at: https://www.sciencedirect.com/science/article/pii/S0378778811004051

163. Kane, A.N. and V. Verma, *Performance enhancement of building integrated photovoltaic module using thermoelectric cooling.* International Journal of Renewable Energy Research (IJRER), 2013. **3**(2): p. 320-324. [Accessed: 01/05/18]. Available at: http://www.ijrer.com/index.php/ijrer/article/view/588

164. Sark, W.G.J.H.M.v., *Feasibility of photovoltaic – Thermoelectric hybrid modules.* Applied Energy, 2011. **88**(8): p. 2785-2790. [Accessed: 01/05/18]. Available at: https://www.sciencedirect.com/science/article/pii/S0306261911001073

165. Liao, T., B. Lin, and Z. Yang, *Performance characteristics of a low concentrated photovoltaic–thermoelectric hybrid power generation device.* International Journal of Thermal Sciences, 2014. **77**: p. 158-164. [Accessed: 01/05/18]. Available at: https://www.sciencedirect.com/science/article/pii/S1290072913002494

166. Zhang, J., Y. Xuan, and L. Yang, *Performance estimation of photovoltaic–thermoelectric hybrid systems.* Energy, 2014. **78**: p. 895-903. [Accessed: 01/05/18]. Available at: https://www.sciencedirect.com/science/article/pii/S0360544214012377

167. Xu, X., S. Zhou, M.M. Meyers, et al., *Performance Analysis of a Combination System of Concentrating Photovoltaic/Thermal Collector and Thermoelectric Generators.* Journal of Electronic Packaging, 2014. **136**(4): p. 041004-041004. [Accessed: 01/05/18]. Available at:

http://electronicpackaging.asmedigitalcollection.asme.org/article.aspx?articleid=1891630

168. Bjørk, R. and K.K. Nielsen, *The performance of a combined solar photovoltaic (PV) and thermoelectric generator (TEG) system.* Solar Energy, 2015. **120**: p. 187-194. [Accessed: 01/05/18]. Available at: https://www.sciencedirect.com/science/article/pii/S0038092X15004065

169. Deng, Y., W. Zhu, Y. Wang, et al., *Enhanced performance of solar-driven photovoltaic–thermoelectric hybrid system in an integrated design.* Solar energy, 2013. **88**: p. 182-191. [Accessed: 01/05/18]. Available at: https://www.sciencedirect.com/science/article/pii/S0038092X12004173

170. Hsueh, T.-J., J.-M. Shieh, and Y.-M. Yeh, *Hybrid Cd-free CIGS solar cell/TEG device with ZnO nanowires.* Progress in Photovoltaics: Research and Applications, 2015. **23**(4): p. 507-512. [Accessed: 01/05/18]. Available at: https://onlinelibrary.wiley.com/doi/full/10.1002/pip.2457

171. Park, K.-T., S.-M. Shin, A.S. Tazebay, et al., *Lossless hybridization between photovoltaic and thermoelectric devices.* Scientific Reports, 2013. **3**: p. 2123. [Accessed: 01/05/18]. Available at: https://www.nature.com/articles/srep02123

172. Bottner, H. *Micropelt miniaturized thermoelectric devices: small size, high cooling power densities, short response time*. in *ICT 2005. 24th International Conference on Thermoelectrics, 2005.* 2005. [Accessed: 01/05/18]. Available at: http://ieeexplore.ieee.org/abstract/document/1519873/

173. Wang, N., L. Han, H. He, et al., *A novel high-performance photovoltaic-thermoelectric hybrid device.* Energy & Environmental Science, 2011. **4**(9): p. 3676-3679. [Accessed: 01/05/18]. Available at: http://pubs.rsc.org/-/content/articlehtml/2011/ee/c1ee01646f

174. Attivissimo, F., A.D. Nisio, A.M.L. Lanzolla, et al., *Feasibility of a Photovoltaic-Thermoelectric Generator: Performance Analysis and Simulation Results.* IEEE Transactions on Instrumentation and Measurement, 2015. **64**(5): p. 1158-1169. [Accessed: 01/05/18]. Available at: http://ieeexplore.ieee.org/abstract/document/7067396/

175. Rezania, A., D. Sera, and L.A. Rosendahl, *Coupled thermal model of photovoltaic-thermoelectric hybrid panel for sample cities in Europe.* Renewable Energy, 2016. **99**: p. 127-135. [Accessed: 01/05/18]. Available at: https://www.sciencedirect.com/science/article/pii/S0960148116305699

176. Lin, J., T. Liao, and B. Lin, *Performance analysis and load matching of a photovoltaic–thermoelectric hybrid system.* Energy Conversion and Management, 2015. **105**: p. 891-899. [Accessed: 01/05/18]. Available at: https://www.sciencedirect.com/science/article/pii/S0196890415008080

177. Zhang, J., Y. Xuan, and L. Yang, *A novel choice for the photovoltaic–thermoelectric hybrid system: the perovskite solar cell.* International Journal of Energy Research, 2016. pp 1400-1409. [Accessed: 01/05/18]. Available aT: https://onlinelibrary.wiley.com/doi/full/10.1002/er.3532

178. Lamba, R. and S.C. Kaushik, *Modeling and performance analysis of a concentrated photovoltaic–thermoelectric hybrid power generation system.* Energy Conversion and Management, 2016. **115**: p. 288-298. [Accessed: 01/05/18]. Available at: https://www.sciencedirect.com/science/article/pii/S0196890416300917

179. Hashim, H., J.J. Bomphrey, and G. Min, *Model for geometry optimisation of thermoelectric devices in a hybrid PV/TE system.* Renewable Energy, 2016. **87, Part 1**: p. 458-463. [Accessed: 01/05/18]. Available at: https://www.sciencedirect.com/science/article/pii/S0960148115303827

180. Xu, Q., Y. Ji, B. Riggs, et al., *A transmissive, spectrum-splitting concentrating photovoltaic module for hybrid photovoltaic-solar thermal energy conversion.* Solar Energy, 2016. **137**: p. 585-593. [Accessed: 01/05/18]. Available at: https://www.sciencedirect.com/science/article/pii/S0038092X16303954

181. Narducci, D. and B. Lorenzi, *Challenges and Perspectives in Tandem Thermoelectric-Photovoltaic Solar Energy Conversion.* IEEE Transactions on Nanotechnology, 2016. **15**(3): p. 348-355. [Accessed: 01/05/18]. Available at: http://ieeexplore.ieee.org/abstract/document/7398080/

182. Guo, X.-Z., Y.-D. Zhang, D. Qin, et al., *Hybrid tandem solar cell for concurrently converting light and heat energy with utilization of full solar*

spectrum. Journal of Power Sources, 2010. **195**(22): p. 7684-7690. [Accessed: 01/05/18]. Available at: https://www.sciencedirect.com/science/article/pii/S037877531000858X

183. Su, S., T. Liu, Y. Wang, et al., *Performance optimization analyses and parametric design criteria of a dye-sensitized solar cell thermoelectric hybrid device.* Applied Energy, 2014. **120**: p. 16-22. [Accessed: 01/05/18]. Available at: https://www.sciencedirect.com/science/article/pii/S0306261914000671

184. Verma, V., A. Kane, and B. Singh, *Complementary performance enhancement of PV energy system through thermoelectric generation.* Renewable and Sustainable Energy Reviews, 2016. **58**: p. 1017-1026. [Accessed: 01/05/18]. Available at: https://www.sciencedirect.com/science/article/pii/S1364032115015956

185. Cui, T., Y. Xuan, and Q. Li, *Design of a novel concentrating photovoltaic–thermoelectric system incorporated with phase change materials.* Energy Conversion and Management, 2016. **112**: p. 49-60. [Accessed: 01/05/18]. Available at: https://www.sciencedirect.com/science/article/pii/S0196890416000248

186. Chávez-Urbiola, E.A., Y.V. Vorobiev, and L.P. Bulat, *Solar hybrid systems with thermoelectric generators.* Solar Energy, 2012. **86**(1): p. 369-378. [Accessed: 01/05/18]. Available at: https://www.sciencedirect.com/science/article/pii/S0038092X11003872

187. Fisac, M., F.X. Villasevil, and A.M. López, *High-efficiency photovoltaic technology including thermoelectric generation.* Journal of Power Sources, 2014. **252**: p. 264-269. [AccesseD: 01/05/18]. Available at: https://www.sciencedirect.com/science/article/pii/S0378775313019678

188. Mizue, M., M. Masashi, and O. Kimihiro, *Thermal–Photovoltaic Hybrid Solar Generator Using Thin-Film Thermoelectric Modules.* Japanese Journal of Applied Physics, 2012. **51**(6S): p. 06FL07. [Accessed: 01/05/18]. Available at: http://iopscience.iop.org/article/10.1143/JJAP.51.06FL07/meta

189. Elsarrag, E., H. Pernau, J. Heuer, et al., *Spectrum splitting for efficient utilization of solar radiation: a novel photovoltaic–thermoelectric power generation system.* Renewables: Wind, Water, and Solar, 2015. **2**(1): p. 16.

[Accessed: 01/05/18]. Available at: https://jrenewables.springeropen.com/articles/10.1186/s40807-015-0016-y

190. Dallan, B.S., J. Schumann, and F.J. Lesage, *Performance evaluation of a photoelectric–thermoelectric cogeneration hybrid system.* Solar Energy, 2015. **118**: p. 276-285. [Accessed: 01/05/18]. Available at: https://www.sciencedirect.com/science/article/pii/S0038092X15002947

191. Zhu, W., Y. Deng, Y. Wang, et al., *High-performance photovoltaic-thermoelectric hybrid power generation system with optimized thermal management.* Energy, 2016. **100**: p. 91-101. [Accessed: 01/05/18]. Available at: https://www.sciencedirect.com/science/article/pii/S0360544216000852

192. Cui, T., Y. Xuan, E. Yin, et al., *Experimental investigation on potential of a concentrated photovoltaic-thermoelectric system with phase change materials.* Energy, 2017. **122**: p. 94-102. [Accessed: 01/05/18]. Available at: https://www.sciencedirect.com/science/article/pii/S0360544217300877

193. Pang, W., Y. Liu, S. Shao, et al., *Empirical study on thermal performance through separating impacts from a hybrid PV/TE system design integrating heat sink.* International Communications in Heat and Mass Transfer, 2015. **60**: p. 9-12. [Accessed: 01/05/18]. Available at: https://www.sciencedirect.com/science/article/pii/S0735193314002814

194. Kossyvakis, D.N., G.D. Voutsinas, and E.V. Hristoforou, *Experimental analysis and performance evaluation of a tandem photovoltaic–thermoelectric hybrid system.* Energy Conversion and Management, 2016. **117**: p. 490-500. [Accessed: 01/05/18]. Available at: https://www.sciencedirect.com/science/article/pii/S0196890416301546

195. Zhou, Z., J. Yang, Q. Jiang, et al., *Large improvement of device performance by a synergistic effect of photovoltaics and thermoelectrics.* Nano Energy, 2016. **22**: p. 120-128. [Accessed: 01/05/18]. Available at: https://www.sciencedirect.com/science/article/pii/S2211285516000690

196. Zhang, J., Y. Xuan, and L. Yang, *A novel choice for the photovoltaic–thermoelectric hybrid system: the perovskite solar cell.* International Journal of Energy Research, 2016. **40**(10): p. 1400-1409. [Accessed: 01/05/18]. Available at: https://onlinelibrary.wiley.com/doi/full/10.1002/er.3532

197. Lee, J.J., D. Yoo, C. Park, et al., *All organic-based solar cell and thermoelectric generator hybrid device system using highly conductive PEDOT:PSS film as organic thermoelectric generator.* Solar Energy, 2016. **134**: p. 479-483. [Accessed: 01/05/18]. Available at: https://www.sciencedirect.com/science/article/pii/S0038092X16300986

198. Willars-Rodríguez, F.J., E.A. Chávez-Urbiola, P. Vorobiev, et al., *Investigation of solar hybrid system with concentrating Fresnel lens, photovoltaic and thermoelectric generators.* International Journal of Energy Research, 2016: p. 377-388. [Accessed: 01/05/18]. Available at: https://onlinelibrary.wiley.com/doi/full/10.1002/er.3614

199. Pang, W., Yu, H., Zhang, Y., & Yan, H. The Electrical Characteristics Evaluation of Hybrid Photovoltaic/Thermoelectric Generator System. *Energy Technology, 2018*. [Accessed: 02/05/18]. Available at: https://onlinelibrary.wiley.com/doi/epdf/10.1002/ente.201700801

200. Dimri, N., Tiwari, A., & Tiwari, G. N. Effect of thermoelectric cooler (TEC) integrated at the base of opaque photovoltaic (PV) module to enhance an overall electrical efficiency. Solar Energy, 2018. 166, 159-170. [Accessed: 02/05/18]. Available at: https://www.sciencedirect.com/science/article/pii/S0038092X18302433

201. Beeri, O., O. Rotem, E. Hazan, et al., *Hybrid photovoltaic-thermoelectric system for concentrated solar energy conversion: Experimental realization and modeling.* Journal of Applied Physics, 2015. **118**(11): p. 115104. [Accessed: 01/05/18]. Available at: http://aip.scitation.org/doi/abs/10.1063/1.4931428

Chapter 3 : CPV-TE Hybrid Receiver Designs and Validation as an Effective Experimental Platform

3.1 Background

3.1.1 The CPV-TE Integration and Contacting Challenge: *Creating the Hybrid*

One of the major challenges for CPV-TE hybrid devices is ensuring good thermal coupling for effective heat flow, especially with the increased irradiance from high concentration ratios. There were three main factors considered simultaneously during design, to eliminate any unnecessary spurious or data-skewing artefacts within the hybrid designs themselves. III:V triple-junction CPV cells are inherently very fragile due to the nature of their material compositional and design structure. Their crystallographic nature and the sub-millimetre (<200 µm) thickness epitaxy layers, necessary for effective light absorption, means that the substrate choice to contact such a device is paramount. CPV cell areas are minimised to both reduce the material used for the device active area, and increase the potential design concentration ratio. The cells used within this work predominantly have dimensions of a 5.5mmx5.5 active area with two 200µm thick gold bus bars for the negative top contact.

3.1.2 Silver epoxy

For the first and second generation hybrid receivers, a manufacturing method was developed where the cell could be directly in thermal contact with the thermoelectric module - without shorting the connection from the bottom to the top of the cell. This “direct bonding” (DB) approach minimises the amount of thermal interfaces and the cumulative thermal resistances this would entail. An electrically and thermally conductive, two-part epoxy “H20E” sourced from Epotek was used for this purpose [1]. In the H20E, silver nano-particles are suspended within an epoxy polymer matrix, giving a representative datasheet thermal conductivity of 29W/mK and volume electrical Resistivity of <0.0004 Ωcm at 23^{O}C [1, 2].

There were many different curing regimes given by the manufacturer’s datasheet, but higher temperatures were recommended to achieve maximum mechanical strength. A critical constraint of 100^{o}C was implied from the TEM’s

specification maximum operation temperature, with an additionally recommended 85^{o}C maximum degradation temperature for the H20E. The epoxy was applied in as small a quantity as possible, to minimise thickness-dependant thermal resistances and potential cell shorting from excess epoxy. The quoted by weight outgassing when cured at 150^{o}C for 60 minutes was 0.25% [1]. A curing temperature of 80^{O}C was chosen with a bonding time of 4 hours. Epoxy was a good alternative to using solder with eutectic points as the epoxy cure temperature was far less than any low temperature solder alternative investigated. The mechanical robustness of the epoxy bond was assessed by attempting to remove a thermoelectric module post-cure. It was found that the TEM broke due to the applied force before the epoxy. Such results were enough to satisfy the robust location requirement for the hybrid devices, and ensure the devices did not move under test. Figure 3-1, shows the receiver post-cure alongside the underneath of the thermoelectric after it was removed. As can be seen, there was minimal outgassing or air pockets from these cure temperatures and application procedure, promoting good thermal and mechanical contact. As can be seen by Figure 3-1 b, c and d, the TEM broke from the force before the epoxy mechanical bonding strength was overcome – with even some TEM's pre-coated metallisation coating being pulled off by the epoxy in the process. A further summary is given in Figure 3-2

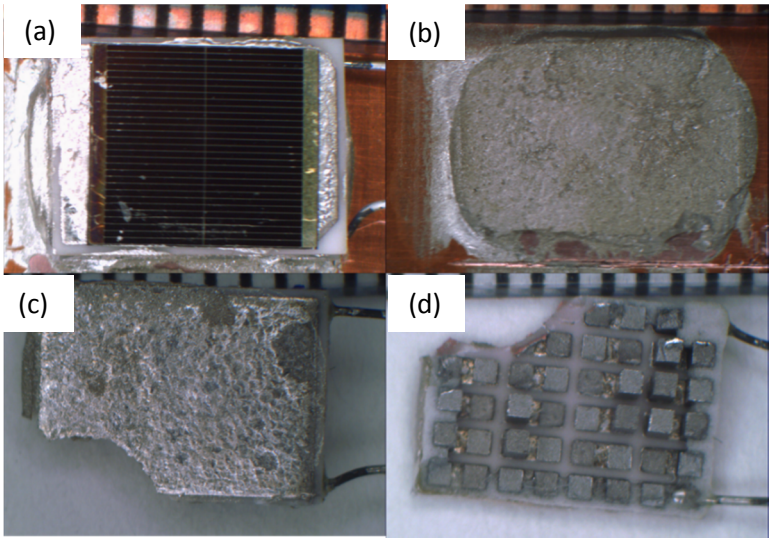

Figure 3-1. The Pulled-Apart Gen I Hybrid Receiver (1mm/div scaling rule). Here (a) Shows the Full CPV-TE Device Prior to Dis-assembly. (b) Shows Underneath the TEM After Removal. (c) and (d) Show the Damage to the TEM, Post-removal.

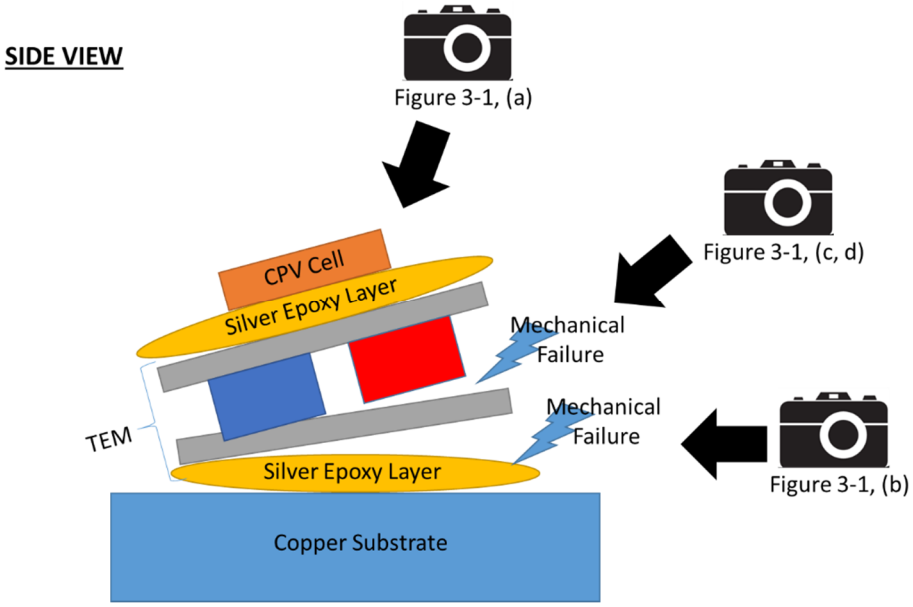

Figure 3-2. A Further Overview Diagram Explaining the Pictures as shown in Figure 3-1 for Context.

3.1.3 Wire Bonding

Wire-bonding was highlighted during the literature and CPV industrial surveys as a common manufacturing technique for CPV receivers, and small-scale semiconductors in general. The cleanroom facilities at Cardiff University included this capability for top contacting. Generation III included wide tracks on the PCB to facilitate wire bonding. The height of the supporting PCBs around the TEM were designed to be at the same height as the cell top contact in order to minimise mechanical stresses on the bonds themselves. A "Bi-layer" PCB structure was adopted with central holes placed on both PCBs for direct bonding and thermal coupling of the TEM rear side to the copper. Single-active device receivers (1 CPV cell and 1 TEM per receiver) were made to eliminate inter-device effects (such as string limiting) and allow for independent hybrid device testing. Soldered electrical connecting wires were added for interfacing with the PCB. The cell back electrical contact was achieved through using an epoxied back contact ribbon from the TEM top side, made from silver. This was done using the silver epoxy to be able to contact the CPV cell effectively. A current density safety factor was calculated to determine the silver ribbon thickness for the cell operating at high concentration

current conditions. Silver was chosen due to having a lower electrical resistivity than copper (ρ_{Copper} = 1.68x10^{-8} Ωm, ρ_{Silver} = 1.59x10^{-8} Ωm). To further improve this cell back contact, the TEMs included a pre-metallisation coating on the ceramic surfaces of Indium/Tin with a "Gold flash" to further minimise sheet resistance arising from the lateral electrical conduction through the epoxy.

3.1.4 Encapsulation

The final stage of the hybrid receiver manufacturing was done in the cleanroom to prevent debris and particles falling upon the cell during manufacture. These particles would block a percentage of light reaching the cell, and over time the cumulative effect would have a detrimental effect on cell conversion efficiency. Likewise, encapsulation of the cell using elastomers is an effective way to extend the lifetime of cells at the expense of optical transmission. The encapsulant used in this work was Sylguard 184 silicone-based two part curing elastomer [3]. The encapsulant-dependant transmission losses are quantified in Section 3.3.2.b.

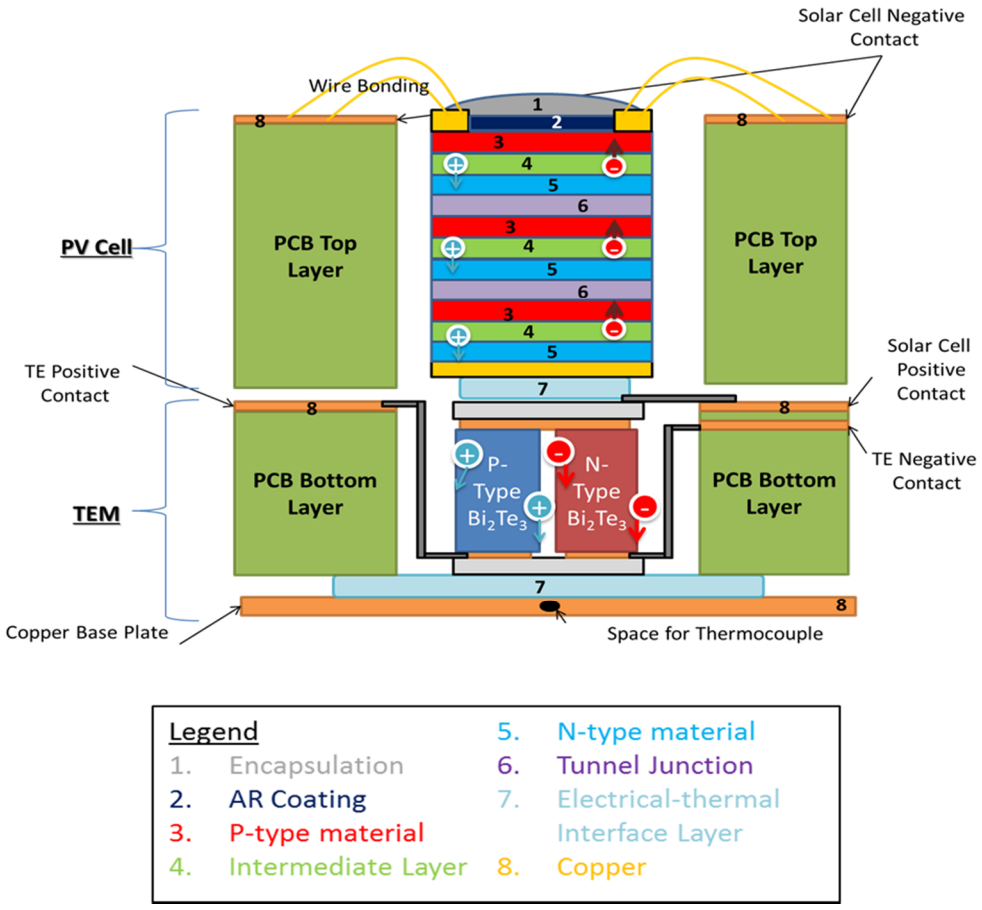

Figure 3-3. A Detailed Overview Diagram of the Triple-Junction GEN IV CPV-TE Hybrid Receiver [Not to Scale] [16]

3.1.5 The Generations of the CPV-TE Hybrid Receiver (GEN I to GEN IV)

3.1.5.a The Design Methodology Behind GEN I to GEN III

Throughout the design process, there were many unsuccessful design choices and avenues that were investigated before a fully-functional prototype was achieved. This incremental design process began with a collaborative effort with Exeter university as part of the EPSRC SUNTRAP consortium. A 3x3 array of CCPC SOEs was provided as part of this collaboration, and GEN I was designed around this. The CPV cells were provided by IQE as part of the funding for the PhD, with the challenge for electrical contacting and connection. GEN I attempted using a mechanical-only substrate for hybridisation, through 3D printing. A polymer "tracking" was on the surface of a 1mmm thick plastic space to locate the 2x2 (nine total) TEMs. This approach was unsuccessful due to the inadequacy of the plastic to locate the active devices in a robust fashion. GEN II attempted to use the in-house PCB milling facilities at Cardiff University, to investigate using this method of contacting the solar cell and TEM independently. However after manufacture, it was found that the soldering of the thermocouple on the side was too large to be effective, and the flux from the industry-standard lead-tin solder damaged the solar cell through shorting. Successful connection to the TEM was achieve using GEN II. GEN III improved the idea of using a PCB by transitioning to a bi-layer PCB for mechanical mounting. This occurred as the thickness of the PCB boards was the same height as the TEM, which in turn allowed for wire bonding from the PCB to the CPV cell without "sagging" which would be detrimental to performance. Additionally from the transition to GEN III, it was decided to focus on only using a single active hybrid device integration to further minimise complexity. A 2through-hold" was cut into the PCB board to eliminate any additional thermal resistances being introduced in the thermal conduction path from the FR4 fibreboard. It was shown that this bi-layer mechanical location, and the through-hole location of the TEM was an effective approach, as the CPV cell could be easily bonded to the TEM top ceramic using silver epoxy. GEN II still has design issues regarding the overall height of the bi-layer PCB for wire bonding, and as such GEN IV using 1.6mm boards as opposed to the GEN II 2mm boards to achieve the correct height to allow for robust wire bonding. GEN IV were the first electrically active devices, where the

CPV cell was contacted is such a way as to give representative I-V curves under testing, whilst also allowing the TEM to be independently controlled using current sources. The mechanical layout and approximate dimensions of the design is shown in Figure 3-4 below (not to scale). As can be seen, the total PCB thickness and required epoxy is on the left side of the diagram. This total is equivalent to that on the right side, equating to the thickness of the CPV cell, the TEM and the bonding silver epoxy layers between the mechanical surfaces of both devices.

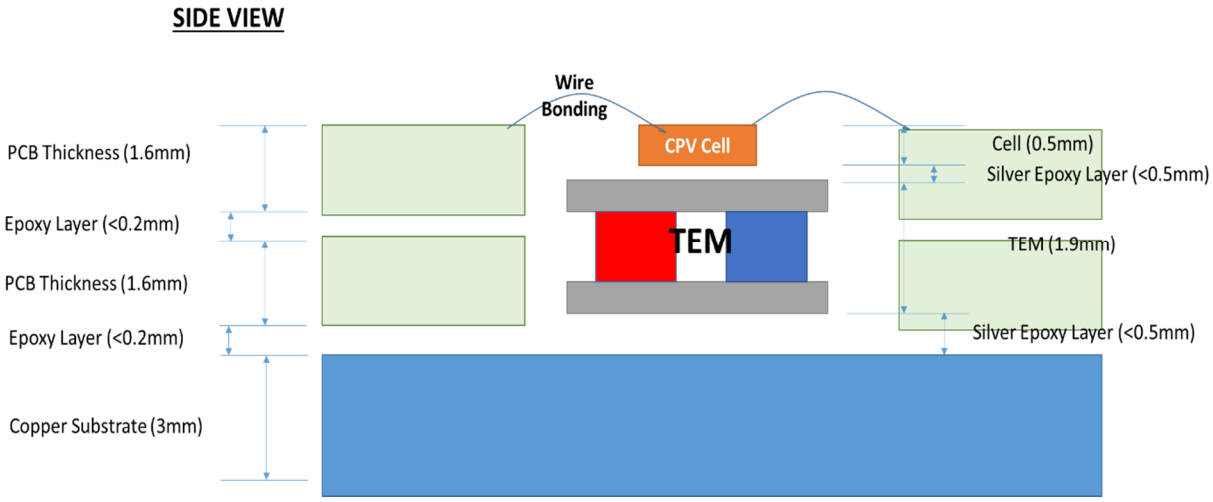

Figure 3-4. A Side-view Schematic Showing the Necessity of using a Bi-layer PCB for Mechanical Height

3.1.5.b The GEN IV CPV-TE Hybrid Receiver

The GEN IV receiver built upon previous design innovations, such as the H20E bonding mechanism in GEN I, the though-hole design and PCB tracking from GEN II and the GEN III Bi-layer PCB construction. Figure 3-3 gives a high-level overview of the hybrid design. Pre manufacture, the GEN IV PCB receivers were mechanically designed using Solidworks CAD, with a 3D rendering of the produced design shown in Figure 3-5. To manufacture the PCBs the circuit layouts were designed in Altium CAD, and CNC-milled from copper-coated 1mm FR4 fibreboard – both shown in Figure 3-5. The fibre board had a pre-deposited 350µm copper layer that was used for electrical connection. GEN IV included independent connections to the cell contacts and the thermoelectric module contacts, to facilitate independent component testing. A copper base was chosen as the overall device substrate due to the high thermal conductivity of this material (~385 W/mK at STC), alongside cost, availability and ease-of-machinability factors. A thermocouple hole was included within the copper base to allow for cold-side temperature measurement of the thermoelectric - an essential parameter for evaluating its performance.

After manufacturing the hybrid devices in the cleanroom, the electrical resistance of the connection to the CPV cell was measured using a multi-meter. No measureable electrical resistance was shown at the resolution of the meter, highlighting less than a 0.1 Ω resistance value (<1% of the cell series resistance). Under primary optics the current generated by the cell is expected to be around 1A, the number of wire bonds required were calculated. Additional wire bonds were added as a safety factor to pre-emptively further lower any series resistances under high current conditions. Twelve bonds were used as opposed to the industry standard of ten. The distance between the cell bus bars and the wire bonding track was minimized to reduce length-related wear stress and wire bond resistance. The cell was laid flat on the TEM top surface, with the cell bus bars orientated toward the PCB tracks. Copper core “alpha wire” was used, rated up to 300V, and soldered using industry standard lead/tin solder to further minimise electrical contact resistance. Particular care was taken to ensure that the high temperature required

for this was done in a separate step, prior to the active devices being added eliminating thermal extremity cycling and premature damage.

The cell internal resistance of the CPV cell was obtained from available datasheets and measured using the multimeter to be in the region of ~1Ω. The total cumulative contribution of the PCB contacts, wire bonds and epoxy on a finished device was once again of the order of 0.1 Ω, measured lower than the resolution of the multimeter. A visual review of a cell I-V trace was used to determine if there were any series resistance drops on the system, due to having a different shape and hence fill factor. The typical fill factor obtained through experimentation was ~85% at one-sun which was characteristic of provided datasheet values for the cells used (triple junction, III-V). Hence, the additional resistance of the PCB is negligible (<< 1% relative) with regards to electrical performance. The final Gen IV hybrid receiver design is shown in Figure 3-5.

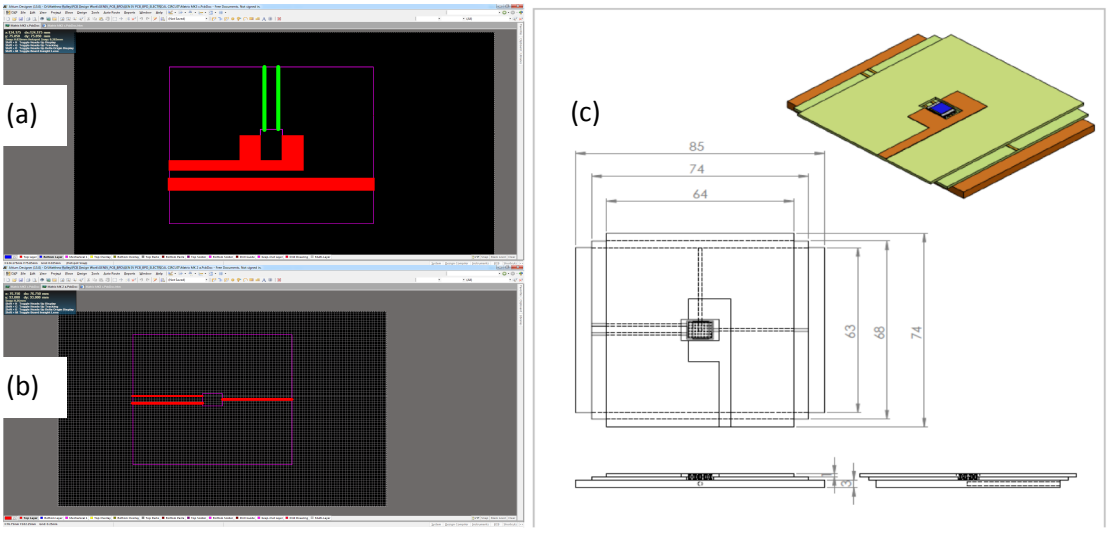

Figure 3-5. Electrical Altium PCB Layouts (a, b), and Solidworks CAD Drawing (c)

3.1.6 Transitioning from GEN IV to Gen V: Design Changes

There were four major design changes made moving from GEN IV to GEN V. A Bi-Pass Diode (BPD) was included to be closer to industry-analogous design, with the focus of progressing testing to in-string measurements of the devices. The overall area footprint (hence the material usage and cost during manufacture) was reduced to 23.31% ($A_{GEN\ IV} = 5.255x10^{-3}$ m^2, $A_{GEN\ V} = 1.225x10^{-3}$ m^2). A cell-

encapsulating SOE was added to investigate hybrid device characteristics under low concentration (<5 Suns). From the work on the Closed Loop Integrated Cooler (CLIC) (see Chapter 4) a temperature reference IC was built into the receiver design to match its vertical profile, and investigate the thermal contacting potential of its through-hole component packaging (A 1mm deep milled pocket into the surface of the copper substrate for the IC flat side to be bonded to improve IC case-to-Copper thermal contact). Likewise this pocket geometry was carried through to the bi-layer PCB layouts. Figure 3-6 gives a detailed overview of the GEN V receiver device, named "KAPPA".

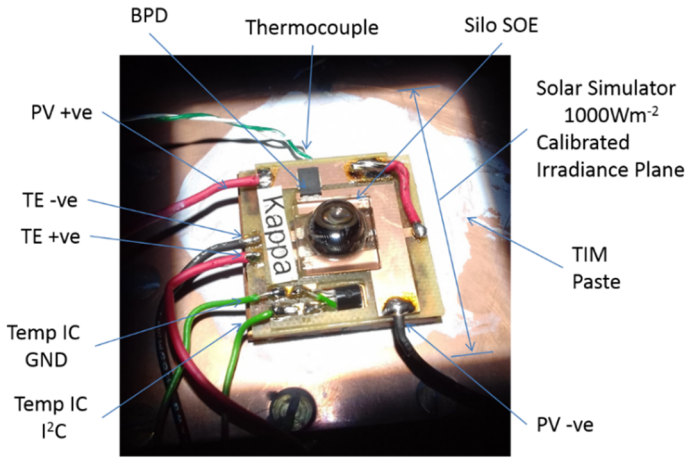

Figure 3-6.An Annotated Picture of Gen V Receiver "KAPPA" Under Test

The contacts for these additional device were also encapsulated with the Sylguard elastomer to pre-emptively reduce any humidity-related corrosion issues of the epoxy on these contacts. The Sylguard was also used as a weak adhesive (through a capillary vacuum created from the cure outgassing), to attach the SOE to the receiver and as an opto-coupling medium between the lens and the cell due to the two materials having comparable refractive indexes (Average $n_{Sylguard}$ = ~1.4, Average n_{SOE} =~1.45). This facilitated opto-coupling by minimising light refraction once received by the input aperture of the SOE-CPV-TE device. The full manufacturing procedure is shown in Figure 3-7. An additional "GEN VI" design was made to enable future research of CPV-TE devices with smaller area solar cells, however is included in Appendix A due to not being directly relevant to the following results sections.

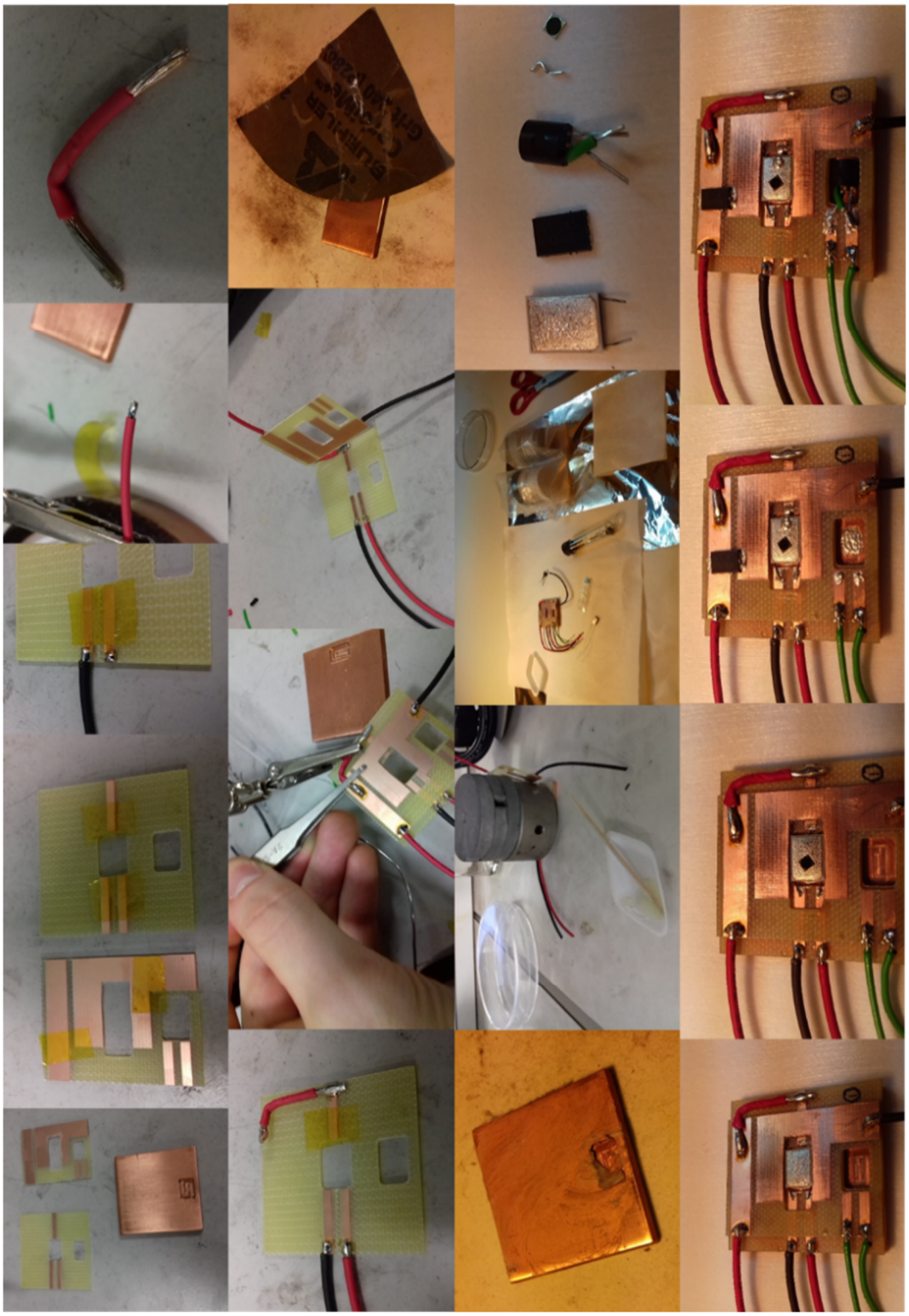

Figure 3-7. The manufacture of the GEN V and GEN VI Receivers

3.1.7 Full Summary of Receiver Generations I to VI

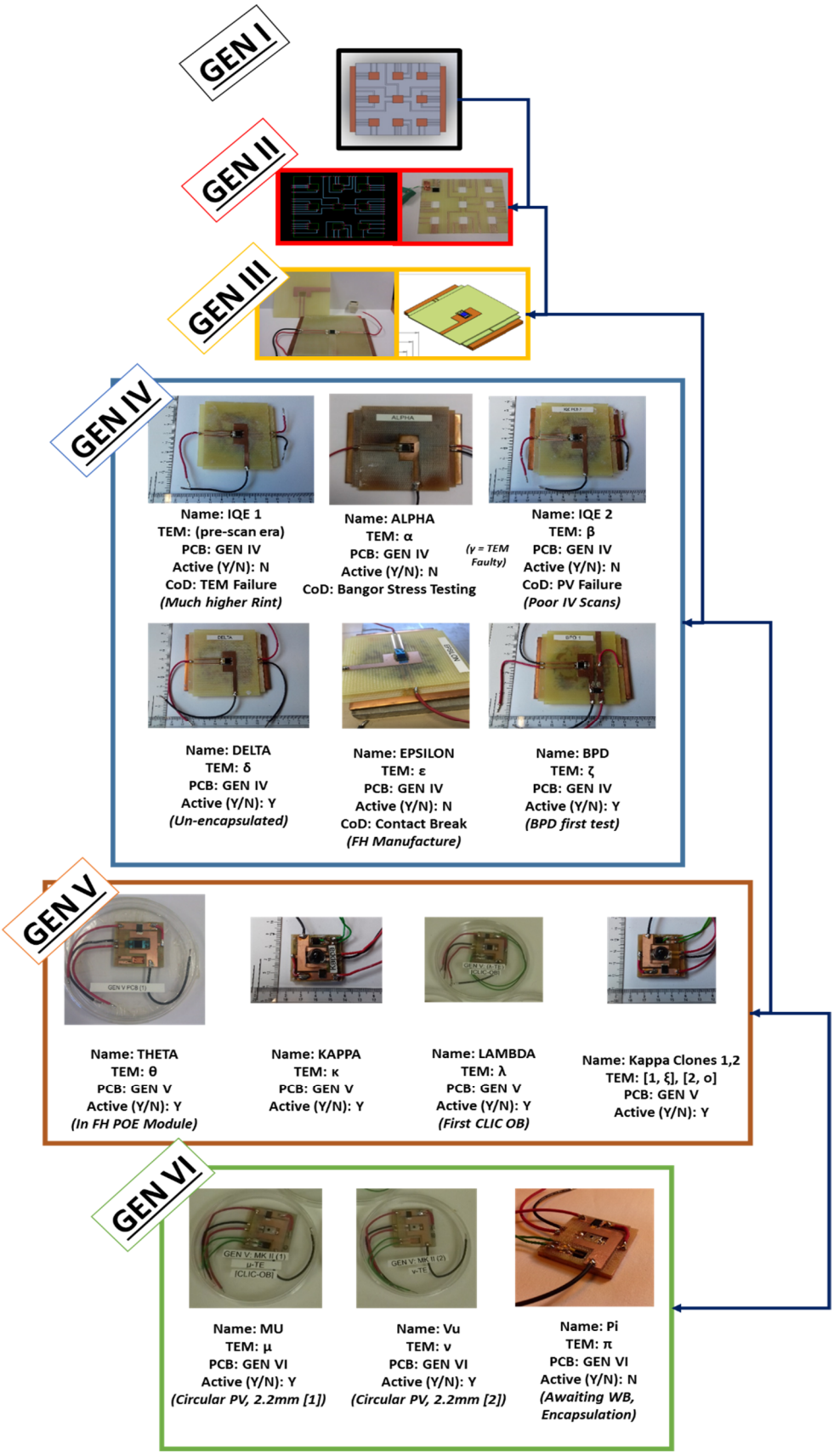

Figure 3-8. Overview of all Manufactured Receivers up to GEN VI

3.1.8 Design of Outdoor Testing Gyroscope

An experimental testing apparatus was designed for outdoor "on-sun" testing. A three-axis aluminium space frame "gyroscope" (affectionately named "the gyro") was designed around a central pivotal axis. Atmospheric metrology equipment was mounted to accurately and adequately characterise the solar resource. The Gyro was designed as a manual dual-axis tracker to replicate the system deployment conditions seen for typical CPV systems. Aluminium "space-frame" was chosen due to its corrosion resistance properties, ease of machining, and speed of assembly offered. Upon this axis a central U-section held the square mounting frame for a central instrument cluster. The instruments included a pyranometer mounting bracket, a clamp for the sample module, and a mount for a silicon reference cell. It was paramount that the three items on this central cluster had the same positional alignment.

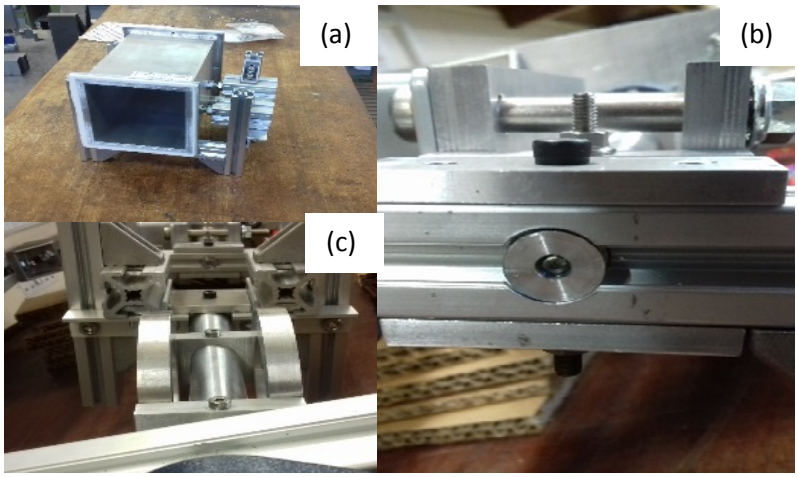

Figure 3-9. Pictures of the Central Sample Mounting Clamp (a) and Load Supporting Brackets (b, c) Included throughout the Gyro

A split-central axis design was used, with the central sample clamp locating the two halves with their respective metrology components, see Figure 3-9, (a) and Figure 3-10, (g). To mitigate rolling frictional resistance on the predominant moving axis, SKF flanged bearings were chosen for all the axles. To achieve the high rotational accuracy and minimal gear backlash necessary for testing, three bespoke gearboxes were designed and manufactured with a 1:45 degree gearing ratio. An appropriately designed milled aluminium handle with the appropriate mating negative pattern was made with Electrical discharger machined (EDM). The internal axles of the gearbox were chosen to be made from stainless steel to achieve the

required load torque strengths for operation, with tool-steel keyway inserts being added to the large gear internal diameters additional to the included grub screws, shown in Figure 3-10, (b, c). Other gears were held using tool-steel pins that were hammered into interference-fit holes through the axle (Figure 3-10, (a)). Case-hardened steel gears were used as to satisfy their load specification. Hollow grub-screw held aluminium spacers were included to all internal gearbox axles to prevent any lateral movement (and hence misalignment) through gyro operation. The total setup is shown during testing in Figure 3-11.

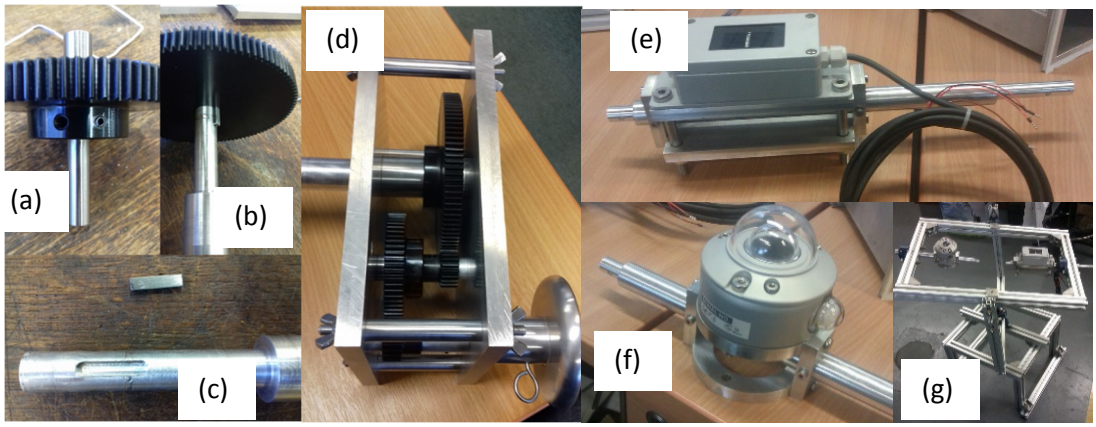

Figure 3-10. Pictures of the Gearbox Internal Re-enforcement (a-d), Silicon Reference (e) and Pyranometer Mounting Brackets (f), Alongside the Split Central Axle Design (g)

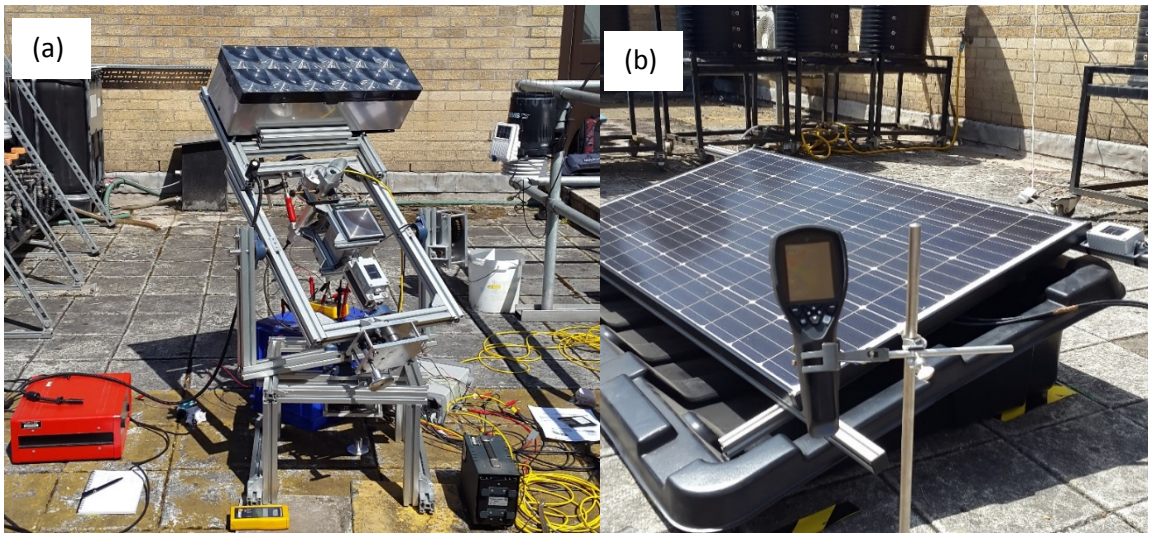

Figure 3-11.The total Outdoor Setup for both CPV (a) and Flat-plate (b) Technologies

3.2 Experimental Methods

3.2.1 Indoor Photovoltaic Cell Experimental Setup

To effectively evaluate the receiver electrical performance of the multi-junction cells, a LOT Oriel LCS-100 solar simulator with a Xenon lamp and an AM1.5G filter was used as the light source. This equipment, Class "ABB" rated for small area solar simulators. 'A' for its spectral content (within 75% – 125% absolute intensity value as compared to the spectrum at all wavelength intervals within the specified range), 'B' for its spatial uniformity (within 5% of max-min deviation percentage, "S_{NE}", as defined within the standard) and 'B' for its temporal stability (within 5% max-min deviation percentage over the time duration to take one data point, typically 1 second with quoted absolute deviation dataset for 1 minute and 1 hour) [4]. The lamp was switched on for 30 minutes before testing to heat up and establish its steady state operation conditions. Additionally, before testing each receiver, a Kipp and Zonen CMP11 pyranometer (Sensitivity of 9.01 $\mu V/Wm^{-2}$, 285nm to 2800nm detection range [5, 6]) was used to find a calibrated 1000 Wm^{-2} irradiance plane distance from the output aperture. This was done to counteract any long-term power level degradation effects of the bulb as shown in the simulator's operation datasheets [7, 8].

The height of the hybrid receiver sample under test was set using an adjustable laboratory jack. A water cooler was used with an appropriate thermal interface material underneath the receivers (RS "Heat sink compound plus", thermal conductivity = 2.9W/mK) to maintain a constant cold-side sample temperature. The receiver was held at STC under test through use of the hybrid integrated TEM (see Chapter 4, the CLIC technique). The cold side temperature of the samples were recorded using a K-type thermocouple and a FLUK 52II handheld thermometer. Additional temperature measurements of the cell top surface were taken using a FLiR i7 thermal imaging camera, held using a clamp-stand to keep positional-based errors consistent between tests. I-V curves were taken using an AUTOLAB Potentiostat system and the entirety of the experiment was conducted within a blackened box to eliminate any spurious ambient light incident on the device-under-test (DUT). An overview of the setup is given in Figure 3-12.

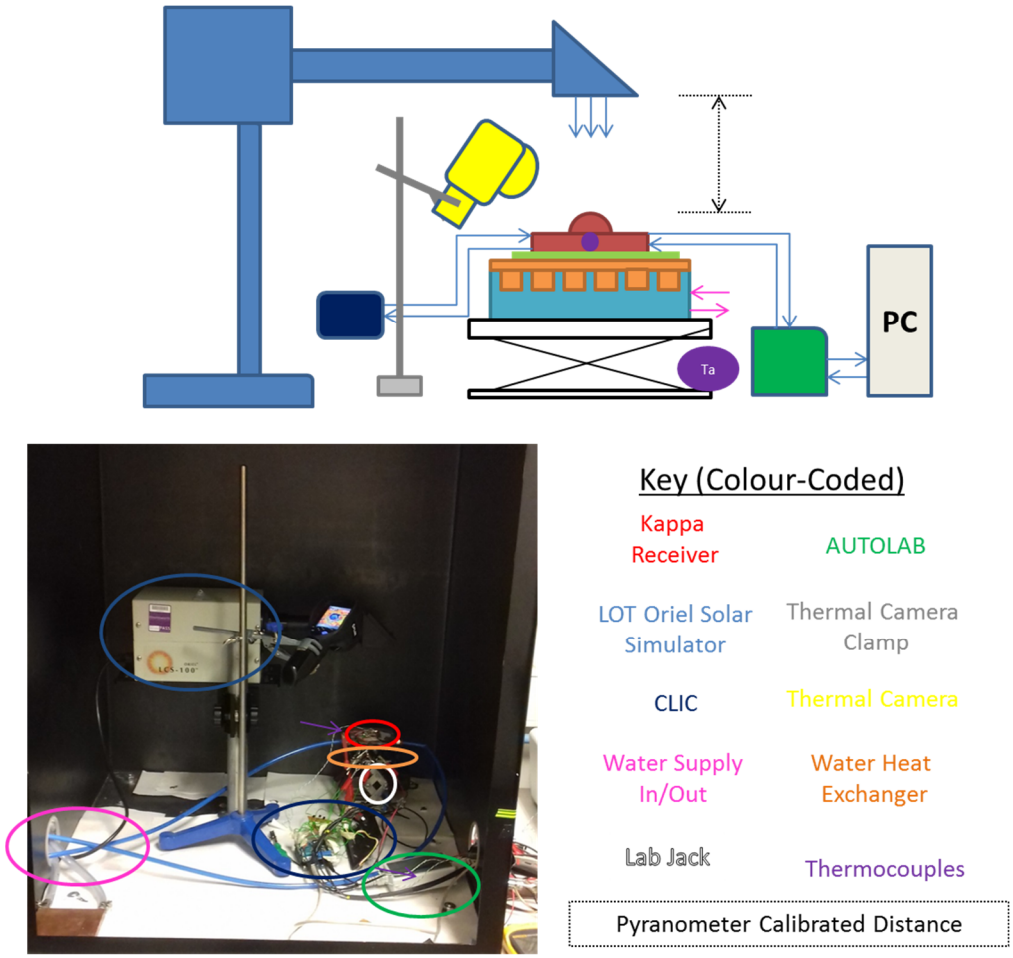

Figure 3-12. The Experimental Setup for Hybrid Receiver Testing [20]

3.2.2 Outdoor Testing Metrology and Experimental Setup

"On-sun" data exhibits many artefacts that are only simulated within tolerance limits in solar simulators, such as the Aerosol optical depth of a particular location (AOD). Additionally full day-production data can be obtained, with the incident spectrum received by the device being directly representative of nominal real-world operating conditions. Outdoor testing was done as a side-by-side direct comparison of commercial CPV module (consisting of 12 individual receivers in a series string) and flat-plate HIT silicon technologies as a benchmark dataset alongside hybrid module performance (see Figure 3-11).

The solar resource is intermittent and as such must be constantly monitored. To characterise the solar resource, two pyranometers (Kipp and Zonen CMP 11, sensitivities 9.01μv/Wm^{-2}, and 8.89 μv/Wm^{-2}) were used to measure the "In-Plane" irradiance received by the samples, and the "Global Horizontal

Irradiance" (GHI). The In-plane pyranometer (IPP) was mounted directly to the gyro and captured the tilted horizontal irradiance as seen by the sample at its tracked orientation. An in-plane Pyrheliometer (PH) (Hukseflux DR01, sensitivity 10.79 $\mu V/Wm^2$) was used to measure the Direct Normal Irradiance on the sample in the instrument cluster clamp, with the PH being clamped to the gyro. A silicon reference cell was included on the gyro powered by a 12V DC input, along with a hand-held silicon reference cell (Seaward Solar Survey) used in conjunction for its bearing and tilt angle measurements of the Gyro absolute position during tracking. A multimeter was used as the tracking feedback signal, through the detection of the peak V_{oc} of the CPV cell verses alignment for a manually iterated tracking position of the DUT. Two K-type thermocouples were attached to the base of the commercial CPV module at two equally spaced locations on the rear passively-cooled finned heat-sink. The CLIC technique (see Chapter 4) was used in conjunction with a dummy hybrid receiver analogue and Fresnel-lens assembly placed within the central sample holder to measure a representative POE-SOE-CPV-TE hybrid temperature. I-V curves were taken using a Keithley 2401 source meter at 30 minute intervals through the day. The environmental metrology was logged using a Keysight 34972A switch unit, with a 34901A 20 channel multiplexor. Figure 3-13 shows an overview of the metrology setup. The flat-plate HIT (Heterojunction with Intrinsic Thinlayer) Silicon module was measured using an EgniTec data logger, which tracked the panel's I_{sc}, V_{oc}, I_{mpp} V_{mpp} and P_{mpp} parameters every minute. The EgniTec unit, developed as a variable load for data logging and real-time monitoring of solar farms, was wired directly to the HiT panel. I-V curves were taken and these parameters extracted automatically and stored via an external computer, running a database software. A second silicon reference cell, inclined at the plane-of-array of the flat plate module was also logged. The temperature of the module was measured using the FLIR i7 thermal imaging camera.

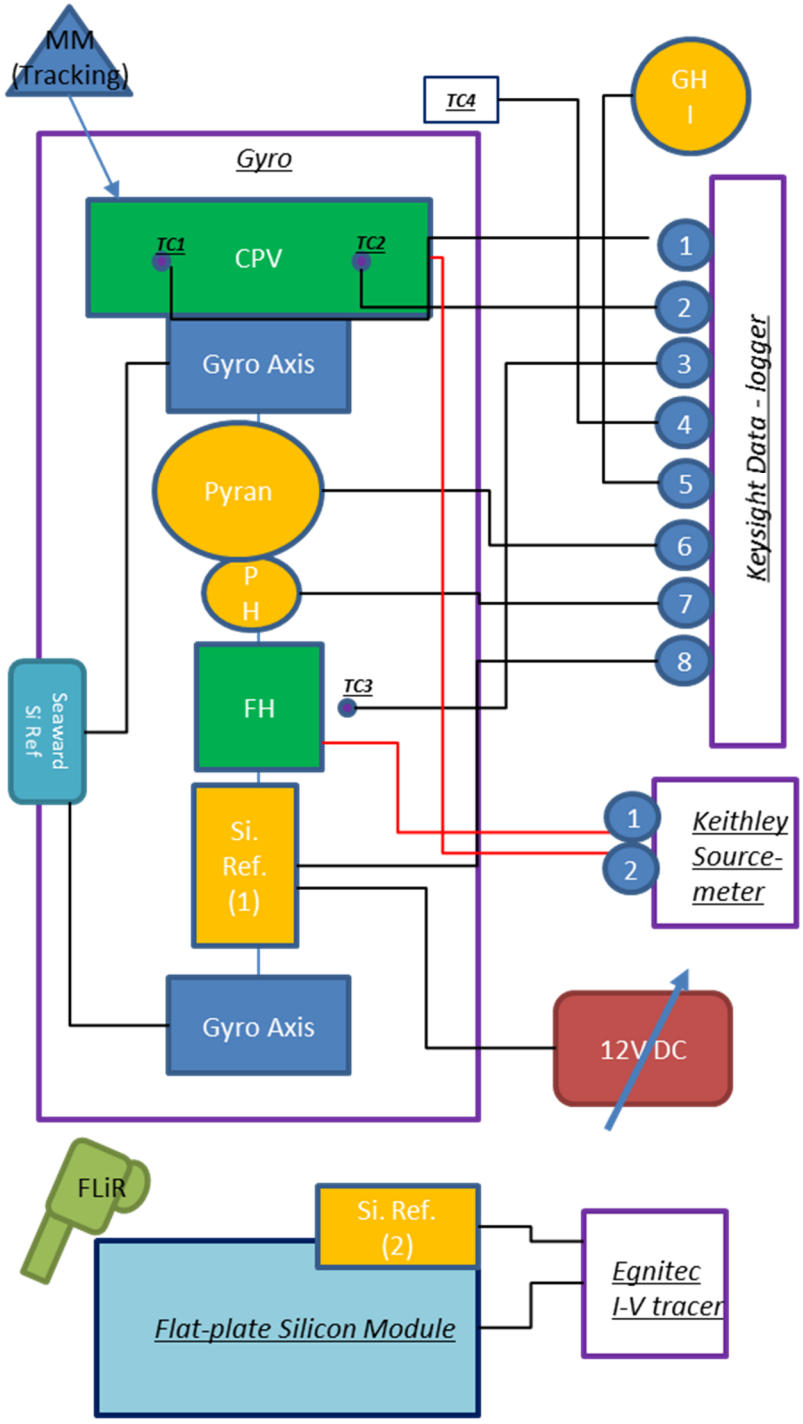

Figure 3-13. An Overview of Experimental Metrology Used During Outdoor On-Sun Testing at Cardiff

3.2.3 Pre-manufacture IV Scans

Throughout the manufacture of the GEN IV receivers, two devices exhibited premature failure after testing through TEM failure. To address this issue pre-manufacture I-V scan data was obtained for the TEMs to detect any poor quality devices prior to inclusion. This was done using the AUTOLAB potentiostat, and a "FAST I-V" scan (<100ms) using an automated procedure. Fast I-Vs were used to minimise any temperature rise that would normally occur from the applied currents, creating an effective constant temperature testing condition. A Pass/Fail criterion was set, through comparing the module internal resistance (R_{int}), calculated from the gradient of the fast-IV curve using Ohm's law. A "Pass" rating was given if internal resistance was no more than ± 5% of the previously approved batch average R_{int} and hence no major operational failure had occurred during the device manufacture through internal shorting or broken electrical contacts.

3.3 Experimental Results

3.3.1 Methodology Substantiation

3.3.1.a Solar Simulator Collimation Effects on Measured Irradiance

Characterisation tests were done on the solar simulator itself to quantify its performance was within its rated specification. Due to the equipment being out of date for calibration, concern was therefore expressed on the integrity of the result obtained through using the system. A full solar simulator characterisation was done to ensure that the equipment operated as defined within manufacturer guidelines and ensure integrity in subsequent work in this thesis. This was done using multiple pyranometers, firstly with readings taken from the "dome height" and repeated at the "detector height" for comparison. A silicon reference cell was used to compare the obtained absolute power value, and to improve confidence in the obtained results. Testing was done on two separate days to include systematic errors induced by the setup. The sensitivity values of the three pyranometers A, B and C were 5.12 $\mu V/wm^{-2}$, 8.89 $\mu V/wm^{-2}$ and 9.01 $\mu V/wm^{-2}$ respectively. It was found that the effective amount of concentration increased in an exponential trend with relation to decreased aperture-to-sensor distance. The voltage recorded from the pyranometer was divided by the stated calibrated voltage at 1-sun measurement for each of the pyranometers, thereby calculating a representative number of

effective suns. Figure 3-14 shows the resulting traces that were obtained during the two experiments, with the silicon reference cell data plotted for comparison. The multiple pyranometers used in each experiment showed good cross-calibrating agreement for each of the three devices [9, 10]. The results here suggest that the appropriate measurement plane to be taken as 1000Wm^{-2}, correlates to the apex height of the pyranometer dome.

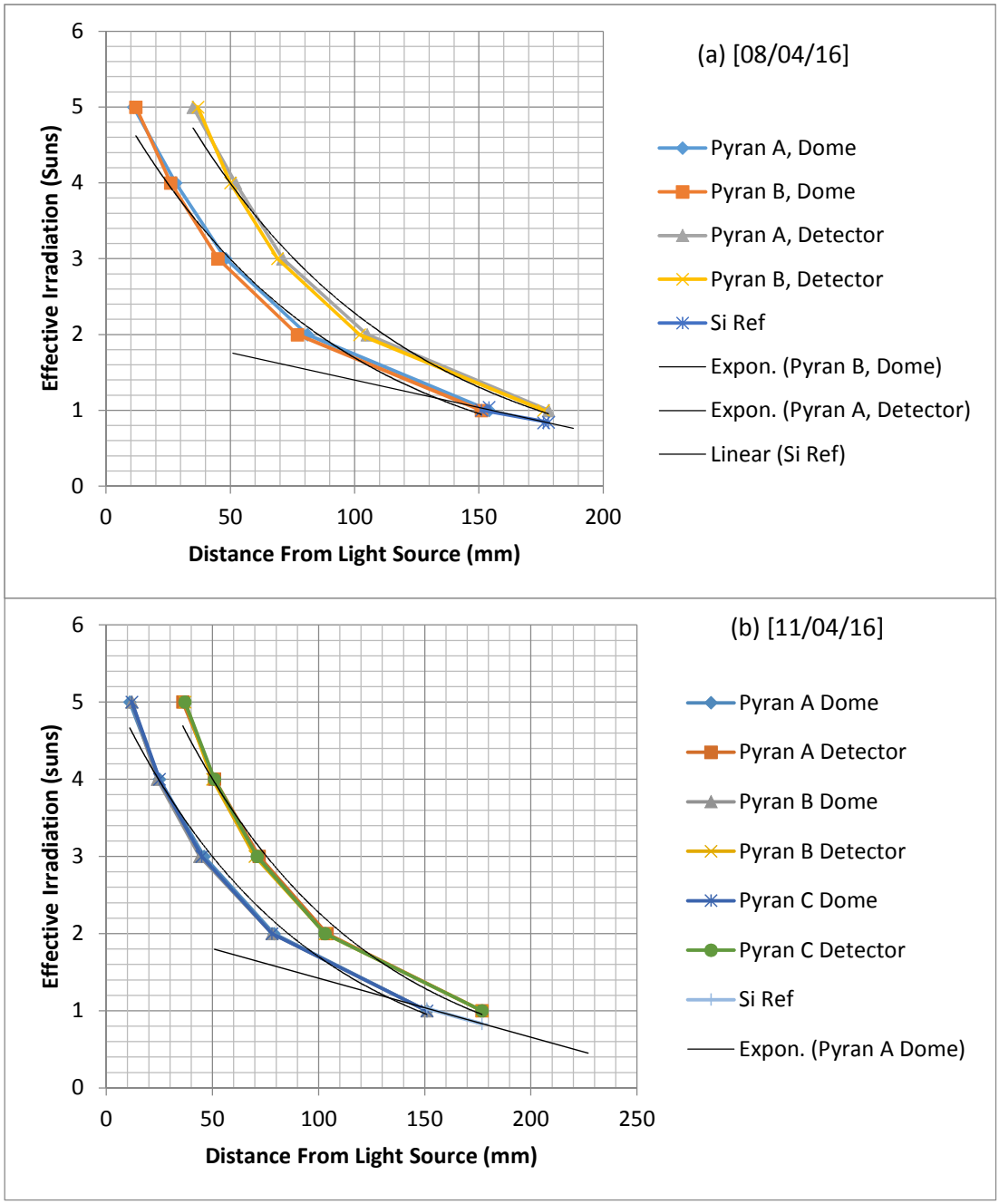

Figure 3-14. Displacement verse Pyranometer-Measured Irradiance Effects within the Solar Simulator on two days (a, b)

3.3.1.b Solar Simulator Spatial Distribution Evaluation

To evaluate the irradiance uniformity of the simulator, spatial distribution measurements were done. The light plane vertical distance was calibrated with the Seaward Solar Survey reference cell reading 1000Wm^{-2} in the centre of the visible light plane, in addition to cross-referencing this to the pyranometer measurement. This light square was then divided up into an indexed grid, with spaces the size of a Seaward "solar survey" silicon reference cell. The grid's dimensions was split into three silicon reference cells across, and six down. Care was taken to always have the full area of the silicon reference cell within the light square. Figure 3-15 shows a surface plot of the relative irradiation intensity deviation values from the 1000Wm^{-2} standard.

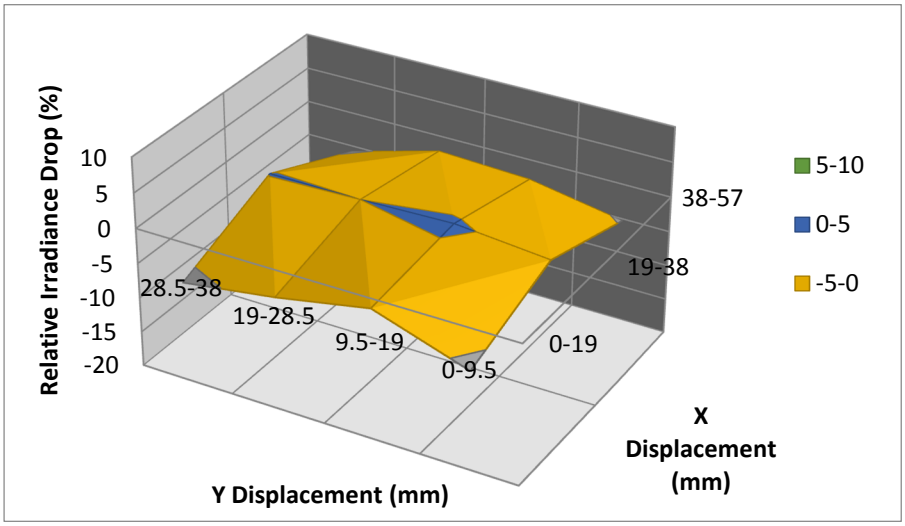

Figure 3-15. Experimentally Measured Spatial Uniformity of the Solar Simulator

The results were then plotted as a percentage deviation from the 1000Wm^{-2} rated value. The solar simulator irradiances within the datasheet specified tolerances (within the rated active area of 40mmx40mm for the simulator) with an applicable grid size of 57mmx38mm in the tests. The specification-based dimension wasn't chosen as the experimental grid size for two reasons. Firstly the solar simulator showed a bigger light-square in practice which limited the measurement of the centre 40mmx40mm square during testing, and secondly due to the rectangular geometry of the silicon cell limited testing. As can be seen from the data in Figure 3-15, the solar simulator performed within its rated B classification of <±5% deviation across the stated active area.

3.3.1.c Simulator Spectra and Cumulative Power

To determine the output spectrum of the solar simulator was recorded using a Macam SR9910-V7 Spectroradiometer (SR) for comparison with reference spectra. The Spectroradiometer itself used a known intensity light source (KILS) before and after testing using a separate to quantify the detector's temporal variation throughout each scan, increasing confidence in the data obtained. The two obtained curves for the (KILS) pre and post experiment showed good agreement and a negligible drift in relative calibration throughout the duration of the testing. The SR was placed under the solar simulator in the centre of the light plane, at a pre-adjusted pyranometer calibrated 1000Wm^{-2} plane height. Full spectral scans were taken (0.5nm step resolution, 240-800nm range). The irradiance power was then calculated using a compound integral described in Equation 3-1.

$$Total\ Irradiance\ of\ Simulator = \int I_{sim}(\lambda)d\lambda \quad -(Equation\ 3\text{-}1)$$

This integral was calculated and plotted alongside the spectral data on a secondary axis (shown in Figure 3-16), to show the cumulative power distribution of the simulator.

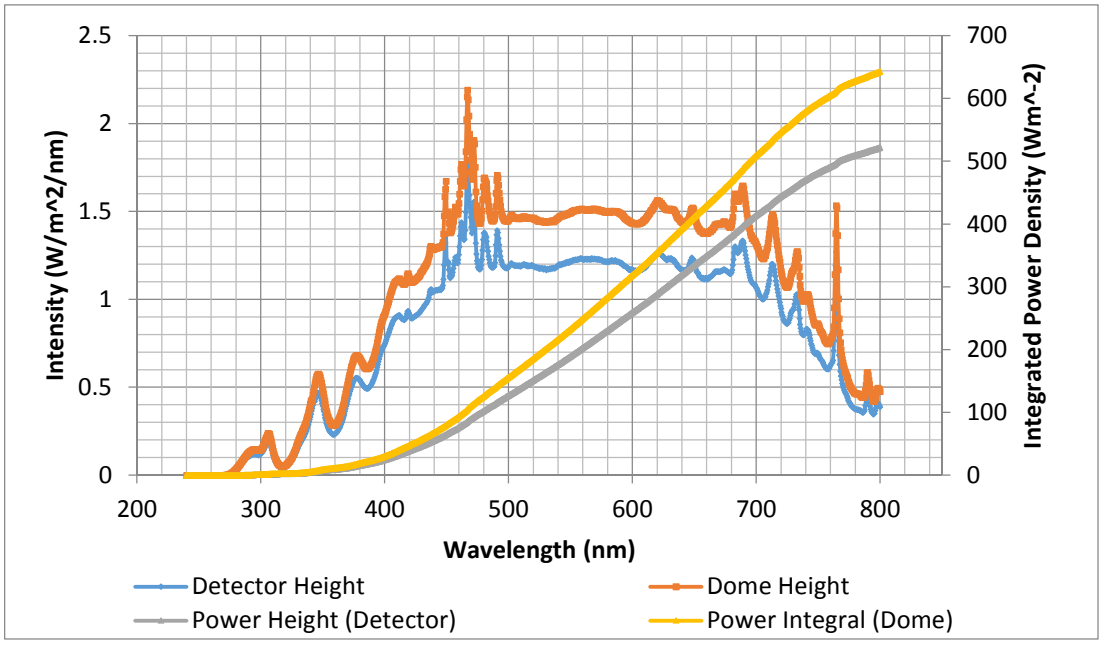

Figure 3-16. Spectral Output of the LOT Solar Simulator

The irradiance power integrals gave cumulative power values of 643.22 Wm^{-2} at the dome height, and 522.0 Wm^{-2} at the detector height. The SR used,

didn't encompass the entire rated spectral range of the simulator, and as such was only be used for an indicative evaluation for the integrated power density. The cumulative power density of the entire spectrum (250-1100nm) is shown to be 797.5Wm^{-2} - as defined by the simulator manual and the IEC 60904-3 (also known as the BS EN 60904-3:2016) [11, 12]. The simulator's contribution to the cumulative irradiance power as a percentage from 240-800nm (limits of the SR measurement range), is 83.41% of the full standard spectrum. Using these two values; a manufacturer-stated estimate of the integrated power to be expected to be output by the simulator for this frequency range is 665.19Wm^{-2}. The obtained value from the experiment shown above was 643.22 Wm^{-2}, showing that the solar simulator was operating within 3.3% of the standard for cumulative power output over the measured frequency range and validating the dome height of the pyranometer as being the 1000Wm^{-2} plane.

3.3.1.d Receiver Repeatability

A series of identical experiments were run on three separate days to evaluate the experimental repeatability error. These tests were done using the same GEN IV receiver, "ALPHA". The tests were done under 1000 Wm^{-2} conditions, with the same experimental setup and methodology as described in Section 3.2.1. Shown in Table 3-1, over the three experiments the V_{oc} was found to be identical within measurement resolution on all three tests.

Table 3-1. Experimental Repeatability Data Obtained on 3 Separate Experimental Setups on 3 Different Days

Test Number	1	2	% change 2 to 1	3	% change 3 to 1
Isc (mA)	4.122	4.167	1.10	4.100	-0.52
Voc (V)	2.257	2.257	0.00	2.257	0.00

The V_{oc} of a triple junction cell is inherently sensitive to spectral variation due to internal optimised sub cell bandgaps for current matching. Additionally the V_{oc} is sensitive to temperature changes due to changes in the bandgaps within the materials. The change measured (0.00%) showed a negligible deviation of spectral

output and highlighted accurate temperature control from the setup over these three days. There was a high sensitivity of simulator output-aperture-to-cell distance on the irradiance incident upon the cell, as demonstrated in Section 3.3.1.a. From this repeatability study, these effects were quantified by the change in the I_{sc} as this parameter is the most sensitive, and scales linearly to changes in irradiance. This total systematic experimental variation for the I_{sc} was found to be within 1.1% for all three tests.

To evaluate the error contribution and measurement resolutions of the specific individual experimental equipment, an in-depth review of the manufacturer datasheets and specifications was done. The data was collated and is summarised in Table 3-2 below for future context and reference throughout the rest of the work in this thesis.

Table 3-2. Measurement Uncertainties for the Experimental Apparatus Used [13]

Equipment	Interval (resolution)	Interval +-	Range of reading	Uncertanty	Other
AUTOLAB	I: 6E-6 A	3E-7A	+- 2A	Accuracy: +-0.2%	
	V:0.3E-6 V	0.15E-6V	+- 10		
Pyranometer (Kipp & Zohon CMP11)	A: 5.12 uV/W/m^-2	2.56 uV/W/m^-2	285-2800 nm	Temperature Change: <1%	Range: -40 -> 80 DegC
	B: 8.89 uV/W/m^-2			Time Change: <5s	4000 W/m^-2 max
	C: 9.01 uV/W/m^-2				
Spectral Radiometer	1nm	0.5m	24-800	+- 2DegC Stability	-10-40DegC Operating Range
Silicon Refernce Cell (Seaward Solar Survey 100)	1 W/m^-2	0.5 W/m^-2	100-1250 w/m^-2		1Deg +- 0.5 Deg (res angles)
FLIR i7	0.1DegC	0.05DegC	-20-250 DegC		9Hz, 75 - 13 um detection
IR Themometer (Maplin TN439L0)	3DegC	1.5Degc	-25 - 265 DegC	Area :	0.08m^2 @ 0.6m
				Distance Explansion:	0.13m^2 @ 1m
Thermocouples (Type K, PTFE, 1m,	3DegC	1.5Degc	-75 - 250DegC		
Thermocouple reader (Fluke 52	0.1DegC	0.05DegC	0-9999 DegC		Resolution depends on thermocouple
Multimeter (Chauvin Arnoux	V: 0.01 mV	0.005mV	0-1000V		
	Ohms: 0.1	0.05Ohm	0-60MOhm		

3.3.1.e CREST Experimental Methodology Accuracy and "Round Robin"

A Gen IV receiver (ALPHA) was built and tested extensively at Cardiff for characterisation I-V data. The same receiver then tested at Loughborough's Centre of Renewable Energy System Technology (CREST) for independent evaluation of the cell within the hybrid device. CREST is a United Kingdom Accreditation Service (UKAS) certified test centre, and uses a Wacom dual-source AAA solar simulator with adjustable spectral matching for independent testing of solar devices. The experiments are done within a secure, temperature controlled laboratory, as is required of the UKAS accreditation. A CPV-TE hybrid receiver (ALPHA) was sent to this centre, to further evaluate and substantiate the experimental testing methodology, procedure and apparatus used at Cardiff University. One-sun tests were done at controlled STC conditions. The device was then re-tested at Cardiff to evaluate any changes. The cell V_{oc} data at Cardiff and Loughborough's CREST were identical to six decimal places. This confirms the frequency match and temperature stability of the test conditions at Cardiff. The I_{sc} data compared agreed to within 1.7%. The absolute deviation between the two I_{sc}, was found to be 0.0747mA, with the quoted absolute error on the CREST measurement to be ±0.084 mA. Therefore the error between the absolute measurements achieved at Cardiff and CREST were

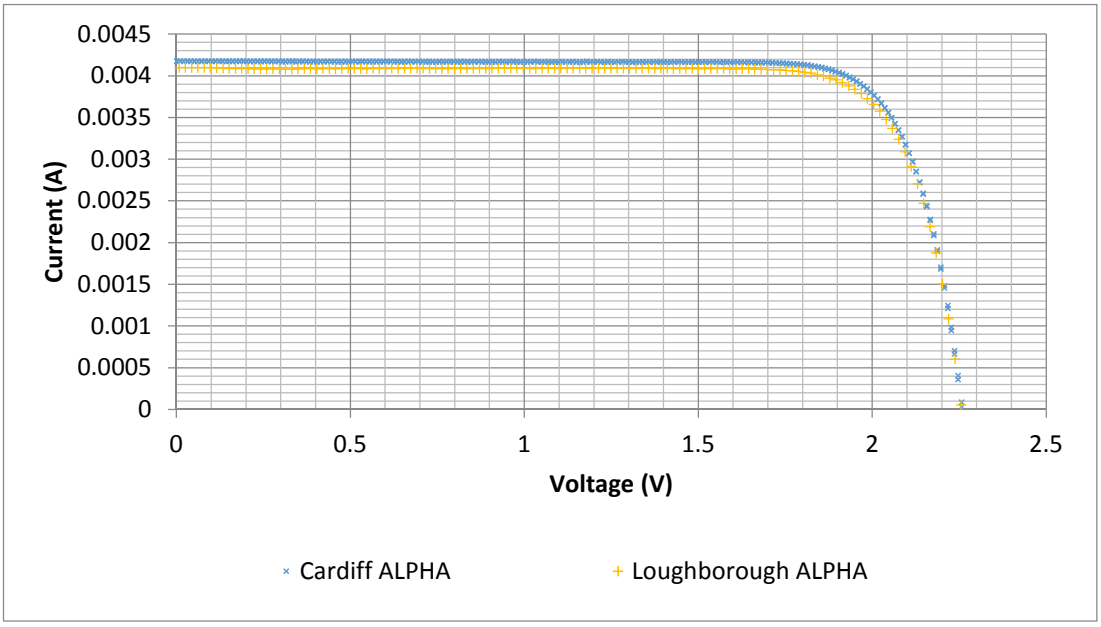

Figure 3-17. I-V Cross-correlation of ALPHA at Cardiff and CREST

within the quoted accuracy of the received CREST dataset. The two I-V curves obtained from Cardiff and CREST are shown in Figure 3-17 [14].

3.3.2 Receiver Design Substantiation

3.3.2.a CPV Cell Encapsulation testing and Cleanroom Manufacture

To prevent any of the inherent dust and particulates that are found within air from falling on the active device areas, the CPV cell wafer was kept within a cleanroom. The CPV cell unpacking, bonding process and encapsulation was also done inside the cleanroom to stop the particles from accruing on the CPV cell surface during manufacture of the hybrid device. This would otherwise block a percentage of light over time, and reduce cell performance. The encapsulant used in this work was Sylguard 184 silicone-based two part curing elastomer [3]. To characterise the performance drop associated with the loss in optical transmission through this encapsulant, I-V scans were obtained from two different Silicon cell areas, with two samples ((1) and (2)) using the setup as described in Section 3.2.1. The spectral response change of the silicon cells was negligible, as the Sylguard exhibited a negligible deviation of refractive index (<0.25%) over the entire functional frequency range of the simulator. The total transmission-induced loss on the conversion efficiency for the silicon cells was a consistent -0.3% absolute for both cell sizes (see Table 3-3).

Table 3-3. Critical Cell I-V Parameters Pre and Post Sylguard Encapsulation

	Cell Size	Isc (mA)	Voc (V)	Impp (mA)	Vmpp (V)	Pmpp (W)	FF (%)	Efficiency (%)	Δefficiency (Pre-post) (%)	Average Efficiency Drop (Abs) (%)
(1cmx1cm)	(1) Pre-Sylguard	0.042	0.575	0.039	0.484	0.02	76.99	18.74		
	(1)Post-Sylguard	0.042	0.575	0.037	0.495	0.02	76.68	18.31	0.42	
	(2)Pre-Sylguard	0.042	0.565	0.039	0.474	0.02	77.65	18.57		
	(2) Post-Sylguard	0.042	0.565	0.038	0.484	0.02	78.34	18.38	0.20	0.31
(5cmx5cm)	(1) Pre-Sylguard	0.873	0.555	0.815	0.454	0.37	76.42	14.82		
	(1)Post-Sylguard	0.868	0.545	0.799	0.454	0.36	76.80	14.52	0.29	
	(2)Pre-Sylguard	0.874	0.555	0.813	0.454	0.37	76.11	14.77		
	(2) Post-Sylguard	0.868	0.545	0.812	0.444	0.36	76.24	14.42	0.34	0.32

It was also shown that through manufacturing the devices in the cleanroom verse a general lab environment increased hybrid receiver efficiency through

Table 3-4. Pre-and Post-Cleanroom Manufacture Device Comparison

	Vmpp (V)	Impp (A)	Isc (A)	Voc (V)	Pmpp (W)	Efficiency (%)
IQE2	1.884	3.700	-0.004	2.217	0.01	23.04
Alpha	1.924	3.980	-0.004	2.277	0.01	25.31
Change (Abs)	0.040	0.280	0.000	-0.060	0.00	N/A
Change (%)	2.079	7.035	2.307	2.726	8.97	2.27

mitigating dust-related transmission losses. Shown in Table 3-4 are the comparative cell performance parameters, extracted from I-V scans for the first built receiver "IQE2" compared with "ALPHA" which was made exclusively in the cleanroom. Both devices had the Sylguard encapsulant applied.

3.3.2.b TEM Encapsulation

To further improve long-term stability and reliability of the PCB device, encapsulation was used to protect the individual components. The modules used for all GEN IV hybrid receivers was a Marlow CM23-1.9 TEM, with the device properties summarised in Table 3-5 [15, 16].

Table 3-5. The Properties of the used Marlow TEM

Parameter	**TE module**
Number of legs	46
Leg geometry (mm)	0.6 x 0.6
Leg length (mm)	1.20
Module length x width (mm)	8.3 x 6.0
Fill Factor (%)	33.25
Total metallisation thickness (mm)	0.3
R_{int} (Ω)	1.23

The thermoelectric modules were evaluated as both un-encapsulated and encapsulated variants. Fast I-V traces facilitate constant ΔT testing conditions across the module, due to minimising transient thermal effects such as Joule heating to occur throughout the trace. “Slow” I-V traces were additionally needed to fully characterise the modules. Slow I-V traces allow steady-state conditions to be reached with different applied ΔTs. This allows all the transient effects to fully establish themselves before the I-V trace is done to describe the steady-state operating conditions of the module. Figure 3-18 shows the P-V and I-V graphs obtained for both encapsulated and un-encapsulated thermoelectric modules. The encapsulation process showed negligible effect to the electrical characteristics of the thermoelectric modules. Therefore future hybrid designs exclusively used

encapsulated modules onwards to improve device resistance to environmental based degradation modes, such as moisture ingress or particulate shorting.

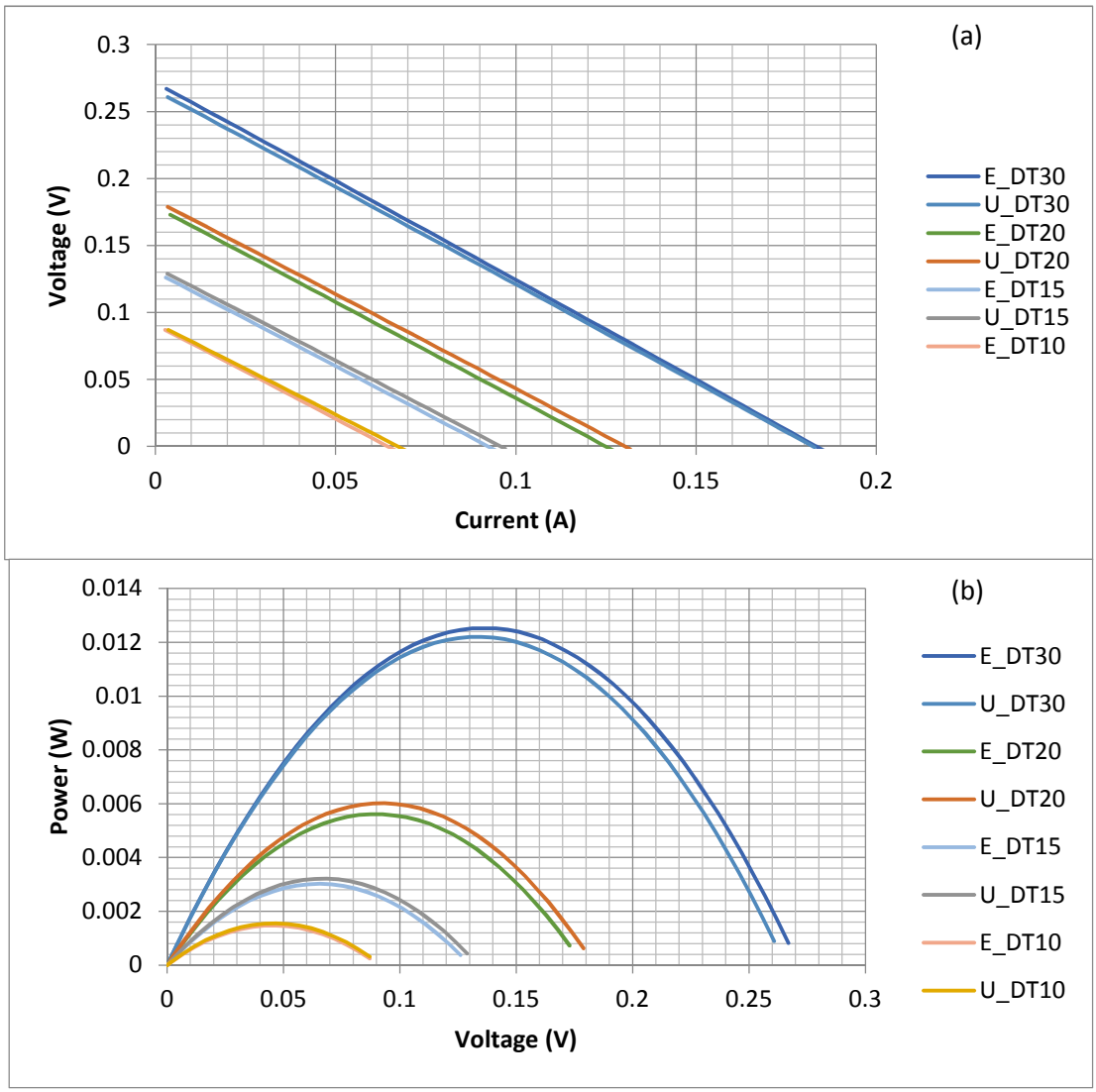

Figure 3-18. Encapsulated and Un-encapsulated TEM I-V (a) and P-V (b) Characteristics [Note: In the legend, E_ = Encapsulated, U_ = Un-encapsulated and DTxx = a delta T temperature gradient across the TEM in xx kelvin]

3.3.2.c Pre-manufacture TEM scans

The internal resistance is directly related to the quality of the internal electronic contacts made within TEM manufacture. A "fast I-V scan" allows a preliminary evaluation of the TEM's internal resistance parameter to be obtained. Poorly manufactured modules exhibiting a high internal resistance can subsequently be eliminated (see Section 3.2.3). Catastrophic failure modes could also be detected with this method, as is shown in Figure 3-19 through obtaining non-linear traces. Shown in the graphs are the fast I-V curves of the TEM within two such hybrid devices which had a premature failure from manufacturer, and failure during use, post manufacture. The failure mode for the first receiver (Figure 3-19 (a)) could be from an internal short within the module, as reverse currents were measured at very small applied excitation voltages, and hence implied a very small resistance in the current path - atypical for thermoelectric material. Likewise, for the second receiver (Figure 3-19(b)), high through excitation voltages were achieved with very low currents indicated that a broken or poor contact had occurred within the device - giving an uncharacteristically high resistance for a TEM. The duration for the I-V scans during testing was calculated to be approximately <100 ms from the internal software procedure and the quoted speed of the operation for the AUTOLAB device.

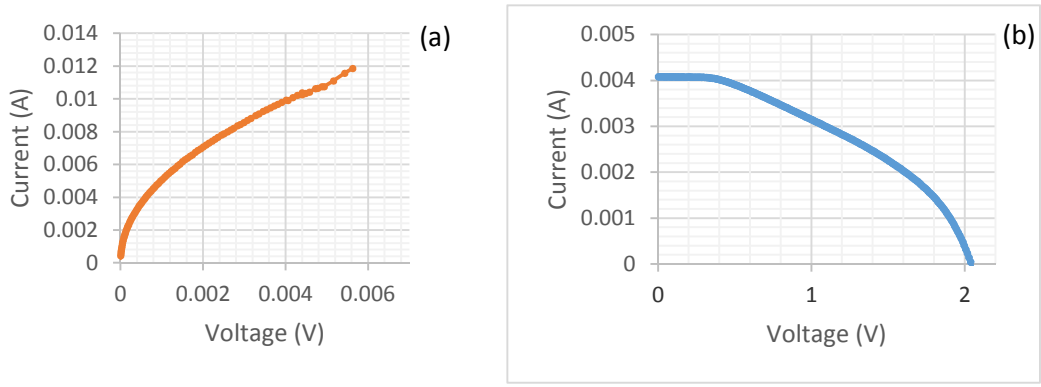

Figure 3-19. Catastrophic Failure TEM I-V Curves from Two Different Hybrid Receivers: IQE2 (a) and ALPHA (b)

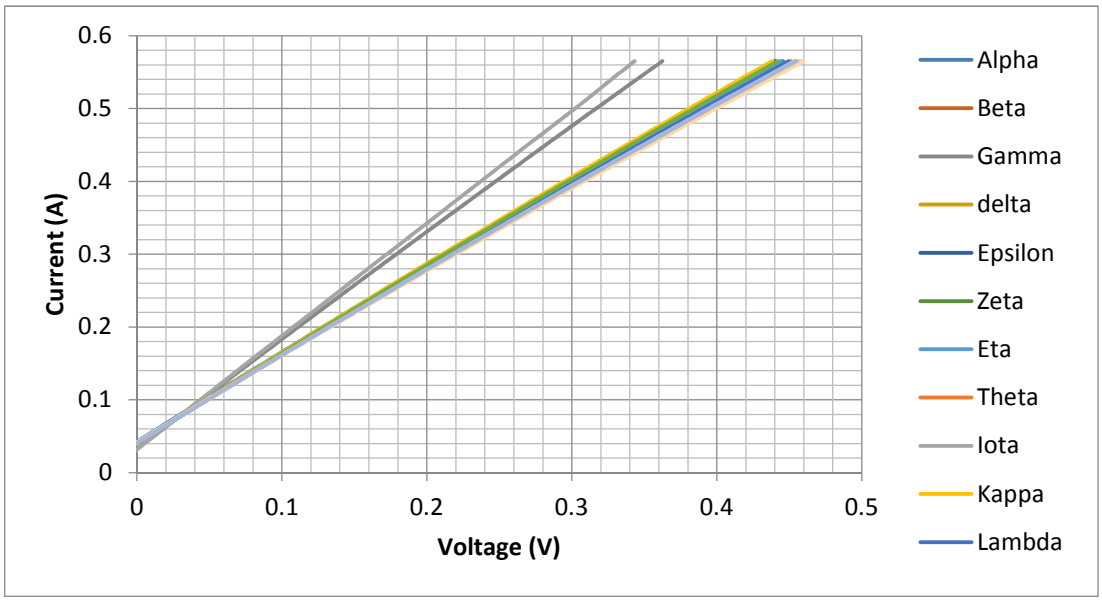

Figure 3-20. Fast IV Traces of TEMs Pre-manufacture into Hybrid Receivers

The effectiveness of this technique can be seen from the cumulative fast I-V datasets obtained throughout the manufacture of all receiver up to GEN VI. Figure 3-20 shows this data, with both the Gamma and Iota TEM exhibited much higher internal resistances (R_{int}) than the other TEMS (+25.435% and +32.035% respectively from batch average). Therefore these TEMs were omitted from further use in device manufacture, preventing the building of a defect hybrid device.

3.3.3 GEN IV Data (CPV-TE Hybrid Receiver)

3.3.3.a Temperature Control Proof

One major advantage of having a directly bonded CPV-TE hybrid architecture device, is the sensitive temperature control functionality of the TEM. The small thermal mass of the cell, combined with the well-established solid-state performance of thermoelectric devices allows for accurate and highly controllable cooling to be achieved quickly. To evaluate cooling effectiveness, experiments were done with GEN IV hybrids to measure the input current (and hence power consumption) of the TEM device to achieve different cell temperatures. The temperature was measured with a FLiR thermal imaging camera. A thermal emissivity value of 0.6 was selected, equating to the “semi-glossy” nature of the Sylguard encapsulant. The hybrid receiver used with the experimental procedure and setup described in Section 3.2.1, and the temperature controlled using the TEM under 1-sun conditions. I-V scans were then taken and plotted for comparison

(Figure 3-21) [15]. The temperature co-efficient property of the triple-junction cell was evaluated for the V_{oc}, the I_{sc} and the total conversion efficiency. Table 3-6 shows the obtained data. The V_{oc} temperature co-efficients obtained through this work were compared with and found consistent with previously published literature values at low concentration values [17-19] (see Table 3-7). The difference between the published results and the data obtained in this work could be due to subsequent advancement in multi-junction cell composition and strain relaxing techniques since publication. The relative change in temperature co-efficients due to increasing concentration were found to be consistent with prior art.

Table 3-6. A Summary of the Critical Solar Cell Performance Parameters

Run	Temp	Isc (A)	Voc (V)	FF (%)	MPP (W)	Efficiency (%)	Δη (%)
1	68.000	0.013	2.186	77.46	0.02	21.96	0.00
2	52.400	0.013	2.237	77.73	0.02	22.29	0.32
3	41.400	0.013	2.287	78.34	0.02	22.77	0.80
4	33.000	0.013	2.327	78.45	0.02	23.11	1.15
5	9.900	0.012	2.378	78.91	0.02	23.48	1.52
6	1.600	0.012	2.489	80.20	0.02	24.34	2.37

Table 3-7. Cross-comparison of Obtained Voc Temperature Co-efficients with Previously Published Values (POE Concentration values shown for comparison were calculated from later experimental data– see Section 4.3.5.c)

Reference	Voc Temperature Co-efficient @1 sun (mV/K)	Voc Temperature Co-efficient @ ~250 sun (mV/K)	Relative Change Due to POE Concentration (%)
Sweet, T., Rolley, M. et al. (2016)	-4.550	-2.549	43.978
Seifer, G et al. (2012)	-6.790	-3.560	47.570
Cotal H., Sherif, R. (2006)	-7.500	-4.600	38.667

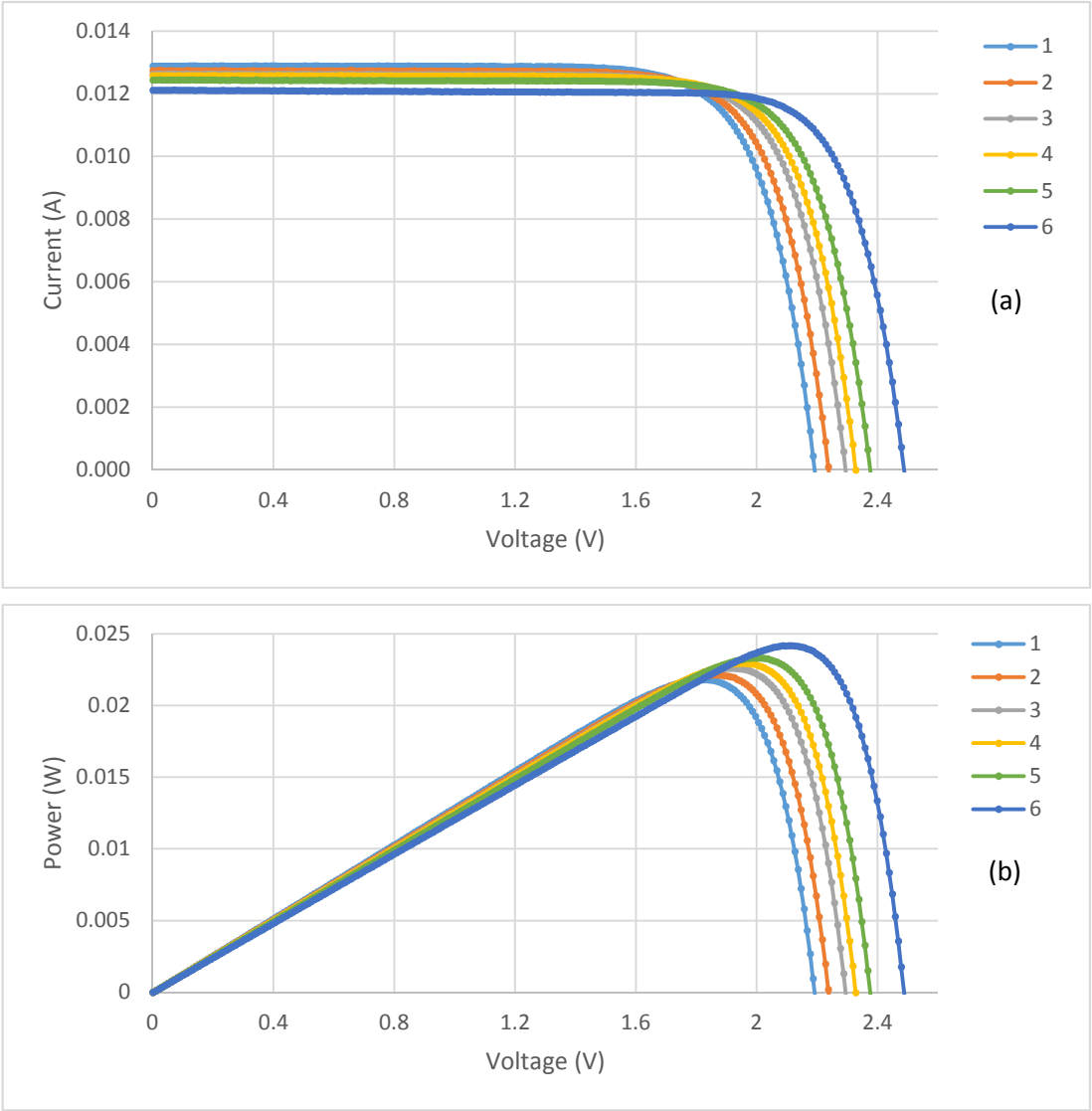

Figure 3-21. Solar Cell I-V (a) and P-V (b) Graphs Obtained for ALPHA at Multiple TEM-Controlled Temperatures, Constant AM1.5G Irradiance

A range of different irradiance conditions were applied using different aperture-cell distances as described in Section 3.3.1.a. The TEM temperature was stabilised and I-V and P-V data were obtained at each point for 0°C, 25°C (STC), and 50°C (realistic CPV cell operating temperatures) and is shown in Figure 3-23. The maximum power point at all three temperatures and irradiance values were plotted and trend lines fitted to the data. For all three temperatures, positive linear correlations were found for MPPT vs Irradiance, (see Figure 3-22) with high R^2 values for all irradiance conditions (>0.99). The temperature co-efficients as

measured were -4.551 mV/°C for the V_{oc}, and +0.001mA/°C for the Isc. The linearity of P_{mpp} as shown in Figure 3-22 indicates that highly sensitive and consistent changes in the temperature conditions were achieved. As expected, slight increases in irradiance values caused increases in the absolute P_{mpp} recorded.

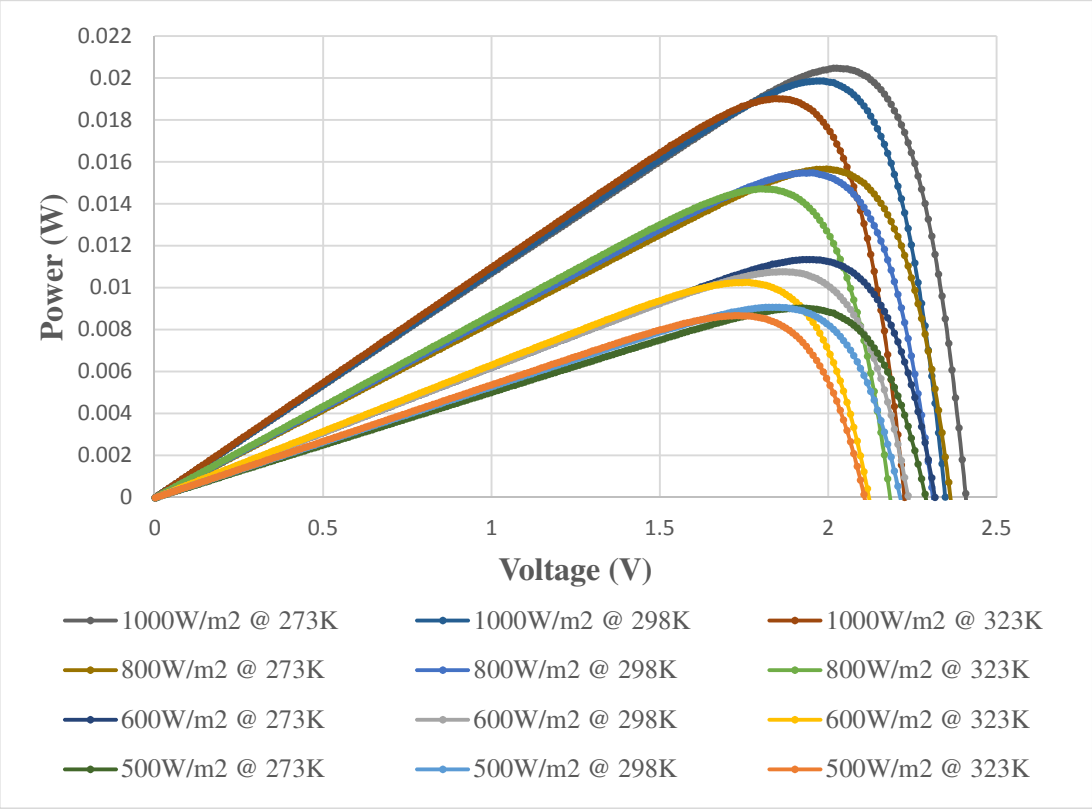

Figure 3-23. Performance of the Triple Junction Cell at Various Irradiances and TEM-Temperature Controlled Conditions

Figure 3-22. Linear MPP vs Irradiance Trend for Each Temperature Condition

A relative irradiance-induced P_{mpp} change (ΔP_{mpp}) was calculated and compared to the relative change in irradiance (ΔG) for each temperature condition (shown in Table 3-8). The average error between ΔP_{mpp}, and ΔG was found to be <5% for each temperature (-3.75 % error at 0°C, -3.03% error at 25°C, and -3.26% error at 50°C). This was within the rated incident output power of the solar simulator. This trend implies that the temperatures achieved through TEM control were accurate enough not to influence the recorded dataset outside of the pre-defined experimental apparatus specification and confirms the sensitivity of measurement alongside the thermal camera datum. The "ΔG - ΔP_{mpp}" error showed an increasing trend with irradiance further implying that it was more likely to be caused due to an inaccurate incident irradiance rather than temperature control inaccuracy. Additionally, the error across the three temperatures was comparable for a given irradiance condition. These preliminary conclusions further indicate the sensitive functionality of the TEM for temperature control, giving feasible reaction to changes in incident conditions of the same order which would happen in real-world deployment. Later chapters will focus on more accurately quantifying the TEM temperature control accuracy and sensitivity.

Table 3-8. The Calculated Deviation of Pmpp Verses Irradiance for Each Temperature

G	ΔPmpp @ 0DegC (%)	Deviation from ΔG @ 0DegC (%)	ΔPmpp @ 25DegC (%)	Deviation from ΔG @ 25DegC (%)	ΔPmpp @ 50DegC (%)	Deviation from ΔG @ 50DegC (%)
1000	0.00	0.00	0.00	0.00	0.00	0.00
800	23.38	-3.38	22.08	-2.08	22.64	-2.64
600	44.81	-4.81	45.77	-5.77	46.06	-6.06
500	56.80	-6.80	54.28	-4.28	54.36	-4.36
	Average deviation (%)	-3.03		-3.26		-3.75

3.3.3.b GEN IV Reliability data

Preliminary reliability studies were undertaken to investigate the robustness and hence effectiveness of the mechanical and electrical design in collaboration with Bangor University's Centre for Lifetime and Reliability Testing (CLARET). Before the accelerated conditions were applied, the ALPHA GEN IV CPV-TE hybrid receiver was characterised at Cardiff University using the setup as in Section 3.2.1. The accelerated ageing conditions subjected the sample to elevated temperatures of up to 120°C (see Figure 3-24) using a plasma arc lamp. A Newport 94041A solar simulator (class AAB) was used for device characterisation and periodic I-V scans were taken at regular time intervals. The sample was replaced after each test. The long-term data up to 1100 hours is shown in Figure 3-25.

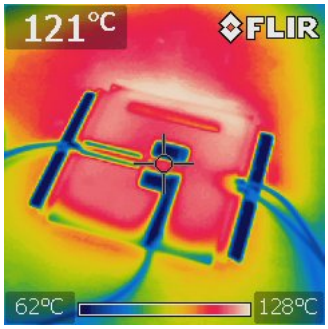

Figure 3-24. Thermal Camera Image of ALPHA under Bangor's Sulphur-Plasma Ageing Lamp

The ALPHA receiver for the first 600 hours under accelerated ageing, showed negligible degradation [14]. For the second period of an additional 500 hours, the ageing conditions were increased up to approximately "2 sun" power densities. However, visual inspection showed a premature ageing condition for the fibreboard itself. This had the potential to create misalignment conditions or increase the likelihood of wire-bonding failure from resulting PCB degradation. To evaluate the existing design's thermal performance and to further understand the mechanisms of degradation shown form the reliability data, an analogous model of the receiver was evaluated using COMSOL and similar conditions applied.

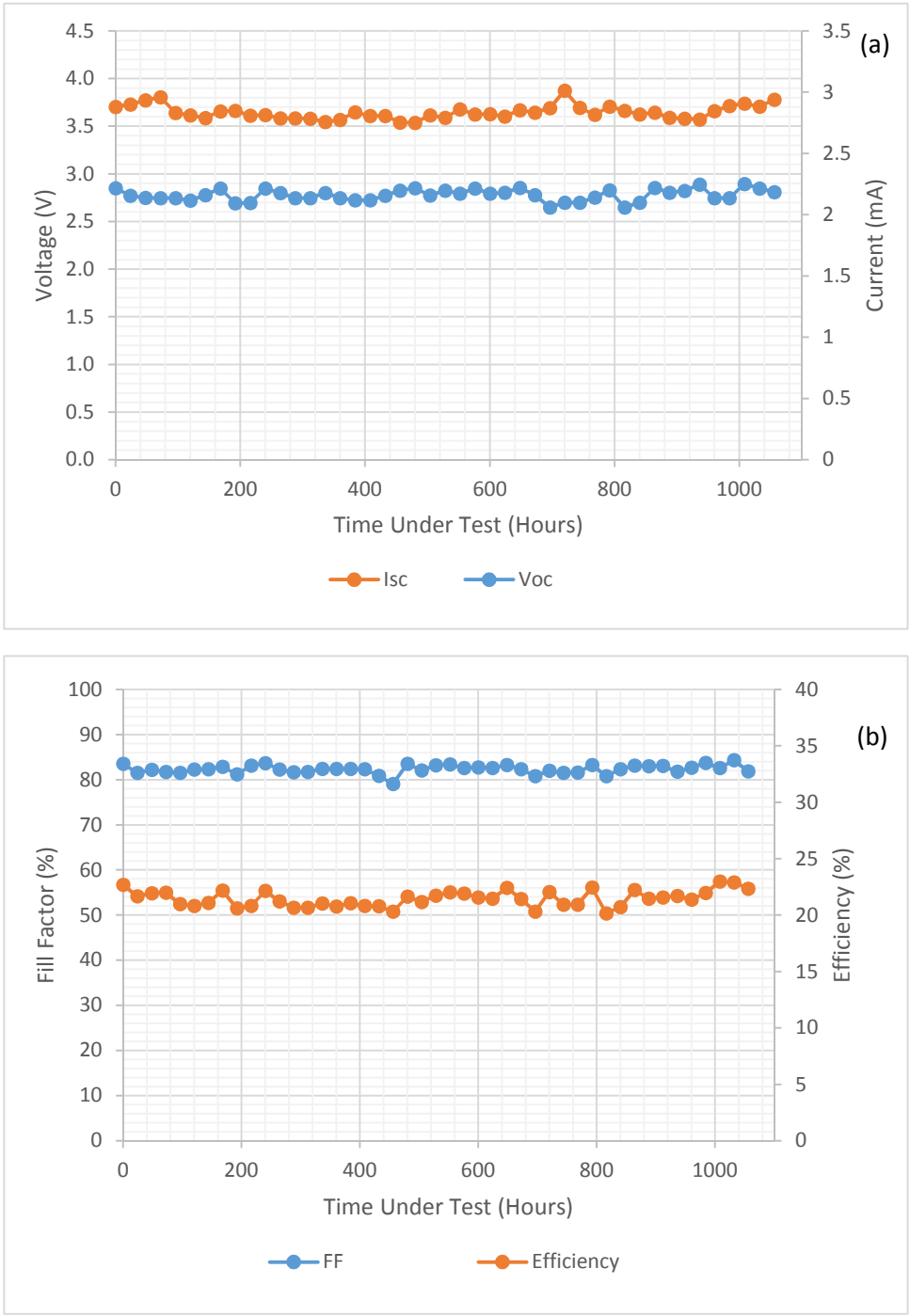

Figure 3-25. Long-term Measurements of ALPHA's Solar cell Degradation Parameters throughout Testing for the Isc and Voc (a), and the FF and Efficiency (b)

It was shown from the COMSOL model that the lack of thermal contact to the copper substrate on the PCB "overhangs" led to a drastically increased temperature in these regions (see Figure 3-26).

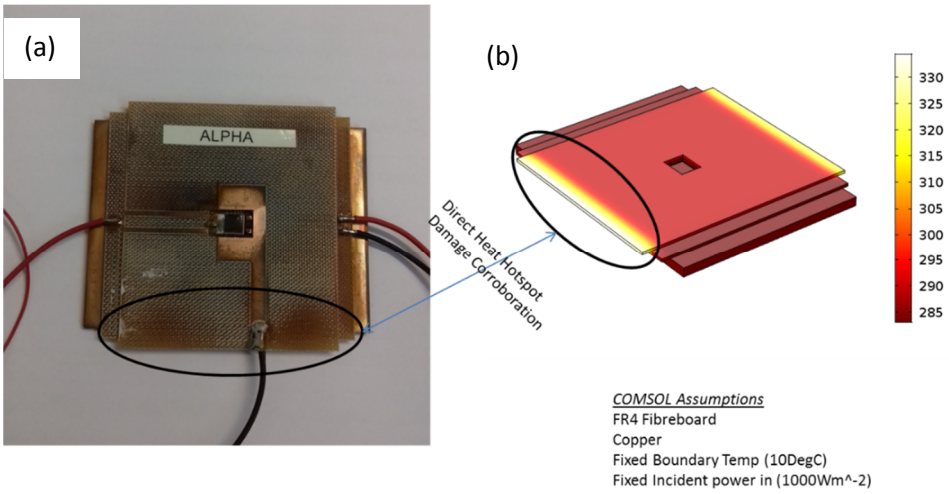

Figure 3-26. A Direct comparison of the Visual thermal Degradation of the ALPHA PCB against the COMSOL Model Results. Receiver picture post 1200h under the Plasma Lamp (a) and the COMSOL Simulation Results (b).

Additionally on further inspection of thermal camera images taken throughout other experiments with the ALPHA receivers, it was shown on multiple occasions that consistent "thermal anomalies" could be seen in the gen IV receiver design (See Figure 3-27). These pictures were taken throughout the testing at multiple orientations compensating for reflective or diffusive errors, and at a range of absolute temperatures to negate any thermal camera drift calibration errors. To

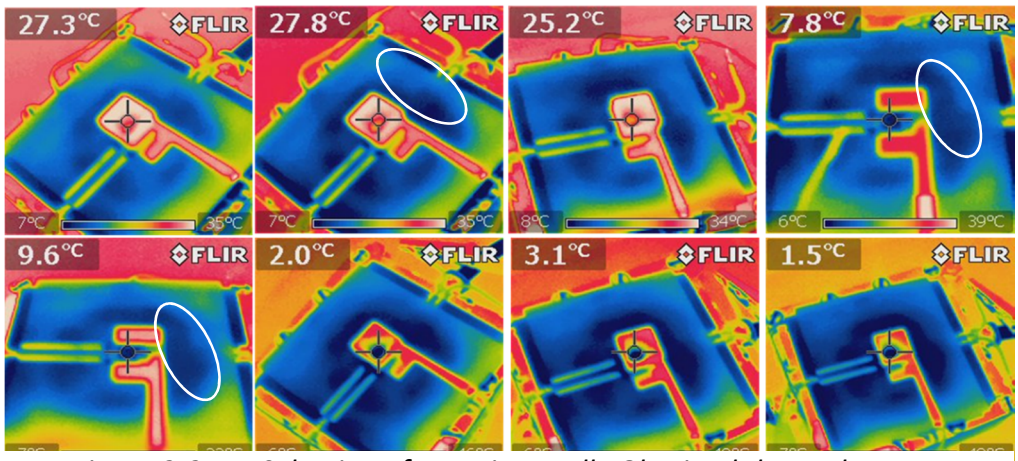

Figure 3-27. A Selection of Experimentally Obtained thermal Images Exhibiting the "Thermal Anomalies" (Examples Circled) within the Bi-layer PCB structure

counteract this issue of the PCB overhang ageing, the designs of the hybrid receiver PCBs was modified to be entirely in contact with the copper substrate from Generation V onwards.

3.3.4 GEN V Data (SOE-CPV-TE Hybrid Receiver)

To evaluate the performance of the SiLO SOE on the hybrid receiver output when fully bonded using Sylguard, experiments were done comparing a GEN V receiver "KAPPA" with the previously tested GEN IV receiver, ALPHA at STC conditions. As tested here, KAPPA had a SiLO SOE applied, and ALPHA was tested with the bare cell only. The temperature of Kappa was monitored in these experiments using the CLIC technique (see Chapter 4), as the addition of the SOE made it infeasible to obtain accurate temperature readings from the thermal imaging camera due to the spectral reflective and refractive properties of the SOE. It was found that the SOE achieved an effective optical concentration of 2.44x, as calculated from the ratio of short-circuit currents See Figure 3-28. The V_{oc} was shown to also increase by +6.69%.

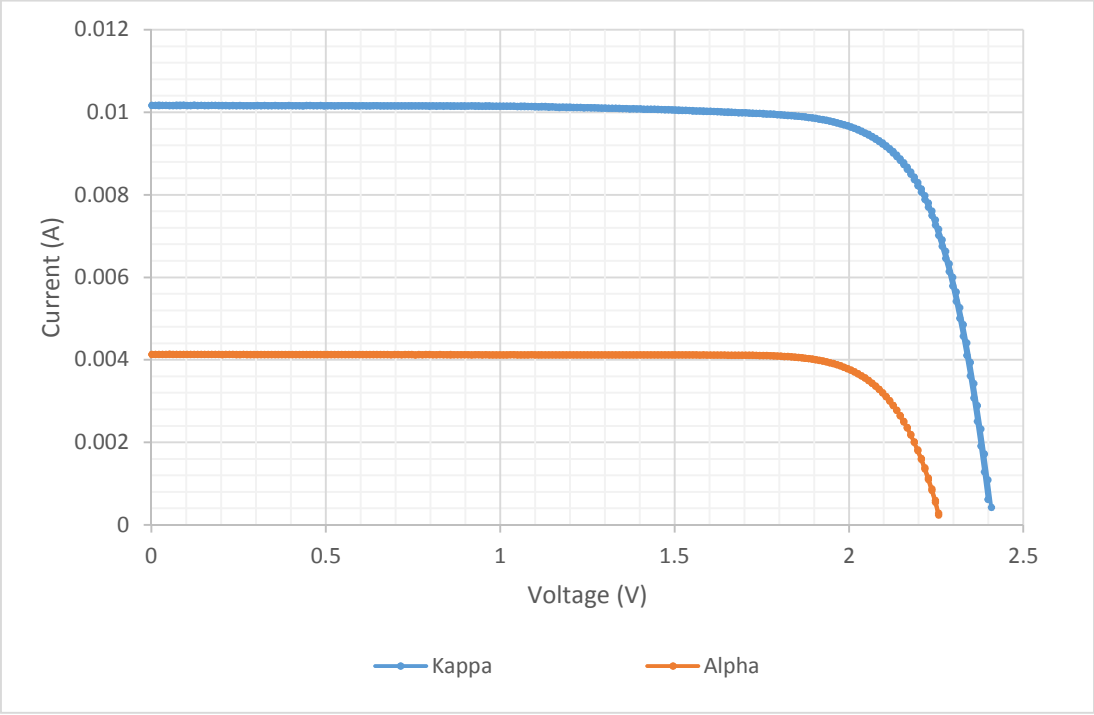

Figure 3-28. 1-sun I-V Data for GEN V Kappa Compared with Gen IV ALPHA

Following a similar process to that in Section 3.3.3.a, Kappa was then measured under various incident temperatures and irradiance conditions. The effect of the receiver design changes was to directly evaluate and the effect thereof

of the SOE on the TEM cooling functionality within the CPV-TE device. Similar cell temperature co-efficients were found as previously (Example for V_{oc}: Gen V = -4.61 mV/^{o}C, Gen IV = -4.55 mV/^{o}C, see Section 3.3.3.a) further validating the temperature measurement method, receiver manufacture and experimental methodology repeatability. Figure 3-29 shows the I-V characteristics measured, alongside the obtained critical cell performance parameters in Table 3-9.

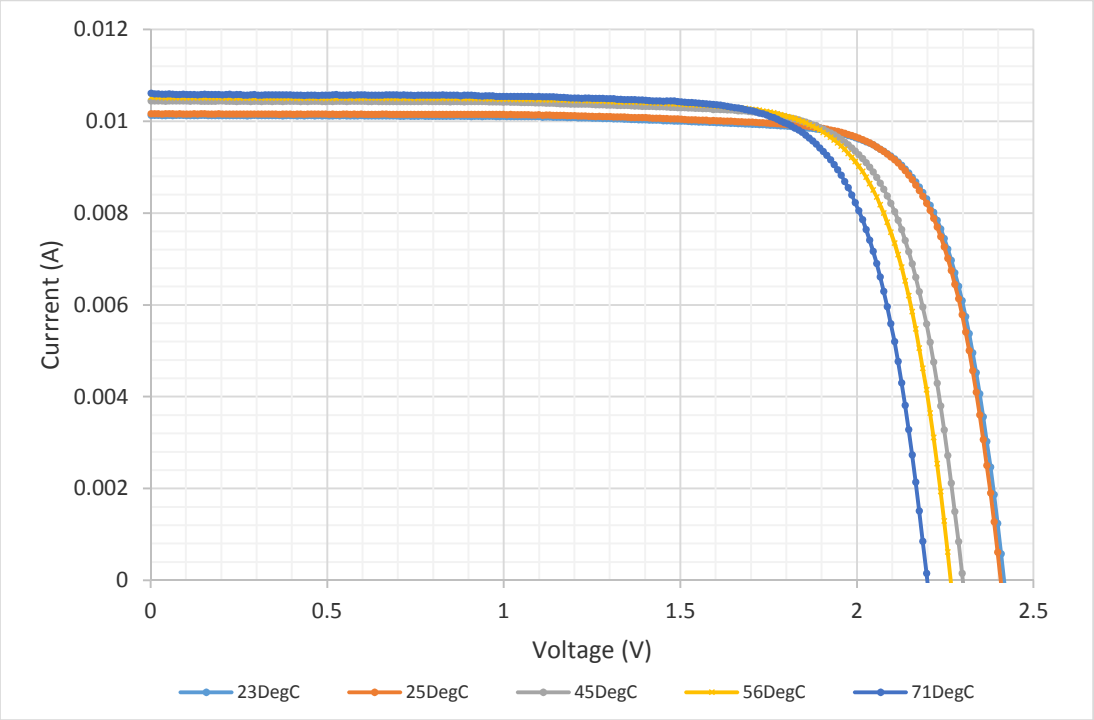

Figure 3-29. I-V Curves Obtained for GEN V "Kappa" Obtained at Various TEM-Controlled Temperature Conditions, with AM1.5G Irradiance

Table 3-9. Summarised Critical Solar Cell Performance Characteristics for Kappa

Temperature (DegC)	Isc (A)	Voc (V)
23.0	0.010	2.418
25.0	0.011	2.408
45.0	0.012	2.297
56.0	0.013	2.257
71.0	0.015	2.197
Isc Temperature Co-efficient: (mA/K)		0.105
Voc Temperature co-efficient: (mV/K)		-4.616

Figure 3-30 shows the obtained I-V data for kappa at these different irradiance conditions, alongside a summary of the critical cell parameters in Table 3-10. Linear trends similar to that found for the GEN IV receivers, were achieved when plotting the MPP output of the SOE-CPV-TE hybrid device against the input irradiance conditions (see Figure 3-31). This linearity shows that minimal SOE mis-alignment had occurred during manufacture, as the average Fill Factor was measured to be 75.06%.

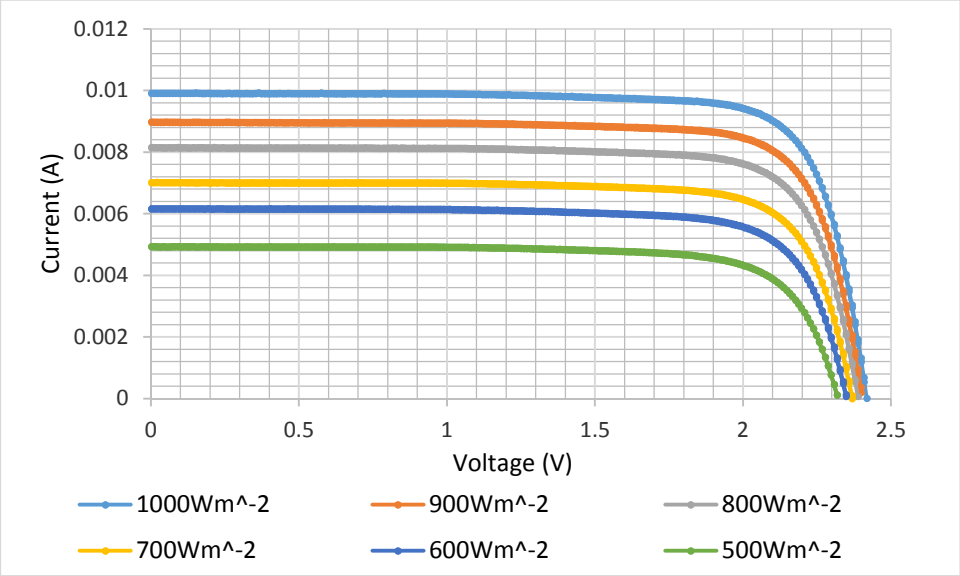

Figure 3-30. Kappa I-V Curves at Various Irradiances and 25°C

Table 3-10. Critical Solar Cell Performance Parameter for Kappa with Different Irradiances

Irradiance (Wm^-2)	Isc (A)	Voc (V)	Impp (A)	Vmpp (V)	Pmpp (W)	η (%)	FF (%)	Relative Deviation Comparing ΔG with ΔPmpp
1000	0.010	2.418	0.009	2.106	0.02	17.39	78.92	0.00
900	0.009	2.398	0.008	2.136	0.02	15.33	77.59	1.82
800	0.008	2.388	0.007	2.136	0.01	13.62	76.21	1.70
700	0.007	2.368	0.006	2.136	0.01	11.37	74.48	4.64
600	0.006	2.348	0.005	2.116	0.01	9.74	73.21	3.98
500	0.005	2.317	0.004	2.116	0.01	7.35	69.93	7.74
Average	0.008	2.373	0.006	2.124	0.01	12.47	75.06	3.31

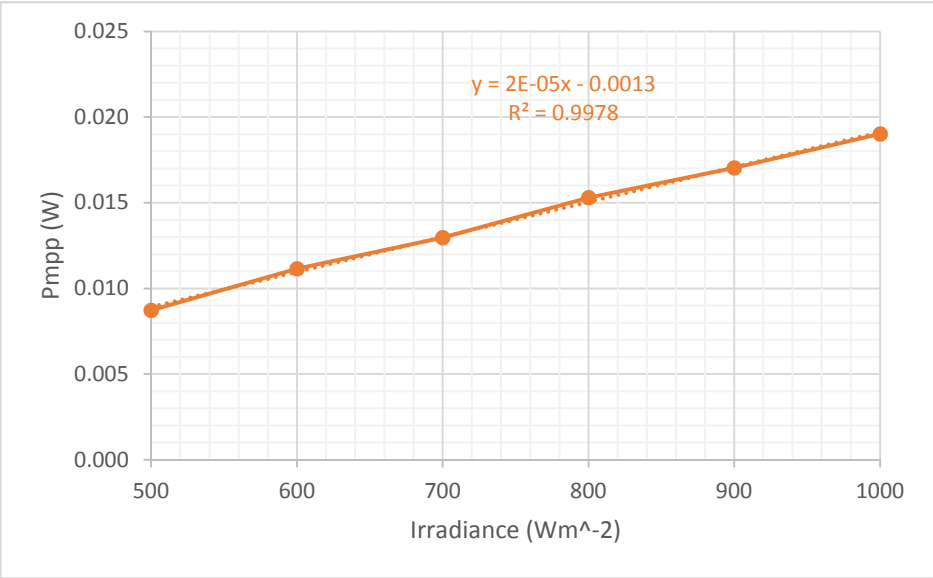

Figure 3-31. Linear MPPT Trend Verses Irradiance for Kappa

In addition to the evaluation of the hybrid receiver performances at these irradiance conditions, the high sensitivity temperature control achieved once more using the TEM through with this improved GEN V CPV-TE hybrid receiver, allowed high-resolution I-V data to be measured for use in further simulation and model validation of the cell itself [13, 20]. With an average deviation comparing the relative ΔP_{mpp} with the ΔG of 3.31%, the temperature control using the TEM once again demonstrated its ability to control very small temperature changes as induced by small step sizes of irradiance, whilst maintaining the resulting knock-on error on the measured datasets to be within experimental error (solar simulator rated irradiance deviation ±5%). Although a maximum deviation error of 7.74% was shown at 500Wm^{-2}, in this region the simulator was operating far outside its specification.

3.3.5 Thermoelectric Cooling Power Consumption Comparison with (GEN V) and without (GEN IV) SOE

The thermoelectric power consumption was measured at each current excitation using a multimeter. The thermoelectric power exhibited similar quadratic relationships verse the excitation current, for both the IQE2 receiver (GEN IV) with and without CCPC SOE, and KAPPA.

All traces plotted had >0.99 R^2 confidence values (see Figure 3-32). The TEM excitation current was also plotted alongside the achieved cell temperature for these three experiments. It was shown that with the KAPPA receiver with the SiLO SOE achieved the least effective cooling rate (-21.352 $^oC/A$), as it to be expected from having a larger thermal mass in contact with the compared to the CCPC or the bare cell and the increased heat flux from the larger irradiance. The IQE2 with CCPC exhibited an effective cooling co-efficient of 86.455 $^oC/A$, with the bare cell being the most effective case with a 119.08 $^oC/A$ cooling co-efficient (See Figure 3-33).

Both of these gradients show promise for the integration of the TEM for active cooling within hybrid devices. The linearity of the cell temperature achieved show that the controllability of the TEM and resulting cell temperature to be highly scalable and predictable. Likewise, trend extrapolation could be done to extend eh functionality past the ranges tested here, especially as the R^2 values achieved through the data points are >0.98 for all three tests. The quadratic nature of the TEM power consumption indicates that during use of the device, one should expect to see an optimum applied current condition arise for TEM input current – especially as the temperature co-efficient multi-junction solar cells, and the temperature gradients are both linear. These three effects (the quadratic TEM power verse TEM current, the linear cell temperature co-efficient and the linear cell temperature verses TEM current input) should reach an equilibrium in such a way, so that over a critical value the power TEM power consumption will increase far beyond that of the gained solar cell conversion efficiency.

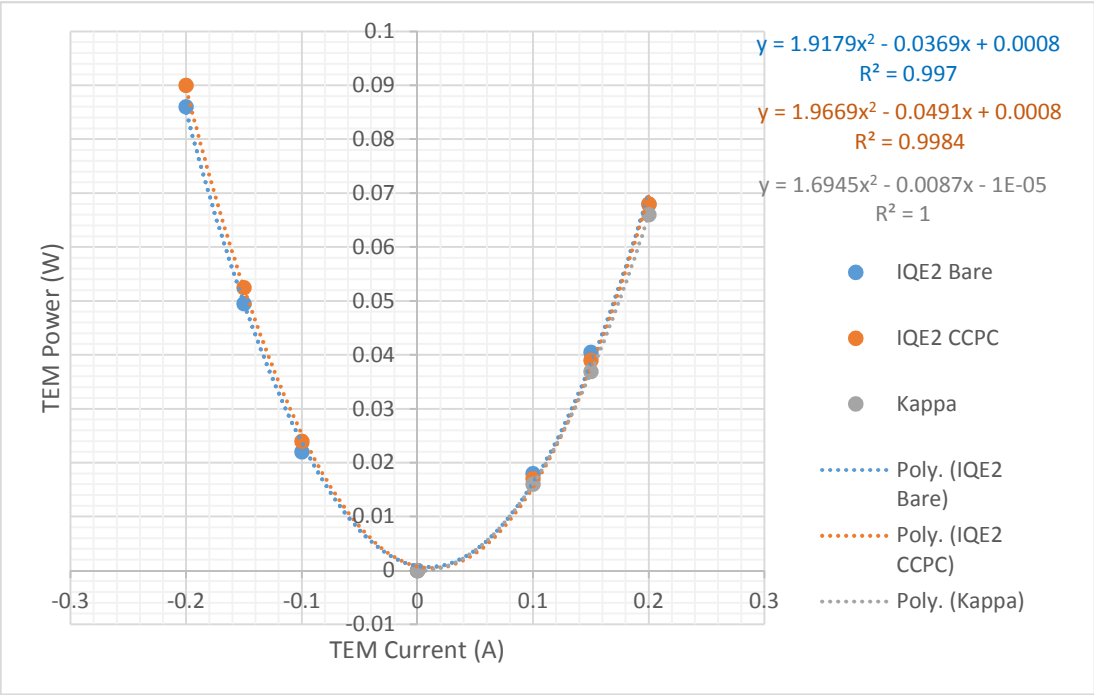

Figure 3-32. TEM Power Consumption Verse Excitation Current for Kappa, IQE2 with a bare cell, and IQE2 with a CCPC SOE

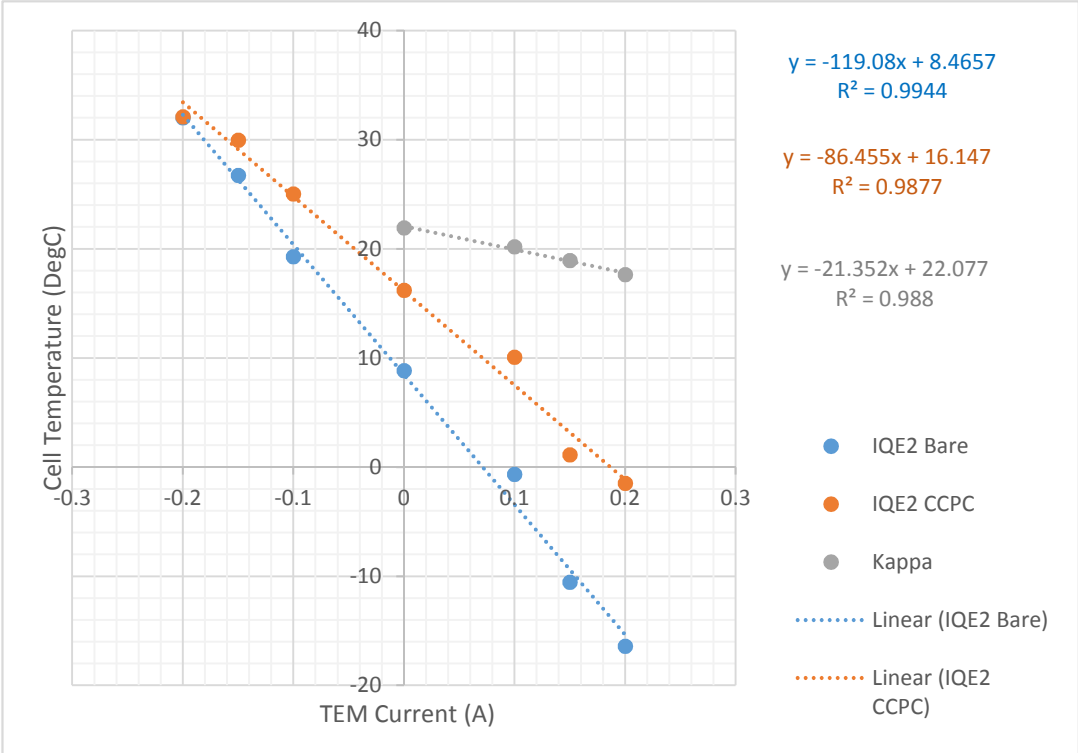

Figure 3-33. Measured Cell Temperatures for KAPPA, IQE2 with CCPC Optics and IQE with a Bare Cell

3.3.6 Outdoor Testing of a HiT Flat-plate Module Verses a Commercial CPV Module

From the metrology as described in the experimental setup above (see Section 3.2.2), the effective Direct Normal Irradiance (DNI) fraction (DNI/GHI) was calculated and plotted alongside the In Plane Pyranometer (IPP) and Global Horizontal Irradiance (GHI) data. The data in Figure 3-34 is selected from data obtained through outdoor testing during the week of the summer solstice.

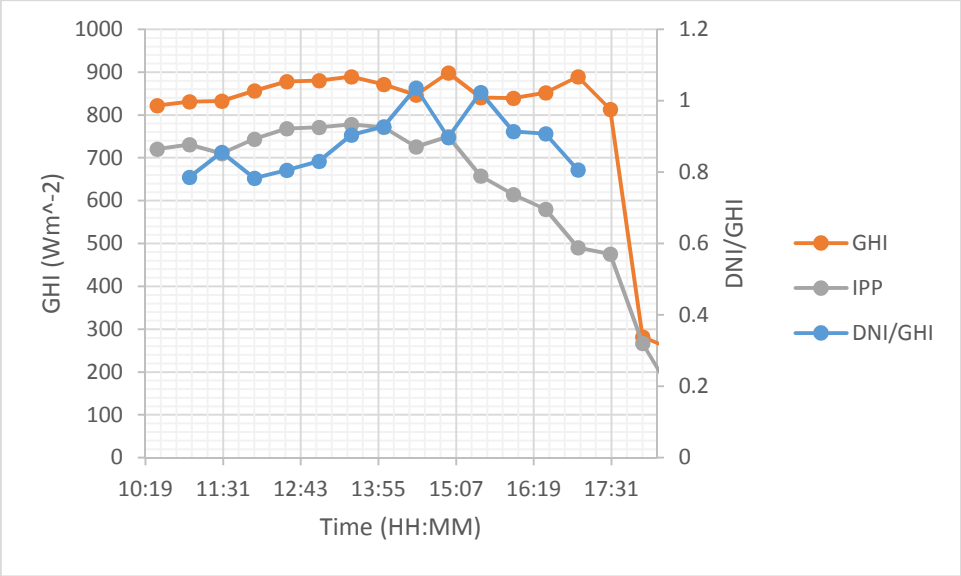

Figure 3-34. Measured Solar Resource throughout the Day

Consistent DNI and GHI close to ideal conditions were recorded throughout the day's testing, with an average DNI of 750 Wm^{-2}, and a GHI of 900Wm^{-2} (as compared to the ASTM standard for cell testing: 1000Wm^{-2} DNI). The hours of sun was limited by shading in the rooftop in which the experiments took place. Solar irradiance cut-off times were exhibited between approximately 10:30am and 6pm, due to the geometry of the rooftop. Due to health and safety limitations, no other rooftop location was available for testing. The DNI/GHI fraction as shown in the above figure was calculated These values were not calculated post-cut-off times to improve figure clarity and eliminate this spurious data from further analysis. Two anomalous data points were recorded in the DNI data, where it exceeded that of the recorded GHI, which was potentially caused by partial shading of the pyranometer during the test. Consistent GHI/DNI ratios of approximately 0.8 were measured throughout the tests.

At 30 minute intervals, an I-V scan was taken from the commercial CPV module. The results were plotted as both raw data, and with linearly 'scaled' I_{sc} representing the data as if it was under 1000Wm^{-2} conditions. This normalisation step was crucial for dataset comparison between the two PV technologies. During the I-V scans, all the metrology listed above was logged every second to detect variation of conditions throughout the ten-second measurement procedure. As can be expected, the peak solar irradiance (and hence module performance) occurred at solar noon with the CPV module V_{oc} being recorded as 35.1V with a scaled I_{sc} of 1.17A. Negligible deviation of the irradiance conditions were observed during this scan, with an average GHI of 856.1 Wm^{-2}, an average IPP reading of 743.1 Wm^{-2}, and average DNI of 665.4 Wm^{-2}. Both CPV module rear temperatures were similar, with averages of 50.8^{o}C and 52.9^{o}C respectively. The ambient temperature was recorded as 32.6^{o}C.

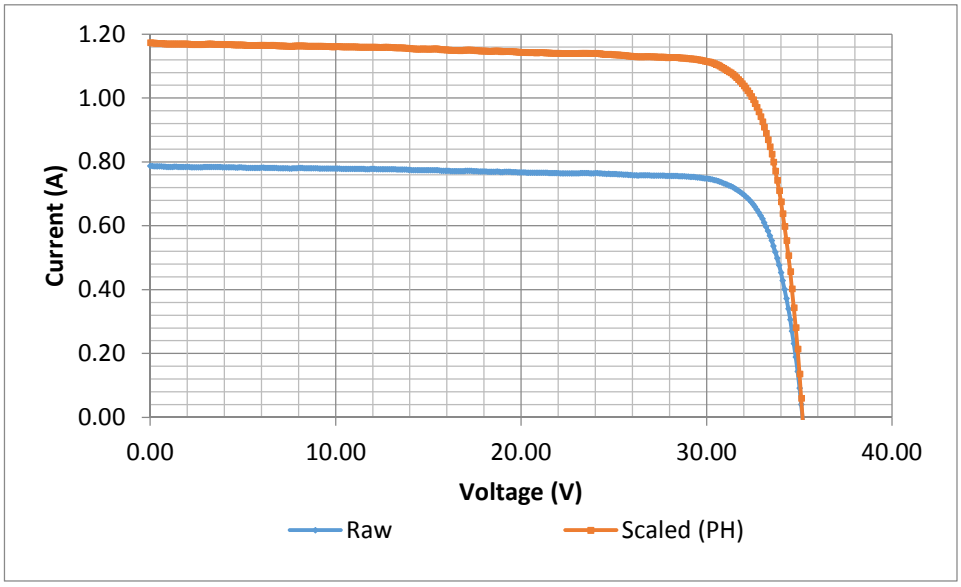

Figure 3-35. Champion I-V Characteristics of the CPV Module; Measured at 12pm. The "Raw" I-V was taken at 850Wm-2, plotted alongside the data scaled for 1000Wm-2.

The EgniTec logged data values for the HIT module were retrieved for the same timestamp as the data obtained for the commercial CPV module. The active areas of both devices was measured. The output powers for both technologies were then scaled as per the irradiance monitoring equipment closest to the sample for comparison (the PH for the CPV module, and the inclined Silicon reference cell for the flat plate). The specific power per unit areas of each technology was calculated for direct cross-comparison. It was found the commercial CPV module exhibited a scaled specific power of 1.6x that of the flat plate technology. This related to an effective module efficiency of ~28% and 17% was calculated for the CPV for the flat plate respectively. In deployment, this would mean that a "solar farm" built using the CPV systems would take 62.5% less land to generate the same amount of power as compared to the HiT panels. These data and calculations are listed in Table 3-11.

Table 3-11. Comparison Study Results of Flat-plate Verse the CPV Module

Recorded Data at 12pm		
Module Name	Flat Plate	CPV
Irradiance (W/m^-2)	862 (Si Ref)	670 (PH)
Sacling Factor	1.159	1.491
Unscaled Power Output (W)	168.34	22.45
Scaled Power Output (W)	216.04	33.48
Specific Power Output (Wm^-2)	170.92	278.97
Efficiency (%)	17.09	27.90

3.4 Conclusions

- A novel method for the integration of a thermoelectric module and a CPV cell was designed, manufactured and tested. Iterative design changes created a series of geometries and layouts - with design generations IV, V and VI developed.
- Simultaneous thermal, electrical and mechanical parameters for the design were considered to satisfy experimental deployment limitations. Any detrimental effect of the supporting structure to the CPV cell or thermoelectric module performance was minimised. A thermally and electrically conductive silver epoxy was found to be effective, in a "direct bonding" approach of the cell to the TE.
- The cells within the hybrid devices were encapsulated using Sylguard elastomer. The conversion efficiency losses associated with reduced optical transmission were quantified as ~-0.5% absolute at 1-sun conditions.
- Manufacture for these hybrid CPV-TE devices was done inside a cleanroom environment. Cell conversion efficiency was higher than 2% absolute at 1-sun conditions, compared with the receivers made in a general laboratory.
- Encapsulation of the TEM itself was experimentally investigated. The P-V curves for the performance of the module itself were not affected, whilst simultaneously offering protection against humidity-related degradation.
- A pre-manufacture "fast I-V scan" method was introduced prior to device manufacture to quickly evaluate the internal resistance of the TEMs. It was shown to be an effective method to eliminate under-performing TEMs before integration into a hybrid receiver. The failure limit for the TEM scans was set with a measured R_{int} > ±0.5% from the batch average.
- Experiments were done to determine the effectiveness of controlling the cell temperature using the integrated TEM in combination with varying the irradiance level. Accurate and repeatable temperature control was achieved by varying the current excitation input to the TEM. The I_{sc} and V_{oc} temperature co-efficients of the CPV cell were obtained both with and without SOEs. These were found to be βI_{sc} = +0.11596 mA/^{o}C, and βV_{oc} = -

4.5512 mV/^{o}C for the receiver named ALPHA (bare cell), and βI_{sc} = +0. 104904 ma/^{o}C and βV_{oc} = -4.615784 mV/^{o}C for the receiver named KAPPA (SiLO SOE).

- Whilst varying the irradiance, a linear MPP trend was found with a 0.99 R^2 confidence, indicating good optical alignment achieved in the manufacture of KAPPA, in addition to confirming accurate temperature control.
- The power consumption of the TEM within the CPV-TE and SOE-CPV-TE hybrid devices was measured during active cooling. It was shown that for both experiments, the TEM power consumption exhibited a quadratic trend against the applied current, with the higher CR SOE giving less effective cooling per Amp applied to the TEM – as expected from the increased heat flux through the device.
- Preliminary accelerated life testing was done on ALPHA (GEN IV) for 1000 hours, with 600 hours under 1 sun and the remaining 500 hours under a higher 2-sun condition. Negligible changes ($\Delta\eta$ = <1% absolute) were observed in the cell conversion efficiency through both highlighting good thermal stability for the directly-bonded hybridisation approach and for the receiver designs built.
- A bespoke outdoor testing gyroscope was designed and built for on-sun testing and sun tracking. A baseline comparison dataset was obtained for both a flat-plate HiT module and a commercially-sourced CPV module. The normalised 1-sun conversion efficiencies for the devices were found to be 17.09% and 27.89% respectively. The CPV system was shown to have 1.6x greater power generation per m^2 as compared to the HiT flat plate alternative.

3.5 References

1. Epotek, *Adhesive Applciation Guide*. 2015. p.48. [Accessed: 01/05/18]. Available at: http://www.epotek.com/site/files/brochures/pdfs/adhesive_application_guide.pdf .
2. Epotek, ***EPOTEK H20E Technical Datasheet***, Epotek, Editor. 2015. [Accessed: 01/05/18]. Available at: http://www.epotek.com/site/administrator/components/com_products/assets/files/Style_Uploads/H20E.pdf .
3. Dow Corning., *Product Information: Sylguard 184 Silicone Elastomer*. 2014. p.4. [Accessed: 01/05/18]. Available at: http://igem.org/wiki/images/2/29/T--Technion_Israel-HardwarespecsPDMS.pdf
4. ASTM, *Standard Specification for Solar Simulation for Terrestrial Photovoltaic Testing*. 2010. Version purchasable from: https://compass.astm.org/Standards/HISTORICAL/E927-10.htm
5. Zonen, K.a. *Pyranometer & Pyroheliometer Calibration Traceability*. 2014.
6. Zonen, K.a., *CMP Series Instruction Manual*. 2006.
7. Núñez, N., et al., *Instrumentation for accelerated life tests of concentrator solar cells.* Review of Scientific Instruments, 2011. **82**(2): p. 024703. [Accessed:01/05/18]. Available at: https://aip.scitation.org/doi/abs/10.1063/1.3541800
8. [Online] Instruments, O., *LCS-100 Series Small Area Solar Simulator Datasheet*. [Accessed: 01/05/18]. Available at: https://assets.newport.com/webDocuments-EN/images/32057.pdf
9. Ossenbrink, H. *Calibration procedures - state of the art*. in *Photovoltaic Energy Conversion, 2003. Proceedings of 3rd World Conference on*. 2003. [Accessed: 01/05/18]. Available at: https://ieeexplore.ieee.org/abstract/document/1305016/
10. McArthur, L.J.B., *World Climate Research Programme - Baseline Surface Radiation Network (BSRN) - Operations Manual Version 2.1*. 2005, Experimental Studies Division, Atmospheric Environment Service:

Downsview, Ontario, CANADA. [Accessed: 01/05/18]. Available at: http://epic.awi.de/45991/1/McArthur.pdf

11. IEC *Standard, IEC 60904-3: photovoltaic devices.* Part 3: Measurement Principles for Terrestrial Photovoltaic (PV) Solar Devices With Reference Spectral Irradiance Data, 1987. [Accessed: 01/05/18]. Available at: https://infostore.saiglobal.com/preview/is/en/2016/i.s.en60904-3-2016.pdf?sku=1881672
12. IEC Standard, *60904-3, Photovoltaic Devices—Part 3: Measurement Principles for Terrestrial Photovoltaic (PV) Solar Devices with Reference Spectral Irradiance Data, International Electrotechnical Commission, Geneva, Switzerland.* International Electrotechnical Commission, Geneva, 2007.
13. Li, W., et al., *A coupled optical-thermal-electrical model to predict the performance of hybrid PV/T-CCPC roof-top systems.* Renewable Energy, 2017. **112**: p. 166-186. [Accessed: 01/05/18]. Available at: https://www.sciencedirect.com/science/article/pii/S096014811730397X
14. Rolley, M., et al. *Triple-junction concentrator photovoltaic-thermoelectric hybrid receivers: robustness, validation and preliminary reliability studies*. in *13th Photovoltaic Science, Application and Technology Conference (PVSAT-13); Bangor, Wales, UK, 5- 7 April 2017.* 2017. [Accessed : 01/05/18]. Available at : http://orca.cf.ac.uk/id/eprint/100662 .
15. Sweet, T.K., et al. *Novel hybrid III: V concentrator photovoltaic-thermoelectric receiver designs*. in *AIP Conference Proceedings*. 2017. AIP Publishing. [Accessed: 01/05/18]. Available at: https://aip.scitation.org/doi/abs/10.1063/1.5001447
16. Sweet, T.K., et al. *Scalable solar thermoelectrics and photovoltaics (SUNTRAP)*. in *AIP Conference Proceedings*. 2016. AIP Publishing. [Accessed: 01/05/18]. Available at: http://aip.scitation.org/doi/abs/10.1063/1.4962105
17. Siefer, G. and A.W. Bett, *Analysis of temperature coefficients for III–V multi-junction concentrator cells.* Progress in Photovoltaics: Research and Applications, 2014. **22**(5): p. 515-524. [Accessed: 01/05/18]. Available at: https://onlinelibrary.wiley.com/doi/full/10.1002/pip.2285

18. Cotal, H. and R. Sherif. *Temperature Dependence of the IV Parameters from Triple Junction GaInP/InGaAs/Ge Concentrator Solar Cells*. in *2006 IEEE 4th World Conference on Photovoltaic Energy Conference*. 2006. [Accessed: 01/05/18]. Available at: http://ieeexplore.ieee.org/abstract/document/4059762/

19. Kinsey, G.S., et al., *Concentrator multijunction solar cell characteristics under variable intensity and temperature.* Progress in Photovoltaics: Research and Applications, 2008. **16**(6): p. 503-508. [Accessed: 01/05/18]. Available at: https://onlinelibrary.wiley.com/doi/abs/10.1002/pip.834

20. Li, W., et al., *A scaling law for monocrystalline PV/T modules with CCPC and comparison with triple junction PV cells.* Applied Energy, 2017. **202**: p. 755-771. [Accessed: 01/05/18]. Available at: https://www.sciencedirect.com/science/article/pii/S0306261917307456

Chapter 4 : The Closed-Loop Integrated Cooler (CLIC)

4.1 Background

This section describes a novel technique for simultaneous temperature measurement and control, investigated through the work in this thesis. The thermoelectric module within the Concentrator Photovoltaic – Thermoelectric (CPV-TE) hybrid receiver was used for this purpose. Temperature control was achieved through using the solid-state cooling functionality of the TE, whilst the temperature measurement was simultaneously done through the synergetic Peltier-Seebeck modes of operation within thermoelectric devices. See Chapter 3: *"CPV-TE Hybrid Receiver Designs and Validation as an Effective Experimental Platform"* for the design and information regarding the CPV-TE hybrid receiver.

4.1.1 Limitations of current Existing Temperature Metrology

The accurate measurement of the CPV cell temperature was imperative throughout all of the experimental set-ups as a monitoring and evaluation technique to compare I-V data. The measurement of the thermoelectric module hot side temperature is necessary for evaluation of the heat flow through the device. There exist many inherent limitations for measuring this parameter accurately. The mechanical attachment of a thermocouple to the cell surface was infeasible due to the bonding mediums typically used, would short or damage the cell. Any physical or mechanical attachment would shade the active cell area and affect I-V data obtained during the measurement. Attaching a thermocouple to an area that is close to but not on the cell will also have different lateral heat conduction, thermal mass and convective or radiative conditions giving further error and slower time response in the measured temperature. "Contactless" techniques such as Infrared (IR) thermometers, or thermal imaging cameras offer an alternative. However, the IR thermometers used had a large specified absolute error as they measure the temperature defined by a pre-calibrated plane distance to eliminate dispersion of the measured IR radiation. The thermometer also emitted IR radiation upon the cell surface which had the potential to further skew results as triple junction cells exhibit sensitivity in this wavelength range. Thermal imaging cameras measure emitted thermal radiation in the IR region, and perform a calculation based on a

given thermal emissivity to calculate a temperature measurement. A wide range of errors for this measurement was introduced when used at inclined angles, required to remove cell shading effects. Additionally, when measuring the hybrid receiver with the inclusion of SOEs, both the reflective (CCPC) and the refractive (SiLO, CP) type unavoidably increase error in the cell temperature reading due to optical effects.

4.1.2 The CLIC Temperature Measurement Technique

Through the Seebeck effect, when a temperature differential is applied between the hot and cold sides of a TEM, a voltage is generated. Typically used for electricity generation, a TEM is made from a series array of thermocouples to increase this voltage. The amount of power produced is defined by the TEMs figure of merit, alongside the p-i-n semiconductor material choice. Likewise, a TEM can act as a heat pump through the Peltier effect. As has been previously described in Chapter 2.1.5: *"The Thermoelectric Effect and Figure-Of-Merit"*, the active material for the TEMs within this work is Bismuth Telluride (Bi_2Te_3), due to having a well-documented performance in low temperature ranges (<100^{o}C) [1, 2].

The CLIC technique allows a current source to establish the Peltier heat-pumping during normal operation (temperature control) within hybrid CPV-TE receivers. A switching circuit then disconnects the source power briefly to allow for the measurement of this Seebeck Voltage, then the supplied power is reconnected. The temperature difference across the TEM can then be directly calculated using the Seebeck Co-efficient (α). Combined with a cold-side temperature reference, this allowed for the hot side absolute temperature of the TEM to be measured. Rigid calibration procedures were performed to mitigate systematic temperature measurement inaccuracies.

4.2 Experimental Methodology

4.2.1 The CLIC Calibration Rig

To accurately calibrate the measured temperature differentials, an experiential characterisation rig was built. This provided a robust and reliable datum for use in technique calibration. K-type thermocouples were chosen, due to

their temperature sensitivity (the larger of ±1.1^{o}C, or 0.75% above 0^{o}C), large functional range (-200^{o}C to 1250^{o}C) [3], and availability. An additional procedure was included to compare and quantify the manufacturing deviation of the used thermocouples (see section 4.3.2).

A Marlow TEM identical to that in the hybrid receivers (See module "BETA" in the pre-manufacture scans, Section 3.3.2.c) was used at the centre of the calibration rig to be consistent with the hybrid CPV-TE receivers. The same bonding epoxy was used and cured under the same conditions for cross-comparison of the device thermal contact resistivity and bulk thermal resistances. Fast I-V scans were taken to compare with the TEM included within the ALPHA receiver. This is similar to the pre-manufacture procedure detailed in section 3.2.3, with negligible difference being shown (+0.61% relative internal resistance (R_{int}) increase, from "pass" batch average). The pass is defined as having < ±5% R_{int} deviation from the same datum, see section 3.2.3. Two copper sheets with two thermocouple holes drilled via the plate edge to the geometrical centre on either side of the TEM were used due to copper's high thermal conductivity value (~400 W/m K), see Figure 4-1. An additional FR4 fibreboard was used for mechanical location of the TEM and calibration rig robustness, bonded to the copper plated using Araldite two-part epoxy.

A cold-side temperature reference Integrated Circuit (IC) was included in the design to evaluate accuracy as compared to a thermocouple. The supporting 4.7KΩ I^2C "one-wire" pull-up resistor was included on a small daughter board, along with the outward connections. This mounting was done using silver epoxy for the active device, and araldite for the mechanical bonding of the track board.

(a) Side View

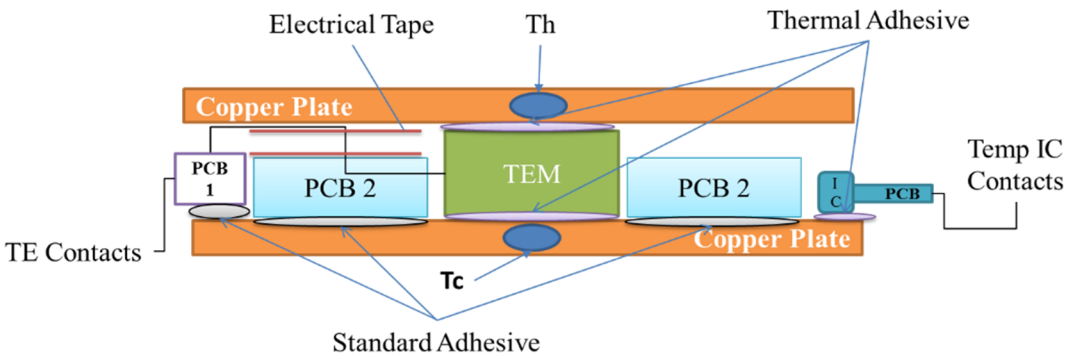

(b) Top View

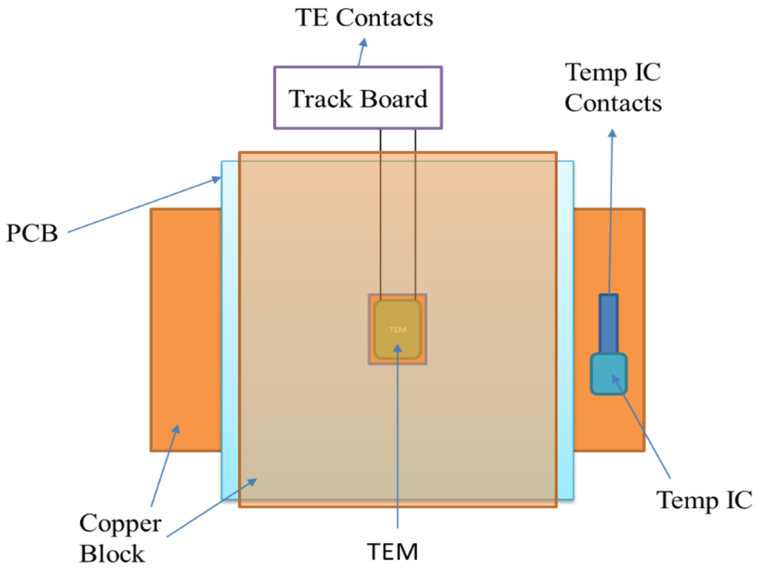

Figure 4-1. Side (a) and Top (b) Views of the CLIC Calibration Rig

This rig was used in an experimental set-up designed to achieve hot side temperature representative of the cells in nominal CPV operation [4] of up to 70°C. The hot side temperature was achieved using a 200Ω nominal resistive heater, comprised of two 100Ω heaters placed inside a copper block with holes milled to-size. A 30W (60V, 0.5A) laboratory current supply was used for the heater. The cold side was kept constant using a water cooler with a nominal flow. Thermal interface paste was used (RS metal oxide thermal grease, 0.65W/m K). To improve the thermal contact during the experiment and eliminate any air gaps and hence

parasitic thermal resistances to the heat transfer in the rigs. The thermocouples were used with a Fluke 52II hand-held thermometer and the data values recorded. This setup is shown as a schematic diagram in Figure 4-2 and the equipment used is shown in Figure 4-3.

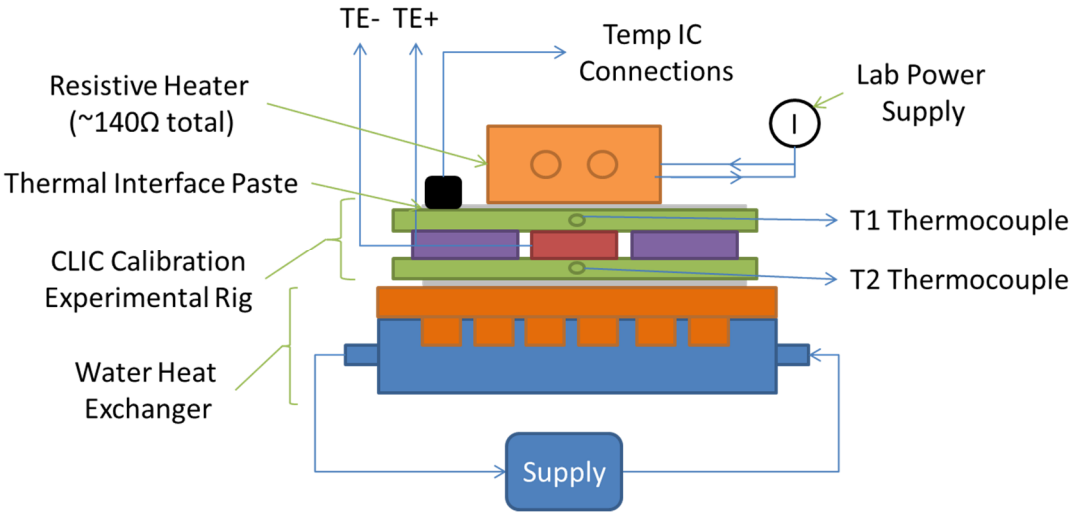

Figure 4-2. Schematic Diagram of the Experimental Setup Used for CLIC Calibration

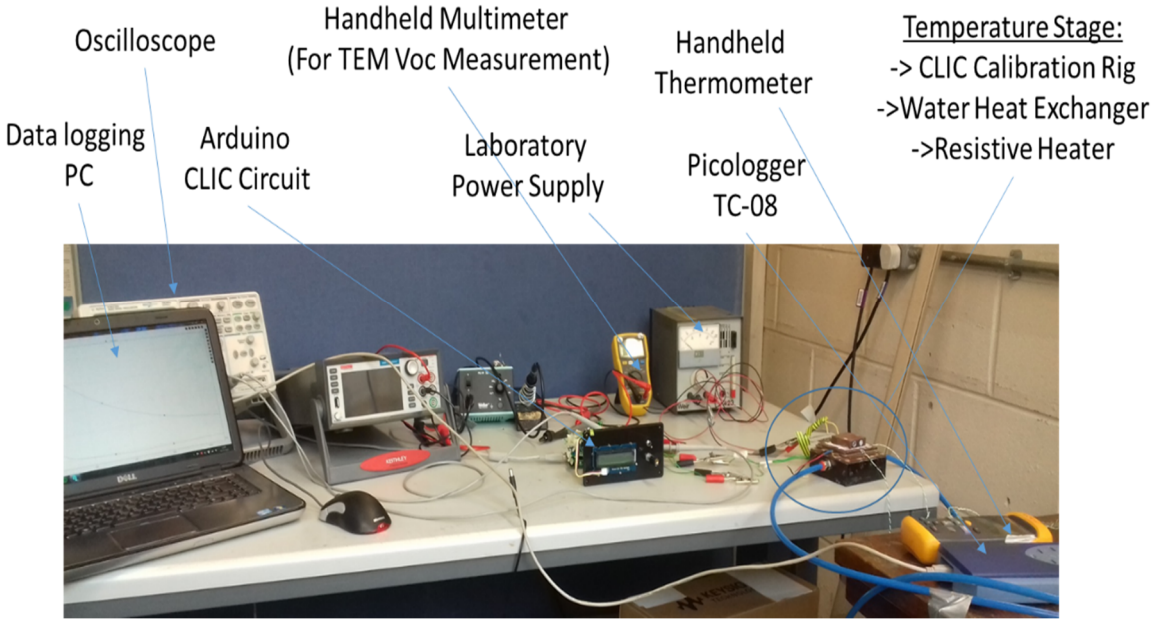

Figure 4-3. An Overview of the Experimental Setup for CLIC Calibration

4.2.2 The Arduino-based Circuit

To deploy the measurement technique for evaluation purposes and with a future focus of integrating the CLIC device in combination with CPV-TE hybrid receivers, a functional prototype circuit was built using an Arduino UNO micro controller, with an ATMEL ATmega328/P processor. The circuit used the on-chip ADC with a 10-bit resolution for the voltage measurement. A PWM-controlled 2A motor driver board, based on a L298 Full H-bridge driver IC was used as a demonstrator for driving and controlling the TEM in Peltier mode. To provide the circuitry switching functionality, three bi-polar NPN transistors were used to provide total ground-isolation for the TEM V_{oc} measurement. Simple 10KΩ resistors were used at the bases of the transistors to limit the current applied. The temperature IC used required a 4.7KΩ pull up resistor to facilitate its "1-wire" I^2C communication protocol for data transfer to the Arduino. However, in deployment this provided the largest time delay to the system, due to the on-board temperature IC Analogue-to-Digital Converter (ADC) conversion time. Hence, this was done within the source code, previous to switching the transistors for the Voc measurement to minimise the off-time of the applied TEM cooling.

4.2.3 The Data-logger-based Circuit

To overcome the Voc measurement limitations of the Arduino based CLIC circuit, the same technique was subsequently deployed using a Keysight 34972A switch unit. A 34901A 20 channel multiplexor added data logging capability for cell temperature evaluation. Calibrated K-type thermocouples were used to give the bottom cold-side receiver temperature reference. This used the hybrid receiver thermocouple substrate, shown in Figure 4-4. This technique was tested within a solar simulator, using a GEN V receiver (KAPPA) thermally coupled to the heater using a thermal interface material (TIM), see experimental set-up Figure 4-5.

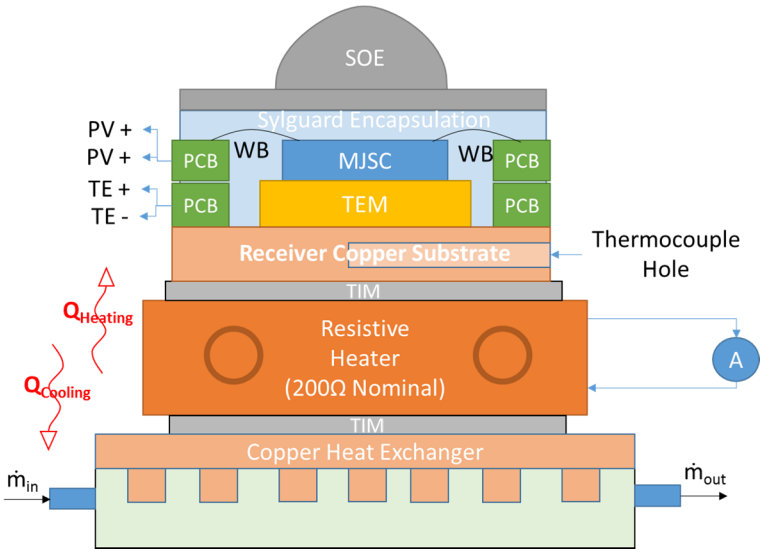

Figure 4-4. An Overview of the Used Experimental Rig for CLIC Hybrid Receiver Temperature Measurements

A water heat exchanger was used, with the resistive heater block positioned underneath the GEN V base substrate. This gave temperature control of the receiver, with the CLIC purely used for temperature measurement. Thermal interface material (heat sink compound plus) was used between the heat exchanger and the heater, and the heater and the rear copper substrate facilitating good thermal contact. The entire setup was then placed inside the Faraday cage, and subject to the same "1-sun" irradiation calibration procedures and testing methodology outlined in Section 3.2.1. The receiver was allowed to reach a steady state temperature, and the heater power/water flow rate was adjusted finely to get high resolution temperature as determined by the CLIC (See Section 4.3.5).

Experimental Setup

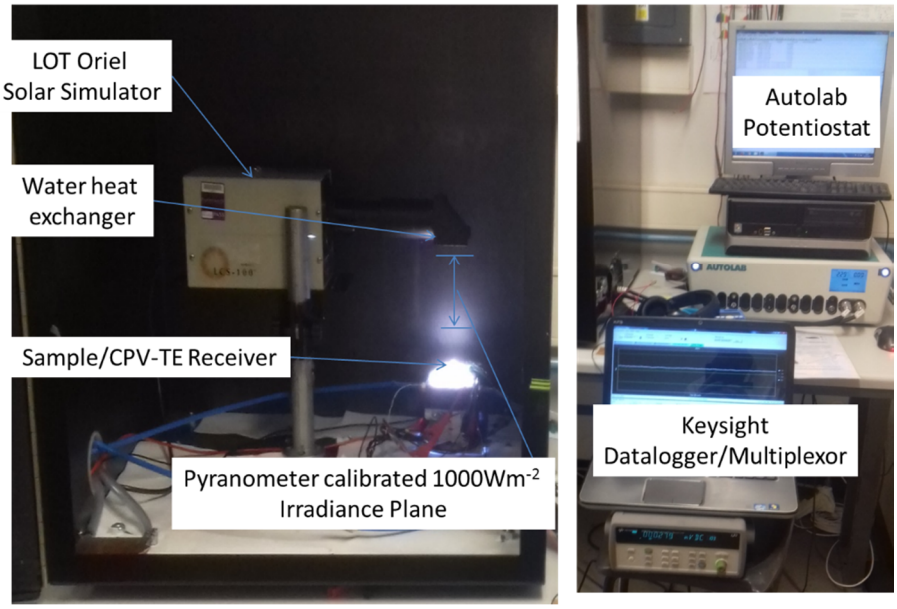

Figure 4-5. The DL-CLIC Experimental Setup as Used in the Solar Simulator

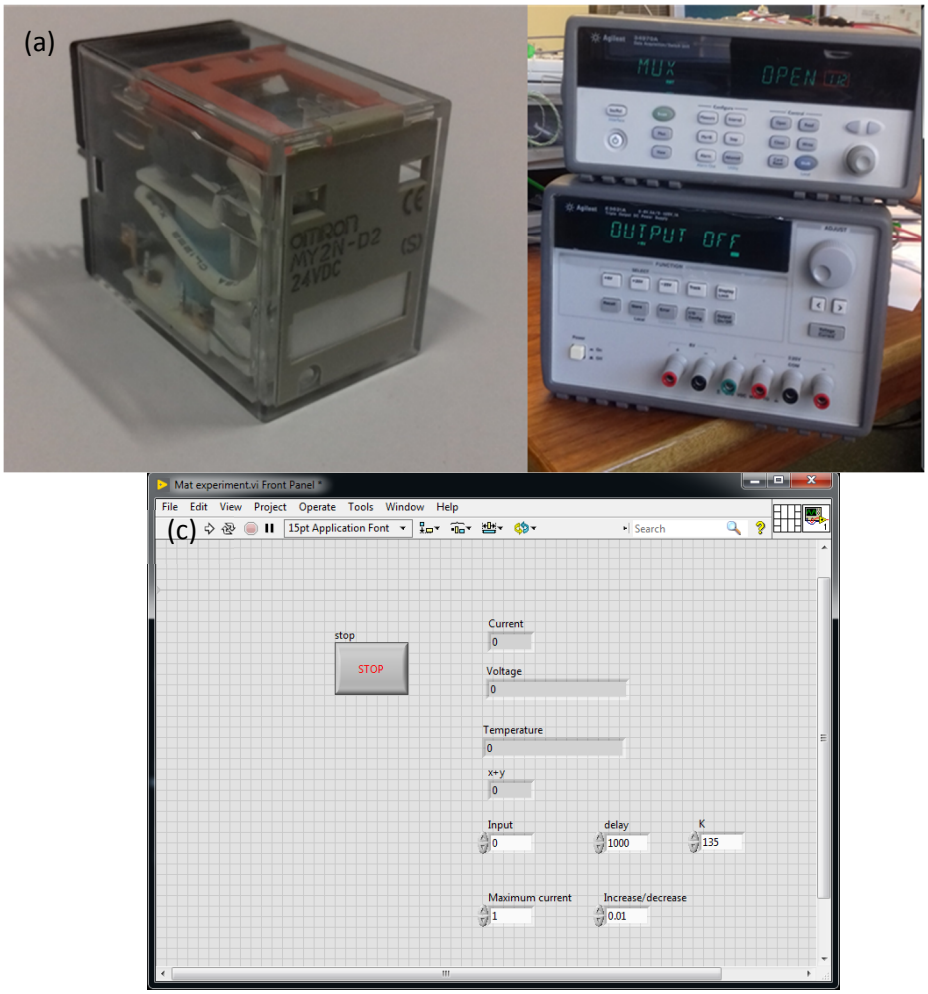

Figure 4-6. Decoupling Relay (a), Agilent PSU and Switch Unit (b) and LabVIEW UI (c).

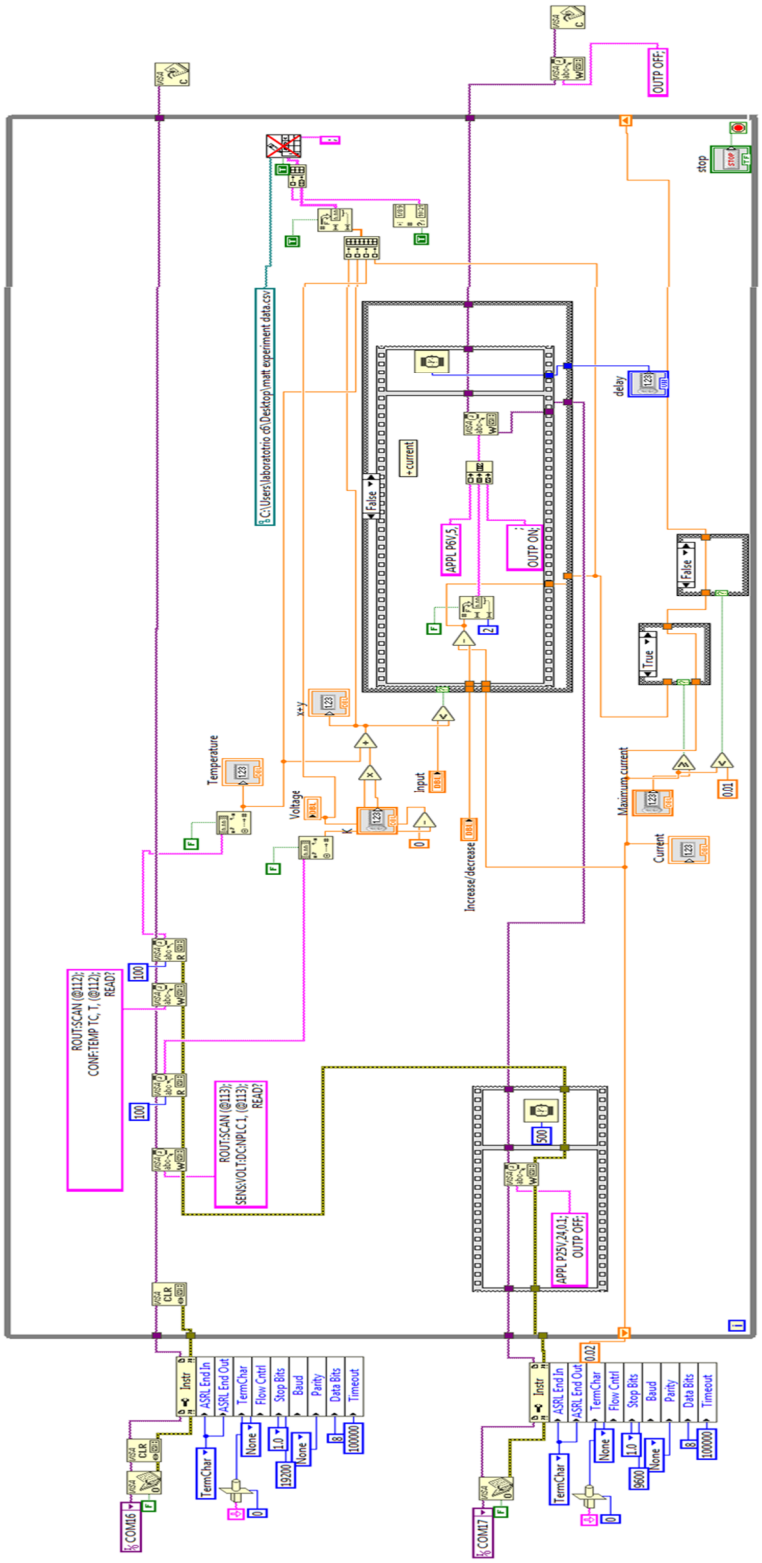

Figure 4-7. LabVIEW Block Source Code for CLIC Data-logger Circuit

4.2.4 The LabVIEW-based Circuit

Furthering the progress made using the data logger-CLIC (DL-CLIC) approach, a system was design using LabVIEW for streamlined operation. A programmable Agilent E3631A power supply was combined with the 34972A switch unit. The LabVIEW code controlled the supplied current to the TEM, whilst simultaneously switching and measuring the CLIC-calculated cell temperature. On the user interface (UI), the current increase/decrease step size, the maximum applied TEM current, the Input temperature, the delay between readings and the effective module Seebeck (shown as 'K') could be controlled during operation. Figure 4-6 shows the used equipment, relay and LabVIEW UI. Figure 4-7 shows the LabVIEW code block diagram. A 24V DC "decoupling-relay" (Citron MY2N-D2) was used to de-couple the output ports of the current supply to ground during the V_{oc} measurement step, to compensate for errors that occurred from imperfect open circuit conditions when the PSU output was turned off.

4.3. Results and Discussion

4.3.1 The CLIC Calibration Rig

A COMSOL Multiphysics thermal simulation was completed to evaluate the mechanical location of the TEM before use in the experimental calibration steps. The heat flux distributions were evaluated for the experimental set-up.

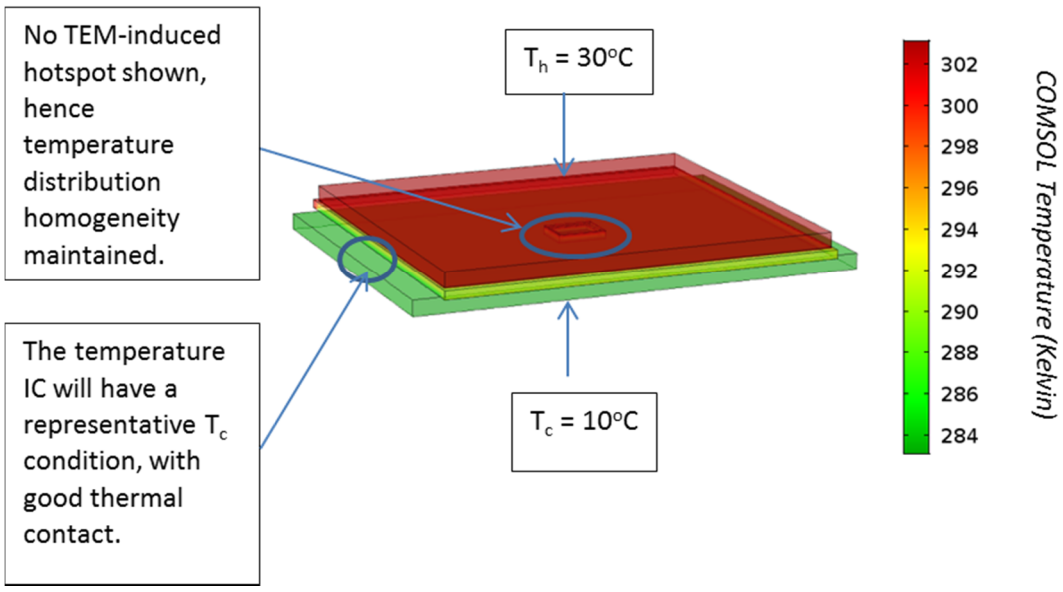

Figure 4-8. COMSOL Results for CLIC Calibration Rig Study

A steady-state simulation was used, and fixed cold-side temperature constraints applied. Convection effects were added into the model calculations, and a representative thermal resistance of 1.4W/mK was selected for the TEM active material. A hot side temperature of 30 °C was input as a fixed parameter. The results of the simulation are shown in Figure 4-8. The inherent thermal resistances due to the thermoelectric module had a negligible effect on the temperature homogeneity at the hot and cold sides of the module. This was due to the large thermal mass of the copper. Additionally it was shown that the mechanical fibre board did not substantially change the heat flow path through the thermoelectric module, and hence the conditions shown in the test rig (and likewise the calibration datasets) would be representative of the TEM within the hybrid receivers.

4.3.2. Thermocouple evaluation

Thermocouples were compared to minimise the manufacturing and couple-to-couple variance, and the resulting effect on the CLIC calibration. A copper plate was used with two holes drilled as close as possible to the thermocouples, effectively to measure the same spot. A cross-examination was done between five K-type thermocouples to determine the pair whose respective measurements

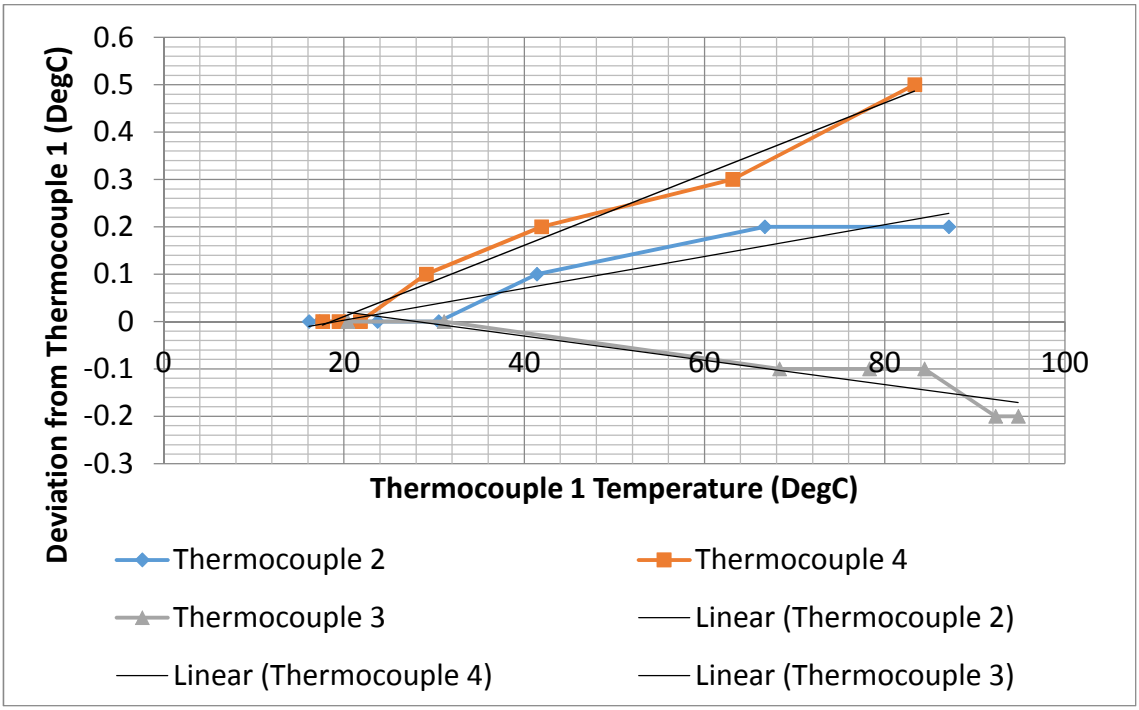

Figure 4-9. Thermocouple Deviation Comparison Data

exhibited the least difference. The experiment was done over a temperature range greater than that used for the calibrations to ensure confidence in the measured deviation (See Figure 4-9). It was found that the worst pair of thermocouples (#1 and #4) exhibited a +0.5^{o}C discrepancy over the total experimental range of approximately 15^{o}C-90^{o}C. The best performing pair, thermocouple 1 and 2, exhibited a +0.2^{o}C absolute for temperatures up to 83^{o}C, over the testing range and were selected for use in the subsequent experiments.

4.3.3 TEM Voc and effective module Seebeck Coefficient

As part of the CLIC temperature measurement technique as described in section 4.1.2, an effective Seebeck co-efficient was necessary for temperature difference calculations. Typically, the Seebeck co-efficient is used as a method of measuring the material property. Ideally, the n and p doped semiconductor material used within the module's legs are as closely matched as possible. The overall module Seebeck co-efficient was measured. This also took into account the additional resistive losses of the internal and external electrical contacts of the TEM. This effective module Seebeck coefficient also includes other parasitic effects which occur within modules only. These current-limiting conditions are achieved with a non-uniform thermal distribution across the thermoelectric ceramic substrates, or discrepancies between individually generated thermocouple current. These measurements were done using the experimental testing rig as described in section 4.3.1. The rig was subjected to a range of hot-side temperatures, and the V_{oc} of the TEM was measured at each applied ΔT value. The experiment was conducted three times to evaluate the experiential repeatability and improve results confidence. Figure 4-10 shows the data obtained.

As can be seen from the experimental data, the thermoelectric Voc was linear within this temperature range. This linearity was expected due to the ZT curves of n-type and p-type Bismuth Telluride within the region of the experiment temperature range[5, 6], (ΔT conditions < 100 ^{o}C, absolute hot side temperature <400K). The effective module Seebeck coefficient was calculated from the gradient of the three plotted linear trends. These three values were averaged and a value of

7.4023 mV/°C was found for the Marlow TEMs and hence carried through to the rest of the temperature measurement calculation via the CLIC calibration.

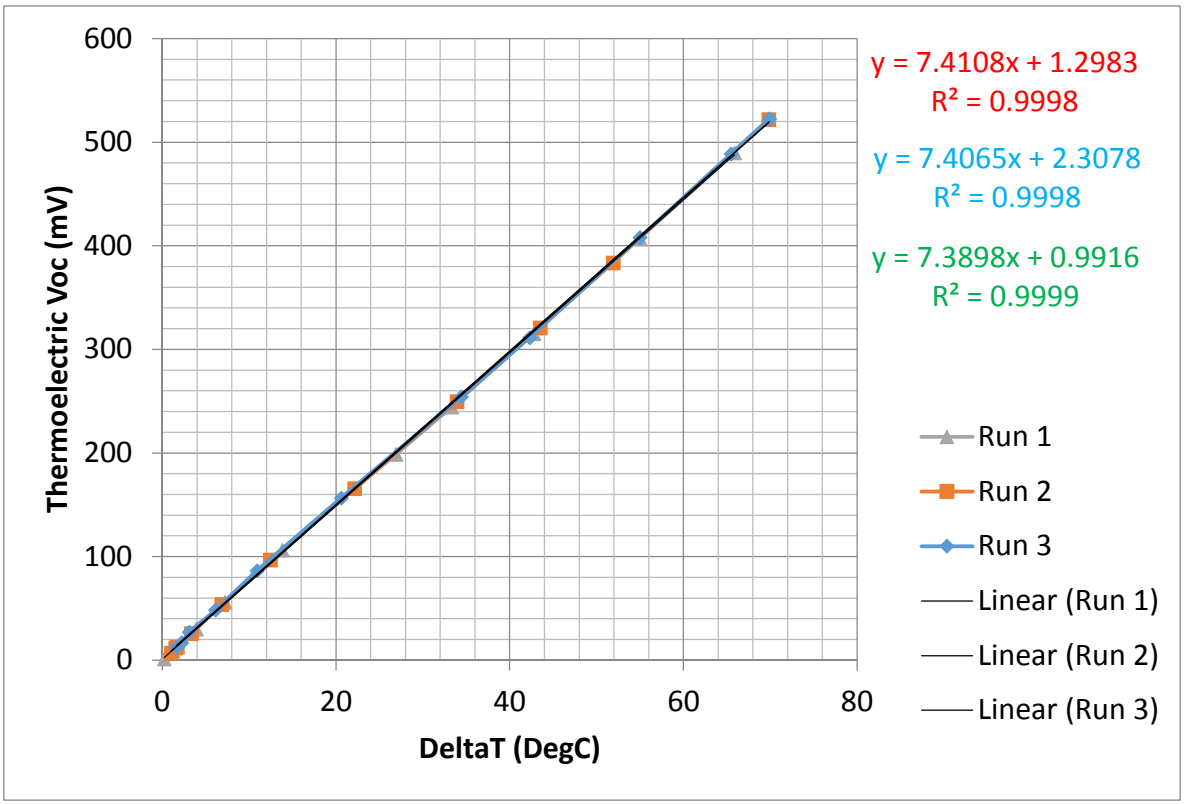

Figure 4-10. "Effective Module Seebeck", Voc Verses ΔT Data

4.3.4 Arduino-based Circuit Results

4.3.4.a Experimental Bit-based data

The voltage measurement of this CLIC design was limited by the ADC resolution and uncalibrated circuitry. Therefore, an Arduino-measured bit resolution was plotted against temperature, to obtain the effective module Seebeck with the units "Bit/°C (ΔT)", shown in Figure 4-11. It was found that at temperatures greater than 12 °C the Arduino measurement bit had an adequate resolution for testing (>6.5 bit/°C) and good linearity (R^2 of ~0.99). At lower temperature differences, and hence smaller TEM V_{oc}, the resolution of the measured Arduino bit resolution dropped. This was due to operating at the lower extremity of the ADC. The resolution was ~2.5 bit/ °C, thereby achieving reliable resolution of within 1°C. Additionally good repeatability was shown through the three experimental tests.

4.3.4.b Trend fitting and "Calibration" based decision

Three different trend regimes were applied to evaluate the obtained data. These were an exponential, a two linear region regime and a quadratic fit. The two linear fits were best, with the highest R^2 fitting values for each dataset compared to the other techniques (0.997 average for the second linear fitting regions compared to 0.9947 for quadratic fitting, and 0.9939 for exponential). The exponential trend exhibited comparative performance in R^2 error, with the overall averaged R^2 value being lower overall. This fit was omitted on this occasion to prevent overfitting of the data. Additionally, a linear fit could be loosely extrapolated outside of the experimentally measured temperature range. This extends the rough indicative (uncalibrated) functionality within the circuit deployment. A calibration gradient of 6.8679 bit/^{o}C for regime 1, 2.6291 bit/^{o}C for regime 2 and a zero-offset of 152.7267 bits was applied within the Arduino CLIC source code, calibrating the device as obtained from the experimental data (See Figure 4-11). This calibration data showed the limitations of using the on-board Arduino ADC, and as such future work in this area is recommended to investigate the use of amplifier circuits (especially instrumentation amplifiers such as the AD524). Additionally, Pulse-Width Modulation (PWM) is an inefficient way to power a thermoelectric module due to resistive losses arising from the current direction changes. As such a linear current supply could in future exhibit greater Peltier driving efficiency, at a greater circuit cost and complexity. Likewise, the bipolar switching transistors used within this circuit could be replaced using a Metal-Oxide Semiconductor, Field-Effect Transistor (MOSFET) with appropriate gate drivers. Alternatively multiplexed DC relays would minimise the consumed switching current and improve device response times.

Table 4-1. Extracted Fitting Co-efficients from Figure 4-11

	m	c
1,a	3.095	150.070
2,a	2.478	153.440
3,a	2.314	154.670
1,b	6.899	54.658
2,b	6.874	57.287
3,b	6.830	59.818
av,a	2.629	152.727
av,b	6.868	57.254
Std. Dev a	0.336	1.945
Std. Dev. b	0.028	2.107

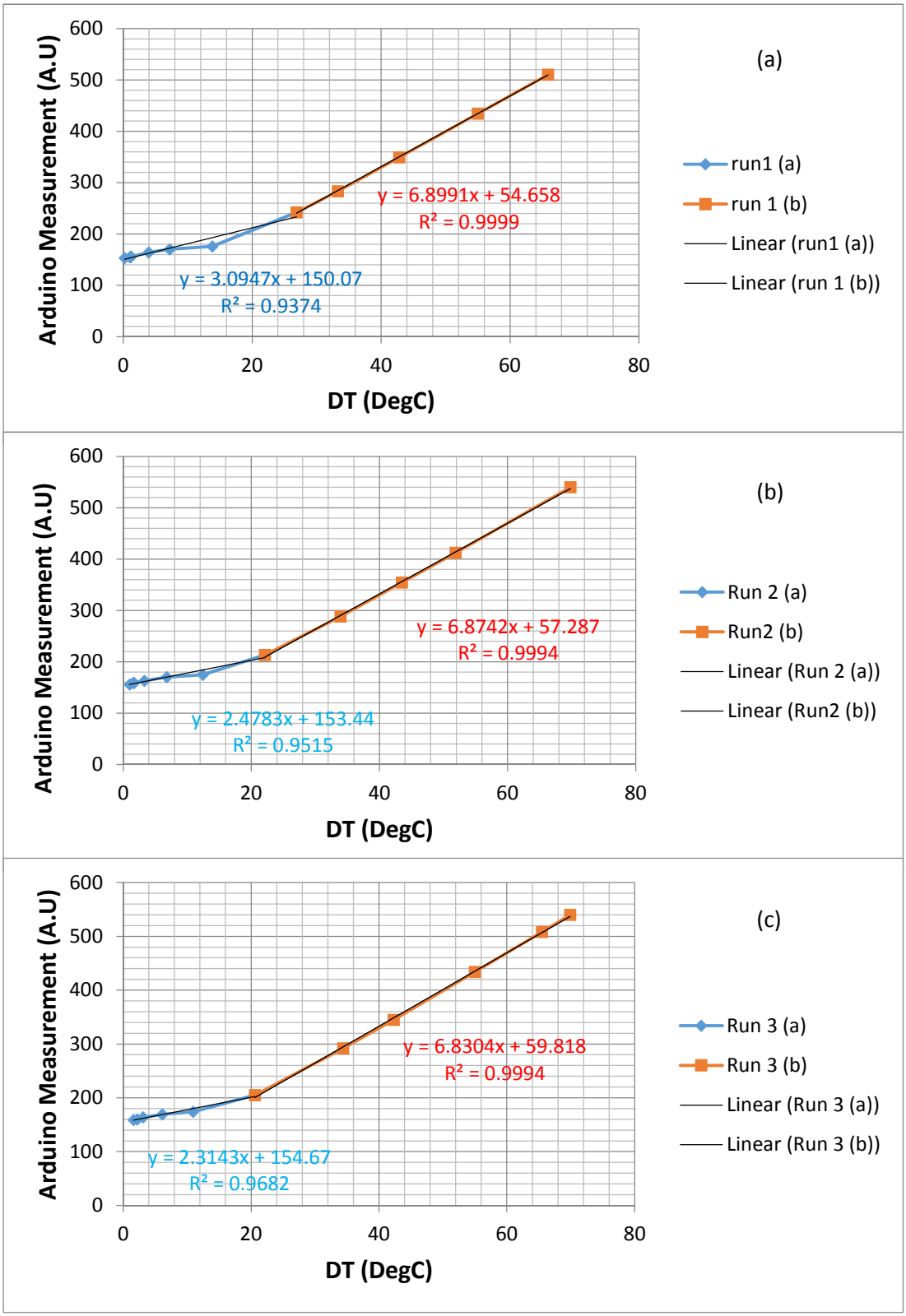

Figure 4-11. Three CLIC Calibration Datasets (Run 1 (a), Run 2 (b) and Run 3 (c)) with the Two-Linear Trend Line Regime Fitted (numbered).

4.3.4.c "Off-Time" Error from the switching

There inevitably was a drop in the delta Temperature across the TE module whilst the Arduino circuit was switched into the open-circuit condition for measurement. This was due to the lack of applied Peltier current during this time period. This drop in the temperature differential and hence the measurement switching's effect on both the temperature measurement resolution quantified in two experiments. The first experiment measured the actual time periods of the switching achieved using this demonstration circuit. Secondly, the thermal time constant of the experimental rig was measured. The time periods of the voltage changes received by the ADC input pins on the Arduino was measured with a laboratory oscilloscope. The driving current "off-time" (Δt1) and the time period between the measurements (Δt2) were found. The temporal resolution was limited in part by the response times of the bi-polar transistors, 200ms, in addition to the conversion time taken by the ADC. Δt1 and Δt2 were found to be 30ms and 750ms respectively (See Figure 4-12).

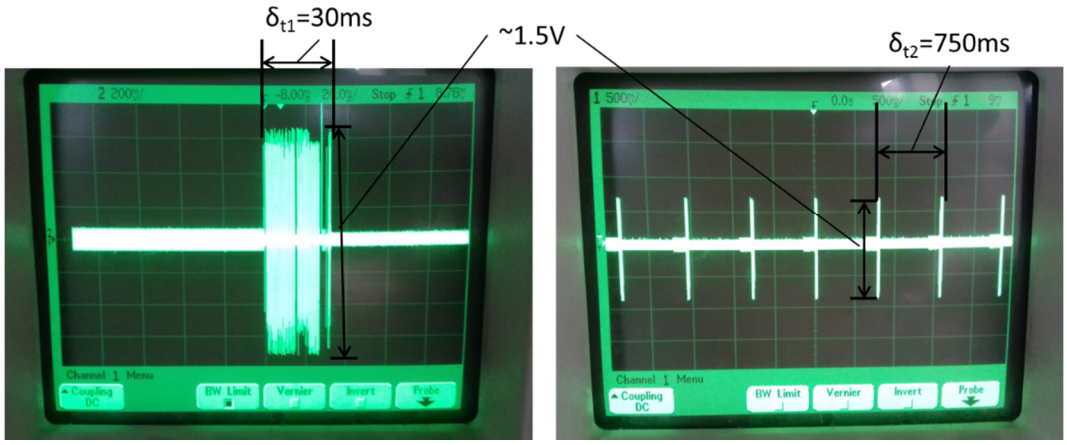

Figure 4-12. Measured Oscilloscope Traces Investigating Circuit Switching Time

A Picologger TC-08 was used to log both hot (T_h) and cold-side (T_c) thermocouple temperatures to evaluate the thermal time constant of the test rig. The same investigated thermocouples (1 and 2) were used as previously. "Worst case" thermal transient conditions were applied during the experiment. After the experimental rig was allowed to equilibrate with the ambient temperature, a voltage was immediately applied using the laboratory supply to the heater. The temperature was logged verses time. This was described as the "worst case" as it

equated to a specific heat flux density of 31.25 kW/m^2, as calculated from I^2R heat being produced (I_{heater} = 0.5A, R_{heater} = 200Ω, $Area_{heater}$ = 40mmx40mm = 1.6x10^{-3} m^2). This heat flux would roughly be equivalent to a cell undergoing instantaneous irradiance changes from dark (0 W/m^2) to >43 suns, (~30 kW/m^2) assuming 5.5mmx5.5mm cell, 1000 Wm^2 and 30% representative cell efficiency, and adiabatic conditions (without transfer of heat across the boundary/to the environment) for the cell rear side was assumed. The initial temperature rate-of-change conditions were calculated, to determine the instantaneous thermal impact upon the cell that would be analogous to this experimental deployment setup. As no time period passed during the simulation, the heat could not possibly diffuse or be transmitted through to an external heat exchanger – as would be realistically present in a non-steady state simulation and also in deployment. Arguably, the steady- state equilibrium that would be established under realistic conditions would mean that this calculation is a slight over-estimation (and perhaps over-simplification) of the instantaneous applied number of suns and hence temperature error reached. However, it is also worth stating that it is highly unrealistic to expect incident irradiance changes of this magnitude in such a short time period. Realistically, considering the movement speed of a tracker, the current tracker's accuracy and the changes in irradiance that are exhibited from sun-rises and sunsets it is logically infeasible for such irradiance flux changes to occur in such a short time period. As such, this thermal time constant from the applied heat flux input can be conserved as a representative value for the temperature measurement inaccuracies from the off-time switching.

An exponential decay curve was manually fitted to the data in excel using the Solver function. The graph combined with the curve fitting coefficients are shown in Figure 4-13 and Table 4-2.

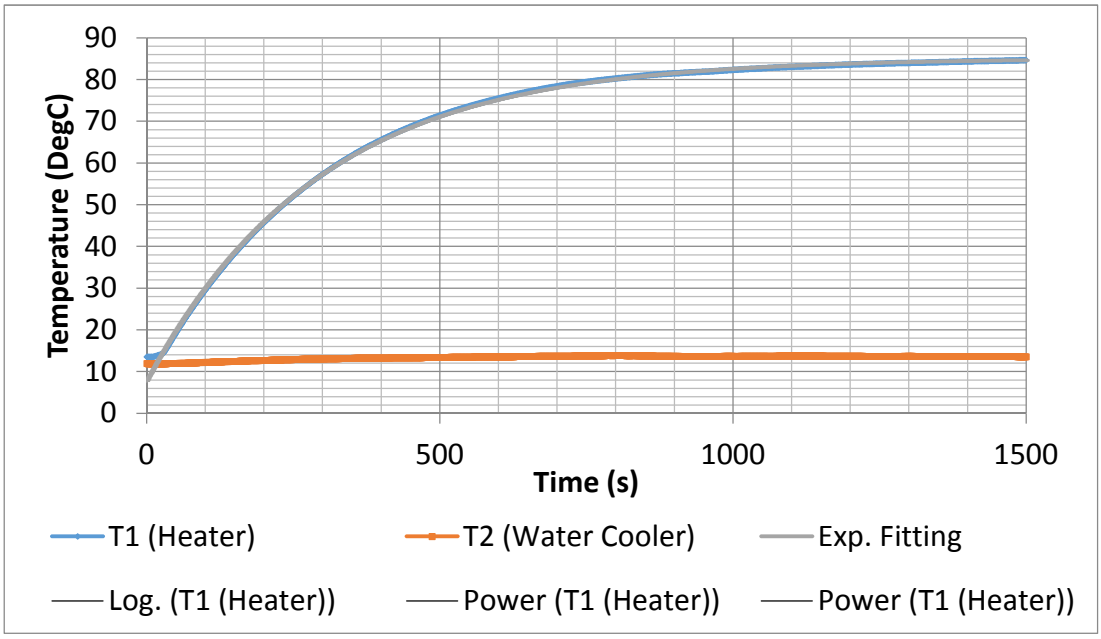

Figure 4-13. Experimentally Measured Thermal Time Constant Data of CLIC Calibration Rig

Table 4-2. The Used Fitting Co-efficients for Figure 4-13.

A	77.275
k	0.003
c	7.830
x^2	0.266
1/K	292.719

The experimental "worst-case" thermal time constant of the experimental set-up was found to be 0.003416 ^{o}C/s. It was estimated that the temperature inaccuracy exhibited by the switching "off-time" was 1.0248×10^{-4} ^{o}C, negligible when compared to the previously described Arduino ADC measurement resolution.

4.3.4.d Measurement Back-Validations

Deployed on the Arduino circuit, the calibration and a demonstrative technique accuracy of the CLIC technique was evaluated. The technique was used to measure the temperature of the same applied range of temperatures, and the measurement re-compared with the datum, the thermocouple. The measurement

accuracy was found to be within +0.99 ºC, -1.08ºC. This is presented in Figure 4-14, represented as absolute error bars. Although this number of datasets (3) is not statistically significant, this work provides a good indication of proof-of-principle for the technique.

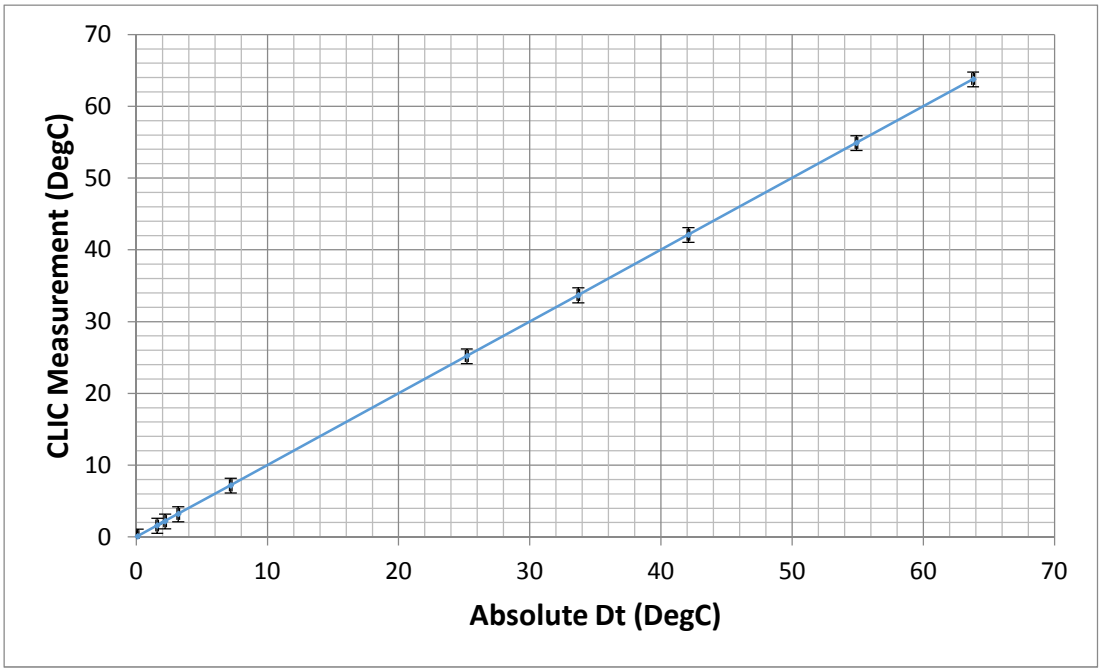

Figure 4-14. The Back-validated CLIC Measurement

4.3.4.e Cooling Proof-of-Concept

A motor driver Arduino shield was used in conjunction with the measurement circuit for Peltier cooling control. It was demonstrated using a GEN IV hybrid receiver that temperatures down to 6ºC were achievable, see Figure 4-15.

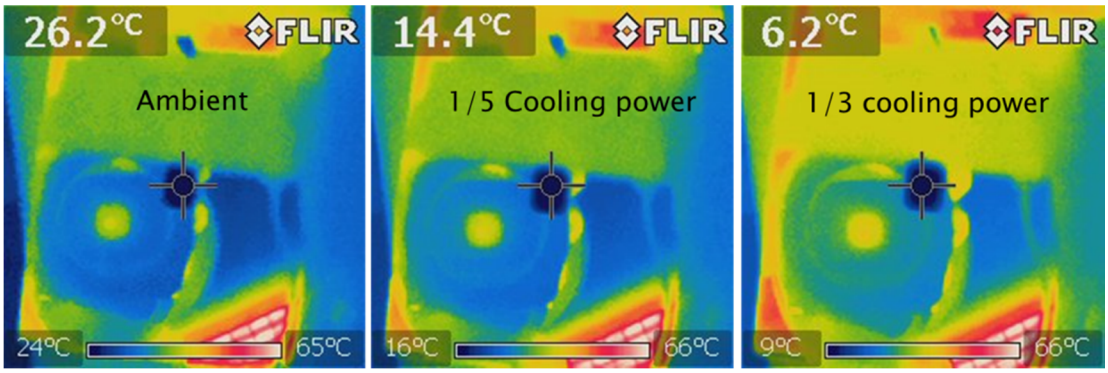

Figure 4-15.Proof-Of-Concept CLIC Driven Cell Cooling

4.3.5 Datalogger-based Circuit Results

4.3.5.a Sample I-V data

As a further technique substantiation the data logger deployed-CLIC was used to establish STC and off-STC conditions for the CPV cell within a GEN V hybrid receiver. Cell I-V scans were obtained for comparison with previous datasets, see Figure 4-16. Four I-V graphs were taken at the CLIC-measured temperatures 23°C, 25°C, 58°C and 71°C. Throughout the I-V scans, the temperature deviations were data logged as shown in Figure 4-17. Throughout the CLIC-controlled cell temperature during the I-V scans, the temperature achieved were shown to be constant. Slight temperature fluctuations were shown for the 71°C temperature, however, the temperature achieved through the CLIC control was still within the 1°C specification of operation.

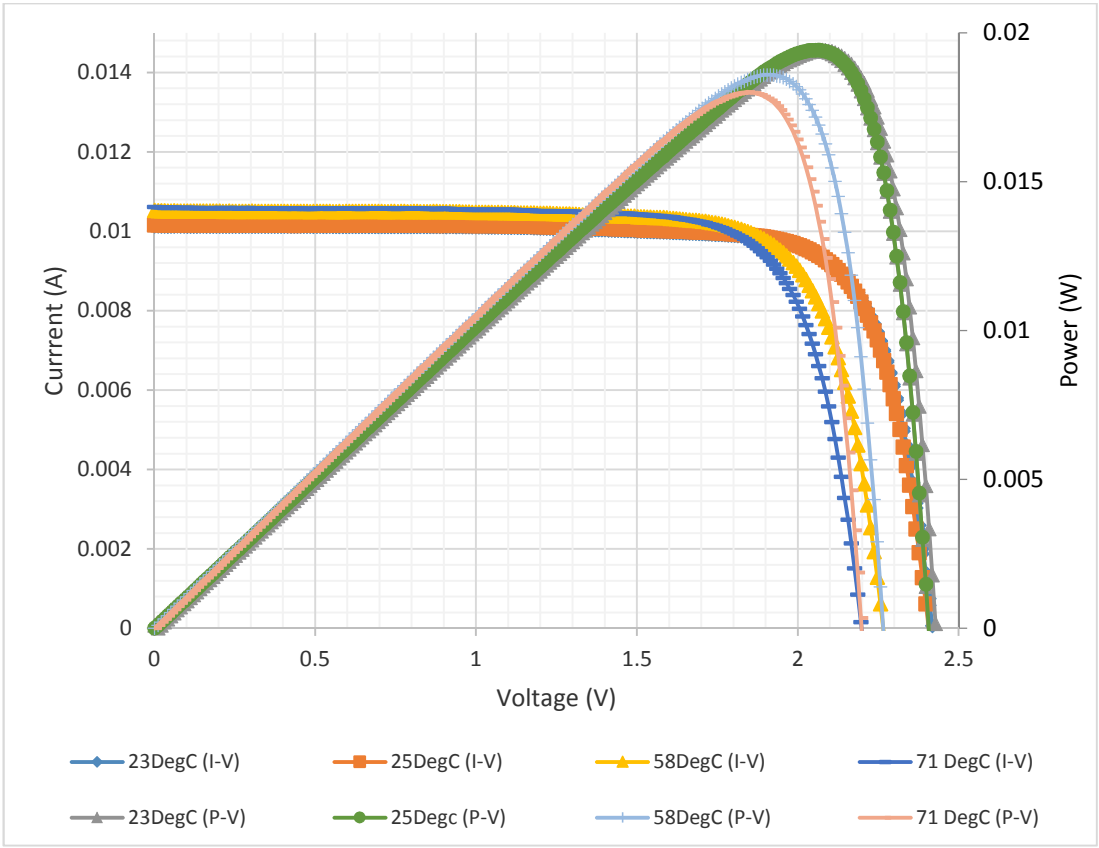

Figure 4-16. Obtained I-V and P-V Curves at 4 CLIC-Measured Temperatures

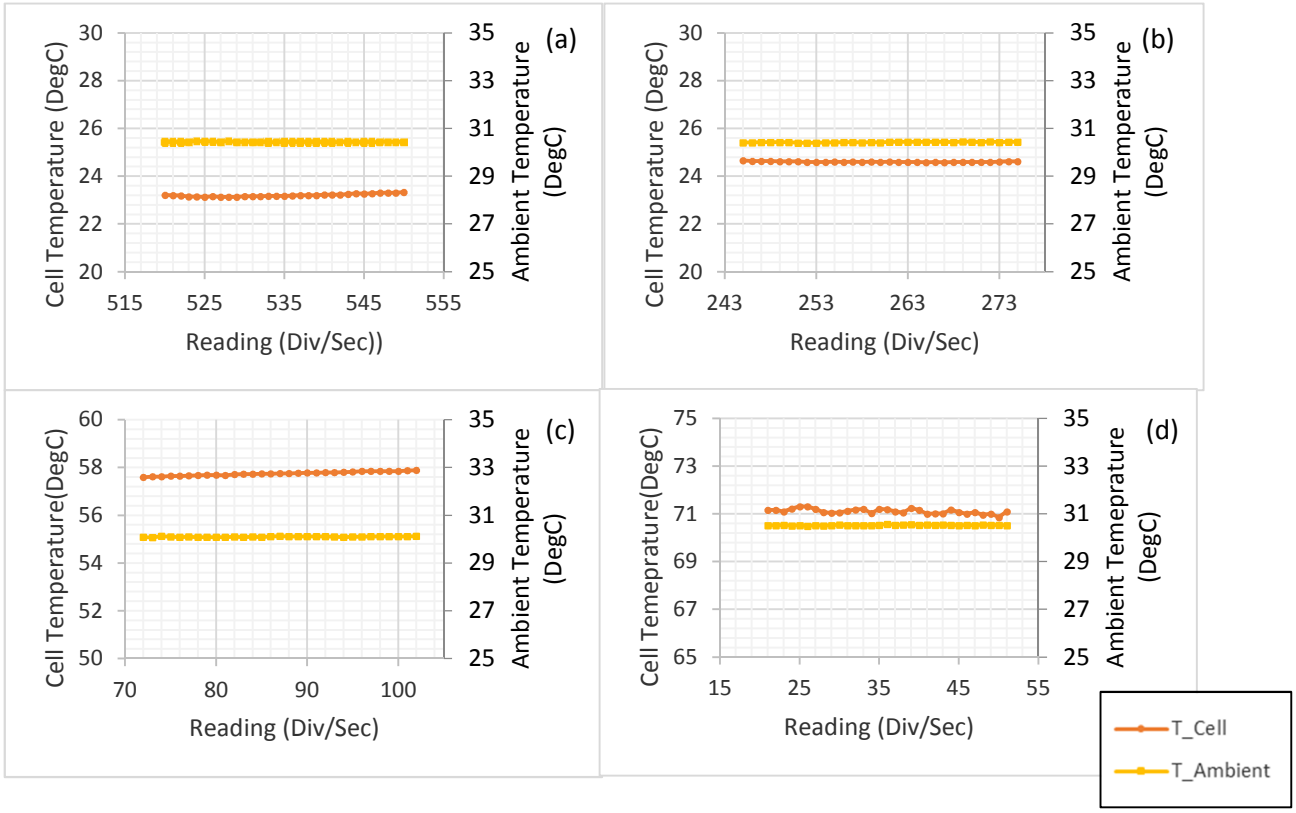

Figure 4-17. The Data logged Temperatures during the above I-V Scans

(a = 23°C, b = 25°C, c = 58°C, d = 71°C)

4.3.5.b Measured Temperature Artefacts during an I-V Scan

During this experiment it was found that "temperature artefacts" were measured throughout an I-V scan. This is due to the high temperature measurement sensitivity achieved using the DL-CLIC, shown in Figure 4-18. As can be seen from Figure 4-18, an overall excitation steady state error was found from the starting conditions of 0.13 °C. The peaks temperature differences recorded for the conditions tending to the I_{sc} conditions (max excitation currents) and the V_{oc} conditions were found to be 0.35°Cand 0.91°C absolute deviation respectively, from the original steady state temperature.

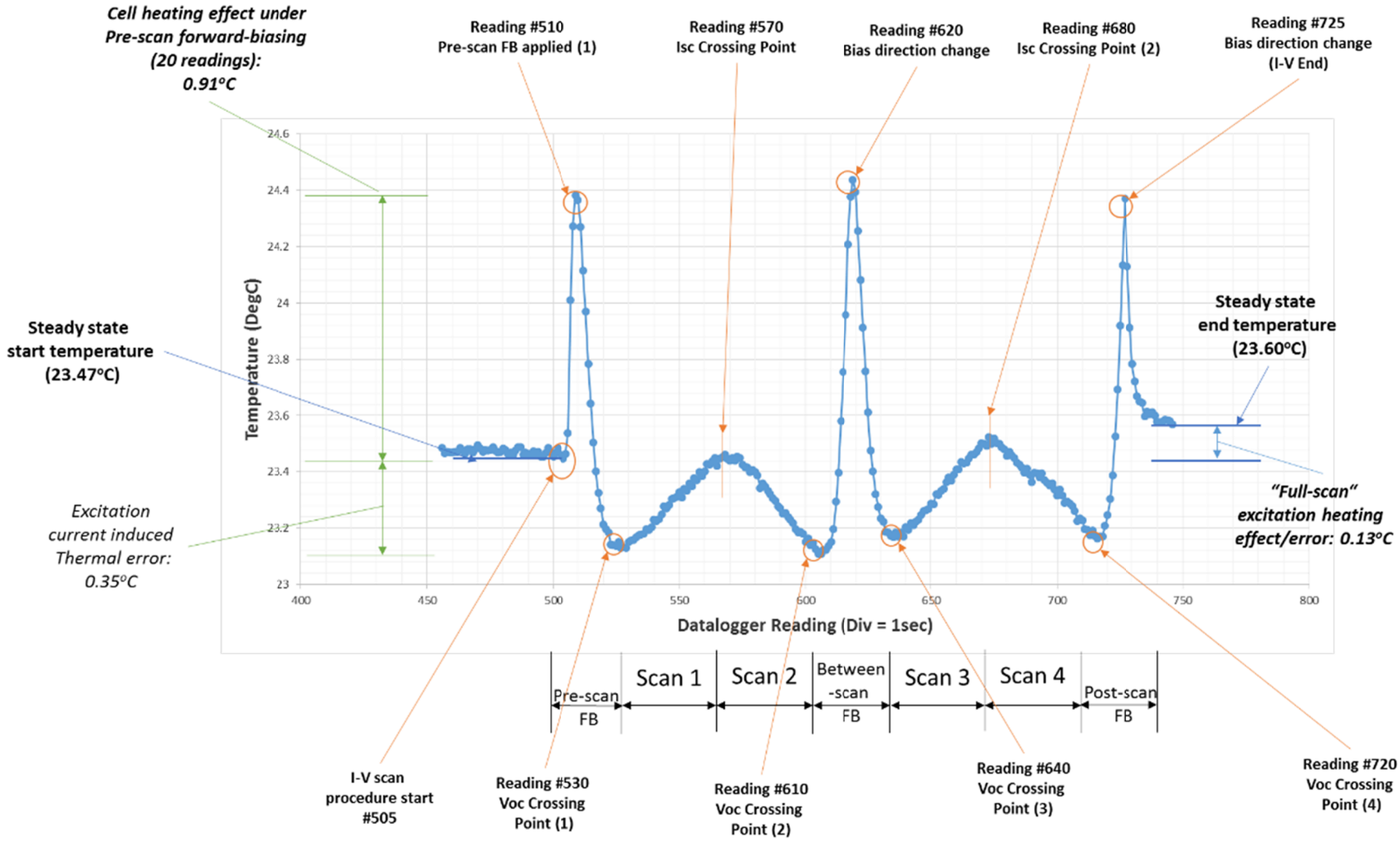

Figure 4-18. The Measured Temperature Artefacts Obtained During an I-V Scan

Alongside their related causes, these artefacts were caused by various internal cell-phenomena that occurred as a result of the applied excitation and measurement time periods. A PV cell exhibits two main resistances internally, as is characteristic of a diode's operation and defined within the one-diode model [7]. These are the series and shunt resistances. The series resistance, (R_S) represents the voltage drops and current losses that occur within the cell, and the contact resistances. The shunt resistance comprises the manufacturing defects and effect detrimental to current generation such as carrier recombination and leakage current through the cell. This series resistance contributes to the I_{sc} induced heating as seen in Figure 4-18, through the I^2R power dissipation through these losses. The larger shunt resistances create the temperature spike, as seen when the cell is forced into the pre-scan reverse-bias condition. The I_{sc}, current increase and V_{oc} crossing point are distinctly detected using the DL-CLIC's measurement accuracy, not previously observable using thermocouples.

The artefacts measured using the DL-CLIC technique from the I-V procedure did not affect the measurement of the CPV cells used, due to the low temperature co-efficient of these devices. The excitation-induced error for previous data obtained was found to be negligible (a 1^oC temperature change equates to a change in I_{sc} of ~$1x10^{-4}$ A, and V_{oc} of ~5mV as calculated using the temperature co-efficients found in Chapter 3.3.4 "Gen V Data")) . However, if these hybrid device designs were to be used with more temperature sensitive semiconductor material or optoelectronic devices, these small temperature fluctuations (0.97^oC forward bias contribution, 0.35^oC I_{sc} heating) could influence electrical data obtained from samples. A compromise would then be necessary, to balance the measurement temporal resolution (data points recorded per sec or speed of measurement) versus the error that would occur due to the temperature increase from applied excitation. Having a short overall excitation time period has the potential to fully remove these effects with the same reasons for the TEM "fast-I-V scans" (see Section 3.2.3). The total scan time is shortened until the temperature rise, and hence the effect on the obtained data, becomes negligible.

4.3.5.c LabVIEW Data of Final CLIC Deployment

Experiments were then done using the flash-lamp solar simulator at the University of Jaén at a range of CLIC-controlled cell temperatures. At each temperature, an I-V Curve was taken. The key cell performance parameters of V_{oc}, I_{sc} and P_{mpp} were extracted and calculated and shown in Figure 4-19.

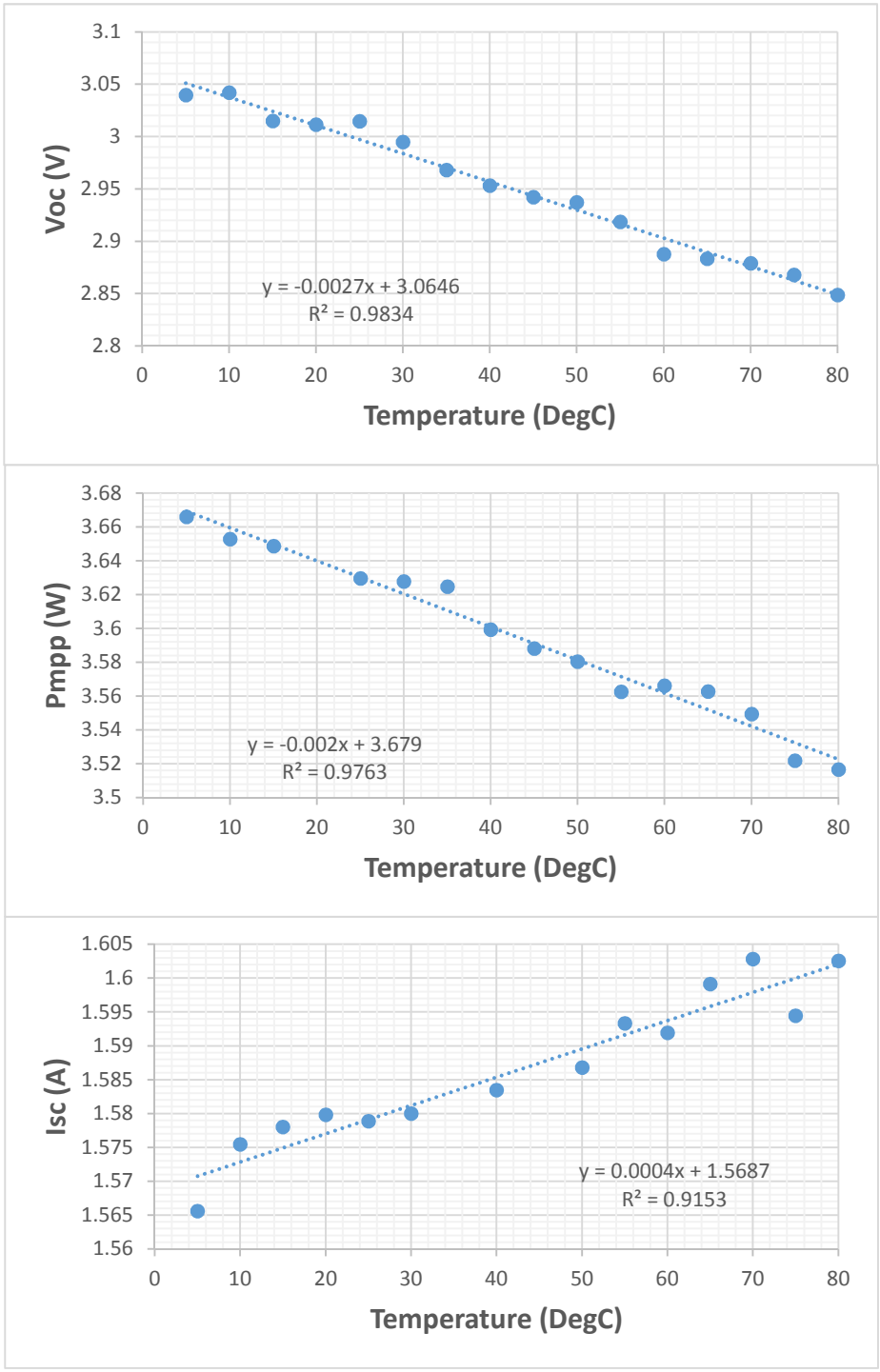

Figure 4-19. CPV Cell Parameters measured using CLIC-Controlled Cell Temperature for a CPV-TE Hybrid Receiver

The parameters are plotted for GEN VII hybrid receiver #9 (see Chapter 5 for detailed description of the GEN VII design, and Section 5.2.2 for the experimental method). A linear trend was shown for the V_{oc}, I_{sc} and the P_{mpp} – showing that automated accurate and consistent control of the cell temperature was achieved using the CLIC technique deployed in a LabVIEW program.

4.4 Future Work

Further characterisation and design of accurate linear current supply circuits for the thermoelectric within the CLIC measurement technique would improve the accuracy of the cell temperature control. After successfully transitioning to the LabVIEW Keysight Data logger/Keysight PSU system, the full technique could be deployed using only a Keithley source meter to reduce complexity. Likewise the V_{oc} measurement accuracy limitations of the Arduino would be overcome, and the power source could be accurately controlled. Implementing a full Proportional Integral Derivative (PID) control system would be beneficial, using the CLIC measurement as the feedback error signal. The overshoot, controller gain and other control parameters could be simulated using MATLAB Simulink or equivalent, and the system design optimised for power consumption efficiency and dynamic performance. A dynamic, irradiance dependant control signal could also be investigated to create an intelligent condition-aware control system, specifically for hybrid devices within CPV systems.

Alternatively the counter direction could be investigated, by producing a commercially-viable cheap controller design for integration directly within the receivers themselves creating “intelligent receivers” for per-cell condition monitoring within CPV systems. This is something that will become increasingly prevalent should the current industry trends keep moving to more complicated systems which include individual module control. Further reliability study data could investigate specific cooling regimes depending on measured environmental parameters, to improve CPV cell lifetime and performance.

4.5 Conclusions

- A novel technique for evaluating the temperature of a CPV cell within hybrid receivers was investigated.
- A bespoke calibration rig was designed and simulated in COMSOL and used to set the reference datum for device calibration.
- The variance and deviation of the thermocouples used within the experiments was characterised over the experimental range, and found to be +0.2^{o}C over the experimental range 15^{o}C-90^{o}C.
- With an Arduino-based circuit deployment, a proof-of-principle temperature measurement accuracy within +0.99^{o}C, -1.08^{o}C was achieved.
- The detrimental "off-time" inaccuracy of the Arduino circuit was measured and evaluated as 1.0248×10^{-4} ^{o}C absolute, with a thermal time constant of 0.003416 $^{o}Cs^{-1}$ and an off-time of 30 ms.
- A second deployment solution using a data logger was developed and investigated.
- Subsequent temperature measurement resolution and sensitivity of up to 6.d.p were hence obtained, with sub-degree artefacts measured due to the inherent temperature influences within an I-V scan.
- Future designs were discussed including transitioning to circuit manufacture or deploying on a Keithley source meter.

4.6 References

1. Rowe, D.M., *Materials, preparation, and characterization in thermoelectrics*. Vol. 1. 2012: CRC press.
2. Goldsmid, H., A. Sheard, and D. Wright, *The performance of bismuth telluride thermojunctions.* British Journal of Applied Physics, 1958. **9**(9): p. 365. [Accessed: 01/05/18]. Available at: http://iopscience.iop.org/article/10.1088/0508-3443/9/9/306/meta
3. [Online] Omega, *Revised Thermocouple Reference Tables*. [Accessed: 01/05/18]. Available at: https://www.omega.co.uk/temperature/Z/pdf/z204-206.pdf.
4. Micheli, L., et al., *Performance, limits and economic perspectives for passive cooling of High Concentrator Photovoltaics.* Solar Energy Materials and Solar Cells, 2016. **153**: p. 164-178. [Accessed: 01/05/18]. Available at: https://www.sciencedirect.com/science/article/pii/S0927024816300307
5. Goldsmid, H.J., *Bismuth Telluride and Its Alloys as Materials for Thermoelectric Generation.* Materials, 2014. **7**(4): p. 2577-2592. [Accessed: 01/05/18]. Available at: http://www.mdpi.com/1996-1944/7/4/2577/htm
6. Yamashita, O., S. Tomiyoshi, and K. Makita, *Bismuth telluride compounds with high thermoelectric figures of merit.* Journal of Applied Physics, 2003. **93**(1): p. 368-374. [Accessed:01/05/18]. Available at: https://aip.scitation.org/doi/abs/10.1063/1.1525400
7. Chan, D.S.H. and J.C.H. Phang, *Analytical methods for the extraction of solar-cell single- and double-diode model parameters from I-V characteristics.* IEEE Transactions on Electron Devices, 1987. **34**(2): p. 286-293. [Accessed: 01/05/18]. Available at: https://ieeexplore.ieee.org/abstract/document/1486631/

Chapter 5 : Further Hybrid Receiver Progress and Transitioning to Module Level

This chapter describes the hybrid receiver design changes that were implemented, facilitating full integration within a POE-SOE CPV module. The individual GEN VII receivers were characterised with bare cells, SOE, and SOE with POE. The unique performance of the TEM for temperature control was investigated during on-sun testing within a POE-SOE-PV-TE module.

5.1 Background

5.1.1 Transitioning to a Full-scale GEN VII Module – *Mechanical Design*

Improvements were made to the receiver PCB design, based on the testing experience from the GEN V and VI receivers described in Section 3.3. This included removing the long curing times the epoxy used within the design to streamline the manufacture process, and improving the thermal conductivity between the CPV cell and TEM by using a very thin layer of solder. Low-eutectic point solder is frequently used in the manufacture of TEMs. Solder compounds consisting of Indium and Tin (InSn) are one such solder, with a melting point of around 118^{o}C. This was selected to replace the silver epoxy used in the GEN VII hybrid deign (see Section 5.1.2). Maintaining vibrational rigidity was crucial for effective wire bonding to the cell top contact tracks. The clamping pressure previously achieved with two-part mechanical only epoxy was replaced, using four screws included within the corners of the PCBs. Holes were drilled through all component boards, with care given to ensure accurate co-incident boards. Screws of two different sizes were chosen as a DFMA consideration (M3 and M2) to allow future machine to automatically detect a board orientation. Clearance holes were used to ensure a good fit. The bi-layer PCB architecture was conserved from the previous generation designs for independent device contacting. The vertical dimensions were modified slightly to incorporate different geometries of TEM for optimisation in this area, without compromising compatibility for the previously used Marlow modules. The bottom PCB was made from 1mm thickness board, with the top 1.6mm board giving a

2.6mm overall PCB thickness. The copper substrate used counter-sunk holes for the screw heads, keeping the receiver flat eliminating vertical optical alignment error.

Previously the SOE alignment with regards to the cell active area was found to be critical to the hybrid receiver performance. To improve this optical alignment positional marks were included in the copper tracking layout of the PCB board, to facilitate manual and future pick-and place alignment of the SOEs. Track separation distances >0.9mm were included for the PCB tracking, in accordance to the IPC-2221A standard for PCB design [1]. This distance was calculated using a 1.5x safety factor considering the maximum 12-receiver in-series string conditions at 1-Sun, STC, and at a 330x representative module concentration ratio. Appropriate bonding pads were added for the inclusion of the Bi-pass diode (BPD) onto the top surface, minimising the amount of thermal mass of copper to be heated up by the soldering iron for soldering. Tracks and cut-out location holes for the TEMP IC were included conserving the functionality of the CLIC technique for experimental testing. The mechanical design was modelled in Solidworks and the electrical design was done using Altium, with the technical dimensions and layout shown in Figure 5-1.

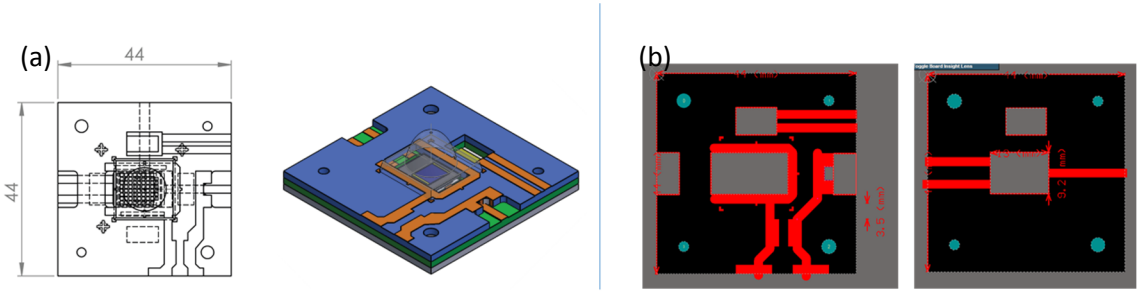

Figure 5-1. Detailed Designs of a GEN VII Receiver (a) Solidworks Design, (b) Altium Design

As with the previous generation receivers, the manufacturing procedure was split into three stages: pre-cleanroom, pre wire-bonding and bond/encapsulation. The boards were assembled with the screws tightened using an electric hand drill with the torque limiter set to number 5, ensuring consistent assembly. The copper tracks, were pre tinned, the wires stripped twisted and tinned then soldered together using the iron at 350^{o}C to limit heat damage to the fibreboard binding epoxy. The external connection wires had a 90^{o} bend added

using fine nose tweezers. These ensured that any load pressures on these wires was subsequently dissipated by a counter-spring effect. The BPD for GEN VII was soldered with the iron being placed on a track a small distance (<1mm) away on the copper track. The track itself was heated, the solder reflowed and the BPD placed with tweezers whilst the solder was molten. Figure 5-2 shows a hybrid substrate blank, pre-TEM bonding.

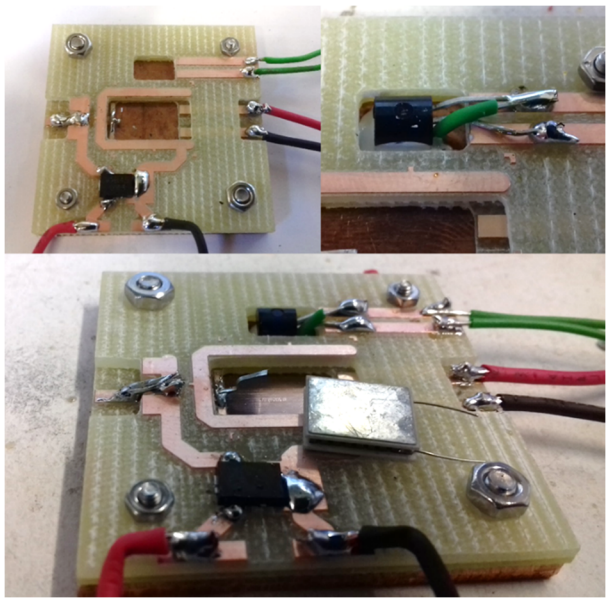

Figure 5-2. The GEN VII Prepared pre TEM soldering

5.1.2 An overview of the Novel, Epoxy-less, TEM "self-soldering" technique

The active components (the TEM top side and the CPV cell rear) were bonded together using an improved approach. This different method of assembly drastically reduced the time for manufacture of the CPV-TE hybrid devices, as most of the long epoxy cure times were removed or replaced with alternatives. The four-hour silver epoxy cure time and the overnight cure-time of the mechanical araldite epoxy, were removed completely. As has been previously discussed, the mechanical strength of the bond made was crucial to the long-term receiver performance and reliability. Additionally the electrical resistance, contact resistivity and current carrying capability of the solder itself was also critical to maintaining electrical performance. For the GEN VII receivers, Indium Corp. "Indalloy" 1E In-Sn Solder Alloy was used with a 4-0A flux from the same company. The thickness achieved using this $In_{0.52}$ $Sn_{0.48}$ solder used for this process was much thinner (approximately 0.2mm) than the H20E epoxy layer (approximately 0.5-1mm) achieved previously.

The thermal conductivity was stated to be 34 W/mK (+17.24%), with an electrical resistivity of $1.5x10^{-5}$ Ωcm (an order of magnitude smaller) [2] as compared to the previous H20E thermal conductivity of 29W/mK, and electrical resistivity 4x10-4 Ωcm (See Section 3.1.2). This self-soldering process allowed for quicker and more consistent manufacture.

During the typical manufacture process of a TEM, a high temperature solder is used to bond the TE legs, located using a jig. Through careful control and using the typical high thermal resistance of the active thermoelectric material as defined by the figure of merit (ZT). A larger thermal resistance gives larger phonon residence times within the material, improving the potential for heat to electricity absorption and conversion. A second internal solder is used to quickly solder the top ceramic to this other half-module, whilst preventing the reflow condition of the other side.

A novel TEM "self-soldering" technique was devised, tested and evaluated for the GEN VII receivers. The TEM was first bonded to the receiver copper substrate, then the cell was bonded to the TEM in two separate stages. This was done by controlling the temperature and exploiting the difference of the material melting points. This gave a temperature regime, procedure and temperature-tolerance "window". This self-soldering technique exploited the tolerances between the two solders (internal and metallisation) at the temperature where the TEM metallisation was molten but the internal solder joining the thermoelectric legs to the ceramic copper tracking wasn't molten. The technique was to use the metallisation on the supplied TEMs. The bottom side was soldered through using a hotplate. Then the top side was soldered to the cell in the cleanroom with a hotplate set at a "pre-heat" temperature. Then the TEM itself had a current applied to pump additional heat to the top surface, thereby increasing its temperature. This would then make the top metallisation molten, keeping the rear solid. The TEMs used in the GEN VII receivers were sourced from European Thermodynamics Ltd. (ETL) and were specified to be pre-metalized with a thin layer of the lower temperature this $In_{0.52}$ $Sn_{0.48}$ based Indalloy solder for this process.

The high internal thermal resistivity of the module as mentioned previously added control over the process. It allowed the copper substrate to be heated, and the bottom metallisation brought up to melting/reflow temperature, whilst keeping the top metallisation solid. Not only did the self-soldering method directly allow a transition away from the direct bonding using epoxy methods, but also removed two thermal interfaces between the cold side substrate and the cell.

5.1.3 Full module design and Manufacture

The commercial CPV module used for on-sun testing in Section 3.2.5, was modified to include Gen VII hybrid receivers for effective on-sun testing of these designs. The module used an aluminium frame as the basis for the mechanical structure. The rear-side was taken as the datum for construction and designed alignment of the POE, and was made from a formed/stamped sheet of black-painted aluminium. The POE array consisted of a 6x2 matrix of Fresnel lenses, glued onto a metal skeleton with a 330x geometric concentration ratio. The POE were then attached to a black PVC frame, with a designed groove to align with the aluminium frame. The baseplate included holes to facilitate external wiring and connecting. A passive finned heat exchanger was included on the rear side of the baseplate.

The spatial location of the receivers was measured from the focal point of the primary optics, and the receivers attached in their geometric location using a polymer-based double-sided tape. The tape was thin, thereby inherently having a small thermal resistance. This high-temperature tolerance was necessary for on-sun testing under POEs as the temperature typically reaches in excess of 70^{o}C in commercial modules. Preliminary evaluation testing was done on the tape using a soldering iron, a thermally conductive aluminium test plate and a thermocouple to test the adhesion of the mounting tape at higher temperatures. It was shown that at a temperature in excess of 160^{o}C, no change in the adhesion or mechanical properties of the tape was shown.

To protect the connecting wires and temperature sensitive devices on the hybrid receivers, off-axis shielding was added in order to reflect back any solar irradiation that would cause damage. This was done with a piece of 3M mirror film [3], cut to size and held in place using high-temperature antistatic polyimide tape. The vertical distance of the POE was adjusted using spacing wire of a fixed diameter. Right-angle steel mounting brackets and bolts were used at three mounting points to attach the module to the tracker. An image of the fully assembled module and internal structure inside the manufactured module is shown in Figure 5-3.

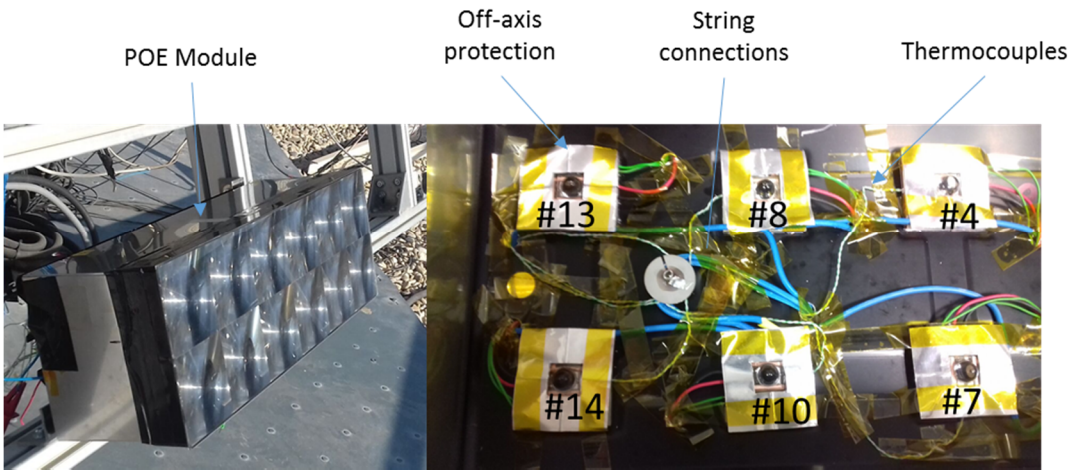

Figure 5-3. Fully assembled POE module and overview of the receivers inside

5.2 Experimental Methods

5.2.1 Self-soldering experimental setup

A hotplate was used to heat the copper-PCB hybrid substrate set via the plate controls at approximately 100°C. A piece of copper sheet with a hole drilled to the centre was placed on top of the hot plate, and a k-type thermocouple with the Fluke 52II handheld thermometer used to monitor the hotplate temperature accurately. (The same thermocouples were used from Section 4.3.2). Figure 5-4 shows the setup used. The sample copper substrate (which also included a thermocouple hole) was placed onto this copper plate with RS metal-oxide Thermal Interface Material (TIM) (Thermal conductivity 0.65 W/mK). The temperature of the sample was measured as incremental temperatures were applied to find the critical melting point of the solder. It was found the application of the 4-0A flux had a drastic effect on the reflow of the Indalloy solder, with both a lower critical temperature for melting and higher mechanical adhesion being observed.

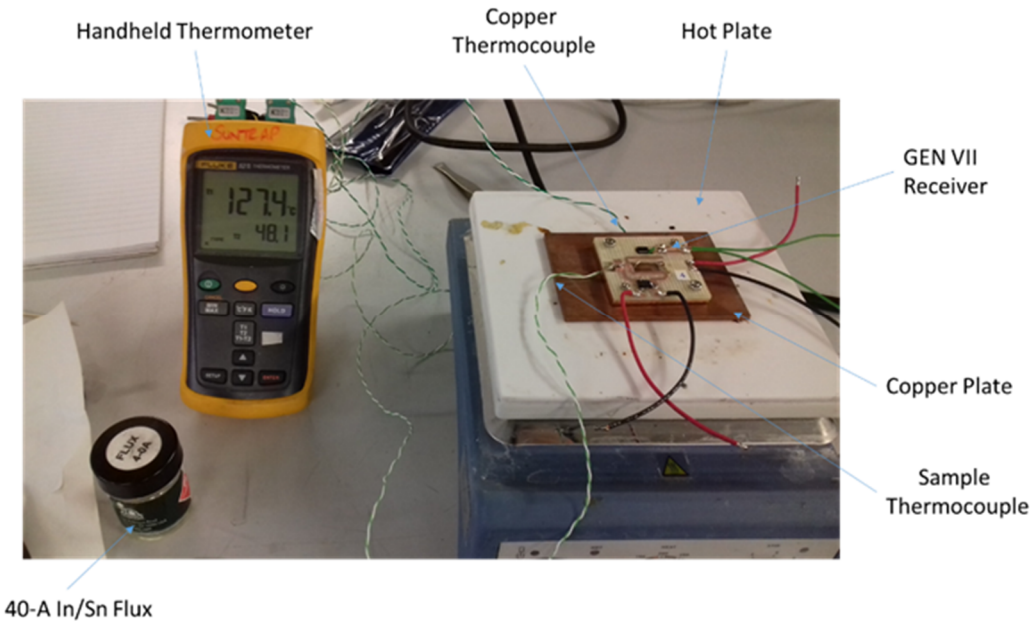

Figure 5-4. The TEM Bottom Contact Soldering Setup

To prevent any particulate contamination of the CPV cell, this TEM self-soldering technique was done inside the cleanroom before the receiver was wire-bonded and encapsulated. A similar technique to the bottom soldering methods was adopted, with a copper plate and two thermocouples to accurately measure the actual sample base temperature (see Figure 5-4 and Figure 5-5). Once the

receiver was at the correct temperature (80^{o}C), the cell was carefully placed onto the top TEM surface solder using a vacuum wand. The cell was aligned visually using fine tweezers to the board indicators at the centre of each cell side. The voltage supplied by the PSU was measured with a multi-meter. Supplying a current to the TEM itself pumped heat to the top ceramic surface from the hot plate, keeping the bottom metallisation solid, and the cell bonded to the pre-applied molten top InSn Solder. The TEM hot side was temporarily increased past the solder melting temperature for approximately 5 seconds (set at 0.45A, 5V limit, Output off).

When the voltage was close to 2V, the top solder was checked using a cleanroom wand for signs of melting. Once molten, a clean wand was used to apply slight downward pressure with care being taken to avoid any misalignment. The current output was switched off and the cell was held for a further 10 seconds to allow for solder cooling and re-solidifying. The sample was then taken off the hotplate, allowed to cool and the mechanical attachment checked using the tweezers. The receivers were then wire bonded with at least 12 bonds each, the SiLO SOE attached and encapsulated using the same procedure as the GEN V receivers (See Section 3.1.4).

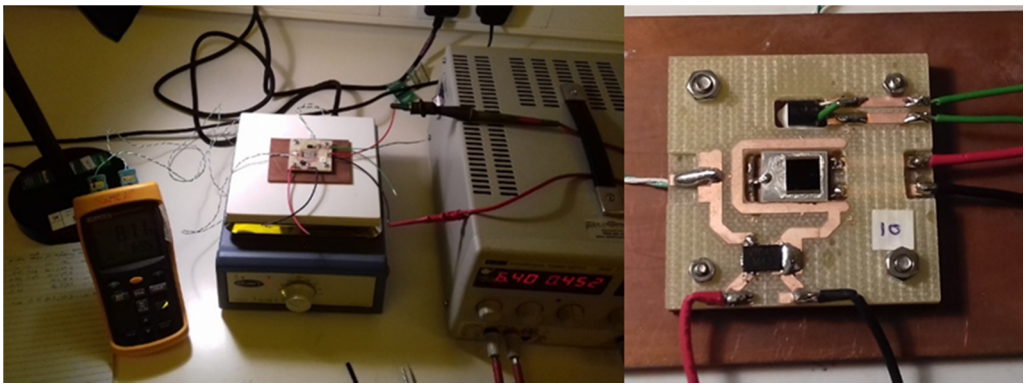

Figure 5-5. A GEN VII Receiver Undergoing Top-side TEM self-soldering in the Clean Room

5.2.2 Manufacturing GEN VII Hybrid Receivers using the "Self-Soldering" approach

5.2.2.a Rear-side Soldering

Table 5-1 below lists the data obtained, with this soldering temperature found to be 135°C for the bottom copper plate, which equated to a 125°C receiver substrate temperature. It was shown that the flux was necessary for any mechanical adhesion to occur.

Table 5-1. Experimentally Measured Rear TEM Solder Data

Rear Plate Temp (DegC)	Sample Temp (DegC)	Bond Copper Only?	Bond with Flux?
103.0	100.0	N	N
114.0	110.0	N	N
118.0	115.0	N	N
123.0	120.0	Y, V Poor	Y, Good
125.0	124.0	Y, Poor	Y, Good
133.0	129.4	Y, Poor	Y, Good
136.0	131.0	Y, Poor	Y, Poor
138.0	135.6	Y, Poor	Y, Poor

It was found that in some cases, beads of excess solder accumulated between the edges of the TEM and the PCB hole. This excess was enough to create large beads that spilled over the bottom TEM ceramic and contacted more than one leg of the internal module thermocouples. This caused an electrical short circuit. Care was therefore taken to remove these beads using tweezers.

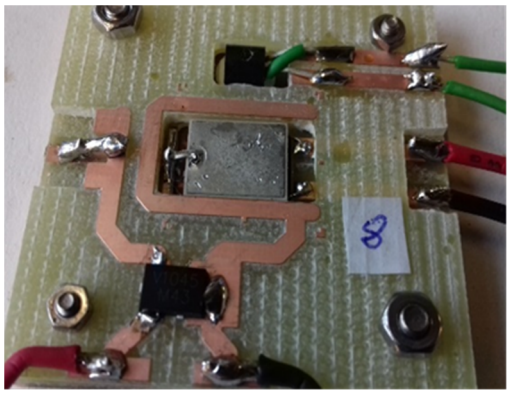

Figure 5-6. The resulting bottom soldered TEM within a GEN VII Receiver

5.2.2.b Top-side Soldering

Once the rear-side was soldered (see Figure 5-6), the samples were transferred into the cleanroom. Prior to bonding, the cells were carefully removed from their wafer packaging and images taken under a microscope to characterise any visible defects of either the material quality, electrical contacts or post-growth debris. In some cases, poor surface quality was shown and as such these cells were omitted from being included into receivers. To preserve the rear soldering of the TEM and also prevent damage to the cell, an additional critical temperature limit of 80^{o}C existed to prevent any degradation of the cell. The CPV cells were pre-selected based on electrical probe characterisation data.

Two different "priming" temperatures (the temperature the hotplate was set at, before the heat pumping stage of the TEM) and a range of TEM "reverse Peltier" excitation currents were applied to evaluate the optimum bonding conditions. The priming temperature was varied up to the critical 85^{o}C. Using current values higher than 0.6A at the hot-plate elevated temperatures was found to de-solder the external TEM leg connections, due to the compound addition of the resistive heating through the legs themselves to the priming temperature. This exceeded the internal solder melting point of 130^{o}C. It was found that using a preheating "primer" hot plate temperature of 80±5^{o}C was effective. A 0.45A constant current source was applied, (safety source limit of 5V).The current supply automatically varied the input voltage to maintain this constant current constraint, matching the changing load to be expected from the temperature dependant parameter inherent for TEM operation. When the applied voltage reached 2.1V, it was consistently shown that this value represented a critical melting V_{oc} for these TEMs within the GEN VII receivers. Given that the hot plate priming temperature remained constant, this voltage value can be equated to describing similar established temperature differentials (ΔT) needed to melt the solder – as shown for all cases of the 12 devices made (images for batch one is shown in Figure 5-7). Table 5-2 below shows the experimental data obtained through the exploratory testing for this self-solder technique in the GEN VII hybrids. Post manufacture in the

cleanroom, photographs were taken of all the manufactured receivers to evaluate the efficacy of the optical alignment that took place – post Sylguard cure.

Table 5-2. Experimentally Measured Top-Surface TEM Bonding Temperature and Current Excitation Conditions for Batch 1 of the GEN VII Receivers

	Ite (A)	Vte (V)	Hot Plate Temp (DegC)	Sample Temp (DegC)	Melt?
50DegC Pre-heat Trial	0.150	0.400	52.8	52.9	N
	0.300	1.300	53.2	53.2	N
80 DegC Pre-heat Trial	0.150	0.690	78.7	75.7	N
	0.200	0.910	79.8	78.5	N
	0.250	1.100	79.2	79.0	N
	0.300	1.370	76.8	76.9	N
	0.350	1.510	75.8	74.9	N
	0.400	1.810	81.4	80.7	N
	0.450	2.100	80.9	80.6	Y
	0.450	2.090	80.4	80.3	Y
	0.450	2.120	79.3	78.9	Y

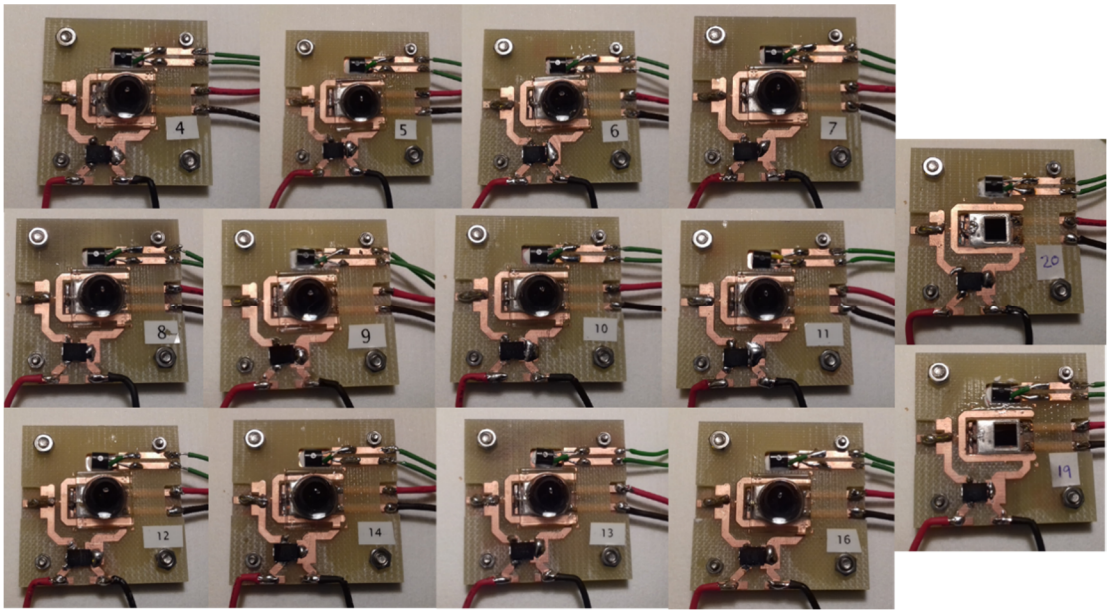

Figure 5-7. The 14 Manufactured GEN VII Receivers (Batch 1)

5.2.3 The Indoor Solar Simulator at Jaen University

A “flash lamp” type solar simulator was used at the University of Jaén to achieve the large-area irradiance flux needed for obtaining I-V characteristic data for the SOE-CPV-TE receivers under primary optics. Jaén university was chosen to be an experimental collaboration partner due to the already-established relationships formed through the EPSRC SUNTRAP consortium. Other larger institutes exist in Spain, including ISFOC Madrid. ISFOC are world-leaders in the field of CPV module design, reliability testing and qualification [5-14]. However, working with these institutions was found to be infeasible in the duration of this work. Jaén university was chosen as an alternative, due to their experience and work in the field of CPV [4, 15-18]. A pulsed Xenon light source was used, with appropriate filters to maintain an AM1.5G spectrum.

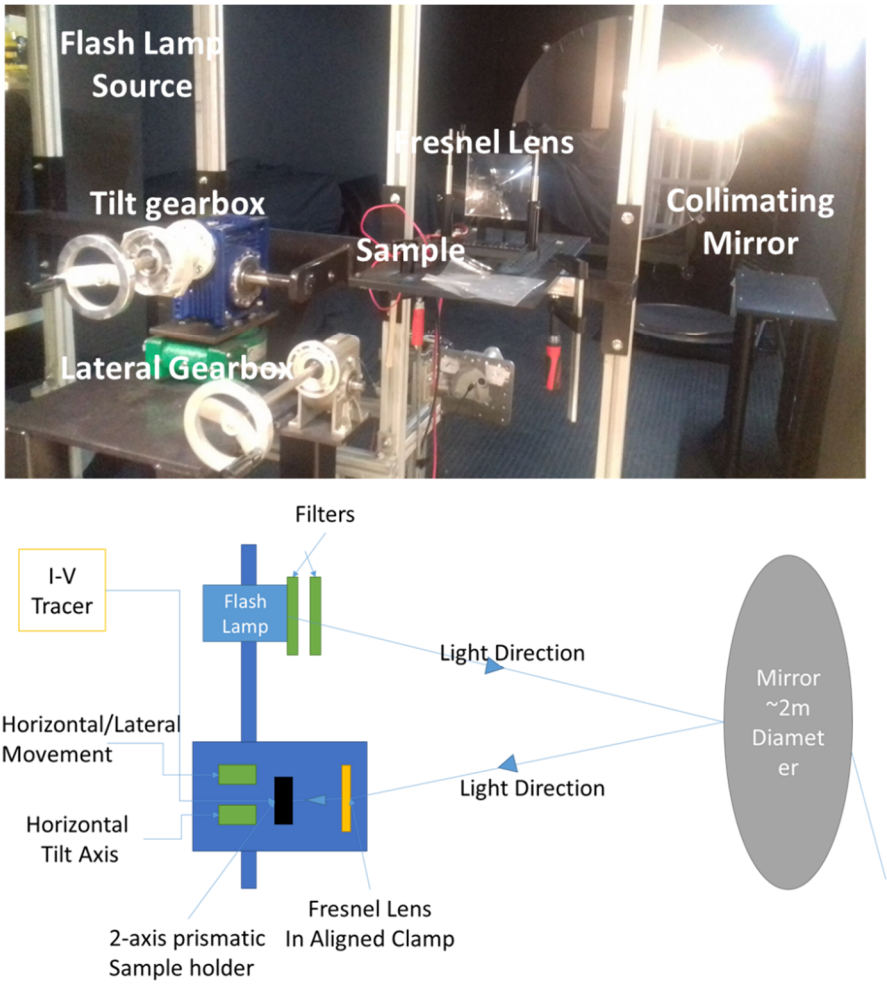

Figure 5-8. An Overview of the Flash-lamp Solar Simulator (Bottom), Alongside a Photo of the Setup (Top)

The benefit of using such a type of light source, allowed adequate testing of large area devices, without the need for thermal compensation of the Device Under Test (DUT), as the time period for each measurement is small (<200ms). Use of a flash lamp simulator also had advantages with relation to the spectrum shift during testing. The short lamp exposure prevented the light from getting hot during operation which would change its emitted spectra. In addition to the AM1.5G filters, 30% and 50% intensity pass filters were used to vary the irradiance. An overview diagram of the setup is shown in Figure 5-8.

The temperature of the laboratory was climate controlled and this ambient temperature was recorded using a k-type thermocouple to maintain 25^{o}C STC throughout testing. Before testing each receiver, the focal distance of the sample was adjusted until a maximum I_{sc} was achieved. Additionally, the light path was visualised in "slices" by using a thin piece of plastic in the cone to project the light cone to get a visual representation (See Figure 5-9). The I-V tracer was based on a SAV HELIOS 3198 system, as designed by Instituto de Sistemas Fotovoltaicos de Concentración (ISFOC), at the Universidad Politécnica de Madrid. A Delta Elektonika SM120-13 power supply unit was used to obtain the I-V measurements.

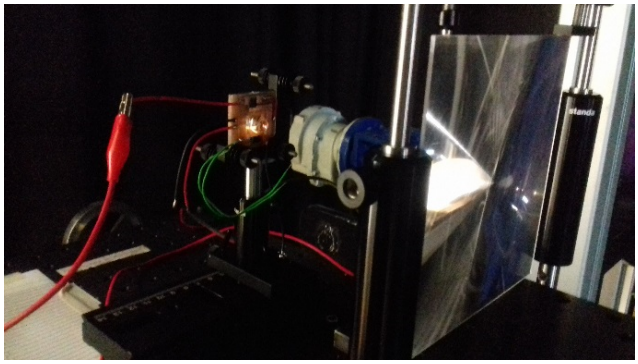

Figure 5-9. A GEN VII Receiver Aligned, Ready for I-V Testing

5.2.4 On-sun Testing Metrology and Methodology at Jaén University

Once the POE module was aligned and characterised using the indoor solar simulator, it was attached to a solar tracker for on-sun testing. The module was aligned to the Plane-Of-Array (POA) on the tracker by visual inspection of the POE light spot position, through two pairs of UV glasses. The module alignment was then adjusted until the spot focused onto the receiver SOEs. As has been previously

mentioned (Section 3.1.9) for the outdoor experiments undertaken at Cardiff, solar resource monitoring is essential when conducting experiments on-sun due to the temporal variability of the solar resource. Three pyranometers were used to gather the GHI, the Inclined Global Horizontal Irradiance (GHI) and the diffuse irradiation (using a tracked shaded pyranometer). An IV tracer was used to evaluate the cell performance. The rear substrate temperatures for all the receivers were recorded during every I-V scan, using k-type thermocouples and logged using two Picologger TC-08s.

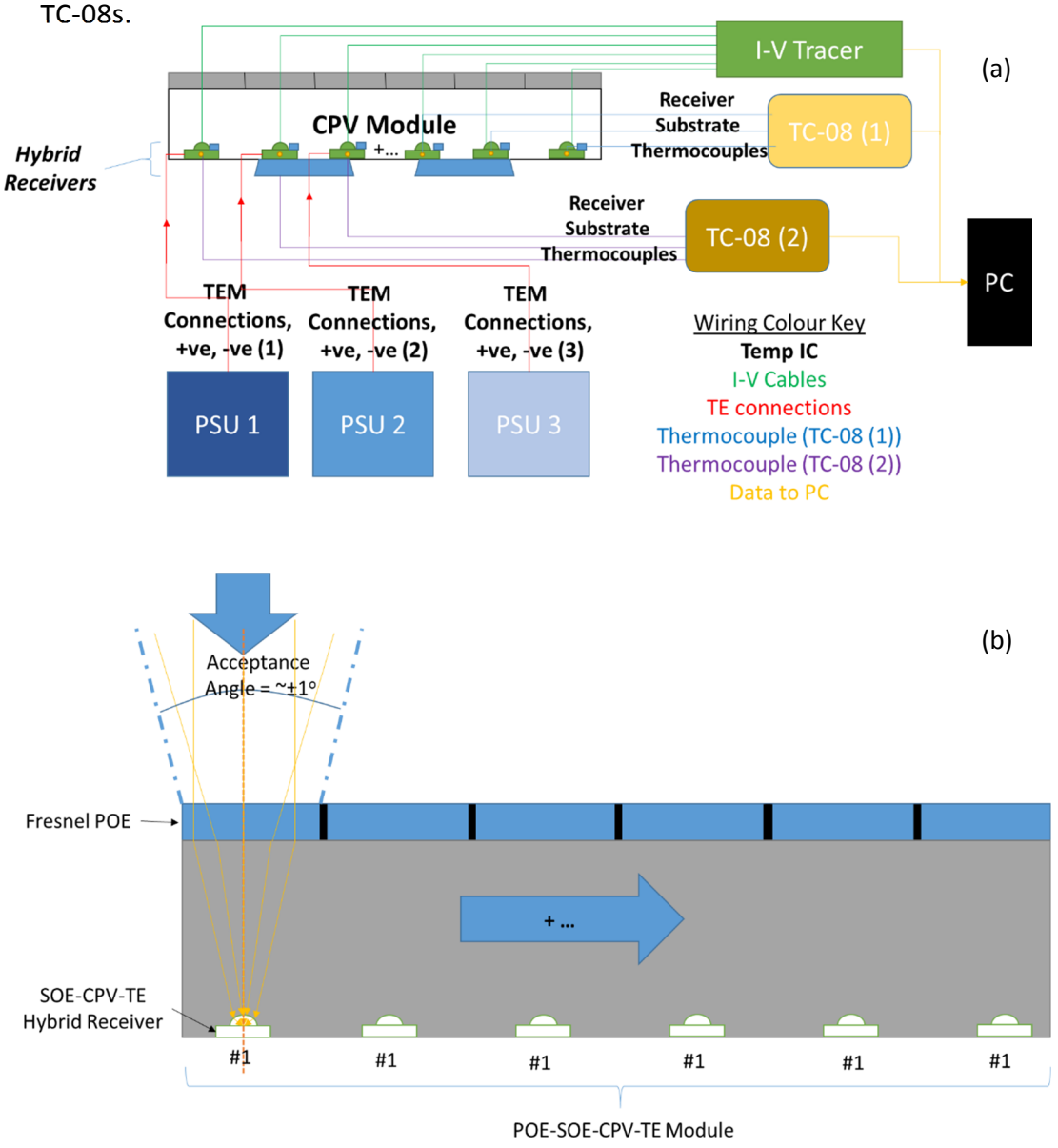

Figure 5-10. (a) Experimental Metrology of the POE hybrid Module. (b) An Overview Schematic of the Internal optical Design within the POE-SOE-CPV-TE Module

Three independent laboratory power supplies were used to supply the excitation current to the TEMs during testing, and the supplied voltages and current were recorded. Figure 5-10 (a) gives an overview of this additional metrology used within the POE-SOE-CPV-TE module, and (b) an overview of the internal optical design used.

5.3 Results and Discussions

5.3.1 GEN V Receiver Data

A GEN V receiver, "Kappa" was tested under primary optics at STC conditions at Jaén University, using the experimental setup as described in 5.2.3. Figure 5-11 shows the data obtained, and compared with the 1-sun STC data obtained at Cardiff under SOE only. The SOE gave a 3.6x effective CR with an optical efficiency of 70.63%. This concentration ratio was calculated using the I_{sc} from the cell only CPV-TE LAMBDA receiver. The LAMBDA receiver was tested with only a bare cell at 1-sun, and was built with a CPV cell of comparable probe performance data to KAPPA. The Voc of KAPPA also increased with the increased CR. It was shown that the I_{sc} and V_{oc} increased drastically with the increased concentration ratio achieved with POEs. Consistency of I-V curve shape was preserved, indicating that the wire bonding was sufficient not to introduce any series resistance related drops in FF or η_{cell}. An effective CR under POEs was also calculated from bare-cell

Table 5-3. Summary of the Key Solar Cell Performance Parameters Obtained from POE + SOE Experiments with Kappa Receiver

	Isc (A)	Voc (V)	Pmpp (W)	FF (%)	Efficiency (%)	Effective CR	Optical Eff. (%)
Cell Only	0.004	2.257	0.01	75.20	22.43	-	-
SOE	0.010	2.418	0.02	78.31	25.03	2.54	70.63
Soe+POE	1.252	3.031	2.90	76.33	30.57	313.17	65.79

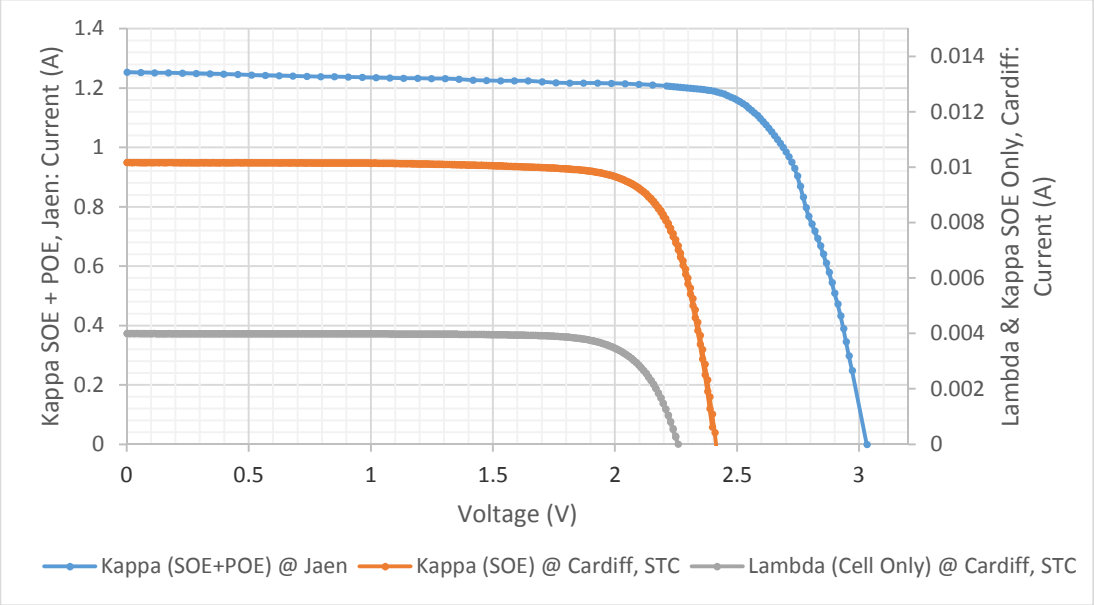

Figure 5-11. I-V Data of Kappa and Lambda at Cardiff (Bare cell and SOE Only) and Jaen (POE)

LAMBDA 1-sun data, and was found to be 313x, with an optical efficiency of 65.79%.Table 5-3 above shows the summarized key cell performance parameters.

The optical efficiency of the POE + SOE optical train (65.8%) exhibited a slightly lower optical efficiency than the SOE only (70.6%). This was to be expected from unavoidable losses in alignment, lens parasitic light absorption and chromatic aberration of the light spot. The effect of the Chromatic aberration is that due to non-perfect manufacturing the lens exhibits non-perfect light refraction of all wavelengths. This generates “fringes” either side of the focal spot where the light wavelengths for Blue and Red light exhibit a slight dispersion. The incident spectrum on the cell is changed and negatively affects performance. The cell efficiency increased with increasing the concentration ratio, as has been well established in literature following an increase of both I_{sc} and V_{oc}. The FF increased with the addition of a SOE, due to the higher photon flux incident upon the cell. The FF decreased when adding a POE, due to the chromatic aberration of the Fresnel lens used giving a slight non-homogeneity for spectrum incident upon the cell surface. Additionally, the optical train could have introduced further misalignment.

5.3.2 Indoor GEN VII Receiver Characterisation at Cardiff

The GEN VII receivers were evaluated using the solar simulator facilities at Cardiff (see Section 3.2.1). I-V curves were taken at 25°C, 1000Wm^{-2} AM1.5G conditions. A water heat exchanger and CLIC temperature control was used to maintain the 25°C temperature during testing. All twelve manufactured receivers from batch 1 were measured, for I-V curves (Figure 5-12), alongside un-encapsulated (#20) and non-SOE (#19) GEN VII receivers to further quantify the Sylguard performance drop. Variation was shown within the batch of receivers, with three exhibiting far lower performances than the average. These numbers as can be seen from the data are #5, #9 and #16. These three receiver were removed from further integration within the POE module due to current matching considerations within a string of receivers.

Table 5-4. Sylguard Losses for the GEN VII Receivers

cell #	Isc (A)	Voc (V)	Vmpp (V)	Impp (A)	Pmpp (W)	FF (%)	Eff (%)
20	0.004	2.126	1.904	0.003	0.01	76.88	21.56
19	0.004	2.146	1.925	0.003	0.01	75.15	20.54
						Δeff	1.02

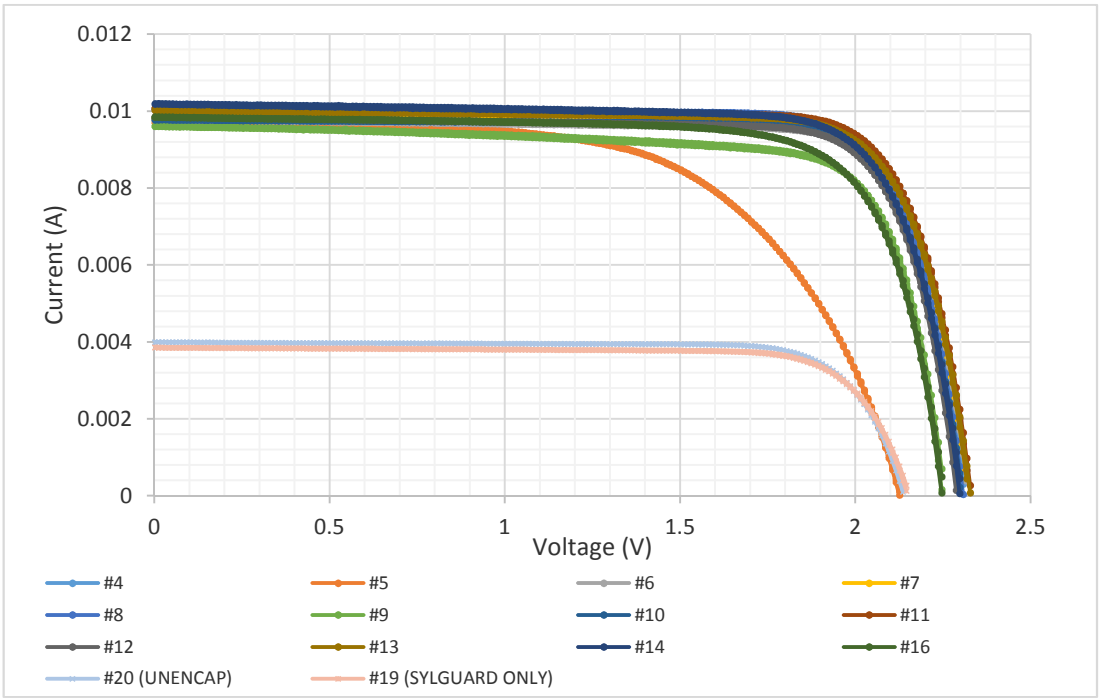

Figure 5-12. I-V STC Data for the GEN VII Receiver Batch I

Comparing Figure 5-12 with the post-manufacture receiver pictures (Figure 5-7, Section 5.3.1.b), receiver #5 showed large optical movement during curing from the datum positions, giving rise to its drastically poor I-V performance. Receivers #9 and #16 also showed the characteristic lower V_{oc} than average, through optical misalignment. These were removed from the full module. This gave a total of 9 functional GEN VII, performance-matched receivers. The CPV cell efficiency loss through lower optical transmission through the Sylguard was found to be -1.02% absolute for the GEN VII receivers, see Table 5-4.

5.3.3 GEN VII "No SOE" Receiver data

The GEN VIIs with and without Sylguard were both measured under POE concentration to evaluate the encapsulant performance drops at higher concentration ratios (data shown in Figure 5-13). The concentration ratio achieved was positively affected by not having the inherent optical absorption losses of the SOE and hence exhibited a higher optical efficiency. The non-consistent I-V curves traces under POE indicate the effects upon the cell with regard to operating under non-homogenous spectral irradiance conditions. This further suggests a spectral homogenisation effect which occurs with the SiLO SOE. The short circuit current drop and hence the absolute drop in efficiency that occurred from the transmission losses of the Sylguard were consistent with the data observed at 1-sun (see Chapter 3, Section 3.3.2.a). This implied a similar optical performance of the encapsulant, even at higher concentration ratios.

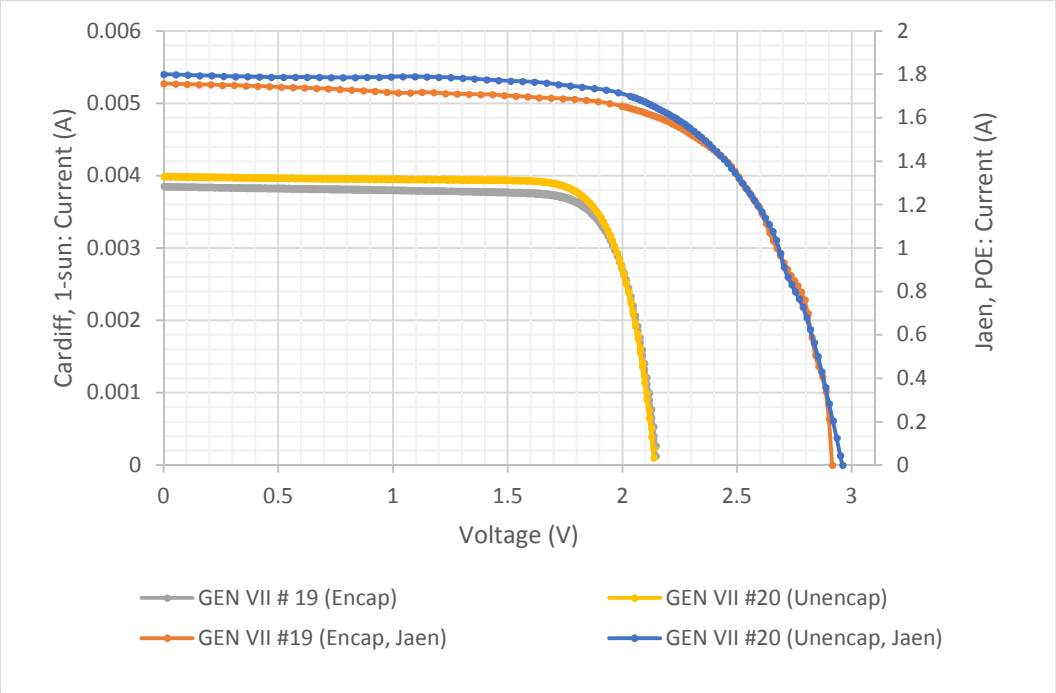

Figure 5-13. Comparative I-V data For GEN VII, Encapsulated and Encapsulated at 1 Sun and Under POE Only. Data is obtained at Cardiff unless otherwise listed.

5.3.4 GEN VII Indoor Data with SOE

I-V data was obtained for the 9 receivers taken to Jaén University using the experimental setup shown in 5.2.2. Figure 5-14 below shows the obtained POE data measured. Comparable values of I_{sc} were measured were of and with a similar spread to that found when compared against the Cardiff 1-sun testing data (Section 5.3.3), showing that minimal degradation had occurred during transit. The receiver were categorised into two strings to evaluate the cells with and without the TEM being powered. It was shown that only 7 out of the tested 9 receivers had similarly matched I_{sc}, giving three receivers for each string. The receivers were sorted in relation to I_{mpp} to eliminate current limiting effect under operation - rather than at the short circuit/"no-load" condition. This allowed the champion string to operate in similar conditions (i.e. at MPP) as it would be in commercial CPV modules. The two strings were organised into "String A" with receiver numbers #13, #8 and #4, and "String B" of receivers #14, #10 and #7. String A was omitted from further work

due to failures on-testing, with data for the three receivers in string B shown in Figure 5-14.

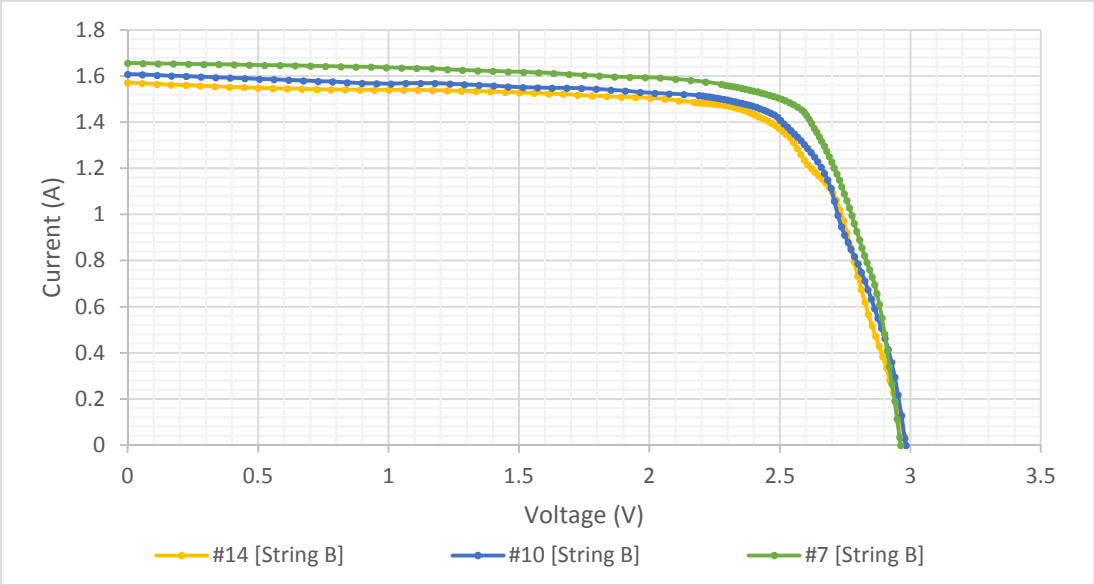

Figure 5-14. I-V data of GEN VII Receivers Tested under POE

5.3.5 Summary of Receiver I-V Performance

A direct comparison was done between the Gen V receivers and the GEN VII receivers under SOE and POE conditions. The SOE only conditions were obtained using the experimental 1-sun simulator at Cardiff University, and the POE data was obtained from the flash-lamp simulator at Jaén University. The data obtained from Kappa (GEN V, with SOE), Lambda (GEN V, no SOE) and receiver # 13 (the best performing GEN VII, with SOE) is shown in Figure 5-15. For reference, the cells used in these two generations were from the same manufacturer, but from two different wafers and hence two different growth regimes. It was shown that at 1-sun conditions, the V_{oc} and I_{sc} of the GEN V cells was similar to that of the GEN VII cells.

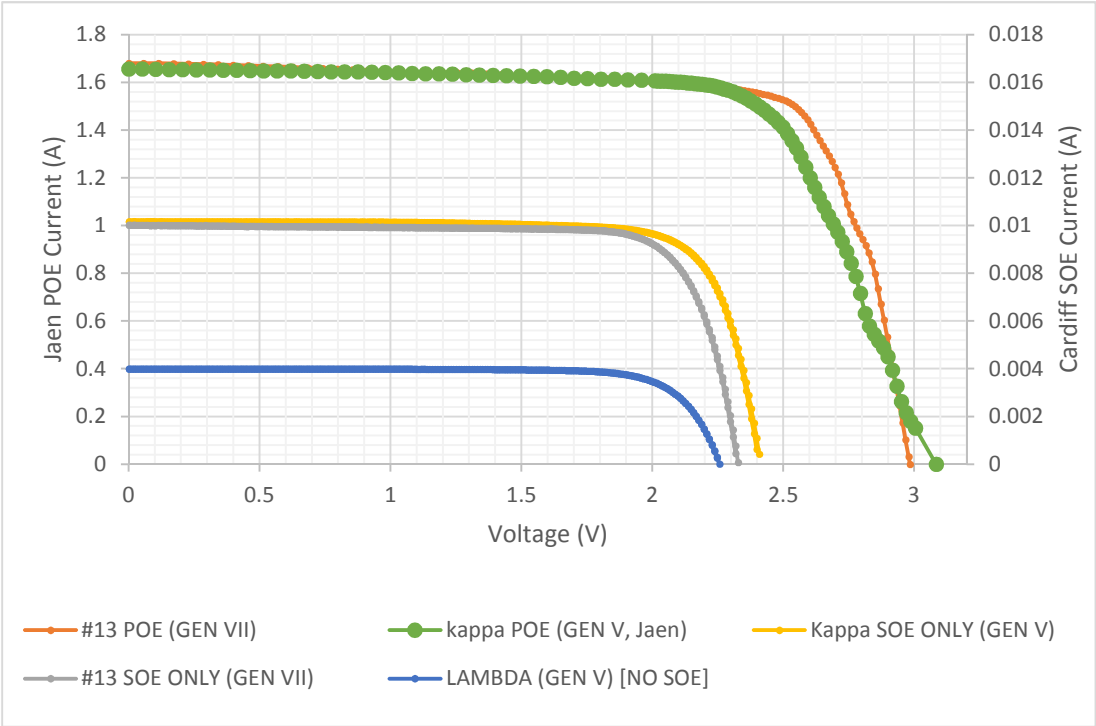

Figure 5-15. I-V Curves for Bare Cell, SOE and POE Experiments of GEN V and GEN VII

5.3.6 Full Module Alignment

To achieve the optimal performance for the POE module, the Fresnel lens in the POE module was aligned using the solar simulator in Jaen (as in Section 5.2.2). The flash-lamp setup highlighted an issue with the BPD. To measure the V_{oc} condition, the I-V tracer measured a reverse-excitation "dark current" of the p-n junctions within the cell. It then normally applied the exact same current as a forward bias to overcome this dark current, hence operating the cell at its "Voc" condition. This voltage was then measured. However, the reverse resistance of the used BPD for the GEN VII receivers, was in the order of ~0.6MΩ per diode, with the maximum input impedance of the I-V tracer being of similar magnitude (>1MΩ rated). Hence, when the reverse dark current measurement was attempted with more than two GEN VII receivers in series, the reverse bias resistance from the diode prevented this and the I-V data wasn't recorded. Therefore, the POE was aligned using a "Four-Quadrant Technique". The two strings in the module were split into four "quadrants" consisting of two receivers, as shown in Figure 5-16. The POE distance was then optimised using the I_{sc} values measured from the two spatial

extremity quadrants Q1 and Q4. This allowed an effective vertical alignment to be achieved for the POE, which was then fixed in place for all resultant testing.

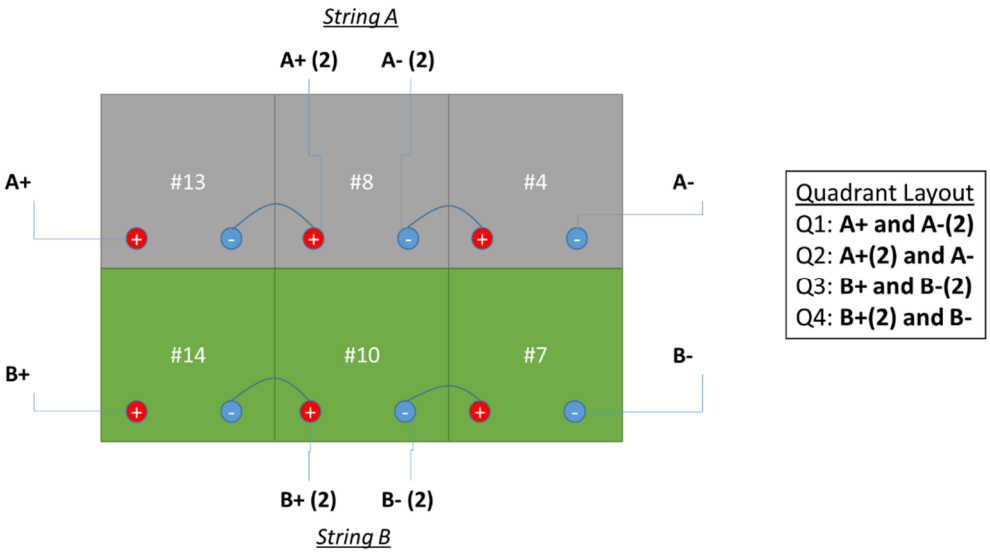

Figure 5-16. Quadrant Layout of the POE Module for Indoor Fresnel Lens Alignment

5.3.7 Acceptance angle testing

Once the POE module was aligned, its acceptance angle was then measured experimentally using the simulator. This was achieved through setting a "0 degree" datum point using a laser pointer mounted on the movable experimental apparatus frame. Using the two gearboxes, an iterative 2D-matrix of tilt angles was tested to determine the angular response of the module and hence derive the acceptance angle. This test was done for quadrants Q1 and Q4 to determine the measured alignment consistency exhibited between the two different strings. Figure 5-17 shows the data obtained.

It was shown in the data that the SOE with the GEN VII receivers exhibited a minimum point of its I_{sc} during perfect orientation. This was to be expected and has been previously discussed in literature for this type of SOE [4]. That being said, the P_{mpp} showed a trend consistent with that expected for a POE module. The acceptance angles of quadrant 1 was found to be 1.00^{o} (1θ), and for quadrant 4 was found to be 0.89^{o} (1θ). These values are comparable to those on most commercial modules and were considered adequate for transitioning to the outdoor measurements as they were within the tracker's miss-alignment accuracy of 0.2^{o}.

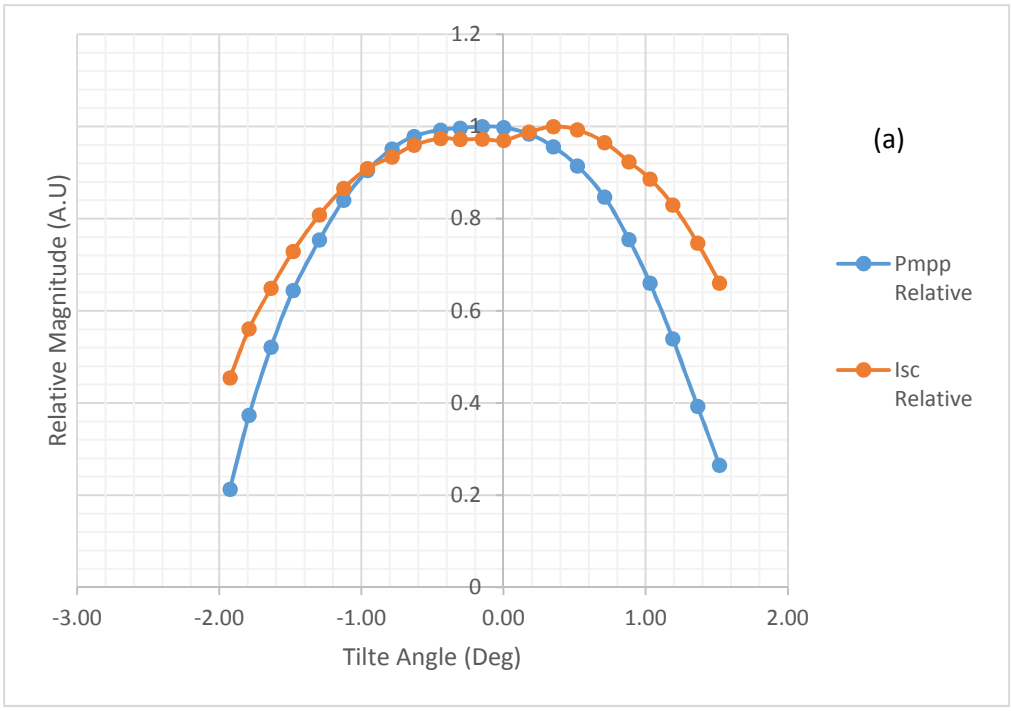

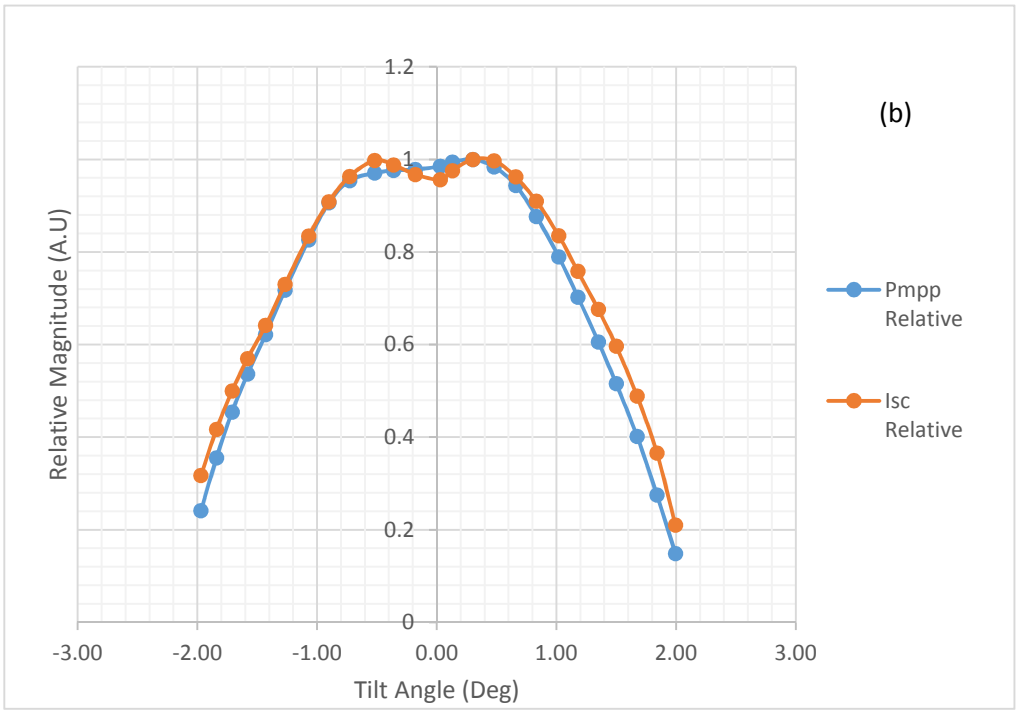

Figure 5-17. Acceptance Angle Data for Quadrant 1 (a) and 4 (b), for the POE GEN VII Module

5.3.8 On-sun Hybrid evaluation and TEM Temperature Control

As described above, monitoring the solar resource using the appropriate metrology was crucial to analyse the data obtained. The measured GHI, DNI and diffuse irradiation as seen by the weather station on the day of testing for String B (13/10/17) is shown in Figure 5-18 below. Although not directly measured, the Albedo Irradiance was calculated using the GHI, DNI and Diffuse components. It was shown to follow a typical daily irradiation cycle for a clear October day in Jaén, with a maximum DNI of approximately 740 Wm^{-2}, a maximum Diffuse of approximately 70 Wm^{-2}, a maximum GHI of approximately 890 Wm^{-2}, and a calculated Albedo Irradiation of approximately 80 Wm^{-2}**.**

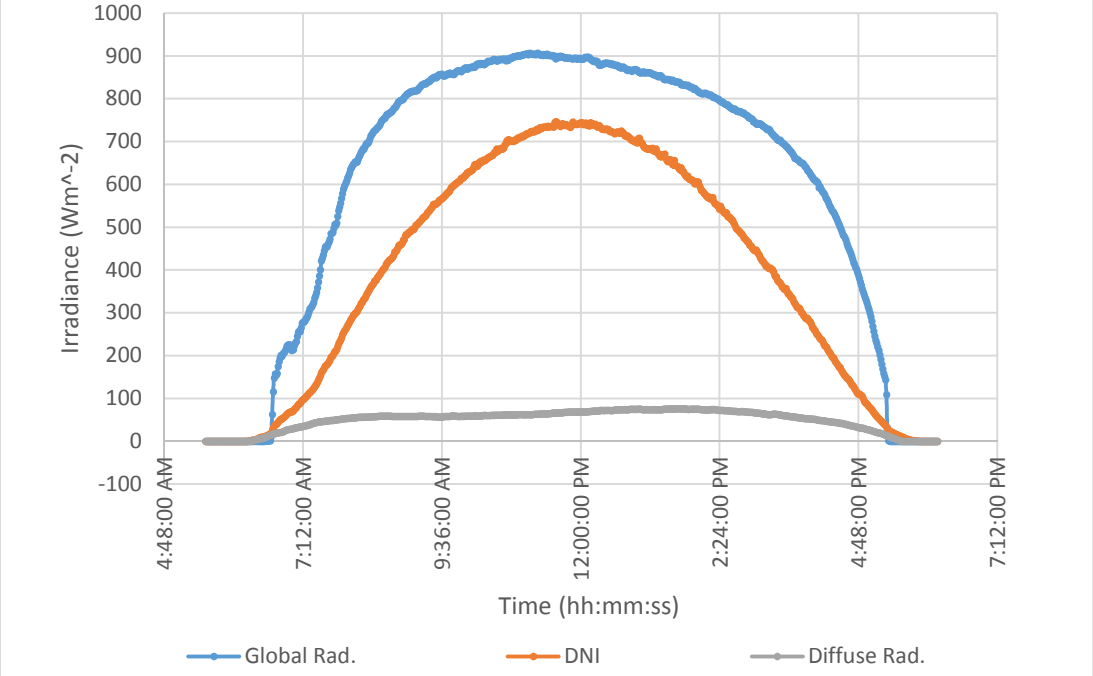

Figure 5-18. Recorded Irradiance Data in Jaén during Day of Testing

Two experiments were done using on-sun testing (see Section 5.2.3) with the POE-SOE-CPV-TE hybrid module. The individual TEMs within each CPV-TE string inside the POE-SOE-CPV-TE module were excited at different current and input powers, with I-V curves of the CPV cell within the CPV-TE receivers being taken at every increment. Both strings of cells were tested with similar irradiance conditions within their respective tests. String A was tested during the late afternoon around 3pm (11/10/17), and string B was tested around solar noon (13/10/17). As such, the IV data for string A had a larger variation of spectral conditions and hence only the

TEM power input data is included here to confirm the TEM performance parameters. String B was tested around solar noon with minimal spectral changes, and within half an hour – reducing the likelihood of irradiance changes. The TEM current and voltages as displayed from the PSU front panel were recorded, alongside the rear side thermocouples of both strings. I-V scans were taken using a source meter, and the outdoor metrology measured. The I-V curves, as measured at the different TEM current for string B, are given in Figure 5-19.

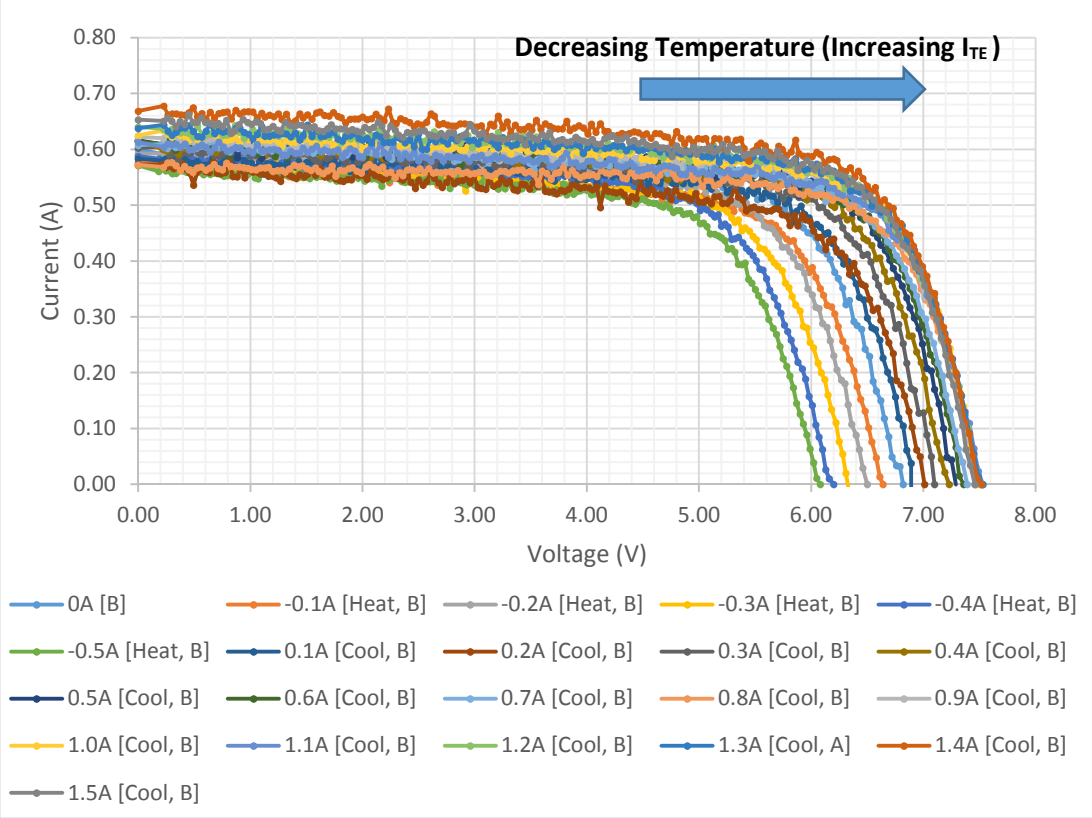

Figure 5-19. On-Sun I-V Data of String B under Various TEM Current Excitations

It was clearly shown that the I_{sc} and V_{oc} exhibited linear trends over the range tested - as to be expected from their temperature co-efficients. The applied TEM current (I_{TE}) increased the power generated at the maximum power point of the cell. The power input to the three TEMs within each string (P_{TE}) was calculated from the input voltage and current, and plotted against the input current in Figure 5-21. It was also shown that the TEM exhibited a quadratic relationship between the set current level and the consumed total power for both experiments. This was due to multiple factors. As the thermoelectric ΔT increased, the parasitic Seebeck

and Joule losses increased and at each temperature and new counter-heat flow potentials were established. A tabulated version of the same data is given in Appendix B for further clarity of Figure 5-19.

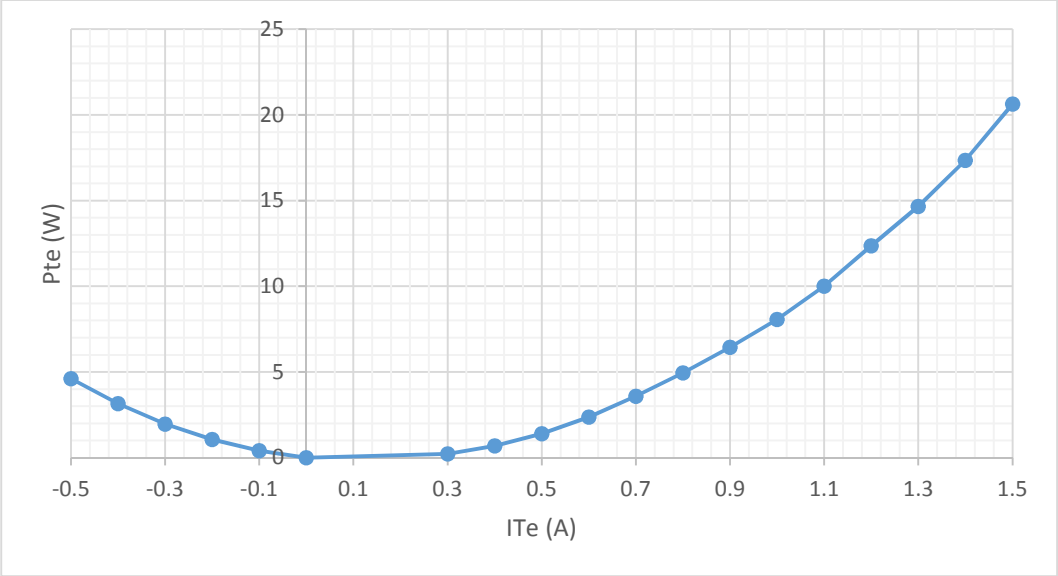

Figure 5-21. Input ITEs Plotted Against Total String TEM Power Consumption for String B

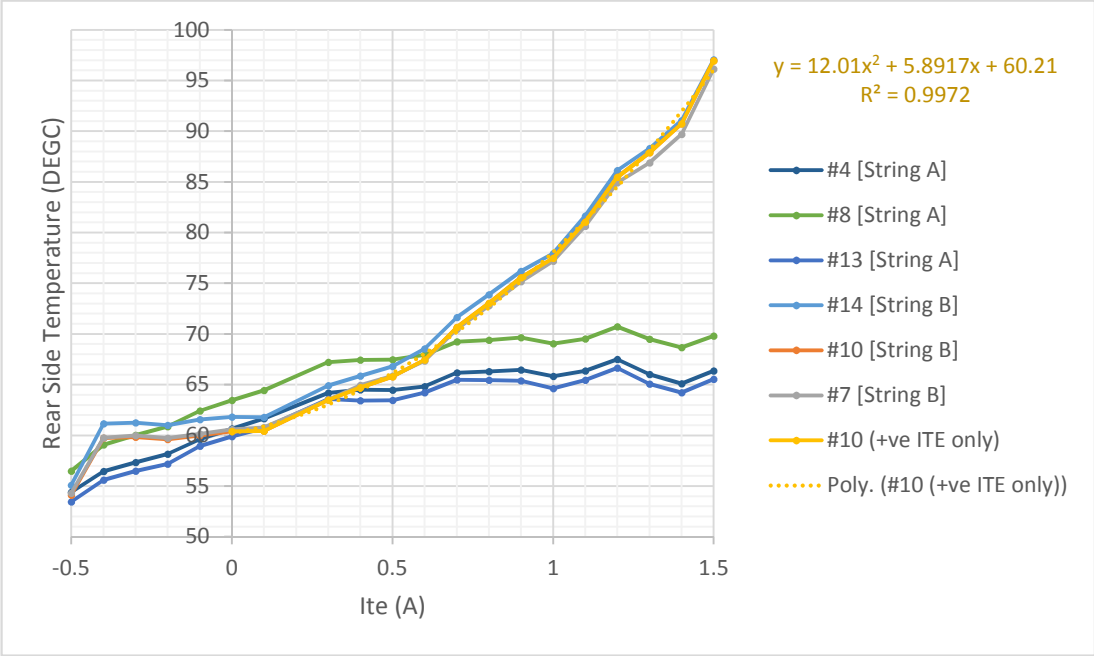

Figure 5-20. Rear-side Receiver Substrate Temperatures, Measured During On-sun Testing of String B

The substrate rear-side temperatures for the two strings within the POE-SOE-CPV-TE module were recorded and plotted. An average value was found throughout the I-V scan for the data above, and the reading plotted verses I_{TE}. The secondary string (String "A") was used to give a comparative "non-operational" datum for the temperature reached by the rear side copper substrate without the active cooling applied. The temperatures were logged using the Pico logger, as described in Section 5.2.4 above. As the applied current level of the TEM increased (string B), more heat was pumped from the cell, and the rear side substrate temperature increased with also a quadratic trend.

Applying a negative (heating) current to the TEM gave a temperature decrease of the rear substrates, and likewise applying a positive current (cooling) raised the rear side temperature – as consistent with the desired heat pumping directions. It was shown that the rear-side temperature increase of the receiver substrate increased quadratically with a linearly applied current.

This temperature increase was caused through an inadequate thermal interface between the receiver and the module fin, or by inadequate heat removal rate of the fin itself. This hotter rear side temperature made it harder for the TEM to reject the heat. At this hotter temperature, the reverse parasitic heat flow back-through the module as described by Fourier's law also increases. This gave rise to two areas for future performance improvement of the hybrid performance. Firstly, decreasing the receiver rear-side temperature with more effective heat removal and "receiver-to-case" thermal resistance. Secondly, further changing the TEM to be optimised for this small current input range of operation would also be beneficial for increasing TEM cooling effectiveness. The total string input power to the TEM for the active cooling, and the increase in power obtained from the string of cells from the induced reduction in temperature were compared. The MPP of all three cells increased comparatively, indicating a similar change in temperature for all three cells within the string. Likewise, this was shown by the I-V traces obtained from the string scans not having any artefacts for the BPDs or any series resistance loss effects. The change in the power at MPP of the CPV cell for each TEM input condition was calculated as compared to the reference "0A" I-V curve, where no

current was supplied to the TEM, with the TEM held at open circuit -hence establishing the steady state operation on-sun of the CPV-TE module. It was shown that at low TEM source currents up to 0.3A, that the increase in the power from the CPV cell string was equal to that of the power consumed by the TEM. A performance break-even for the increase in cell performance due to TEM cooling has been shown. At TEM excitations current over 0.3A, a drastic change was shown due to the quadratic nature of the I_{TE}-T_{PVv} and hence the inter-dependant relationships, with the power being consumed by the TEMs within a string being greater than that of the change in power achieved from the cell temperature change.

The temperature induced change in cell maximum power point power (ΔP_{mpp}) is given in Figure 5-22and plotted against the I_{te}, showing a linear trend with a 0.91 R^2 value. Figure 5-23 shows this calculated ratio of the gained P_{MPP} of the cell (ΔP_{mpp}) to the input power to the TEM string (P_{TEM}). The trend in the figure, was chosen to be quadratic as suggested by the previously shown data in Figure 5-19, and an intercept of (0, 0) chosen for fitting as the 0A excitation condition of the TEM input current was chosen as the comparison datum.

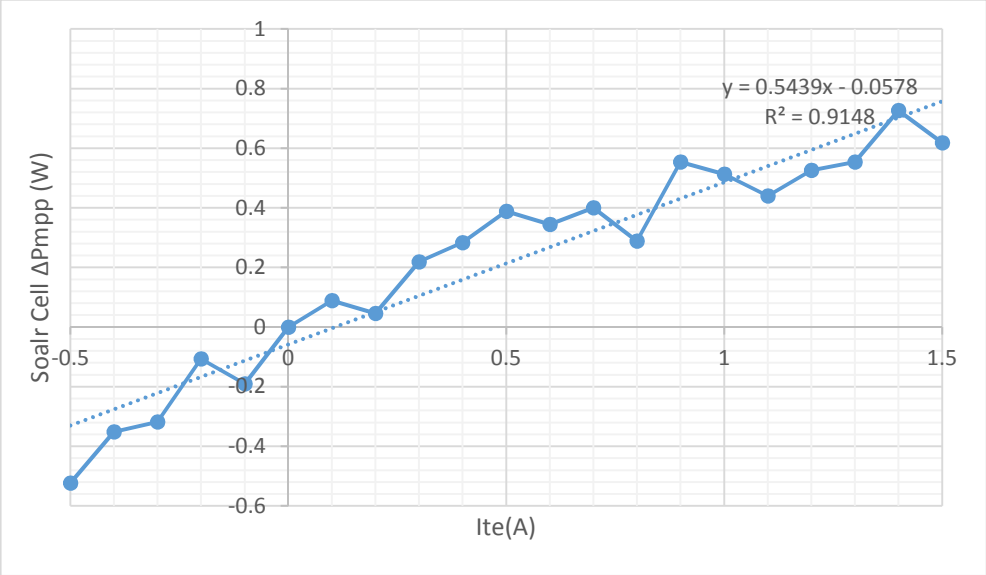

Figure 5-22. Change in cell output power compared to 0A datum, against input TEM current

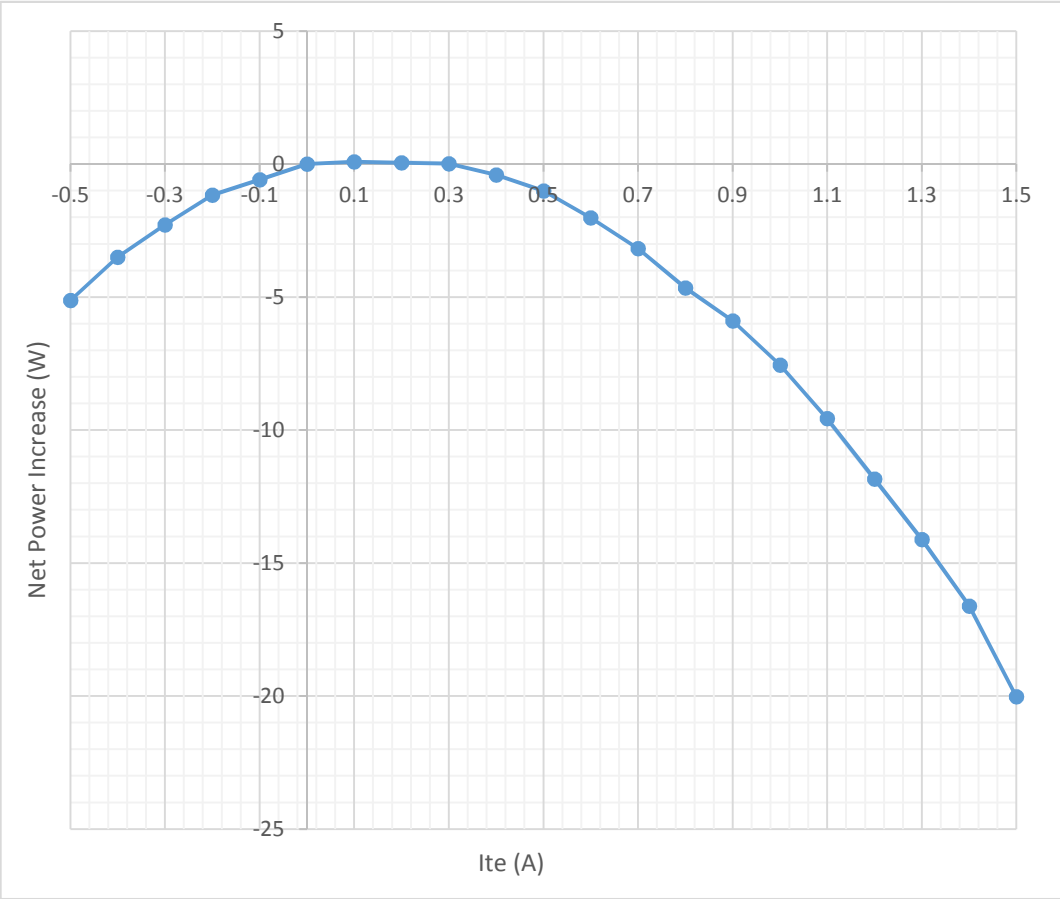

Figure 5-23.Net Power increase to System against Input TEM Current

This result shown in Figure 5-23 above, highlights a trend for the use of active cooling techniques within POE-SOE-CPV-TE hybrid devices. The increase in the overall net power generation as shown here in this data, indicates that with improved optimisation and system-focused design, even higher energy generation is possible as compared to non-powered hybrid systems. Likewise, a system that has the "dual-use" metrology functionality of the included TEM (as shown in Chapter 4) for accurate feedback controlled temperature control of the cell for research or development, has the potential to mitigate some of the inherent thermal-resistance induced temperature changes resulting from the addition of the TEM. This could be achieved through detailed active cooling regimes, as dependant on the system as a whole, or optimised strategies for applying the active cooling power.

5.4 Conclusions

- A GEN VII receiver was designed, incorporating design changes from testing GEN V. This included a revised tracking layout and “epoxy-less manufacture”.
- Manufacturer characterisation data from the used TEMs and CPV cells was gathered and calculated for each receiver made.
- A novel “self-soldering” manufacturing technique was explored and experimentally substantiated for streamlined GEN VII manufacture. This used a combination of hotplate soldering, and hotplate pre-heating with TEM-induced hot side solder melting.
- A batch of 12 GEN VII receivers were made and characterised at Cardiff University under 1-sun conditions. Three receivers exhibited lower-than-average performance and were omitted from the module manufacture – highlighting further areas of process improvement. Nine receivers were carried forward to module level for testing under POE.
- Indoor flash-lamp characterisations were done through collaboration with the University of Jaén. I-V datasets were obtained for all the GEN VII receivers, two Gen V receivers and a GEN VI receiver. Results and performances were analysed and discussed with effective CRs of ~300x being reached.
- The CPV-TE POE module was tested using a “four-quadrant” approach and optically aligned for outdoor testing. Acceptance angle testing was done with the module found to have a 1θ of 1.00^{o} for Quadrant 1 and 0.89^{o} for Quadrant 4.
- Outdoor on-sun testing was done at Jaén, with two strings of receivers in the module – string A and B. I-V scans were done and the TEM current varied. It was found that at low cooling current excitations, an energetic break-even was found with the system with an applied I_{te} of 0.3A, and the implications of this were discussed.

These datasets imply a future area of optimisation for TEMs within CPV-TE hybrid architectures. These are operation within a low current range regime to be designed for use within minimal power deployment scenarios. Additionally, if cells with higher conversion efficiencies were used, the potential conversion power increase gain for the TEM-induced cell temperature change could also be further increased. Additionally, higher concentration rations would create higher temperatures (and hence more potential gain to be had from TEM cooling) would be shown. A definite break-even point was shown with this work, with the potential of further increases to be made with more optimised designs.

5.5 References

1. [Online] IPC, *Generic Standard on Printed Board Design*. 2012, IPC. [Accessed: 01/05/18]. Available at: http://www.ipc.org/TOC/IPC-2221B.pdf .
2. [Online] *Indium Corp. Indalloy® 1E In-Sn Solder Alloy Datasheet*. p. 2. [Accessed: 01/05/18]. Available at: http://www.matweb.com/search/datasheet.aspx?matguid=a20c5153ec1d4a1e95ef2127dadba008&ckck=1
3. [Online] 3M, *Scotchcal™ Opaque Mirror Graphic Film.* 2011. [Accessed:01/05/18]. Available at: http://multimedia.3m.com/mws/media/232107O/product-bulletin-7755-se.pdf
4. Ferrer-Rodríguez, J.P., et al. *Design and characterization of refractive secondary optical elements for a point-focus Fresnel lens-based high CPV system*. in *AIP Conference Proceedings*. 2017. AIP Publishing. [Accessed: 01/05/18]. Available at: https://aip.scitation.org/doi/abs/10.1063/1.5001414
5. Theristis, M. and T.S. O'Donovan, *Electrical-thermal analysis of III–V triple-junction solar cells under variable spectra and ambient temperatures.* Solar Energy, 2015. **118**: p. 533-546. [Accessed: 01/05/18]. Available at: https://www.sciencedirect.com/science/article/pii/S0038092X15003059
6. Rey-Stolle, I. and C. Algora, *High-irradiance degradation tests on concentrator GaAs solar cells.* Progress in Photovoltaics: Research and Applications, 2003. **11**(4): p. 249-254. [Accessed: 01/05/18]. Available at: https://onlinelibrary.wiley.com/doi/full/10.1002/pip.487
7. González, J.R., M. Vázquez, N. Núñez, et al., *Reliability analysis of temperature step-stress tests on III–V high concentrator solar cells.* Microelectronics Reliability, 2009. **49**(7): p. 673-680. [Accessed: 01/05/18]. Available at: https://www.sciencedirect.com/science/article/pii/S0026271409001115
8. Núñez, N., M. Vázquez, J.R. González, et al., *Novel accelerated testing method for III–V concentrator solar cells.* Microelectronics Reliability, 2010.

50(9–11): p. 1880-1883. [Accessed:01/05/18]. Available at: https://www.sciencedirect.com/science/article/pii/S0026271410003586

9. González, J.R., M. Vázquez, N. Núñez, et al., *Reliability Improvement in III-V Concentrator Solar Cells by Means of Perimeter Protection.* 2010. [Accessed: 01/05/18]. Available at: http://aip.scitation.org/doi/abs/10.1063/1.3509196
10. Algora, C., *Reliability of III–V concentrator solar cells.* Microelectronics Reliability, 2010. **50**(9): p. 1193-1198. [Accessed: 01/05/18]. Available at: https://www.sciencedirect.com/science/article/pii/S0026271410003185
11. Núñez, N., M. Vázquez, J. González, et al., *Instrumentation for accelerated life tests of concentrator solar cells.* Review of Scientific Instruments, 2011. **82**(2): p. 024703. [Accessed: 01/05/18]. Available at: http://aip.scitation.org/doi/abs/10.1063/1.3541800
12. Núñez, N., J.R. González, M. Vázquez, et al., *Evaluation of the reliability of high concentrator GaAs solar cells by means of temperature accelerated aging tests.* Progress in Photovoltaics: Research and Applications, 2013. **21**(5): p. 1104-1113. [Accessed: 01/05/18]. Available at: https://onlinelibrary.wiley.com/doi/full/10.1002/pip.2212
13. Espinet-Gonzalez, P., C. Algora, V. Orlando, et al. *Preliminary temperature accelerated life test (ALT) on III-V commercial concentrator triple-junction solar cells*. in *Photovoltaic Specialists Conference (PVSC), Volume 2, 2012 IEEE 38th*. 2012. [Accessed: 01/05/18]. Available at: http://ieeexplore.ieee.org/abstract/document/6750496/
14. Espinet-González, P., C. Algora, N. Núñez, et al., *Temperature accelerated life test on commercial concentrator III–V triple-junction solar cells and reliability analysis as a function of the operating temperature.* Progress in Photovoltaics: Research and Applications, 2015. **23**(5): p. 559-569. [Accessed: 01/05/18]. Available at: https://onlinelibrary.wiley.com/doi/full/10.1002/pip.2461
15. Fernández, E.F., G. Siefer, M. Schachtner, et al., *Temperature coefficients of monolithic III-V triple-junction solar cells under different spectra and irradiance levels.* AIP Conference Proceedings, 2012. **1477**(1): p. 189-193.

[Accessed: 01/05/18]. Available at: https://aip.scitation.org/doi/abs/10.1063/1.4753865

16. Fernández, E.F., A. Soria-Moya, F. Almonacid, et al., *Comparative assessment of the spectral impact on the energy yield of high concentrator and conventional photovoltaic technology.* Solar Energy Materials and Solar Cells, 2016. **147**: p. 185-197. [Accessed: 01/05/18]. Available at: https://www.sciencedirect.com/science/article/pii/S0927024815006510

17. Pérez-Higueras, P. and E.F. Fernández, *High concentrator photovoltaics: fundamentals, engineering and power plants*. 2015: Springer. Pp115 – 152. ISBN: 9783319150390.

18. Fernández, E.F., F. Almonacid, J.A. Ruiz-Arias, et al., *Analysis of the spectral variations on the performance of high concentrator photovoltaic modules operating under different real climate conditions.* Solar Energy Materials and Solar Cells, 2014. **127**: p. 179-187. [Accessed: 01/05/18]. Available at: https://www.sciencedirect.com/science/article/pii/S0927024814002347?via%3Dihub

Chapter 6 : Thesis Conclusions, Major Contributions and Suggested Future work

6.1 Conclusions

The work contained within this thesis focused on the design, development, and experimental evaluation of CPV-TE hybrid receivers for increased CPV power generation and evaluation thereof of the unique functionalities these devices can offer. The major conclusions from this work were as follows:

6.1.1 Chapter Three Conclusions

1. A bi-layer PCB structure, built upon a copper base substrate provided a reliable mounting platform for integrating active CPV and TE components. Wire bonding and the use of silver epoxy were robust and effective contacting methods for the active devices. Clean-room manufacture for the devices improved cell performance by preventing contaminants accruing upon the cell surface. Silver ribbon combined with pre-metallisation of the TEM was a convenient method of obtaining a rear cell contact. Use of a "fast I-V" scan to preliminary evaluate internal resistance was an effective procedure to prevent premature failures of the TEs within the hybrid devices.
2. Through using the thermoelectric module, accurate temperature control of the CPV cell was achieved at a variety of incident irradiance conditions (500-1000Wm^{-2}) and temperatures (0-50^{o}C). This functionality was also conserved when using the thermoelectric to cool the CPV cells within the hybrid receivers that include SOEs. Standard $3.025x10^{-5}$ m^2 cell areas (5.5mmx5.5mm) and cells with areas as small as $2.21x10^{-6}$ m^2 were effectively manufactured into hybrid devices. Robust, repeatable and reliable CPV-TE hybrid devices were built, evaluated and substantiated as valuable testing platforms for CPV cells and other optoelectronic applications.
3. The temperature co-efficients of the solar cell used in this work were experimentally measured using the TEM for thermal control, with and without SOEs. These were found to be βI_{sc} = +0.11596 mA/^{o}C, and βV_{oc} = -4.5512 mV/^{o}C for the receiver named ALPHA (bare cell), and βI_{sc} = +0.

104904 mA/^{o}C and βV_{oc} = -4.615784 mV/^{o}C for the receiver named KAPPA (SiLO SOE).

6.1.2 Chapter Four Conclusions

1. A Closed Loop Integrated Cooler" (CLIC) technique was developed and validated. The TEM within a CPV-TE hybrid device, was measured through using a switching circuit and an effective ΔT calculated. This was further used to determine the cell temperature within a hybrid device, in combination with a cold-side reference IC or thermocouple. The thermoelectric module was then used within this technique to cool the cell to a set temperature and the measured temperature was used as the feedback error signal. A bespoke calibration rig was built and validated using a COMSOL simulation for use to calibrate the thermocouples to a known datum.
2. Two CLIC deployment methods were built and tested. Firstly, that using an Arduino microprocessor with proof-of-concept measurement accuracy to -0.98^{o}C and + 1.08^{o}C compared to the thermocouples. Secondly a data logger system achieved sub-degree cell temperature measurement resolution to six decimal places using this technique. Likewise this technique was further demonstrated by combining with a previously built hybrid receiver, with excitation-induced cell temperature changes measured throughout an I-V scan. Sub-second times between individual measurements were demonstrated to be feasible using this deployment mechanism.
3. This setup was then developed further and programmed using LabVIEW for use as experimental apparatus. The CLIC technique was proven to work as an accurate temperature measurement and control system under 1-sun, SOE, and POE conditions, at a range of chosen temperatures from 5^{o}C to 80^{o}C.

6.1.3 Chapter Five Conclusions

1. A full POE-SOE-CPV-TE hybrid module was designed, assembled and shown to exhibit on-sun cell performance parameters (I_{sc}, V_{oc}, and Efficiency)

comparable to commercial modules. The in-string resistance and string-limited devices were mitigated through careful design and experimental evaluation at multiple stages through the manufacture process. Firstly, this included a detailed evaluation of the receivers under one-sun testing to characterise performance individually and select matched devices. In-depth device testing under low CR and SOE only was done. Finally receiver-only testing was performed under higher CRs and POEs to confirm the device matching under realistic operation conditions. Additionally, for the module a new "four-quadrant" technique for the alignment of module POEs was developed using a flash-lamp simulator to overcome the limitations with BPDs with a high reverse resistance in strings. The acceptance angle was quantified prior to mounting on the solar tracker, and was found to be 1θ of 1.00^{o} for Quadrant 1 and 0.89^{o} for Quadrant 4.

2. It was shown that in certain conditions (I_{te}<0.3A), applying power to the TEM within a POE-SOE-CPV-TE hybrid to actively cool the cell temperature, produced more net power overall than not powering the thermoelectric. This shows huge potential for these device in the field of CPV to increase cell efficiencies to the crucial 50% conversion efficiency target.

6.2 Thesis Contribution Summary

Drawing from the chapter-specific breakdown given in Section 6.1 above, the main contributions of this thesis are summarised as follows:

1) By applying a range of excitation currents, the TE within a CPV-TE hybrid platform was shown to be effective at controlling the CPV cell temperature:

- With and without SOEs applied

For appropriate evaluation of the effect of the additional thermal mass and optical concentration related parameters.

- Over a range of temperatures (0^{o}C to 50^{o}C)

For evaluation of the temperature control functionality for different temperatures that would be realistically seen by a CPV module under on-sun operation.

- With high sensitivity a range of incident irradiance conditions (500Wm^{-2} to 1000Wm^{-2})

For small changes in the temperature required to maintain STC under such small differences was proven as a proof-of-principle. As is also to be expected with a CPV module deployed on-sun, with environmental and real-world factors adjusting the amount of heat.

2) A proof-of-concept evaluation was done for a TEM control technique. It showed that the TEM within a CPV-TE hybrid receiver was capable of simultaneously measuring the temperature and providing active cooling to the CPV cell within a 1°C accuracy (as compared to the k-type thermocouple "calibration" datum).

3) Within a POE-SOE-CPV-TE hybrid module tested on-sun and on a tracker, certain TEM excitation current conditions applied to a string of up to three receivers (0A -0.3A) were found to increase the overall system net power generation - as compared to not powering the TEM within a POE-SOE-CPV-TE hybrid module.

6.3 Future work

Resulting from the work in this thesis, two main avenues of research were highlighted for the future progress of CPV-TE hybrid devices. These consisted of:

1. ***Continuation of Incremental CPV-TE hybrid design:***

   The thermal interfaces for the hybrid devices as used within this work have the potential to be further reduced. Likewise interface such as the thermoelectric ceramic layers could be removed entirely, promoting heat flow through the device. Minor design changes were suggested from the testing of the GEN VII receivers under the flash-lamp simulator. These changes include more wire bonds to minimise series resistance effects at higher concentrations, and different BPDs to facilitate dark-current

compensation methods of measuring CPV cell string Voc. Future optimisation work has been suggested for minimising the thermal resistance of the Case-to-receiver interface.

2. ***Improvements to the CLIC:***

Following from the performance and progresses shown with the CLIC technique, a fully optimised PID control system could be developed and designed for the specific deployment use of TEMs within CPV systems. An intelligent, learning algorithm could be demonstrated and combined with the functionality for lifetime prediction or improvement through intelligent cooling strategies or programs. Per-module control system feasibility could be investigated. An industry 4.0 focus or an entire Internet of Things approach for a solar farm could be simulated, and the benefits of this technique there evaluated. Long-term financial benefits or energy cost/balance calculations would be beneficial.

3. ***Further optimisation of the CPV-TE hybrid Receivers and Modules:***

Capitalising on the increase in solar power generation, further optimised designs of both the module thermal interfaces and of the module itself could lead to higher gains in power production for the enhancement of future CPV systems. TEM module optimisation could be done to further investigate the energetic break-even found in this work with TEMs optimised for very low current levels. Systems of up to UHCPV could be investigated, and the compound improvement from the TEM thereof quantified. Cheaper alternatives to using commercial modules could be investigated, alongside the research of functionality and temperature-differential specific thermoelectric materials. Functional coatings for the rear-side of CPV modules would prove to be a hugely beneficial avenue to follow – either as a cooling option or for native heat scavenging through the Seebeck effect. Likewise, the thermoelectric rear-side to the case or heat exchange could be further improved through use of different bonding or

soldering methods, or through thermoelectric-integrated heat exchangers or CPV module casings. Module-level heat spreaders could also be evaluated to minimise the number of module used in manufacture, or remove the geometrical limitation for the module geometries as was the case in this direct-bonded approach.

4. ***Development of the "self-soldering" approach for automated hybrid manufacture:***

The self-soldering approach developed through transitioning the receiver manufacture to larger batches in chapter five, could be further designed into an automated manufacture process for simplified construction methods. Capitalising on the critical voltage as discovered in Section 5.1.2 for the top side self-soldering of the TEM, an automated interlock technique for these devices could be implemented when transitioning to mass manufacture. A constant current could be applied and the rated currents as defined by the ΔT needed for the self-soldering conditions. Hence the voltage here would be a constant contact critical voltage parameter, with the potential of it to be used as a condition monitoring parameter of the self-soldering process. The consistent self-soldering conditions that could be achieved and self-monitored through the critical voltage could be added as a quality control measure for hybrid production. Likewise, simplistic quality control methods could be done by combining this manufacturing technique with the work in Chapter three of the pre-manufacture TEM fault detection technique.

Appendix A: Gen VI Design Changes

The GEN VI receivers were adapted for future use with smaller cells (type A had active area of 1.41mmx1.57m, type B had a 2.3mm radius Circular cell), and used the same manufacturing procedure as the GEN V receivers. The centre PCB hole clearances were reduced, to reduce the distance necessary for the CPV cell top contact wire bonds. Aluminium wire bonds typically have a maximum lateral travel of 3mm. The resistance contribution of the wire itself increases with length as can be expected from the elementary resistivity equation (see Equation 0-1).

$$R = \frac{\rho L}{A} \qquad \textit{– (Equation 0-1)}$$

Where

R is the total resistance in Ω

P is the resistivity of the material in Ωm^{-1}

L is the length of the conductor in m

A is the area of the conductor in m^2

(a)

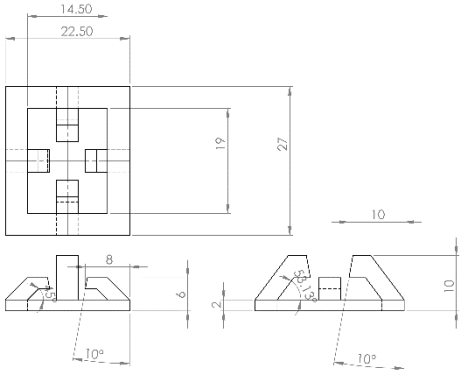

(b)

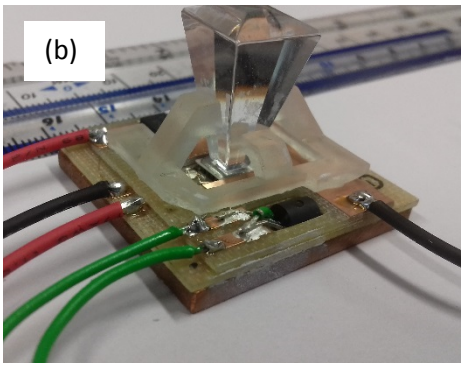

Figure Appendix A-1. The Optical Cradle CAD Designs (a) and Demonstrated on a GEN VI Receiver (b)

A secondary design challenge existed through using cells with smaller cell area, that of mounting the pyramid optic upon the cell long enough for an I-V scan to take place. To solve this, an “optical cradle” was designed and 3D printed using a

laser-forming technique and a PMMA based, optically active material to hold the lens in place during testing. Figure Appendix A-1 shows the design and finished cradle on a GEN VI receiver.

Table Appendix B-1. Measured Values from On-sun GEN VII CPV-TE Hybrid Testing (See Section 5.3.8)

Ite (A)	Voc (V)	Isc (A)	Vmpp(V)	Impp (A)	Pmpp (W)	ΔPmpp (W)	FF (%)	PTEM	P++Overall
-0.5	6.08	0.561	5.1	0.449	2.2899	-0.52353	67.13517	4.6	-5.12353
-0.4	6.2	0.588	5.14	0.479	2.46206	-0.35137	67.53511	3.144	-3.49537
-0.3	6.31	0.572	5.32	0.469	2.49508	-0.31835	69.12881	1.965	-2.28335
-0.2	6.5	0.592	5.48	0.494	2.70712	-0.10631	70.35135	1.056	-1.16231
-0.1	6.64	0.578	5.58	0.47	2.6226	-0.19083	68.33389	0.402	-0.59283
0	6.82	0.6	5.73	0.491	2.81343	0	68.7544	0	0
0.1	6.92	0.583	5.77	0.503	2.90231	0.08888	71.93979		0.08888
0.2	7.01	0.573	5.92	0.483	2.85936	0.04593	71.18626		0.04593
0.3	7.1	0.603	5.82	0.521	3.03222	0.21879	70.82475	0.21	0.00879
0.4	7.23	0.6	6.18	0.501	3.09618	0.28275	71.37344	0.688	-0.40525
0.5	7.32	0.616	6.29	0.509	3.20161	0.38818	71.00299	1.4	-1.01182
0.6	7.36	0.615	6.29	0.502	3.15758	0.34415	69.75919	2.358	-2.01385
0.7	7.39	0.61	6.24	0.515	3.2136	0.40017	71.28818	3.577	-3.17683
0.8	7.47	0.572	6.49	0.478	3.10222	0.28879	72.60323	4.944	-4.65521
0.9	7.46	0.622	6.45	0.522	3.3669	0.55347	72.56062	6.444	-5.89053
1	7.51	0.625	6.3	0.528	3.3264	0.51297	70.86871	8.07	-7.55703
1.1	7.53	0.613	6.28	0.518	3.25304	0.43961	70.47482	10.01	-9.57039
1.2	7.51	0.637	6.3	0.53	3.339	0.52557	69.79705	12.36	-11.83443
1.3	7.53	0.637	6.39	0.527	3.36753	0.5541	70.20646	14.664	-14.1099
1.4	7.52	0.669	6.31	0.561	3.53991	0.72648	70.36363	17.346	-16.61952
1.5	7.46	0.653	6.45	0.532	3.4314	0.61797	70.44	20.64	-20.02203